

**NOVEL REDOX NON-INNOCENT BIS(PHENOXIDE) PINCER
COMPLEXES OF COBALT: CONNECTING ELECTRONIC
STRUCTURES AND REACTIVITY**

A Dissertation
Presented to
The Academic Faculty

by

Caleb Frank Harris

In Partial Fulfillment
of the Requirements for the Degree
Doctor of Philosophy in the
School of Chemistry and Biochemistry

Georgia Institute of Technology
August 2017

COPYRIGHT © 2017 BY CALEB F. HARRIS

**NOVEL REDOX NON-INNOCENT BIS(PHENOXIDE) PINCER
COMPLEXES OF COBALT: CONNECTING ELECTRONIC
STRUCTURES AND REACTIVITY**

Approved by:

Dr. Jake D. Soper, Advisor
School of Chemistry and Biochemistry
Georgia Institute of Technology

Dr. Z. John Zhang
School of Chemistry and Biochemistry
Georgia Institute of Technology

Dr. Joseph P. Sadighi
School of Chemistry and Biochemistry
Georgia Institute of Technology

Dr. Julia Kubanek
School of Biology
Georgia Institute of Technology

Dr. E. Kent Barefield
School of Chemistry and Biochemistry
Georgia Institute of Technology

Date Approved: July 28, 2017

In loving memory of my father, Marvin F. Harris.

TABLE OF CONTENTS

LIST OF TABLES	viii
LIST OF FIGURES	ix
LIST OF SCHEMES	xiii
LIST OF SYMBOLS AND ABBREVIATIONS	xv
SUMMARY	xvii
CHAPTER 1. Introduction	1
1.1 Metal Catalyzed C-C Bond Forming Reactions and Their Significance	1
1.1.1 Cross-Coupling	1
1.1.2 Oxidative Coupling	3
1.2 Importance of Earth-Abundant 3d Metals for C–C Bond Forming Reactions	3
1.3 Introduction to Redox Non-Innocent Ligands	4
1.4 Determination of Ligand and Metal Physical Oxidations States	5
1.5 Electronic Isomers/Valence Tautomerism	6
1.6 Redox-Active Ligated Metal Complexes in Organic Transformations	8
1.7 Project Aims	9
1.8 References	10
CHAPTER 2. Redox-Active Bis(phenolate) N-heterocyclic Carbene Pincer Ligands Support Cobalt Electron Transfer Series Spanning Four Oxidation States	16
2.1 Note on Collaboration	16
2.2 Introduction	16
2.3 Results	20
2.3.1 Synthesis of the Diphenolate NHC Ligands	20
2.3.2 Synthesis and Characterization of the Cobalt Complexes	21
2.3.3 Electrochemistry	28
2.3.4 Synthesis and Structure of the [$^{\text{S}}\text{OCO}$]Co(THF)] Electron Transfer Series	30
2.3.5 EPR Spectroscopy	34
2.3.6 Computed Electronic Structures of 1 , 1 ⁺ , and 1 ²⁺	36
2.3.7 Electronic Spectra of the ET Series	40
2.4 Discussion	50
2.4.1 Physical Oxidation States in the ($^{\text{S}}\text{OCO}$)Co Electron Transfer Series	50
2.4.2 Effects of NHC Unsaturation on Ligand-Centered Oxidations	51
2.4.3 ($^{\text{S}}\text{OCO}$) as a Platform for Multielectron Transformations at Cobalt	53
2.5 Reactivity of the [$^{\text{S}}\text{OCO}$]Co(THF)] Series	54
2.5.1 Transmetalation to Complex 1 ⁺	54
2.5.2 Reaction with One-Electron Halogen Source	54
2.5.3 Reaction with (Tosyliminoiodo)benzene	56

2.6	Conclusions and Future Work	59
2.7	Experimental	60
2.7.1	General Considerations	60
2.7.2	Materials and Methods	62
2.7.3	Synthesis of $[\text{H}_3(^{\text{S}}\text{OCO})]\text{Cl}$	62
2.7.4	Synthesis of $[\text{H}_3(^{\text{Ph}}\text{OCO})]\text{Cl}$	63
2.7.5	Synthesis of Complexes 1 – 3	63
2.7.6	Synthesis of $[(^{\text{S}}\text{OCO})\text{Co}(\text{MeCN})]$ (1)	64
2.7.7	Synthesis of $[(^{\text{S}}\text{OCO})\text{Co}(\text{THF})]$ (1)	64
2.7.8	Synthesis of $[(\text{OCO})\text{Co}(\text{MeCN})]$ (2)	65
2.7.9	Synthesis of $[(^{\text{Ph}}\text{OCO})\text{Co}(\text{MeCN})]$ (3)	65
2.7.10	Synthesis of Complex 4	65
2.7.11	Synthesis of Complex 5	66
2.8	X-ray Crystallography	66
2.8.1	General Considerations	66
2.8.2	$[(^{\text{S}}\text{OCO})\text{Co}(\text{MeCN})]$ (1)	67
2.8.3	$[(\text{OCO})\text{Co}(\text{MeCN})]$ (2)	67
2.8.4	$[(^{\text{Ph}}\text{OCO})\text{Co}(\text{MeCN})]$ (3)	68
2.8.5	$[(^{\text{S}}\text{OCO})\text{Co}(\text{THF})]$ (1-THF)	69
2.8.6	$[(^{\text{S}}\text{OCO})\text{Co}(\text{THF})_2](\text{Ph}_4\text{B})$ (1⁺)	70
2.8.7	$[(^{\text{S}}\text{OCO})\text{Co}(\text{THF})_3](\text{PF}_6)_2$ (1²⁺)	70
2.8.8	Complex 4	71
2.8.9	Complex 5	72
2.9	Computational Studies	73
2.10	References	74
 CHAPTER 3. Photoinduced Radical Trifluoromethylation of (Hetero)Aryl C–H Bonds		
		83
3.1	Introduction	83
3.2	Results and Discussion	85
3.1.1	Synthesis and Characterization of the Complexes	85
3.1.2	Electronic Absorption Spectra of $[(^{\text{S}}\text{OCO})\text{Co}(\text{CF}_3)(\text{MeCN})]$	90
3.1.3	Nuclear Magnetic Resonance	93
3.2	Electrochemistry	97
3.2.1	Stability Studies	100
3.2.2	Calculated Absorbance Spectrum of $[(^{\text{S}}\text{OCO})\text{Co}(\text{CF}_3)(\text{MeCN})]$	101
3.3	Radical Trifluoromethylation	106
3.3.1	Radical Trapping of $\cdot\text{CF}_3$ with TEMPO	106
3.3.2	Radical Trifluoromethylation of Organic Substrates	109
3.3.3	Attempts at Ligand Directed C–H Trifluoromethylation	112
3.4	Towards Catalytic Methods	115
3.4.1	Synthesis and Characterization of a Trifluoroacetate Complex	115
3.4.2	Electronic Absorption Spectra of $[(^{\text{S}}\text{OCO})\text{Co}(\text{O}_2\text{CCF}_3)]$	117
3.4.3	Efforts Towards Catalytic Trifluoromethylation via $[(^{\text{S}}\text{OCO})\text{Co}(\text{O}_2\text{CCF}_3)]$	118
3.5	Conclusions and Future Directions	119
3.6	Experimental	119
3.6.1	General Considerations	119

3.6.2	Materials and Methods	121
3.6.3	Synthesis of [$(^{Ph}OCO)Co(^{Ph}OCO-CF_3)$] (2)	121
3.6.4	Synthesis of [$(^SOCO)Co(CF_3)(MeCN)$] (4)	122
3.6.5	Synthesis of [$(^SOCO)Co(CF_3)(OH_2)_2$] (4 ⁺)	122
3.6.6	Synthehsis of [$(^SOCO)Co(CF_3)(MeCN)_2$] (5)	123
3.6.7	Synthesis of [$(^SOCO)Co(CF_3)(2-ppy)$] (6)	123
3.6.8	Synthesis of [$(^SOCO)Co(O_2CCF_3)$] (7)	124
3.6.9	General Procedure for C-H Trifluoromethylation of (Hetero)Aryls	124
3.7	X-ray Crystallography	125
3.7.1	General Considerations	125
3.7.2	[$(^{Ph}OCO)Co(^{Ph}OCO-CF_3)$] (2)	125
3.7.3	[$(^SOCO)Co(CF_3)(MeCN)$] (4)	126
3.7.4	[$(^SOCO)Co(CF_3)(OH_2)_2$][OTf] (4 ⁺)	126
3.7.5	[$(^SOCO)Co(CF_3)(MeCN)_2$] (5)	127
3.7.6	[$(^SOCO)Co(CF_3)(2-ppy)$] (6)	128
3.7.7	[$(^{Ph}OCO)Co(^{Ph}OCO-CF_3)$] (7)	128
3.8	Computational Methods	129
3.9	References	130
 CHAPTER 4. Metal-ligand Cooperativity Supports CF₃ Radical Generation from Electrophillic CF₃ Sources		135
4.1	Note on Collaboration	135
4.2	Introduction	135
4.3	Results and Discussion	138
4.3.1	Radical Trapping of Electrophilic CF ₃ Reagents with TEMPO	138
4.3.2	Evaluation of High Valent Co–CF ₃ Complexes for [•] CF ₃ Transfer	142
4.3.3	Electronic Spectroscopy	142
4.3.4	Reactivity with Silyl Enol Ethers	146
4.4	Mechanistic Studies	150
4.5	Conclusions and Future Direction	154
4.5.1	Conclusions	154
4.5.2	Future Directions	156
4.6	Experimental	156
4.6.1	General Considerations	156
4.6.2	Materials and Methods	157
4.6.3	General Procedures for Radical Trifluoromethylation	157
4.7	References	158
 CHAPTER 5. Conclusions and Future Directions		161
5.1	Conclusions	161
5.2	Future Directions	163
5.3	References	164
 APPENDIX A. Mechanistic Studies on Nickel-Catalyzed Direct Oxidative Alkynylation of Azole Derivatives		165
A.1	Introduction	165
A.2	Synthesis and Characterization	167

A.3	Results and Discussion	171
A.3.1.	Oxidative Coupling	171
A.3.2.	Base Effects	172
A.3.3.	Synthesis and Characterization of the (^{Ph}OCO)Ni ^{II} Benzoxazole Complex	174
A.3.4.	Attempted Synthesis of the (^{Ph}OCO)Ni ^{II} Acetylene Complex	176
A.4	Conclusions and Future Directions	176
A.4.1.	Activation of Benzoxazole.	177
A.4.2.	H/D Exchange	177
A.4.3.	Substrate Scope	178
A.4.4.	Facile Synthesis of Enynimine Synthons	178
A.5	References	180
 APPENDIX B. Towards Cobalt Catalyzed C–H Bond Amination and an (ONO)		
	Ligand Scaffold	184
B.1.	Introduction	184
B.2.	Project Summaries	184
B.2.1.	C–H Bond Amination of Aryl Sulfonyl Azides	184
B.2.2.	Synthesis and Characterization of an ($^{\delta}OCO$) Cobalt Azide Complex	185
B.2.3.	Synthesis and Characterization of (ONO) Cobalt Complexes	187
B.3.	Experimental	191
B.3.1.	General Considerations	191
B.3.2.	Synthesis of the ONO Ligand	191
B.3.3.	Synthesis of [$^{\delta}OCO$)Co(N ₃)(MeCN) ₂]	192
B.3.4.	Synthesis of [(ONO)Co(MeCN)] ₂	192
B.3.5.	Synthesis of [(ONO)Co(py) ₃]	193
B.4.	X-ray Crystallography	193
B.4.1.	General Considerations	193
B.4.2.	[($^{\delta}OCO$)Co(N ₃)(MeCN) ₂]	194
B.4.3.	[(ONO)Co(MeCN)] ₂	195
B.4.4.	[(ONO)Co(py) ₃]	195
Vita		198

LIST OF TABLES

Table 2.1	Redox potentials (V vs. Fc^+/Fc) of complexes 1 – 3 .	29
Table 2.3	Relevant MOs for 1 . Generated with IboView, iso surface threshold set at 80.0.	43
Table 2.4	Relevant MOs for 1 ⁺ . Generated with IboView, iso surface threshold set at 80.0.	48
Table 3.1	Redox potentials (V) in coordinating vs. non-coordinating solvent.	99
Table 3.2	Relevant calculated MOs for complex 4 generated with IboView with the iso surface set at 80.0.	103
Table 4.1	Radical trifluoromethylation of silyl enol ethers by complex 1 and 3b . Yields were determined by ¹⁹ F yields against an internal standard.	149
Table A.1	Optimization of reaction conditions.	172
Table A.2	Possible substrates for future investigation.	178

LIST OF FIGURES

Figure 1.1	Select bond metrics of an amidophenolate ligated Pd complex in three different oxidation states.	6
Figure 2.1	ORTEP plot of [$(^S\text{OCO})\text{Co}(\text{MeCN})$], complex 1 , with thermal ellipsoids are drawn at 50% probability.	22
Figure 2.2	ORTEP plot of [$(\text{OCO})\text{Co}(\text{MeCN})$], complex 2 , with thermal ellipsoids are drawn at 50% probability.	23
Figure 2.3	ORTEP plot of [$(^{Ph}\text{OCO})\text{Co}(\text{MeCN})$], complex 3 , with thermal ellipsoids are drawn at 50% probability.	23
Figure 2.4	Selected bond lengths [\AA] across the series 1 – 3 .	25
Figure 2.5	Bond lengths [\AA] for the NHC–Co–NCCH ₃ fragments in 1 - 3 .	27
Figure 2.6	Stacked cyclic voltammograms of complexes 1 – 3 in MeCN.	29
Figure 2.7	ORTEP plot of [$(^S\text{OCO})\text{Co}(\text{THF})$], complex 1 , with thermal ellipsoids are drawn at 50% probability.	31
Figure 2.8	ORTEP plot of [$(^S\text{OCO})\text{Co}(\text{THF})_2$][BPh ₄], complex 1 ⁺ , with thermal ellipsoids are drawn at 50% probability.	32
Figure 2.9	ORTEP plot of [$(^S\text{OCO})\text{Co}(\text{THF})_3$][PF ₆] ₂ , complex 1 ²⁺ , with thermal ellipsoids are drawn at 50% probability.	34
Figure 2.10	X-band EPR spectrum of a THF-derived sample of 1 in toluene glass at 20 K.	35
Figure 2.11	Top: Spin density plot of 1 ($S = 1/2$), generated with IQMol (isosurface value 0.005). Bottom: Spin density per atom for the THF adduct of 1 ($S = 1/2$).	37
Figure 2.12	Top: Spin density plot of 1 ⁺ ($S = 1$), generated with IQMol (isosurface value 0.005). Bottom: Spin density per atom for the bis THF adduct of 1 ⁺ ($S = 1$).	38
Figure 2.13	Top: Spin density plot of 1 ²⁺ ($S = 1/2$), generated with IQMol (isosurface value 0.005). Bottom: Spin density per atom for the tris THF adduct of 1 ²⁺ ($S = 1/2$).	39

Figure 2.14	Key resonance structures of the closed-shell (a) and open-shell singlet (b) configurations of the doubly oxidized, charge neutral ($^{\text{S}}\text{OCO}^0$) ligand.	40
Figure 2.15	Calculated and experimental UV-Vis absorption spectrum of 1 in THF.	42
Figure 2.16	Calculated UV-Vis absorption spectrum of 1 in THF with single line absorption energies.	42
Figure 2.17	Calculated and experimental UV-Vis absorption spectrum of 1 ⁺ in THF.	47
Figure 2.18	Calculated UV-Vis absorption spectrum of 1 ⁺ in THF with single line absorption energies.	47
Figure 2.19	ORTEP plot of complex 4 with thermal ellipsoids are drawn at 50% probability.	56
Figure 2.20	ORTEP plot of complex 5 with thermal ellipsoids are drawn at 50% probability.	59
Figure 3.1	ORTEP plot of [$(^{\text{Ph}}\text{OCO})\text{Co}(^{\text{Ph}}\text{OCO}-\text{CF}_3)$], complex 2 , with thermal ellipsoids are drawn at 50% probability.	86
Figure 3.2	ORTEP plot of [$(^{\text{S}}\text{OCO})\text{Co}(\text{CF}_3)(\text{MeCN})$], complex 4 , with thermal ellipsoids are drawn at 50% probability.	87
Figure 3.3	ORTEP plot of [$(^{\text{S}}\text{OCO})\text{Co}(\text{CF}_3)(\text{MeCN})_2$], complex 5 , with thermal ellipsoids are drawn at 50% probability.	88
Figure 3.4	UV-Vis absorption spectra of 4 in Et ₂ O and MeCN at 22 °C.	91
Figure 3.5	Variable temperature UV-Vis spectra of 4 in Et ₂ O with a temperature range of -30 to 20 °C.	92
Figure 3.6	Variable temperature UV-Vis spectra in MeCN with a temperature range of 20 to 80 °C.	93
Figure 3.7	¹ H NMR spectrum of complex 5 in acetonitrile- <i>d</i> ₃ .	94
Figure 3.8	¹ H NMR spectrum of complex 4 in CDCl ₃ .	94
Figure 3.9	VT- ¹ H NMR spectra of 5 in acetonitrile- <i>d</i> ₃ from 25 (purple) to 75 °C (red) in 10 °C increments.	96
Figure 3.10	Cyclic voltammogram of complex 4 in both coordinating and non-coordinating solvents.	98

Figure 3.11	ORTEP plot of complex 4 ⁺ with thermal ellipsoids are drawn at 50% probability.	99
Figure 3.12	UV-Vis spectrum of complex 4 in Et ₂ O over 18 h with scans each hour from T = 0 h to T = 18 h under ambient light.	101
Figure 3.13	UV-Vis spectrum of complex 5 in MeCN at T = 0 h and after 18 h under ambient light.	101
Figure 3.14	Simulated and experimental UV-Vis spectra for complex 4 in Et ₂ O.	102
Figure 3.15	Calculated single line absorption spectrum of complex 4 in Et ₂ O.	103
Figure 3.16	¹⁹ F NMR spectrum of a radical trap experiment in C ₆ H ₆ after 3h under a 16W CFL at ambient temperature.	107
Figure 3.17	¹⁹ F NMR spectrum of a radical trap experiment in MeCN after 3h under a 16W CFL at ambient temperature.	108
Figure 3.18	Qualitative molecular orbital description of the 5- and 6-coordinate complexes.	108
Figure 3.19	Radical trifluoromethylation of arenes and heteroarenes by complex 4 under photolytic conditions.	110
Figure 3.20	Signals observed for HCF ₃ and DCF ₃ when complex 4 was exposed to photolytic conditions in protic vs. deuterated cyclohexane.	111
Figure 3.21	ORTEP plot of [(^s OCO)Co(CF ₃)(2-ppy)], complex 6 , with thermal ellipsoids are drawn at 50% probability.	114
Figure 3.22	Substrates evaluated for ligand directed C-H trifluoromethylation by 4 .	115
Figure 3.23	ORTEP plot of [(^s OCO)Co(O ₂ CCF ₃)], complex 7 , with thermal ellipsoids are drawn at 50% probability.	116
Figure 3.24	UV-Vis spectrum of complex 7 in NMP over 2 h with scans every 10 min from T = 0 min to T = 120 min under 365 nm light.	118
Figure 4.1	Commonly used electrophilic trifluoromethylation reagents.	137
Figure 4.2	Crude ¹⁹ F NMR of the reaction between complex 1 and the Umemoto Reagent, 3b , in the presence of TEMPO.	140

Figure 4.3	Crude ^{19}F NMR of the reaction between complex 1 and the Togni II Reagent, 4a , in the presence of TEMPO.	140
Figure 4.4	Comparison of UV-Vis spectra in CH_2Cl_2 of: 1 , 1 with TEMPO, 1 with TEMPO and 3b , 6 , and 6 with dibenzothiophene.	144
Figure 4.5	Comparison of UV-Vis spectra in CH_2Cl_2 of: 2 with 4a , and 7 .	145
Figure 4.6	Crude ^{19}F NMR of the reaction between 1-phenyl-1-trimethylsiloxyethylene and 1.5 eq. of the Umemoto reagent with 5% loading of complex 1 after 18h.	147
Figure 4.7	Crude ^{19}F NMR of the reaction between 1-phenyl-1-trimethylsiloxyethylene and 1.5 eq. of the Togni II reagent with 5% loading of complex 1 after 3h.	148
Figure 4.8	UV-Vis spectra in CH_2Cl_2 of the crude reaction mixture after each turnover for the first 8 cycles.	151
Figure 4.9	UV-Vis spectrum of $[(^s\text{OCO})\text{Co}(\text{CF}_3)(\text{OH}_2)_2][\text{OTf}]$ in CH_2Cl_2 .	152
Figure 4.10	Proposed reaction mechanism for the catalytic trifluoromethylation of silyl enol ethers.	154
Figure 5.1	Proposed ligands for future studies.	163
Figure A.1	Connectivity plot of the complex 4 .	169
Figure A.2	Connectivity plot of the complex 5 .	169
Figure A.3	Stacked ^1H NMR spectra of complex 3 in CD_2Cl_2 from 6.80 to 8.30 ppm.	171
Figure A.4	Connectivity plot of 6 .	173
Figure B.1	ORTEP plot of $[(^s\text{OCO})\text{Co}(\text{N}_3)(\text{MeCN})_2]$ with thermal ellipsoids are drawn at 50% probability.	186
Figure B.2	ORTEP plots of the complex $[(\text{ONO})\text{Co}(\text{MeCN})]_2$.	188
Figure B.3	ORTEP plot of $[(\text{ONO})\text{Co}(\text{py})_3]$.	190
Figure B.4	ORTEP plot of $[(\text{ONO})\text{Co}^{\text{II}}\text{Cl}](\text{Li-12-c-4})$.	190

LIST OF SCHEMES

Scheme 1.1	General mechanism for transition metal catalyzed cross-coupling.	2
Scheme 1.2	General mechanism for transition metal catalyzed oxidative coupling.	2
Scheme 1.3	Accessible redox states of <i>ortho</i> -quinoid derivatives.	5
Scheme 1.4	Valence tautomerism of N ^N ligated bis(catacholate) cobalt complexes.	7
Scheme 1.5	Valence tautomerism of ONO bis(dioxolene) cobalt complexes.	8
Scheme 2.1	Proposed catalytic cycle for the Negishi-type cross-coupling using the bis(amidophenolate) Co ^{III} .	17
Scheme 2.2	Redox capacity of the proposed ligand scaffold.	18
Scheme 2.3	Synthesis of the (OCO) prolignands.	20
Scheme 2.4	Synthesis of the Co ^{II} complexes 1 – 3 .	21
Scheme 2.5	Possible mechanistic pathway to form complex 5 .	50
Scheme 3.1	Outcomes of complexes 1 and 3 when treated with AgCF ₃ .	76
Scheme 3.2	Possible free radical pathway for Co-mediated trifluoromethylation of arenes.	98
Scheme 4.1	Reaction of a bis(amidophenolate) copper complex with 3b .	123
Scheme 4.2	Reasonable mechanism to produce a 6-coordinate, formal Co ^{IV} complex by treating 1 with 4a .	126
Scheme 4.3	Attempted capture of [•] CF ₃ by TEMPO from formal Co ^{III} and Co ^{IV} Co-CF ₃ complexes	127
Scheme 4.4	Major products likely produced from the reaction of 1 with 3b and 1 with 4a .	129
Scheme 4.5	Proposed mechanism for the reduction of a metal complex by a tertiary organic radical formed under reaction conditions.	130
Scheme A.1	General approach to metal-catalyzed direct oxidative coupling.	166

Scheme A.2.	Methods for alkynylation of heteroaryl moieties.	166
Scheme A.3	Model reaction for mechanistic investigation.	167
Scheme A.4	Synthesis of the (^{Ph}OCO)Ni ^{II} complex.	167
Scheme A.5	Generation of enynimine product 6 .	173
Scheme A.6	Lability of benzoxazole coordination to (^{Ph}OCO)Ni ^{II} .	175
Scheme A.7	Proposed catalytic cycle.	176
Scheme A.8	Base catalyzed deuterium/hydrogen exchange experiment.	178
Scheme A.9	Synthesis of asymmetric enynimines.	179
Scheme B.1	Cobalt catalyzed C-H amination of aryl sulfonyl azide.	185
Scheme B.2	Synthesis of [^{S}OCO)Co(N ₃)(MeCN) ₂].	186
Scheme B.3	Synthesis of the ONO ligand.	187
Scheme B.4	Synthesis of the complex [(ONO)Co(MeCN)] ₂ .	188

LIST OF SYMBOLS AND ABBREVIATIONS

~	About/Approximately
Å	Angstrom
α	Alpha
δ	Chemical Shift
°	Degree(s)
°C	Degree(s) Celsius
λ	Wavelength
ATR	Attenuated Total Reflection
approx.	Approximately
CFL	Compact Fluorescent Lamp
CH ₂ Cl ₂	Dichloromethane
CHCl ₃	Chloroform
CT	Charge Transfer
CV	Cyclic Voltammogram
D	Deuterium
EPR	Electron Paramagnetic Resonance
ESI	Electrospray Ionization
FTIR	Fourier Transform Infrared
g	Grams
HOMO	Highest Occupied Molecular Orbital
IR	Infrared
LMCT	Ligand-to-Metal Charge Transfer

LUMO	Lowest Unoccupied Molecular Orbital
MeCN	Acetonitrile
MeOH	Methanol
mg	Milligram(s)
MHz	Megahertz
min	Minute
mmol	Millimole
mol	Mole
mg	Milligram
nm	Nanometers
ORTEP	Oak Ridge Thermal Ellipsoid Plot
ppm	Parts Per Million
r.t.	Room Temperature
s	Second(s)
SOMO	Singly Occupied Molecular Orbital
TEMPO	2,2,6,6-dimethylpiperdine-1-oxyl
THF	Tetrahydrofuran
TMS	Tetramethylsilane
UV	Ultraviolet
vis	Visible
VT	Variable Temperature

SUMMARY

This thesis details the synthesis, characterization, and reactivity of a variety of new cobalt complexes containing redox-active, pincer-type ligands based on an N-heterocyclic carbene (NHC) centered, bis(phenoxide) scaffold (OCO). Described within are also the first-ever reported direct C–H bond trifluoromethylation reactions facilitated by a cobalt complex.

Chapter 1 provides a general overview of the background relevant to the work outlined in the thesis. In this Chapter, the significance of transition metals in C–C bond forming reactions and some of their mechanisms are briefly discussed. Redox non-innocent ligands are introduced and their electronic and physical properties are examined. The capacity of redox-active ligands to mediate organometallic-type, multielectron reactions at base metals is also highlighted, and a summary of recent successes in using such ligands for redox transformations of small molecules is presented.

Chapter 2 describes, in detail, the synthesis and electronic structures of a new series of (OCO)-ligated cobalt complexes. The complexes span formal oxidation states from Co^{II} to Co^{V} within a 1.5 V applied potential range. Experimental and computational data are presented which describe the physical oxidation states of the non-innocent ligand/metal combinations as well as the effects of altering the degree of saturation in the backbone of the NHC moiety. Preliminary efforts towards utilization of these complexes for C–C and C–N coupling reactions are discussed. Whereas outer-sphere oxidants give isolable high-valent Co complexes, treatment with one- and two- electron oxidants that form new Co–X bonds, instead generally leads to the decomposition of the ligand. The

outcomes suggest new strategies are needed to protect the (OCO) ligand backbone against deleterious attack by reactive small molecule fragments.

One strategy to address this problem is presented in Chapter 3. Two of the (OCO) complexes described in Chapter 2 are treated with a radical CF_3 source and their products are described. In one case, the ligand forms an unexpected $\text{C}-\text{CF}_3$ bond, but in another, a new complex containing a $\text{Co}-\text{CF}_3$ bond is formed. The isolated $\text{Co}-\text{CF}_3$ complex is either 5- or 6-coordinate depending on the solvent and thermal environment. The 5-coordinate complex is photosensitive and is capable of $\text{Co}-\text{CF}_3$ bond homolysis upon exposure to visible light. This allows for the direct trifluoromethylation of unactivated arene and heteroarene $\text{C}-\text{H}$ bonds. Interestingly, the 6-coordinate species is unaffected by visible light. The differences in reactivity are discussed in the context of variations in geometry and electronic structure. A κ^2 -trifluoroacetate complex was also synthesized and found to undergo $\text{Co}-\text{O}$ bond homolysis under visible light. This complex is also competent to trifluoromethylate aryl $\text{C}-\text{H}$ bonds, presumably through a radical decarboxylation mechanism.

Chapter 4 describes the use of one of the (OCO) pincer cobalt complexes in catalytic trifluoromethylation of silyl enol ethers using commercially available electrophilic CF_3 reagents. A single electron transfer mechanism is proposed to impart radical character on the CF_3 reagents, thus destabilizing the compounds and causing them to deliver a CF_3 radical. The radical attacks the unsaturated bond of the enol ether, producing a tertiary organic radical which reduces the oxidized metal back to its original oxidation state. The organic compound then forms an α -trifluoromethyl ketone and an ionic salt byproduct. The cobalt complex is capable of facilitating this SET mechanism

in multiple oxidation states, demonstrating the unique versatility of the ligand/metal platform for catalytic C–C bond formation.

Chapter 5 acts as a conclusion to the thesis and describes future directions for work that may develop from the projects described within. The Appendices which follow, detail the synthesis and characterization of additional (OCO) cobalt and nickel complexes and a structurally similar (ONO) bis(phenoxide) ligand scaffold that contains a pyridine linker in place of the NHC. Preliminary results associated with C–C and C–N bond forming reactions are also discussed.

CHAPTER 1. INTRODUCTION

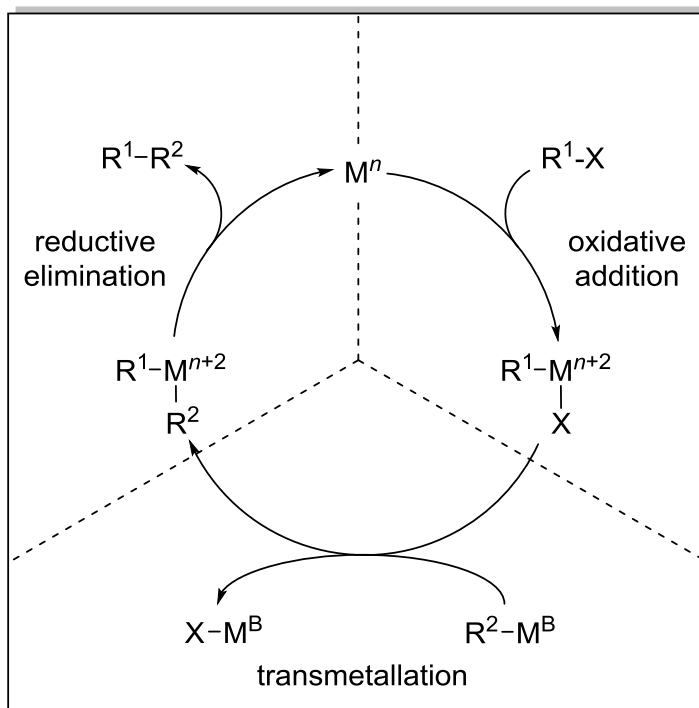
1.1 Metal Catalyzed C-C Bond Forming Reactions and Their Significance

1.1.1 Cross-Coupling

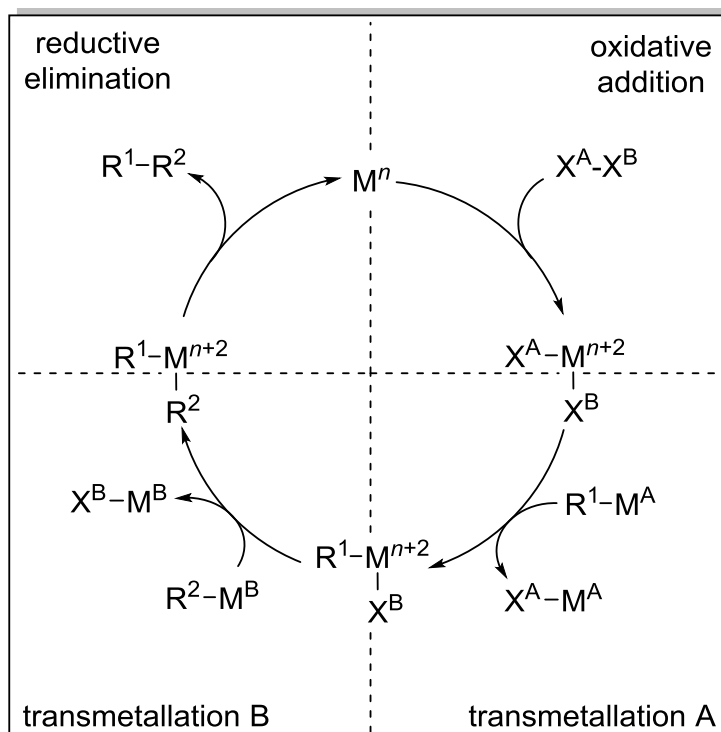
In past decades, transition metal cross-coupling methods have become powerful and reliable tools for C–C and C-heteroatom bond forming reactions, allowing complex molecular structures to be prepared in efficient and economical manners.¹⁻² Cross-coupling reactions involving activated electrophiles, such as aryl-, vinyl-, or alkyl-(pseudo)halides with organometallic nucleophiles (*i.e.* Heck, Kumada, Negishi, Stille, Suzuki–Miyaura, and Hiyama couplings) are now indispensable tools for pharmaceutical, agricultural, and materials industries.¹⁻⁶

The canonical mechanism for metal catalyzed cross-coupling is shown in Scheme 1.1. The three main parts of the mechanism include: (1) *Oxidative addition* of an $\mathbf{R}^1\text{--X}$ compound to a low-valent metal via concerted two-electron reduction of a C–X bond. (2) *Transmetalation* of the organometallic nucleophile to the catalytic metal center to form an intermediate $\mathbf{R}^1\text{--M--R}^2$ species. (3) *Reductive elimination* from the oxidized metal center via a second concerted two-electron step to produce the new $\mathbf{R}^1\text{--R}^2$ bond and reform the initial metal complex. Metals utilized in these reactions are most typically later 4*d* and 5*d* transition metals, including Pt, Ir, Ru, Rh, and especially Pd.^{2-3, 7}

Scheme 1.1. General mechanism for transition metal catalyzed cross-coupling.



Scheme 1.2. General mechanism for transition metal catalyzed oxidative coupling.



1.1.2 Oxidative Coupling

Transition metal catalyzed oxidative coupling represents an alternative to cross-coupling for C–C bond formation, allowing the coupling of two nucleophiles with the use of a sacrificial oxidant.⁸⁻⁹ As outlined in Scheme 1.2, the mechanism for oxidative coupling involves the same basic steps that occur in traditional cross-coupling, however a second transmetallation process is required to introduce both organic moieties to the metal center.

Historically, the development of oxidative coupling reactions lagged behind that of cross-coupling, at least in part due to the requirement for stoichiometric, typically halogen-containing co-oxidants.¹⁰⁻¹² During the past decade, much attention has been paid to developing novel methods for the oxidative coupling of two hydrocarbons by utilizing O₂ as the terminal oxidant, producing only water as the byproduct.¹³⁻¹⁵ However, achieving regioselectivity with this method of C–H activation is difficult.^{10, 16-19} Although this area is still in its infancy, bond formations between two nucleophiles have tremendous potential in the area of sustainable chemistry and environmental impact.

1.2 Importance of Earth-Abundant 3d Metals for C–C Bond Forming Reactions

Cost and toxicity concerns motivate efforts to replace precious metal cross-coupling catalysts with Earth-abundant and benign alternatives.²⁰⁻²¹ In these respects, later first-row transition metals are especially attractive and significant effort has been invested in the development of Fe, Co, Ni and Cu catalysts for such transformations.^{12, 22-25} Some of these metals have demonstrated a capacity to mimic Pd cross-coupling, but have also provided access to entirely new reactions that are challenging with state-of-the-

art Pd methods.^{5, 23} Despite this promise, significant challenges remain for widespread adoption of base metal catalysts, especially those containing Fe and Co, as Pd surrogates. Base metal species are prone to non-selective radical reactions and the catalysts are often very poorly defined, complicating efforts to develop the mechanistic understanding that underpins rational catalyst design.^{5, 12, 21-23, 26}

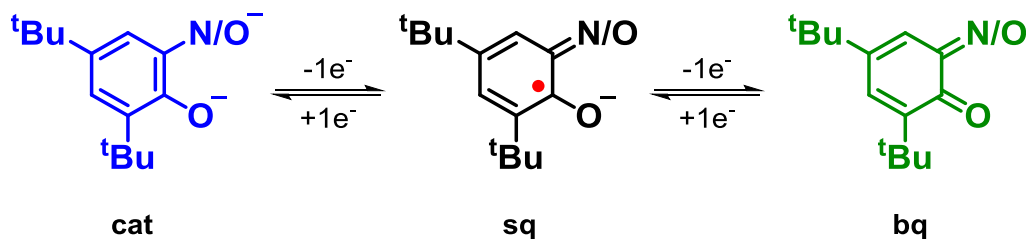
1.3 Introduction to Redox Non-Innocent Ligands

One strategy to impart a multielectron capacity at $3d$ metals and avoid unwanted radical pathways is to expand the redox sphere beyond the metal center.²¹ This is exemplified by metalloenzymes that accomplish multielectron bond making and bond breaking redox reactions via coordinated electron transfer by the metal center and the redox non-innocent protein radicals within the primary coordination sphere.²⁷ Examples of this synergistic reactivity include oxidation of unactivated C–H bonds by cytochrome P450 and aerobic alcohol oxidation by galactose oxidase.²⁸⁻²⁹ The design principles inspired by metalloenzyme reactivity have been translated to functional small molecule models; most notably in high valent metalloporphyrin complexes, but also non-macrocyclic complexes containing redox-active ligands.³⁰

Over the past four decades, coordination chemists have elaborated the unique physical properties of such redox non-innocent ligands.^{21, 31} Early studies focused on *ortho*-quinoid chelates and their derivatives, an example of which is shown in Scheme 1.3. These ligand species can coordinate metal centers in three oxidation states: dianionic catecholate (cat), one-electron oxidized semiquinone (sq), and fully oxidized benzoquinone (bq). Important to the context of this thesis, cobalt complexes have a

particularly good energetic match between the metal and redox-active ligand frontier orbitals of amidophenolate and dioxolene systems, providing a pathway for low-energy metal–ligand charge transfer.³²⁻³⁴

Scheme 1.3. Accessible redox states of *ortho*-quinoid derivatives.



1.4 Determination of Ligand and Metal Physical Oxidations States

Determining the oxidation state of transition metal complexes containing redox non-innocent ligands is not often straightforward.³⁵ These ligands can exist in multiple oxidation states which impart significant changes in the metrical parameters of the systems.^{32, 34, 36-39} Thus, single crystal X-ray diffractometry is a valuable tool for determining the physical oxidation state, although it should not be the only tool utilized for such assignments. Electrochemistry, geometrical optimizations, density functional theory (DFT), electrotonic spectroscopy, electron paramagnetic resonance (EPR) or nuclear magnetic resonance (NMR), magnetometry, and spin density calculations are all powerful tools available to the experimentalist which can aid in proper assignment of physical oxidation states.³⁵

A body of literature has been compiled over the past 30 years containing metrical parameters for redox-active ligands in various oxidations states as well as those coordinated to various metal centers.^{32, 34, 36-39} In the amidophenolate system, a derivative

of which is focus of this thesis, the localization of spin density is evident by the loss of aromaticity in the ring. The ring takes on a quinoid-type pattern of four long and two short C–C bonds and contraction of the C–N and C–O bonds occurs, as evidenced by the palladium complex in Figure 1.1.^{35, 40}

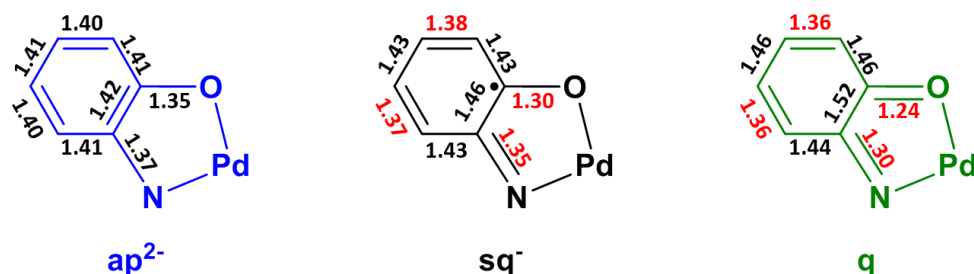


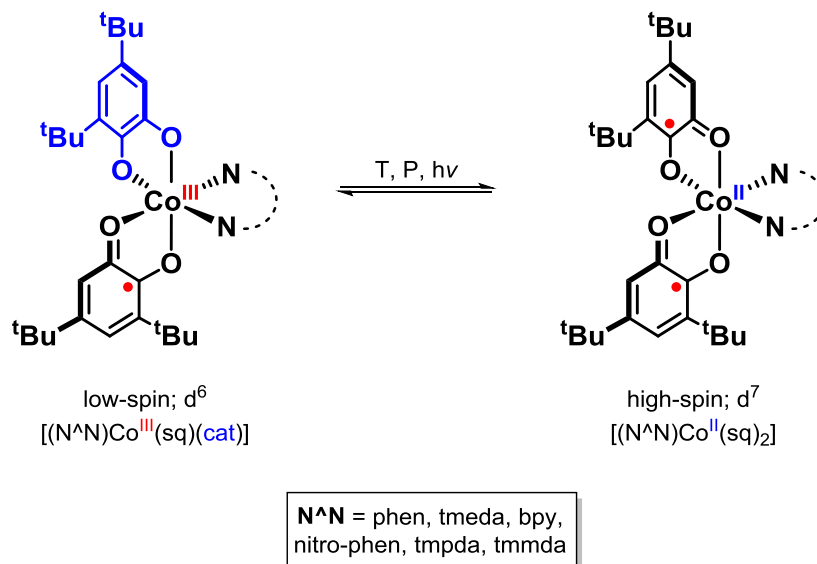
Figure 1.1. Select bond metrics of an amidophenolate ligated Pd complex in three different oxidation states.^{35,40}

1.5 Electronic Isomers/Valence Tautomerism

Accessibility to multiple electronic structures not only affects physical oxidation state assignments, it also invokes the possibility of valence tautomerism within the system.^{32-34, 41} As a result, a completely ligand-centered redox process can occur which does not affect the oxidation state of the metal, a metal-only redox event may occur which does not change the ligand oxidation state, or both the ligand and metal may change oxidation states in a synergistic fashion, resulting in ambiguity of the electronic state of both metal and ligand.^{32-35, 41} Various factors including: geometry, coordination environment, and electronic donor/acceptor ability of the ligand all affect the type of electronic interaction between redox non-innocent ligands and their coordinated metal centers.⁴² For example, a series of N^N ligated $Co(L)_2$ complexes ($L = 3,5$ -di-tert-butylsemiquinone) were observed to persist as Co^{III} metal centers with a mixed-valent

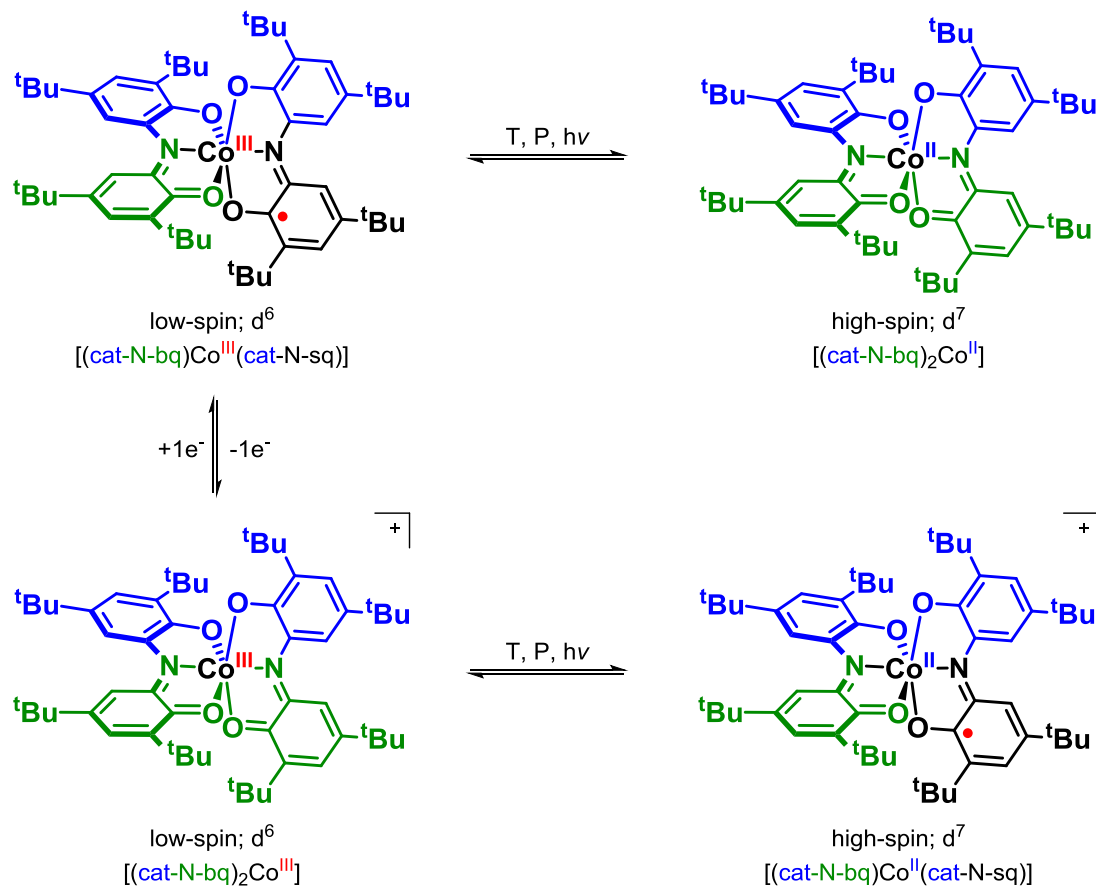
ap^{2-}/sq^- ligand set in the solid state at ambient temperature. However, at elevated temperatures in solution, the observed species is a Co^{II} metal center with two sq^- ligand radicals (Scheme 1.4).^{32, 43}

Scheme 1.4. Valence tautomerism of $N^{\wedge}N$ ligated bis(catacholate) cobalt complexes.



In another example, shown in Scheme 1.5, the complex $[(cat-N-bq)Co^{III}(cat-N-sq)]$ exhibits valence tautomerism under relatively mild perturbations, including changes in temperature, pressure, or under certain light sources.⁴⁶ These induced changes in electronic structure are due to the fact that the frontier ligand orbitals are in close energetic proximity to those of the metal. In this case, both low-spin Co^{III} complexes are capable of ligand-to-metal charge transfers (LMCT) to afford high-spin Co^{II} complexes with one-electron oxidized (ONO) ligands.

Scheme 1.5. Valence tautomerism of (ONO) bis(dioxolene) cobalt complexes.



1.6 Redox-Active Ligated Metal Complexes in Organic Transformations

Over the past decade, simple redox-active chelates have been re-discovered as electron reservoirs for small molecule organometallic-type reactivity. A selection of notable examples includes: aryl–aryl reductive elimination from Zr^{IV} ,⁴⁴ catalytic nitrene transfer at Zr^{IV} and Ta^{V} ,⁴⁵ oxidative coupling of aniline to aryl-diazene via a redox active pincer ligand complex of Ta^{V} ,⁴⁶ CO_2 reduction at Al^{III} ,⁴⁷ iron-catalyzed C–C oxidative addition and reductive elimination,⁴⁸⁻⁵¹ and iron asymmetric hydrogenation and

hydrosilation of alkenes.⁵²⁻⁵⁵ Results from our own lab involve catalytic O₂ activation and oxo transfer at high-valent rhenium,⁵⁶⁻⁵⁹ Co^{III}-catalyzed Negishi-type cross coupling of alkyl halides with alkyl- and arylzinc reagents,⁶⁰⁻⁶³ and manganese catalyzed aerobic alcohol dehydrogenations and oxidative homocoupling of aryl Grignard reagents.⁶⁴⁻⁶⁵

1.7 Project Aims

This thesis will describe the development of new redox-active pincer scaffolds on cobalt and the utility of the complexes for stoichiometric and catalytic C–C bond forming reactions. Our approach harnesses valence tautomerism to avoid thermodynamically stable and substitutionally inert oxidation states (*i.e.* Co^{III}). Specifically, this thesis answers the following questions:

1. What are the physical oxidation states and electronic structures in an electron transfer series of low-coordinate cobalt complexes supported by a family of bis(phenolate) (OCO) pincer ligands?
2. Can the (OCO) ligands support high valent Co-alkyl, -aryl, and -imido complexes which may be key intermediates in C–H bond activation mechanisms?⁶⁶⁻⁷⁰
3. Can redox-active ligand-to-Co intravalence charge transfer be used as a tool to impart radical character to ancillary ligands that might serve as synthons in catalytic processes?
4. Can intermolecular single electron transfer lead to assembly of new C–C bonds via outer-sphere radical processes and what are the oxidation states necessary to support such reactivity?

1.8 References

1. Negishi, E.-i., *Handbook of Organopalladium Chemistry for Organic Synthesis*. John Wiley & Sons: New York, 2002.
2. Meijere, A.; Diederich, F., *Metal-Catalyzed Cross-Coupling Reactions*. Second Completely Revised and Enlarged Edition ed.; Wiley-VCH: 2004.
3. Corbet, J.-P.; Mignani, G., Selected Patented Cross-Coupling Reaction Technologies. *Chemical Reviews* **2006**, *106* (7), 2651-2710.
4. Hartwig, J. F., Transition Metal Catalyzed Synthesis of Arylamines and Aryl Ethers from Aryl Halides and Triflates: Scope and Mechanism. *Angewandte Chemie International Edition* **1998**, *37* (15), 1521-3773.
5. Jana, R.; Pathak, T. P.; Sigman, M. S., Advances in Transition Metal (Pd,Ni,Fe)-Catalyzed Cross-Coupling Reactions Using Alkyl-organometallics as Reaction Partners. *Chemical Reviews* **2011**, *111* (3), 1417-1492.
6. Muci, A. R.; Buchwald, S. L., Practical Palladium Catalysts for C-N and C-O Bond Formation. In *Cross-Coupling Reactions: A Practical Guide*, Miyaura, N., Ed. Springer Berlin Heidelberg: Berlin, Heidelberg, 2002; pp 131-209.
7. Johansson Seechurn, C. C. C.; Kitching, M. O.; Colacot, T. J.; Snieckus, V., Palladium-Catalyzed Cross-Coupling: A Historical Contextual Perspective to the 2010 Nobel Prize. *Angewandte Chemie International Edition* **2012**, *51* (21), 5062-5085.
8. Cho, S. H.; Kim, J. Y.; Kwak, J.; Chang, S., Recent Advances in the Transition Metal-catalyzed Twofold Oxidative C-H Bond Activation Strategy for C-C and C-N Bond Formation. *Chemical Society Reviews* **2011**, *40* (10), 5068-5083.
9. Shi, W.; Liu, C.; Lei, A., Transition-metal Catalyzed Oxidative Cross-coupling Reactions to Form C-C Bonds Involving Organometallic Reagents as Nucleophiles. *Chemical Society Reviews* **2011**, *40* (5), 2761-2776.
10. Liu, C.; Yuan, J.; Gao, M.; Tang, S.; Li, W.; Shi, R.; Lei, A., Oxidative Coupling between Two Hydrocarbons: An Update of Recent C-H Functionalizations. *Chemical Reviews* **2015**, *115* (22), 12138-12204.
11. Liu, C.; Zhang, H.; Shi, W.; Lei, A., Bond Formations between Two Nucleophiles: Transition Metal Catalyzed Oxidative Cross-Coupling Reactions. *Chemical Reviews* **2011**, *111* (3), 1780-1824.
12. Sherry, B. D.; Fürstner, A., The Promise and Challenge of Iron-Catalyzed Cross Coupling. *Accounts of Chemical Research* **2008**, *41* (11), 1500-1511.

13. Campbell, A. N.; Stahl, S. S., Overcoming the “Oxidant Problem”: Strategies to Use O₂ as the Oxidant in Organometallic C–H Oxidation Reactions Catalyzed by Pd (and Cu). *Accounts of Chemical Research* **2012**, *45* (6), 851-863.
14. Wendlandt, A. E.; Suess, A. M.; Stahl, S. S., Copper-Catalyzed Aerobic Oxidative C–H Functionalizations: Trends and Mechanistic Insights. *Angewandte Chemie International Edition* **2011**, *50* (47), 11062-11087.
15. Yeung, C. S.; Dong, V. M., Catalytic Dehydrogenative Cross-Coupling: Forming Carbon–Carbon Bonds by Oxidizing Two Carbon–Hydrogen Bonds. *Chemical Reviews* **2011**, *111* (3), 1215-1292.
16. Dwight, T. A.; Rue, N. R.; Charyk, D.; Josselyn, R.; DeBoef, B., C–C Bond Formation via Double C–H Functionalization: Aerobic Oxidative Coupling as a Method for Synthesizing Heterocoupled Biaryls. *Organic Letters* **2007**, *9* (16), 3137-3139.
17. Stuart, D. R.; Villemure, E.; Fagnou, K., Elements of Regiocontrol in Palladium-Catalyzed Oxidative Arene Cross-Coupling. *Journal of the American Chemical Society* **2007**, *129* (40), 12072-12073.
18. Tsai, A. S.; Brasse, M.; Bergman, R. G.; Ellman, J. A., Rh(III)-Catalyzed Oxidative Coupling of Unactivated Alkenes via C–H Activation. *Organic Letters* **2011**, *13* (3), 540-542.
19. Yin, W.; He, C.; Chen, M.; Zhang, H.; Lei, A., Nickel-Catalyzed Oxidative Coupling Reactions of Two Different Terminal Alkynes Using O₂ as the Oxidant at Room Temperature: Facile Syntheses of Unsymmetric 1,3-Diynes. *Organic Letters* **2009**, *11* (3), 709-712.
20. Bolm, C., A New Iron Age. *Nature Chem* **2009**, *1* (5), 420-420.
21. Chirik, P. J.; Wieghardt, K., Radical Ligands Confer Nobility on Base-Metal Catalysts. *Science* **2010**, *327*, 794-795.
22. Gosmini, C.; Begouin, J.-M.; Moncomble, A., Cobalt-catalyzed Cross-coupling Reactions. *Chemical Communications* **2008**, (28), 3221-3233.
23. Hu, X., Nickel-catalyzed Cross Coupling of Non-activated Alkyl Halides: A Mechanistic Perspective. *Chemical Science* **2011**, *2* (10), 1867-1886.
24. Norinder, J.; Matsumoto, A.; Yoshikai, N.; Nakamura, E., Iron-Catalyzed Direct Arylation through Directed C–H Bond Activation. *Journal of the American Chemical Society* **2008**, *130* (18), 5858-5859.
25. Sarhan, A. A. O.; Bolm, C., Iron(III) Chloride in Oxidative C–C Coupling Reactions. *Chemical Society Reviews* **2009**, *38* (9), 2730-2744.

26. Hess, W.; Treutwein, J.; Hilt, G., Cobalt-Catalysed Carbon-Carbon Bond-Formation Reactions. *Synthesis* **2008**, 2008 (22), 3537-3562.
27. Krüger, H.-J., What Can We Learn from Nature about the Reactivity of Coordinated Phenoxyl Radicals?—A Bioinorganic Success Story. *Angewandte Chemie International Edition* **1999**, 38 (5), 627-631.
28. Whittaker, J. W., Free Radical Catalysis by Galactose Oxidase. *Chemical Reviews* **2003**, 103 (6), 2347-2364.
29. Dawson, J., Probing Structure-Function Relations in Heme-containing Oxygenases and Peroxidases. *Science* **1988**, 240, 433-439.
30. Wang, Y.; DuBois, J. L.; Hedman, B.; Hodgson, K. O.; Stack, T. D. P., Catalytic Galactose Oxidase Models: Biomimetic Cu(II)-Phenoxyl-Radical Reactivity. *Science* **1998**, 279, 537-540.
31. Chirik, P. J., Preface: Forum on Redox-Active Ligands. *Inorganic Chemistry* **2011**, 50 (20), 9737-9740.
32. Hendrickson, D. N.; Pierpont, C. G., Valence Tautomeric Transition Metal Complexes. In *Spin Crossover in Transition Metal Compounds II*, Springer Berlin Heidelberg: Berlin, Heidelberg, 2004; pp 63-95.
33. Sato, O.; Cui, A.; Matsuda, R.; Tao, J.; Hayami, S., Photo-induced Valence Tautomerism in Co Complexes. *Accounts of Chemical Research* **2007**, 40 (5), 361-369.
34. Pierpont, C. G., Studies on Charge Distribution and Valence Tautomerism in Transition Metal Complexes of Catecholate and Semiquinonate Ligands. *Coordination Chemistry Reviews* **2001**, 216, 99-125.
35. Broere, D. L. J.; Plessius, R.; van der Vlugt, J. I., New Avenues for Ligand-mediated Processes - Expanding Metal Reactivity by the use of Redox-active Catechol, *o*-aminophenol and *o*-phenylenediamine Ligands. *Chemical Society Reviews* **2015**, 44 (19), 6886-6915.
36. Eikey, R. A.; Abu-Omar, M. M., Nitrido and Imido Transition Metal Complexes of Groups 6–8. *Coordination Chemistry Reviews* **2003**, 243 (1), 83-124.
37. Petrenko, T.; Ray, K.; Wieghardt, K. E.; Neese, F., Vibrational Markers for the Open-Shell Character of Transition Metal Bis-dithiolenes: An Infrared, Resonance Raman, and Quantum Chemical Study. *Journal of the American Chemical Society* **2006**, 128 (13), 4422-4436.
38. Ray, K.; Begum, A.; Weyhermüller, T.; Piligkos, S.; van Slageren, J.; Neese, F.; Wieghardt, K., The Electronic Structure of the Isoelectronic, Square-Planar Complexes $[\text{Fe}^{\text{II}}(\text{L})_2]^{2-}$ and $[\text{Co}^{\text{III}}(\text{LBu})_2]^-$ (L^{2-} and $(\text{LBu})^{2-}$ = Benzene-1,2-dithiolates): An

Experimental and Density Functional Theoretical Study. *Journal of the American Chemical Society* **2005**, *127* (12), 4403-4415.

39. Ray, K.; Bill, E.; Weyhermüller, T.; Wieghardt, K., Redox-Noninnocence of the S,S'-Coordinated Ligands in Bis(benzene-1,2-dithiolato)iron Complexes. *Journal of the American Chemical Society* **2005**, *127* (15), 5641-5654.

40. Kokatam, S.; Weyhermüller, T.; Bothe, E.; Chaudhuri, P.; Wieghardt, K., Structural Characterization of Four Members of the Electron-Transfer Series $[\text{Pd}^{\text{II}}(\text{L})_2]_n$ (L = *o*-Iminophenolate Derivative; $n = 2^-, 1^-, 0, 1^+, 2^+$). Ligand Mixed Valency in the Monocation and Monoanion with $S = 1/2$ Ground States. *Inorganic Chemistry* **2005**, *44* (10), 3709-3717.

41. Kaim, W., The Shrinking World of Innocent Ligands: Conventional and Non-Conventional Redox-Active Ligands. *European Journal of Inorganic Chemistry* **2012**, 343-348.

42. Abakumov, G. A.; Cherkasov, V. K.; Nevodchikov, V. I.; Kuropatov, V. A.; Yee, G. T.; Pierpont, C. G., Magnetic Properties and Redox Isomerism for 4,4'-Bis(semiquinone) Complexes of Copper. *Inorganic Chemistry* **2001**, *40* (10), 2434-2436.

43. Liang, H. W.; Kroll, T.; Nordlund, D.; Weng, T.-C.; Sokaras, D.; Pierpont, C. G.; Gaffney, K. J., Charge and Spin-State Characterization of Cobalt Bis(*o*-dioxolene) Valence Tautomers Using Co K β X-ray Emission and L-Edge X-ray Absorption Spectroscopies. *Inorganic Chemistry* **2017**, *56* (2), 737-747.

44. Haneline, M. R.; Heyduk, A. F., C–C Bond-Forming Reductive Elimination from a Zirconium(IV) Redox-Active Ligand Complex. *Journal of the American Chemical Society* **2006**, *128* (26), 8410-8411.

45. Munha, R. F.; Zarkesh, R. A.; Heyduk, A. F., Group Transfer Reactions of d^0 Transition Metal Complexes: Redox-active Ligands Provide a Mechanism for Expanded Reactivity. *Dalton Transactions* **2013**, *42* (11), 3751-3766.

46. Zarkesh, R. A.; Ziller, J. W.; Heyduk, A. F., Four-Electron Oxidative Formation of Aryl Diazenes Using a Tantalum Redox-Active Ligand Complex. *Angewandte Chemie International Edition* **2008**, *47* (25), 4715-4718.

47. Myers, T. W.; Berben, L. A., Redox-active Aluminium(III) Complexes Convert CO₂ into MgCO₃ or CaCO₃ in a Synthetic Cycle Using Mg or Ca Metal. *Chemical Communications* **2013**, *49* (39), 4175-4177.

48. Bouwkamp, M. W.; Bowman, A. C.; Lobkovsky, E.; Chirik, P. J., Iron-Catalyzed $[2\pi + 2\pi]$ Cycloaddition of α,ω -Dienes: The Importance of Redox-Active Supporting Ligands. *Journal of the American Chemical Society* **2006**, *128* (41), 13340-13341.

49. Darmon, J. M.; Stieber, S. C. E.; Sylvester, K. T.; Fernández, I.; Lobkovsky, E.; Semproni, S. P.; Bill, E.; Wieghardt, K.; DeBeer, S.; Chirik, P. J., Oxidative Addition of

Carbon–Carbon Bonds with a Redox-Active Bis(imino)pyridine Iron Complex. *Journal of the American Chemical Society* **2012**, *134* (41), 17125-17137.

50. Russell, S. K.; Lobkovsky, E.; Chirik, P. J., Iron-Catalyzed Intermolecular $[2\pi + 2\pi]$ Cycloaddition. *Journal of the American Chemical Society* **2011**, *133* (23), 8858-8861.

51. Sylvester, K. T.; Chirik, P. J., Iron-Catalyzed, Hydrogen-Mediated Reductive Cyclization of 1,6-Enynes and Diynes: Evidence for Bis(imino)pyridine Ligand Participation. *Journal of the American Chemical Society* **2009**, *131* (25), 8772-8774.

52. Hojilla Atienza, C. C.; Tondreau, A. M.; Weller, K. J.; Lewis, K. M.; Cruse, R. W.; Nye, S. A.; Boyer, J. L.; Delis, J. G. P.; Chirik, P. J., High-Selectivity Bis(imino)pyridine Iron Catalysts for the Hydrosilylation of 1,2,4-Trivinylcyclohexane. *ACS Catalysis* **2012**, *2* (10), 2169-2172.

53. Tondreau, A. M.; Atienza, C. C. H.; Darmon, J. M.; Milsman, C.; Hoyt, H. M.; Weller, K. J.; Nye, S. A.; Lewis, K. M.; Boyer, J.; Delis, J. G. P.; Lobkovsky, E.; Chirik, P. J., Synthesis, Electronic Structure, and Alkene Hydrosilylation Activity of Terpyridine and Bis(imino)pyridine Iron Dialkyl Complexes. *Organometallics* **2012**, *31* (13), 4886-4893.

54. Tondreau, A. M.; Atienza, C. C. H.; Weller, K. J.; Nye, S. A.; Lewis, K. M.; Delis, J. G. P.; Chirik, P. J., Iron Catalysts for Selective Anti-Markovnikov Alkene Hydrosilylation Using Tertiary Silanes. *Science* **2012**, *335*, 567-570.

55. Yu, R. P.; Darmon, J. M.; Hoyt, J. M.; Margulieux, G. W.; Turner, Z. R.; Chirik, P. J., High-Activity Iron Catalysts for the Hydrogenation of Hindered, Unfunctionalized Alkenes. *ACS Catalysis* **2012**, *2* (8), 1760-1764.

56. Lippert, C. A.; Arnstein, S. A.; Sherrill, C. D.; Soper, J. D., Redox-Active Ligands Facilitate Bimetallic O₂ Homolysis at Five-Coordinate Oxorhenium(V) Centers. *Journal of the American Chemical Society* **2010**, *132* (11), 3879-3892.

57. Lippert, C. A.; Hardcastle, K. I.; Soper, J. D., Harnessing Redox-Active Ligands for Low-Barrier Radical Addition at Oxorhenium Complexes. *Inorganic Chemistry* **2011**, *50* (20), 9864-9878.

58. Lippert, C. A.; Riener, K.; Soper, J. D., Aerobic Alcohol Oxidations Catalyzed by Oxorhenium Complexes Containing Redox-Active Ligands. *European Journal of Inorganic Chemistry* **2012**, *2012* (3), 554-561.

59. Lippert, C. A.; Soper, J. D., Deoxygenation of Nitroxyl Radicals by Oxorhenium(V) Complexes with Redox-Active Ligands. *Inorganic Chemistry* **2010**, *49* (8), 3682-3684.

60. Liu, Y.; Shao, X.; Zhang, P.; Lu, L.; Shen, Q., Trifluoromethyl-Substituted Sulfonium Ylide: Rh-Catalyzed Carbenoid Addition to Trifluoromethylthioether. *Organic Letters* **2015**, *17* (11), 2752-2755.

61. Luca, O. R.; Crabtree, R. H., Redox-active Ligands in Catalysis. *Chemical Society Reviews* **2013**, 42 (4), 1440-1459.
62. Smith, A. L.; Clapp, L. A.; Hardcastle, K. I.; Soper, J. D., Redox-active Ligand-mediated Co–Cl Bond-forming Reactions at Reducing Square Planar Cobalt(III) Centers. *Polyhedron* **2010**, 29 (1), 164-169.
63. Smith, A. L.; Hardcastle, K. I.; Soper, J. D., Redox-Active Ligand-Mediated Oxidative Addition and Reductive Elimination at Square Planar Cobalt(III): Multielectron Reactions for Cross-Coupling. *Journal of the American Chemical Society* **2010**, 132 (41), 14358-14360.
64. Rolle, C. J. Selective Aerobic Oxidations Catalyzed by Manganese(III) Complexes Using Redox-Active Ligands. Georgia Institute of Technology, Atlanta, GA, USA, **2011**.
65. Rolle, C. J.; Hardcastle, K. I.; Soper, J. D., Reactions of Tetrabromocatecholatomanganese(III) Complexes with Dioxygen. *Inorganic Chemistry* **2008**, 47 (6), 1892-1894.
66. Berry, J. F., Terminal Nitrido and Imido Complexes of the Late Transition Metals. *Comments on Inorganic Chemistry* **2009**, 30 (1-2), 28-66.
67. King, E. R.; Hennessy, E. T.; Betley, T. A., Catalytic C–H Bond Amination from High-Spin Iron Imido Complexes. *Journal of the American Chemical Society* **2011**, 133 (13), 4917-4923.
68. Thu, H.-Y.; Yu, W.-Y.; Che, C.-M., Intermolecular Amidation of Unactivated sp^2 and sp^3 C–H Bonds via Palladium-Catalyzed Cascade C–H Activation/Nitrene Insertion. *Journal of the American Chemical Society* **2006**, 128 (28), 9048-9049.
69. Chong, E.; Kampf, J. W.; Ariafard, A.; Canty, A. J.; Sanford, M. S., Oxidatively Induced C–H Activation at High Valent Nickel. *Journal of the American Chemical Society* **2017**, 139 (17), 6058-6061.
70. Hickman, A. J.; Sanford, M. S., High-valent Organometallic Copper and Palladium in Catalysis. *Nature* **2012**, 484, 177-185.

CHAPTER 2. REDOX-ACTIVE BIS(PHENOLATE) N-HETEROCYCLIC CARBENE PINCER LIGANDS SUPPORT COBALT ELECTRON TRANSFER SERIES SPANNING FOUR OXIDATION STATES

2.1 Note on Collaboration

This chapter contains X-ray crystal structures that were initially featured in the Ph.D. thesis of Dr. Michael B. Bayless, Georgia Tech 2014 (Complexes **1**, **1⁺**, and **1²⁺**). The metrical data has since been refined by Dr. John Bacsá and the updated data is reflected here. Mr. Nicolaas P. van Leest and Professor Bas de Bruin of the University of Amsterdam have provided the TD-DFT calculations, simulated and experimental EPR data, and spin density calculations. Former undergraduate student, Quinton Bruch, synthesized complex **2** from the ligand (*Ph*OCO) which I provided.

2.2 Introduction

Sustainability concerns motivate the continued pursuit of base metals as alternatives to precious metal catalysts for small molecule and fine-chemical transformations, including hydrogenation, C–C and C–X cross coupling, and C–H bond functionalization protocols.¹⁻³ The utility of platinum-group metals for such processes derives from their capacity to mediate the multielectron organometallic bond-making and -breaking steps which comprise most catalytic cycles.⁴⁻⁵ Selectivity in these systems is therefore a consequence of their thermodynamic bias for concerted two-electron transfer.^{4,6} Accordingly, efforts to develop base metal alternatives must

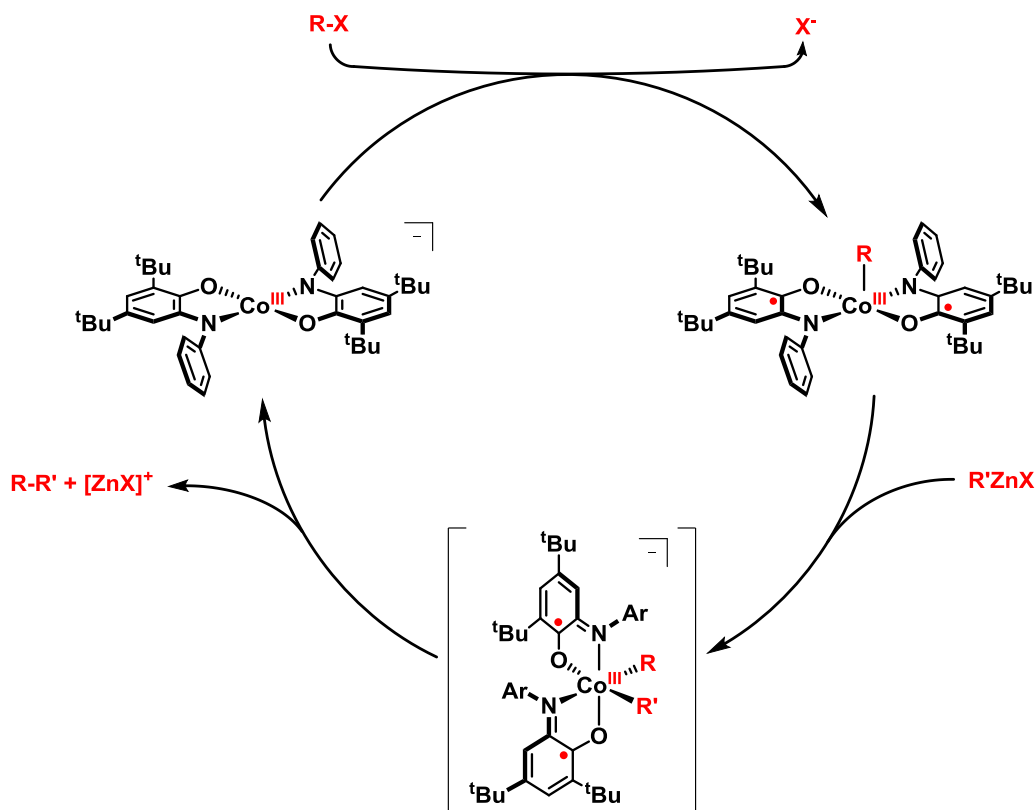
address the propensity of later 3d metals to exist in oxidation states that differ by only one electron.⁷

One potential solution is to expand the redox sphere beyond the metal center by harnessing cooperative metal–ligand redox processes for multielectron chemistry.^{3, 8-12} In this approach, the capacity of redox-active ligands to store and deliver charge is a tool to bring about precious metal-like, two-electron organometallic reactivity at metal ions that are more commonly prone to one-electron transfer, or which are even redox inert. This strategy has recently been applied to a wide array of bond-making and -breaking reactions.¹³⁻¹⁷ But while redox-active ligand complexes have found some applications in base metal catalysis,¹⁸⁻⁴² in most cases, advancements are still needed to make these pre-formed complexes competitive with catalysts generated *in situ* from base metal salts, reductants, and potential ligand additives.^{5, 43-57} Successes in rational base metal catalyst design often begin with robust, tunable ligands. For instance, the redox-active bis(imino)pyridine (NNN) pincers ligands⁵⁸⁻⁵⁹ were termed "privileged" because of their utility in Fe and Co catalysis.⁶⁰ Accordingly, elaborating a library of ligands that stabilize low coordinate, later 3d metals across two or more formal oxidation states is a first step toward designed base metal complexes for sustainable catalysis.

Previous results from our own lab have explored redox-active ligand aminophenol Co complexes for Negishi-type cross-couplings of unactivated alkyl halides with alkyl- or arylzinc halides (Scheme 2.1).⁶¹⁻⁶² Both the C–X oxidative addition and C–C reductive elimination steps apparently occur via Pd-like concerted two-electron steps. Though catalytic turnover is limited because C–C reductive elimination from the putative high-valent dialkyl/aryl intermediate cobalt complexes is inhibited by energetically

unfavorable isomerization of the square planar bis(amidophenolate) ligand field. This precludes access to the *cis* sites required for C–C elimination.

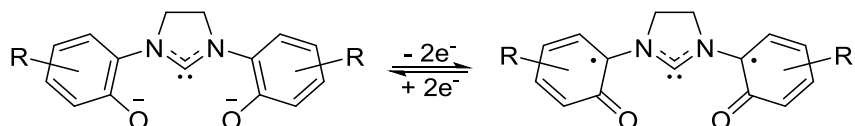
Scheme 2.1. Proposed catalytic cycle for the Negishi-type cross-coupling using bis(amidophenolate) Co^{III}.



To address these issues, we sought a system that would capture the redox-active amidophenolate fragments within a *mer* pincer-type tridentate ligand scaffold. In this regard, the previously reported diphenolate imidazolyl carbene appeared promising.⁶³ As shown in Scheme 2.2, the (OCO) pincer contains two di-*tert*-butylphenolate moieties flanking a central N-heterocyclic carbene (NHC) core. Beyond constraining the coordination geometry to open *cis* coordination sites for oxidative addition and reductive elimination transformations, we envisioned the NHC conferring other advantages. The

strong σ -donating carbene makes the ligand less labile in its oxidized forms, and the increased electron density facilitates oxidative addition at the coordinated metal center. Its significant *trans* influence also enhances the lability of auxiliary ligands,⁶⁴⁻⁶⁵ which is particularly beneficial for generating catalytically relevant species at substitutionally inert metal centers such as Co^{III}. Finally, the modular synthesis allows both lateral moieties as well as the medial NHC core to be easily modified, offering significant steric and electronic tunability.⁶⁶⁻⁶⁷

Scheme 2.2. Redox capacity of the proposed ligand scaffold.



This (OCO) ligand has been reported on metals including Ti, Zr, Hf, V, Mn, Ir, Ni, Pd, Pt and Al.^{63, 68-72} Most of these reports formulate the ligand as a bis(phenolate) dianion, but two previous papers discussed an expanded redox capacity.^{70, 72} Bercaw and coworkers evaluated one- and two-electron oxidations of an [(OCO)Ir^{III}(cod)] complex and suggested the possibility of a ligand-centered radical in the oxidized materials, but a definitive assignment as d^6 Ir(IV) or d^7 Ir(III) ligand-radical complex was not made.⁷² Ligand-centered oxidations were similarly invoked to rationalize the electrochemical and electron paramagnetic resonance (EPR) data for homoleptic bis-(OCO) ligated Group 4 metals Ti, Zr, and Hf, but no structural data were reported and the putative ligand radical complexes were not isolated.⁷⁰

Reported herein are data for three new cobalt electron transfer series, each spanning four formal oxidation states. Structural data are presented that unambiguously

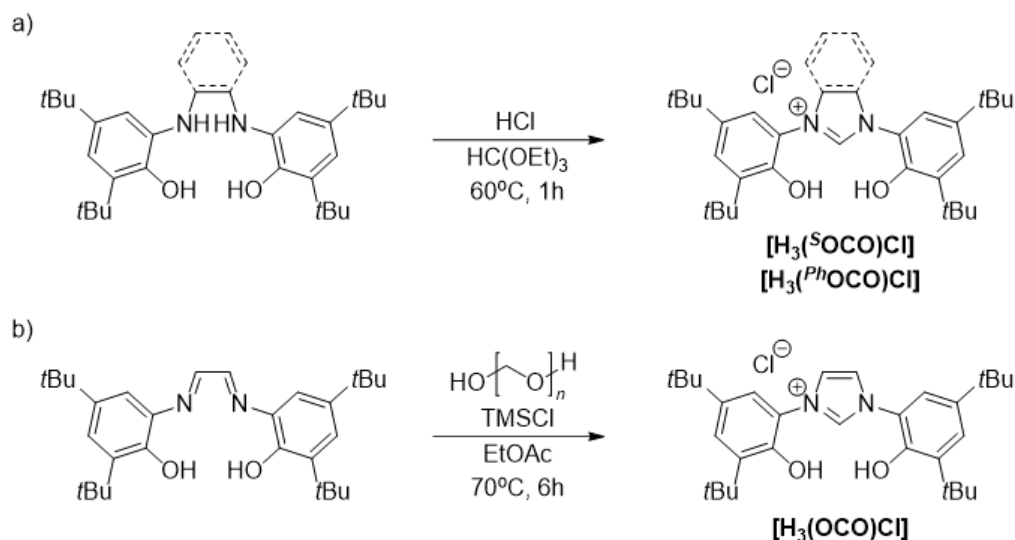
show the (OCO) pincer ligands are redox centers in the highly oxidized complexes and computational data supports their assignments as ligand-centered radicals. Furthermore, variations in the NHC backbone saturation are shown to modulate the redox potential of the ligand-centered oxidations by over 400 mV, providing a convenient handle to tune these ligands for applications in small molecule redox catalysis.

2.3 Results

2.3.1 Synthesis of the Diphenolate NHC Ligands

The chloride salts of three tridentate pincer proligands featuring two di-*tert*-butylphenolate moieties on a central *N,N'*-disubstituted imidazole [$\text{H}_3(\text{OCO})\text{Cl}$], imidazoline [$\text{H}_3(^{\text{S}}\text{OCO})\text{Cl}$], or benzimidazole [$\text{H}_3(^{\text{Ph}}\text{OCO})\text{Cl}$] core, were synthesized via slight modifications of previously reported procedures. The saturated variant [$\text{H}_3(^{\text{S}}\text{OCO})\text{Cl}$] was prepared in 82% yield from triethyl orthoformate-promoted cyclization of *N,N'*-bis(2-hydroxy-3,5-di-*tert*-butylphenyl)ethylenediamine in the presence of concentrated hydrochloric acid (Scheme 2.3a).^{68, 73} Analogous reaction of the *ortho*-phenylenediamine precursor afforded [$\text{H}_3(^{\text{Ph}}\text{OCO})\text{Cl}$] in 79% yield.⁷⁴ The unsaturated NHC core, [$\text{H}_3(\text{OCO})\text{Cl}$], was prepared according to a previously reported method by treating the diimine precursor with paraformaldehyde and TMSCl in ethyl acetate at 70 °C for 6h (Scheme 2.3b).

Scheme 2.3. Synthesis of the (OCO) proligands.



2.3.2 Synthesis and Characterization of the Cobalt Complexes

The cobalt complexes **1** – **3**, formulated $[(^{\text{S}}\text{OCO})\text{Co}^{\text{II}}(\text{MeCN})]$, $[(\text{OCO})\text{Co}^{\text{II}}(\text{MeCN})]$, and $[(^{\text{Ph}}\text{OCO})\text{Co}^{\text{II}}(\text{MeCN})]$, respectively, were prepared by a general method wherein the corresponding ligands were deprotonated with three equivalents of NaOMe and subsequently treated with stoichiometric CoCl_2 (Scheme 2.4). As described below, the four-coordinate Co center is completed by a solvent-derived ligand upon workup. Samples isolated from CH_3CN or THF solutions vary in color from orange to red and the isolated yields ranged from 88-93%. Suspending THF-derived samples in CH_3CN and adding the minimal amount of toluene required to completely dissolve the sample affords analytically pure needle crystals of the corresponding CH_3CN complexes, implying the solvent-derived ligands are labile.

Scheme 2.4. Synthesis of the Co^{II} complexes 1 – 3.

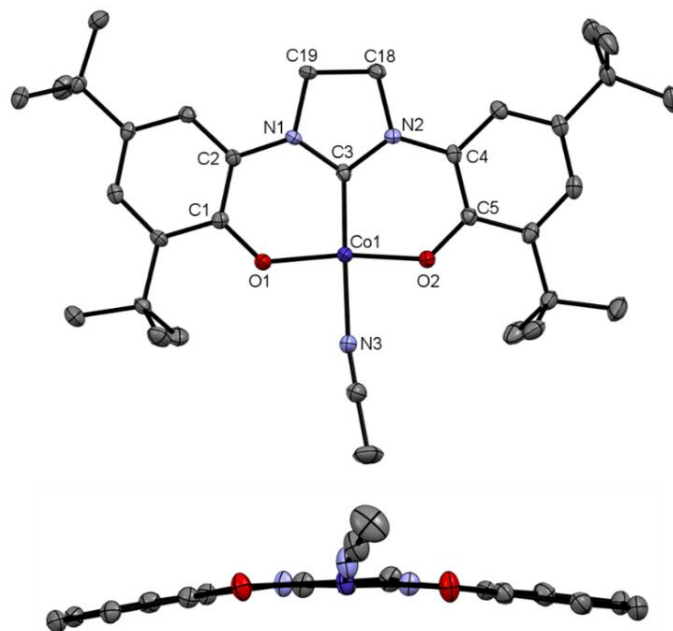
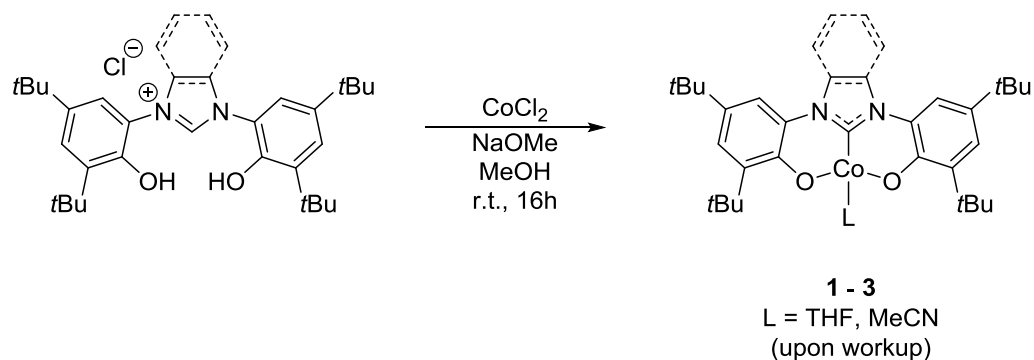


Figure 2.1. ORTEP plot of $[(^s\text{OCO})\text{Co}(\text{MeCN})]$, complex 1, as viewed from front (top) and down the Co1–C3 bond (bottom). Thermal ellipsoids are drawn at 50% probability. Hydrogen atoms and non-coordinated acetonitrile molecules have been removed for clarity.

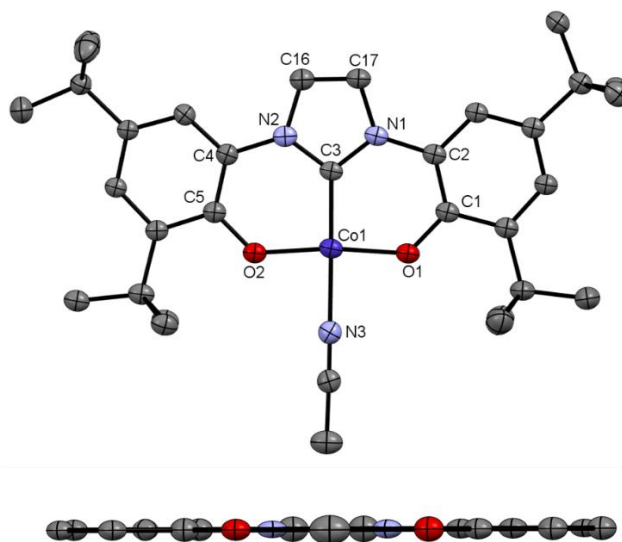


Figure 2.2. ORTEP plot of $[(OCO)Co(MeCN)]$, complex 2, as viewed from front (top) and down the Co1–C3 bond (bottom). Thermal ellipsoids are drawn at 50% probability. Hydrogen atoms and non-coordinated acetonitrile molecules have been removed for clarity.

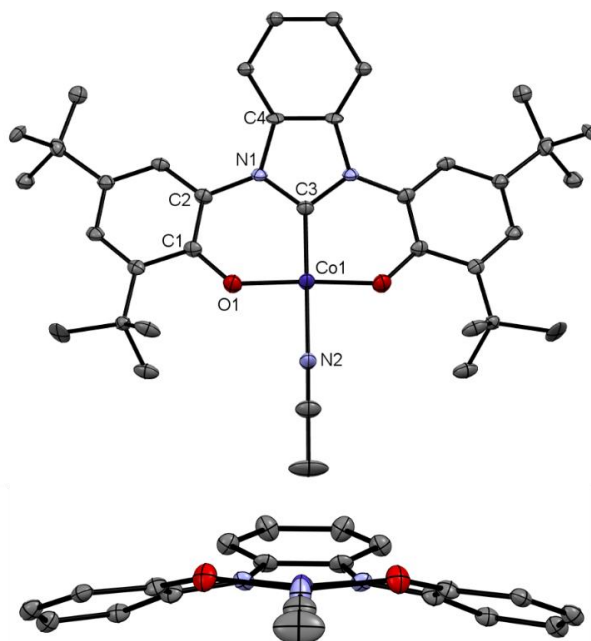


Figure 2.3. ORTEP plot of $[(PhOCO)Co(MeCN)]$, complex 3, as viewed from front (top) and down the Co1–C3 bond (bottom). Thermal ellipsoids are drawn at 50% probability. Hydrogen atoms have been removed for clarity.

Recrystallization of the complexes from concentrated MeCN solutions at $-25\text{ }^{\circ}\text{C}$ afforded orange to red crystals suitable for analysis by X-ray diffraction. As shown in Figures 2.1 – 2.3, the gross geometric features are consistent across the series. In each, the four-coordinate Co center has approximate square planar geometry, with the diphenolate carbene pincer ligand occupying three meridional sites and a solvent-derived MeCN ligand bound *trans* to the carbene.

Unsaturation in the ligand backbone leads to variations in the Co–ligand bonding metrics as well as the overall planarity of the complexes. Selected bond lengths are collected in Figure 2.4. The saturated imidazoline backbone of **1** twists the ligand backbone, as evidenced by the C2–N1–C3–N2 torsional angle of $5.72(1)^{\circ}$. The phenolate arms of **1** are displaced below the cobalt, causing the O1–Co–O2 and C3–Co–N3 bite angles to slightly contract to $170.3(1)^{\circ}$ and $172.2(1)^{\circ}$, respectively (Figure 2.1, bottom). In contrast, the sp^2 carbons in the imidazole backbone of **2** inhibit rotation along the C16–C17 bond, making the ligand coplanar with the Co center. In the solid state, the complex resides on a crystallographic mirror (Figure 2.2, bottom).

The benzimidazole complex **3** exhibits significant puckering about the Co center, causing both phenolic oxygen atoms to bend 7.2° above the N3–Co–C1 plane. The benzimidazole backbone is lifted out-of-plane (Figure 2.3, bottom). The C–C bonding metrics about the flanking phenolate groups are statistically indistinguishable within the rings, across all complexes **1** - **3** (Figure 2.4), consistent with formulation of the phenolate substituents as fully reduced phenoxides,⁷⁵ from which we conclude that the NHC-ligands are dianionic and the Co centers adopt a formal +II oxidation state.

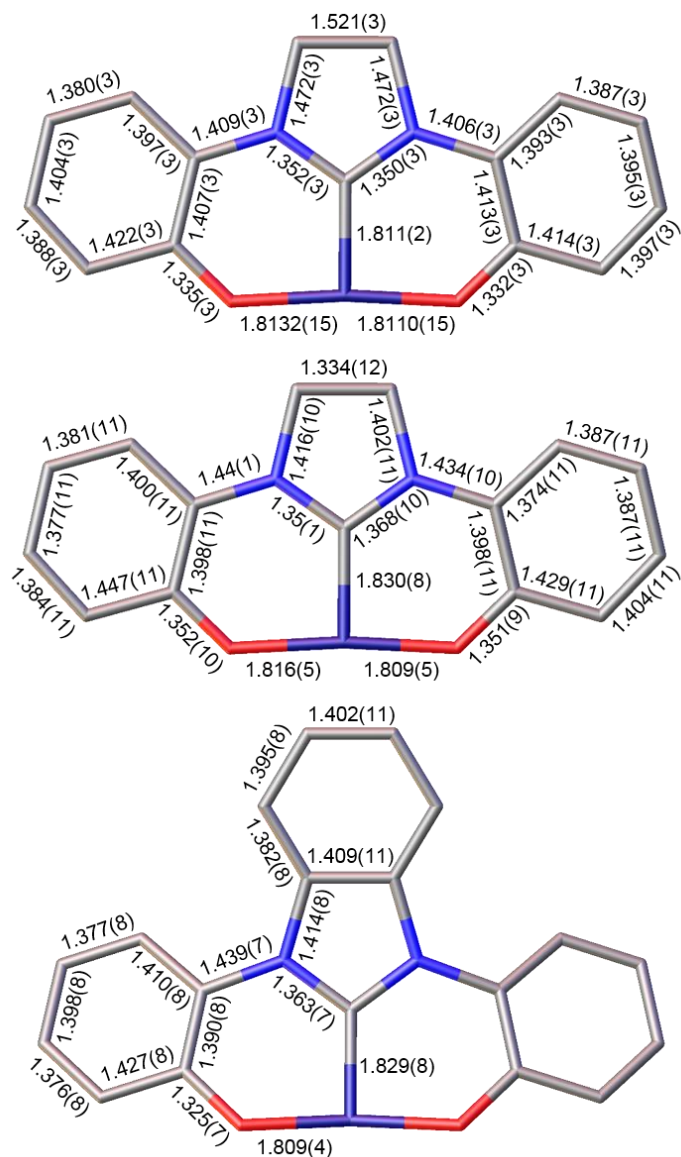


Figure 2.4. Selected bond lengths [Å] across the series 1 – 3 (top to bottom).

The Co–O bond distances remain constant across the series, averaging 1.811 ± 0.005 Å. A search of the CCDC in June 2017 revealed that all three Co1–C3 bond lengths (1.811(2)–1.830(8) Å) are substantially shorter than those in previously reported Co–NHC complexes (1.9135(19) – 2.152(6) Å),^{76–81} likely reflecting both the strong σ -donor ability of the NHC as well as geometric constraints imposed by the chelating

phenolate arms. Notably, unsaturation in the backbone leads to a statistically significant elongation of the Co–C_{NHC} distances along with a contraction of the Co–N bonds to the MeCN ligands and lengthening of the nitrile C≡N bonds (Figure 2.5). These bonding patterns can be rationalized by invoking enhanced π -backdonation from the Co center to the saturated carbene in **1** vs. **2** and **3**, consistent with previous suggestions that imidazoline-derived NHCs are better π -acceptors than their unsaturated imidazole counterparts.^{65, 82} However, nitriles are poor π -acceptors, and similar effects might be expected based only on the relative σ donor abilities of the varying NHCs.

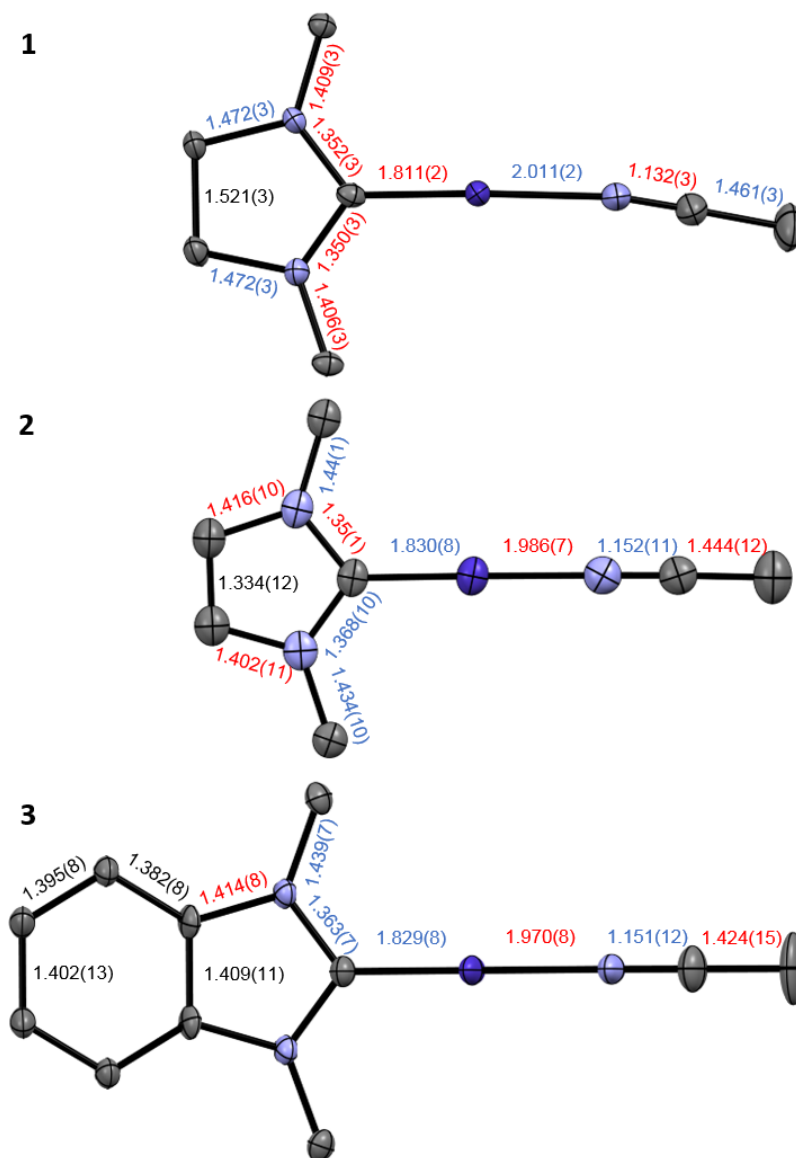


Figure 2.5. Bond lengths [Å] for the NHC–Co–NCCH₃ fragments in **1** - **3**.

All three complexes are paramagnetic, as evidenced by the lack of any observable ¹H NMR spectra in THF-*d*₈ and their solution magnetic moments of 1.88 μ_B, 1.82 μ_B, and 1.90 μ_B for **1** - **3**, respectively (average of three independent runs). These measured moments are higher than the spin-only values for an *S* = ½ center, but square planar Co^{II} species are well known to have significant contributions from the angular momentum

term, L , leading to higher than expected values of μ_{eff} .⁸³ The observed magnetism is therefore consistent with a d^7 configuration with a single unpaired electron.

2.3.3 Electrochemistry

Cyclic voltammograms of **1** - **3** were obtained in MeCN solutions containing 0.1M tetra-*n*-butylammonium hexafluorophosphate ($[n\text{Bu}_4\text{N}][\text{PF}_6]$) as the supporting electrolyte. As shown in Figure 2.6, all three complexes show three quasi-reversible $1e^-$ oxidations between -0.5 V and $+1.5$ V vs. Fc^+/Fc . The potentials are collected in Table 2.1. Substitutions in the NHC backbone minimally impact the position of the first oxidation, $E_{1/2}^1$, which varies less than 95 mV between the most easily oxidized **3** and the least **2**. However, the second and third oxidations, $E_{1/2}^2$ and $E_{1/2}^3$, are strongly influenced by (un)saturation of the NHC backbone. For example, in the saturated NHC complex **1**, the second oxidation event, $E_{1/2}^2$, occurs nearly 300 mV more negative of the unsaturated imidazole-derived complex **2**, and nearly 400 mV below the benzimidazole NHC complex **3**. Similar trends are observed in the $E_{1/2}^3$ values spanning a range of over 400 mV, with **1** < **2** < **3**. $E_{1/2}^2$ and $E_{1/2}^3$ represent formation of complexes two and three redox levels above Co^{II} . However, as discussed below, the relative scarcity and presumed oxidizing power of molecular Co^{IV} and Co^{V} complexes led us to consider alternative formulations containing ligand-centered radicals. In this context, the observed $E_{1/2}^2$ and $E_{1/2}^3$ values are well within the range of reported ligand oxidations in complexes containing aryl oxide chelates (0.33 - 1.04V vs. Fc^+/Fc) that generate phenoxyl radicals.⁷⁵

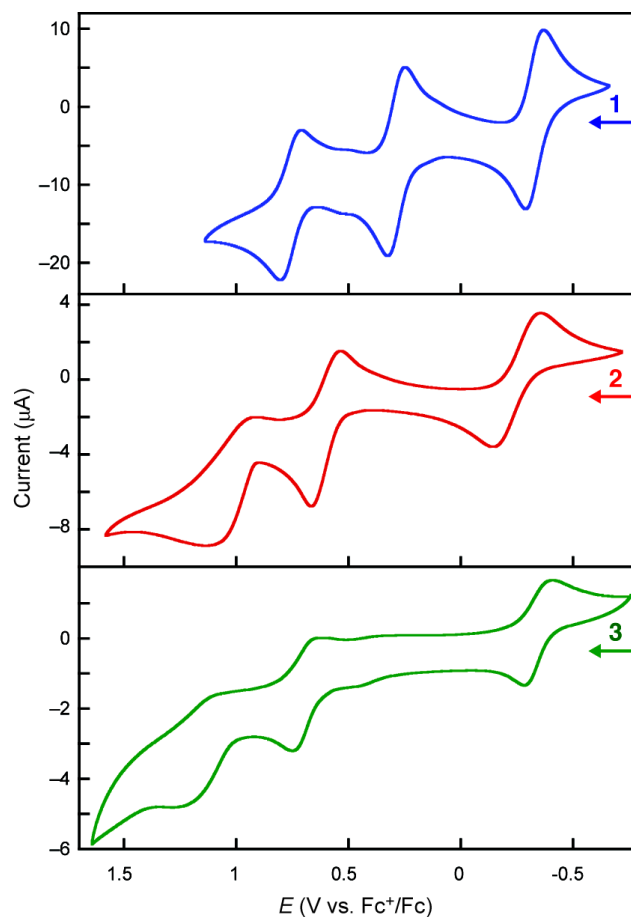


Figure 2.6. Cyclic voltammograms of **1** (black), **2** (red), and **3** (blue) in MeCN. Conditions: 5 mM **1-3**, 0.1 M ([Bu₄N][PF₆]), 1.0 mm Pt electrode, 100 mV/s⁻¹ scan rate.

Table 2.1. Redox potentials (V vs. Fc⁺/Fc) of complexes **1** – **3**.

	$E_{1/2}^1 (\Delta E_p)$	$E_{1/2}^2 (\Delta E_p)$	$E_{1/2}^3 (\Delta E_p)$
1	-0.322 (0.086)	0.299 (0.085)	0.773 (0.108)
2	-0.252 (0.208)	0.596 (0.138)	0.963 (0.169)
3	-0.344 (0.132)	0.694 (0.105)	1.187 (0.189)

2.3.4 *Synthesis and Structure of the [$^{\text{S}}\text{OCO}$ Co(THF)] Electron Transfer Series*

To better understand the structural properties of the high-valent Co complexes observed in the cyclic voltammograms, chemical oxidations of **1** were performed in THF. Treating a dark orange, air-sensitive THF solution of **1** with 1 equiv. of AgOTf afforded a dark green solution from which **1**⁺ was isolated as an air-stable green solid in 92% yield. A sample suitable for X-ray diffraction was prepared by salt metathesis with NaBPh₄ followed by recrystallization from solvent diffusion of pentane into a concentrated THF solution at −25°C. The structure of **1**⁺ is presented in Figure 2.8. For comparison, an X-ray structure of a sample of **1** isolated from THF is shown in Figure 2.7. Bond length data show that, with the exception of Co–C1 bond contraction from 1.811(2) to 1.790(4) Å, the structural perturbations in **1** are minimal on substitution of MeCN for THF.

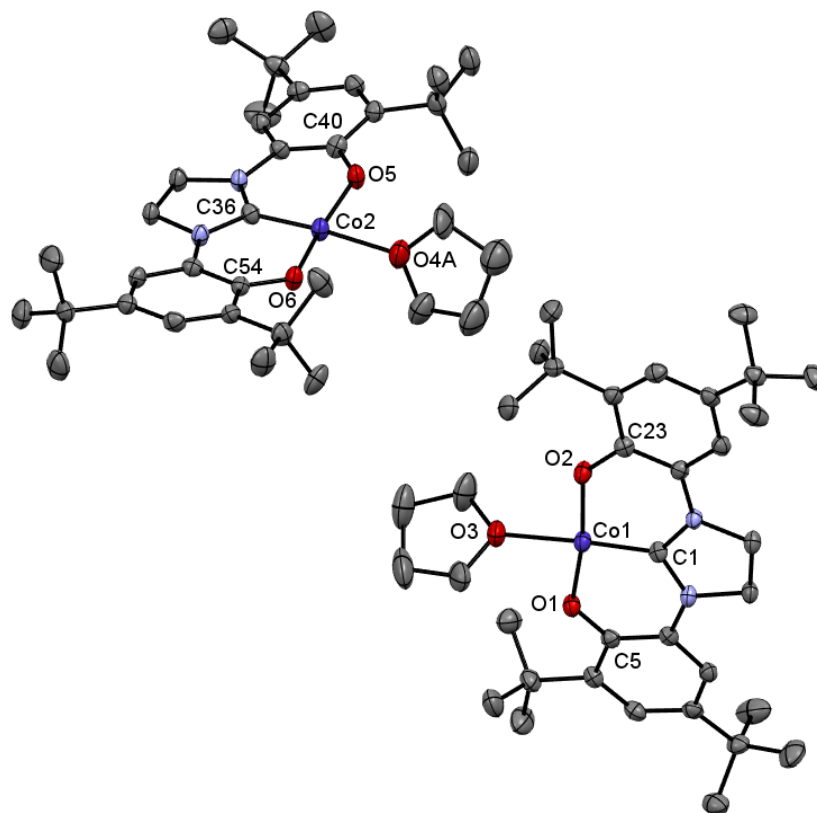


Figure 2.7 ORTEP plot of $[(^s\text{OCO})\text{Co}(\text{THF})]$, **1**, isolated from THF. Thermal ellipsoids are drawn at 50% probability. The rotational disorder of the tert-butyl and THF groups in addition to all hydrogen atoms have been removed for clarity. Selected bond lengths (Å): Co1–C1 1.789(3), Co2–C36 1.791(3), Co1–O1 1.816(2), Co1–O2 1.812(2), Co2–O5 1.808(2), Co2–O6 1.810(2), Co1–O3 2.021(2), Co2–O4A 2.026(2), O1–C5 1.339(3), O2–C23 1.337(3), O5–C40 1.337(4), O6–C54 1.340(3).

The Co center in **1**⁺ is five-coordinate (Figure 2.8), with the pincer ligand occupying three *meridional* sites. Two THF ligands complete the pseudo-square pyramidal geometry with a τ value of 0.13 (*cf.* $\tau = 0$ for a perfect square pyramid and $\tau = 1$ for a perfect trigonal bipyramid) ligand.⁸⁴ Oxidation of **1** to **1**⁺ occurs with contractions of each Co–O and O–C_{Ar} bond by *ca.* 0.01 Å each, and the Co–C1 bond to the carbene is lengthened from 1.789(2) in **1** to 1.849(3) Å. All of the C–C bonds within the phenolate rings are indistinguishable from **1** within the error of the X-ray measurement, but both

rings in $\mathbf{1}^+$ display distinctive quinoid-type bond alternations typical of those expected for phenoxyl radicals,⁷⁵ suggesting some degree of ligand oxidation might be operative.

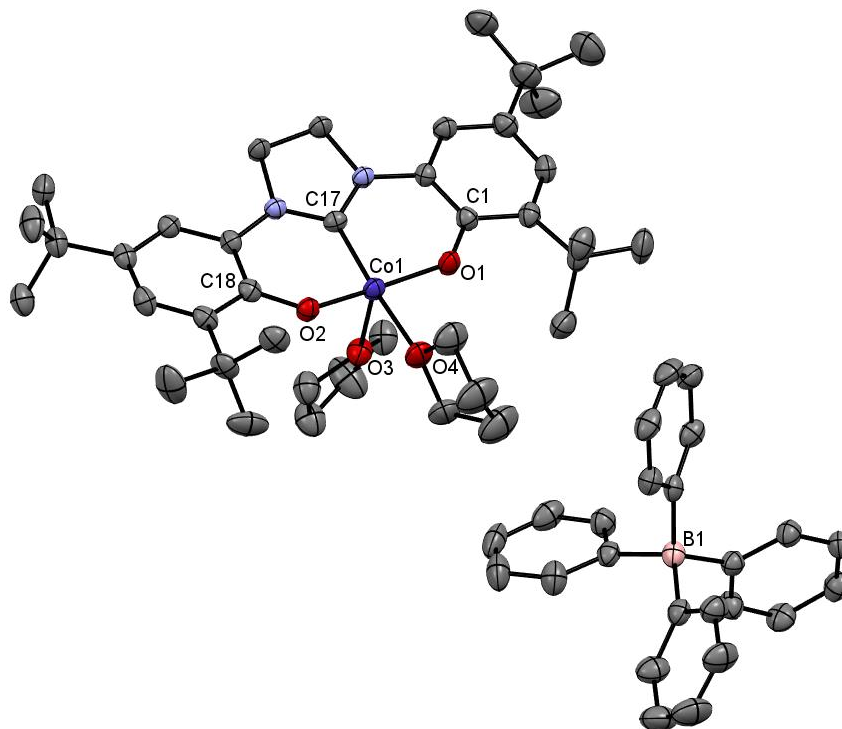


Figure 2.8. ORTEP plot of $[(^s\text{OCO})\text{Co}(\text{THF})_2][\text{BPh}_4]$, $\mathbf{1}^+$. Thermal ellipsoids are drawn at 50% probability. The rotational disorder of the tert-butyl and THF groups in addition to all hydrogen atoms have been removed for clarity. Selected bond lengths (Å): Co1–C17 1.849(3), Co1–O1 1.8014(19), Co1–O2 1.8027(19), Co1–O3 2.115(2), Co1–O4 2.041(2), O1–C1 1.329(3), O2–C18 1.328(3).

THF solutions of $\mathbf{1}^+$ are paramagnetic with a solution moment of $2.88 \mu_B$, consistent with the spin only value for an $S = 1$ center. The sum of these data are therefore consistent with formulation of $\mathbf{1}^+$ as either $[(^s\text{OCO})\text{Co}^{\text{III}}(\text{THF})_2]^+$ containing a closed-shell $(^s\text{OCO})^{2-}$ bis(phenolate) ligand on an intermediate spin Co^{III} center, or $[(^s\text{OCO}^{\bullet})\text{Co}^{\text{II}}(\text{THF})_2]^+$ with a low-spin Co^{II} ion ferromagnetically coupled to an oxidized monoanionic $(^s\text{OCO}^{\bullet})^-$ fragment containing a single unpaired electron distributed across

the (OCO) framework. The X-ray metrical data alone are insufficient to distinguish these possibilities, but computational data discussed below are informative in this regard.

The dication $\mathbf{1}^{2+}$ was prepared directly from a THF solution of $\mathbf{1}$ by treatment with 2.1 equivalents of $\text{N}[p\text{-BrC}_6\text{H}_4]_3[\text{PF}_6]$, yielding immediate conversion to a dark green colored solution which afforded a green-brown powder upon workup. Crystals suitable for single crystal X-ray analysis were obtained by solvent diffusion of pentane into a concentrated THF solution at -25°C . Three THF molecules complete the coordination sphere about a pseudo-octahedral Co center (Figure 2.9). Examination of the ligand metrical data shows a clear quinoid-type pattern of four long and two short C–C bonds in both phenoxide moieties. Additionally, the $\text{C}_{\text{Ar}}\text{--O}$ and $\text{C}_{\text{Ar}}\text{--N}$ bond lengths are contracted by an average of 0.044(4) and 0.022(5) Å, respectively, as compared to $\mathbf{1}$, in line with the contractions expected upon oxidation of the phenoxide arms to phenoxyls. In total, the sum of the ligand data clearly contrast with those in $\mathbf{1}$ or $\mathbf{1}^+$, and are most consistent with formulation of the ligand in $\mathbf{1}^{2+}$ as a charge neutral doubly oxidized ($^{\text{S}}\text{OCO}^0$) ligand. Charge balance implies the Co center is in the +II oxidation state, so the complex is formulated as $[(^{\text{S}}\text{OCO}^0)\text{Co}^{\text{II}}(\text{THF})_2]^{2+}$. The measured THF solution magnetic moment of $2.51 \mu_{\text{B}}$ is substantially above that expected for an $S = 1/2$ ion - suggestive of substantial orbital contributions to the magnetic moment - but well below the spin-only moment for three or more unpaired spins. As discussed below, this could reflect multiple contributors to the ground state of $\mathbf{1}^{2+}$. However, $\mathbf{1}^{2+}$ is also prone to degradation to undefined Co species in solution at ambient temperature, thus complicating magnetic measurements and hence the magnetic data should be interpreted with caution.

Attempts to synthesize a complex representative of the oxidation state accessed after the most positive oxidation wave in the CV were unsuccessful. The use of strong oxidants such as $\text{N}[p\text{-BrC}_6\text{H}_4]_3^+$ or NO^+ derived salts provided only an intractable mixture of products in which $\mathbf{1}^{3+}$ was not isolated.

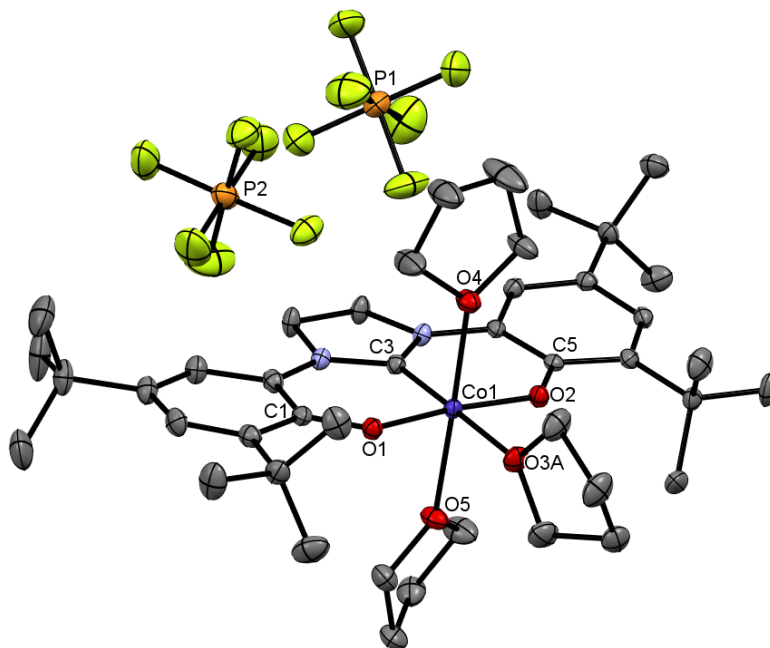


Figure 2.9. ORTEP plot of $[(^s\text{OCO})\text{Co}(\text{THF})_3][\text{PF}_6]_2$, complex $\mathbf{1}^{2+}$. Thermal ellipsoids are drawn at 50% probability. The disorder of the THF groups and all hydrogen atoms have been removed for clarity. Selected bond lengths (Å): Co1–C3 1.840(2), Co1–O1 1.8255(16), Co1–O2 1.8182(16), Co1–O3A 2.0315(15), Co1–O4 2.2044(16), Co1–O5 2.2530(16), O1–C1 1.287(3), O2–C5 1.301(3).

2.3.5 EPR Spectroscopy

The X-band EPR spectrum of a THF derived sample of **1** was obtained in toluene glass at 20 K (Figure 2.10). It displays a rhombic signal with well-resolved cobalt hyperfine coupling interactions (HFIs) along two directions of the g -tensor. The spectrum is characteristic for a metalloradical $S = 1/2$ system, with the unpaired electron being localized mainly at the cobalt center. A satisfactory simulation of the experimental

spectrum was obtained with the EPR parameters shown in Figure 2.10. Spin-unrestricted (collinear) spin-orbit DFT calculated EPR parameters are overall in reasonable agreement with the experimental values (Table 2). The DFT computed A^{Co_x} and A^{Co_y} HFI values are somewhat too high though, while the g_z -value is underestimated. This is suggestive of a slightly overestimated DFT HOMO–SOMO energy gap, perhaps caused by solvation effects and/or concrete toluene solvent adduct formation at 20 K in the experimental system.⁸⁵

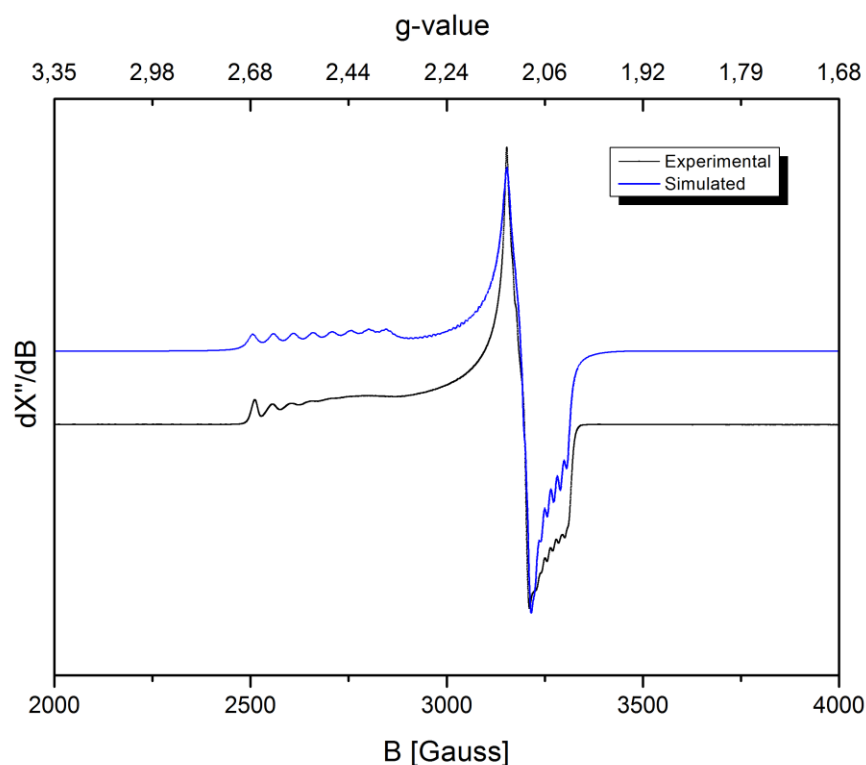


Figure 2.10. X-band EPR spectrum of a THF-derived sample of **1** in toluene glass at 20 K. Microwave frequency = 9.388589 GHz. Power = 0.6325 mW. Modulation Amplitude = 2.000 G.

Table 2.2. (Simulation) and DFT calculated EPR parameters of **1.**

	Simulated	DFT^a
g-tensor		
g_x	2.061	2.056
g_y	2.105	2.102
g_z	2.500	2.302
hyperfine couplings (MHz)		
A^{Co}_x	+45	+145
A^{Co}_y	NR (<30)	+82
A^{Co}_z	-170	-176

^aADF, B3lyp, TZ2, unrestricted collinear spin-orbit calculations.

As can be expected for a metal-based electronic triplet system ($S = 1$, with expected large zero-field splitting parameter D), the X-band EPR spectrum of **1**⁺ measured in toluene glass at 20 K gave no signal in the range of 0-6000 Gauss. The solution instability of **1**²⁺ precluded measurement of an EPR spectrum.

2.3.6 Computed Electronic Structures of **1**, **1**⁺, and **1**²⁺

The electronic structures of the THF adducts **1**, **1**⁺, and **1**²⁺ were computed with unrestricted DFT-D3 calculations (BP86, def2-TZVP, disp3), excluding counterions, and with starting spin states as determined experimentally. Optimized geometries were compared to the single-crystal X-ray structures and found to have maximum bond length deviations of 0.023 Å, 0.023 Å and 0.026 Å for **1**, **1**⁺, and **1**²⁺, respectively, suggesting that the spin states, functional and basis set (BP86, def2-TZVP, disp3) used in the geometry optimizations accurately capture the bond distances in the (^sOCO) ligands

across all three formal oxidation states. The spin densities per atom in optimized geometries were also calculated. Accordingly, complex **1** converged as a doublet ($\langle s^2 \rangle = 0.7611$), with 81% of the total spin density being located at cobalt (Figure 2.11). Some residual spin density is delocalized over both phenoxide arms of the OCO ligand, mainly on the oxygen atoms (total of 12.6%). A small amount of spin down density is observed on the NHC carbon center (4.2%), which can be attributed to spin polarization. The computed structure of **1** is therefore best described as $[(^s\text{OCO})\text{Co}^{\text{II}}(\text{THF})]$, with a closed shell $(^s\text{OCO})^{2-}$ dianion on a low spin Co^{II} center.

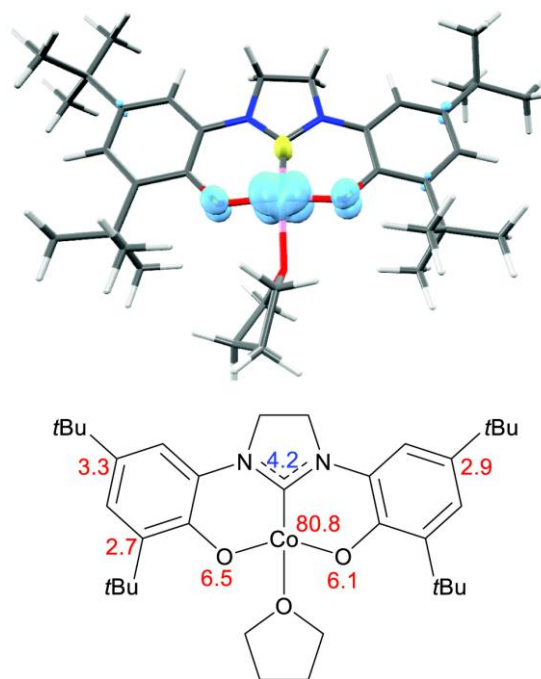


Figure 2.11. Top: Spin density plot of **1 ($S = 1/2$), generated with IQMol (isosurface value 0.005). Bottom: Spin density per atom for the THF adduct of **1** ($S = 1/2$).**

$\mathbf{1}^+$ converged as a triplet ($\langle s^2 \rangle = 2.0156$). The involvement of a quintet state ($\langle s^2 \rangle = 6.0132$) is highly unlikely, as this state is computed to be +20 kcal mol⁻¹ uphill vs. the triplet state. However, the singlet state is found to be only +5 kcal mol⁻¹ above the triplet

state, and the open-shell singlet state is only +4 kcal mol⁻¹ uphill from the triplet state. In the triplet state, 66% of the electron density is localized at Co; the remainder is delocalized over the phenoxide moieties (Figure 2.12). These data are most consistent with description of **1**⁺ as containing a Co^{II} center supported by a monooxidized (^SOCO[•])⁻ ligand radical. However, the accessibility of multiple low-lying excited states suggests that other contributors to the ground state might need to be considered (perhaps requiring multireference calculations, beyond the scope of the present study).

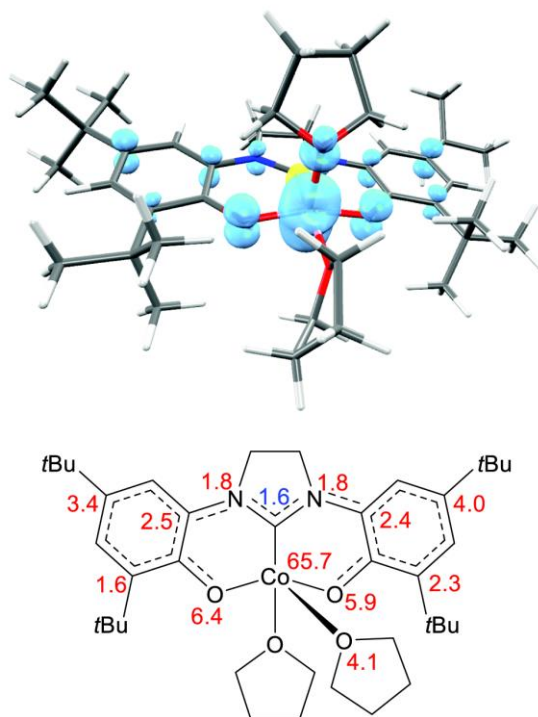


Figure 2.12. Top: Spin density plot of **1⁺ (*S* = 1), generated with IQMol (isosurface value 0.005). Bottom: Spin density per atom for the bis THF adduct of **1**⁺ (*S* = 1).**

Complex **1**²⁺ converged as a doublet ($\langle s^2 \rangle = 0.8342$). The spin density of **1**²⁺ is almost entirely localized at the cobalt center, with some spin polarization causing some negative spin population on the NHC ligand atoms (and hence more than 100% positive spin at cobalt; Figure 2.13). Unrestricted natural and corresponding orbital analysis of the

α and β molecular orbitals revealed the presence of only one α MO without (large) overlap with a corresponding β MO (UCO overlap values of all other α and β MO pairs > 0.96). Accordingly, the computational data suggest the complex is best described as $[(^s\text{OCO}^0)\text{Co}^{\text{II}}(\text{THF})_3]^{2+}$, with a single unpaired electron localized on the d^7 Co^{II} center and a doubly oxidized, charge neutral and closed-shell diamagnetic $^s\text{OCO}^0$ ligand (Figure 2.14a). While the $^s\text{OCO}^0$ ligand could in principle be described as a singlet diradical with very strong antiferromagnetic coupling between the two conjugated ligand-radical electrons (Figure 2.14b), there are actually no indications for such a (broken-symmetry) electronic structure with multiple unpaired electrons. Complex $\mathbf{1}^{2+}$ contains only one unpaired electron according to DFT, which is located at cobalt.

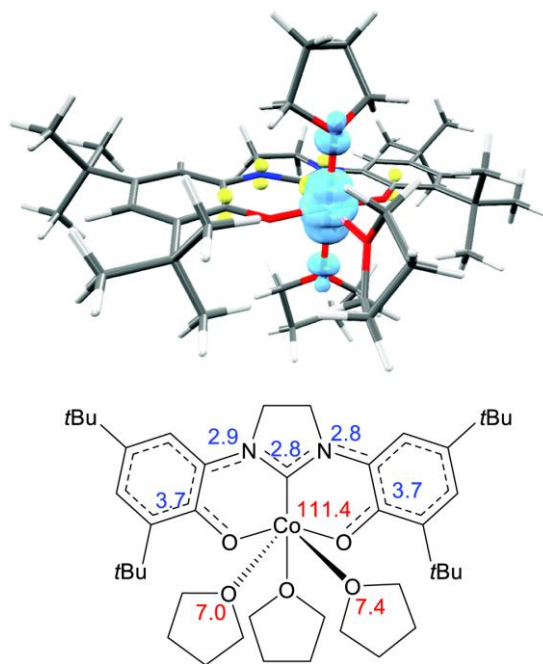


Figure 2.13. Top: Spin density plot of $\mathbf{1}^{2+}$ ($S = 1/2$), generated with IQMol (isosurface value 0.005). Bottom: Spin density per atom for the tris THF adduct of $\mathbf{1}^{2+}$ ($S = 1/2$).

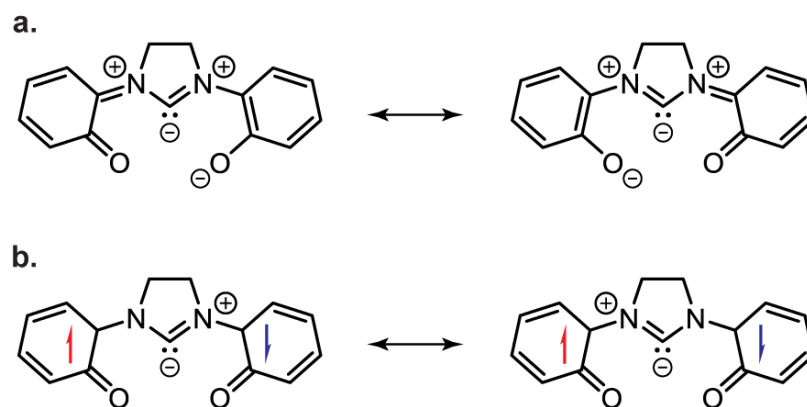


Figure 2.14. Key resonance structures of the closed-shell (a) and open-shell singlet (b) configurations of the doubly oxidized, charge neutral ($^5\text{OCO}^0$) ligand. The closed-shell representation a prevails according to DFT.

2.3.7 Electronic Spectra of the ET Series

The electronic spectra of complexes **1** – **1**²⁺, including molar absorptivities, were previously reported in the Ph.D. thesis of Dr. Michael B. Bayless. The goal of this section in my thesis is to report the TD-DFT calculations of complexes **1** and **1**⁺ in THF, compare them to the experimental UV-Vis data, and assign the transitions associated with each CT band. The current calculations for complex **1**²⁺ did not agree with the experimental electronic spectrum, possibly due to the instability of the doubly oxidized species, and will not be discussed in detail here.

The calculated spectrum of complex **1** is in good agreement with the experimental spectrum. The unpaired electron resides in orbital 163a (SOMO). However, the orbital 163b is empty and is also called the SOMO (as it is orbital 163). The letters ‘a’ and ‘b’ refer to the calculated alpha and beta spins, respectively. The numbering for the relevant orbitals is as follows:

158a/b: SOMO-5

161a/b: SOMO-2

162a/b: SOMO-1

163a/b: SOMO

164a/b: LUMO

166a/b: LUMO+2

167a/b: LUMO+3

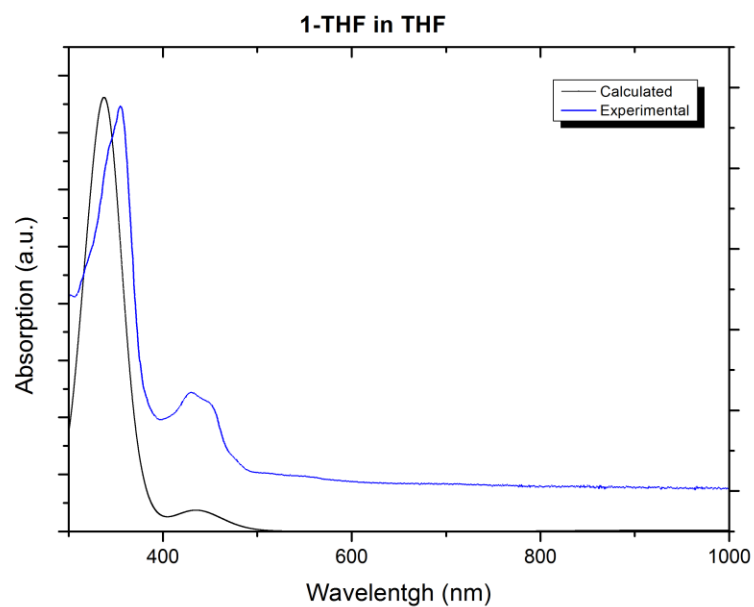


Figure 2.15. Calculated and experimental UV-Vis absorption spectrum of 1 in THF.

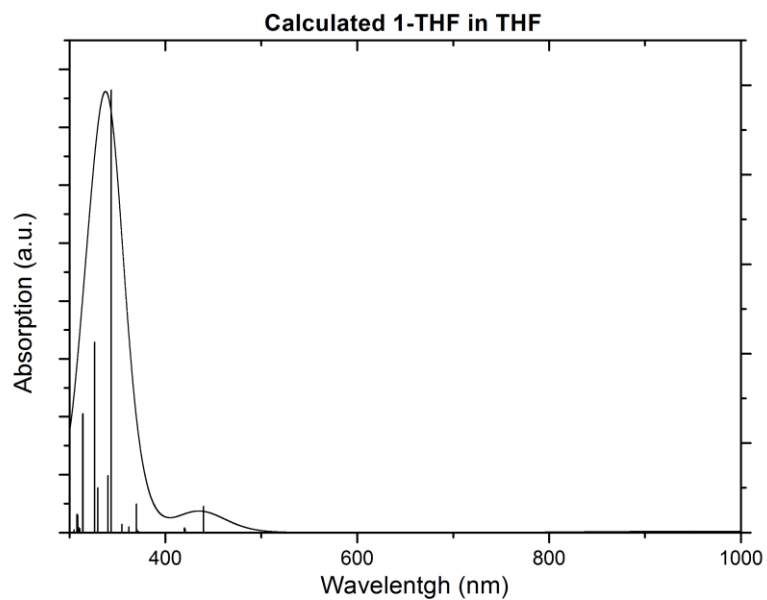
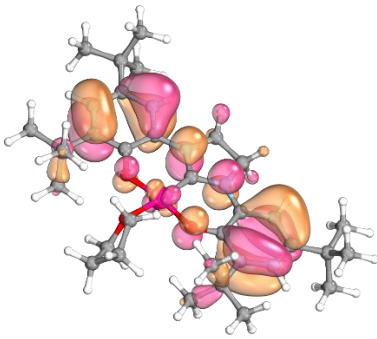
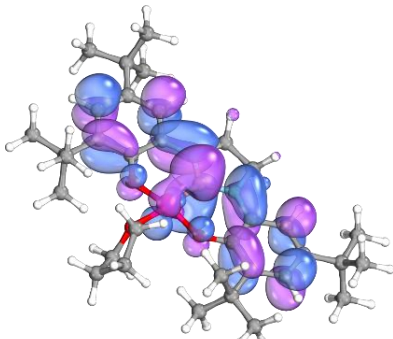
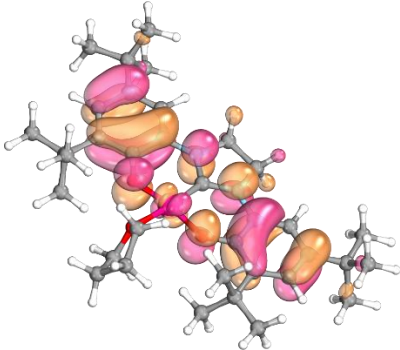
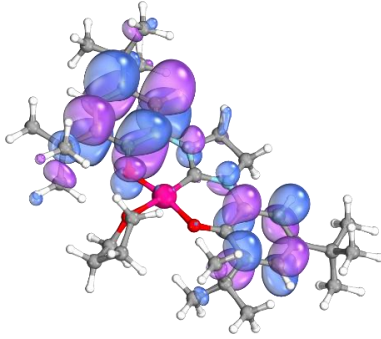
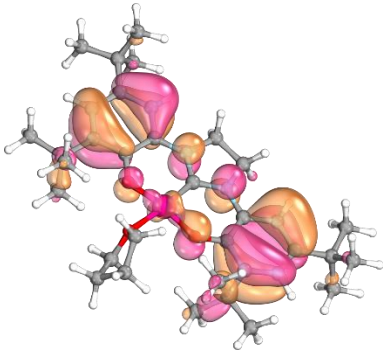
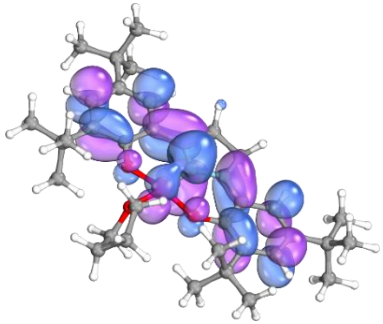
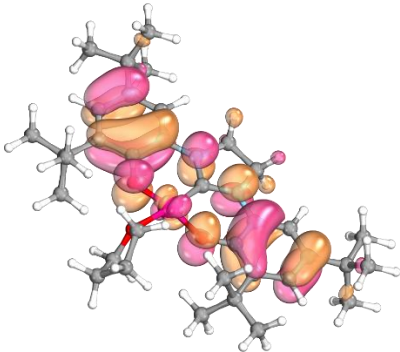
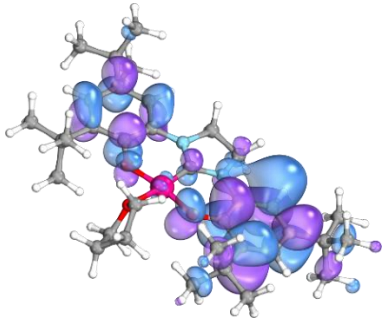
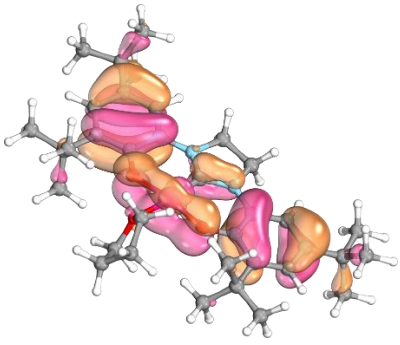
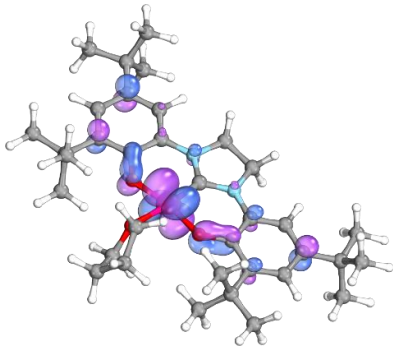
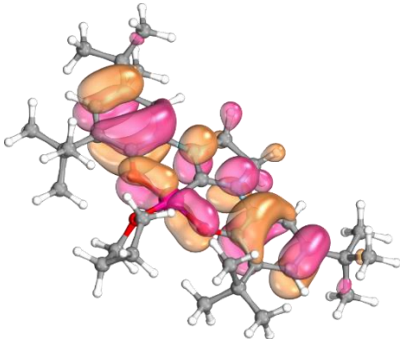
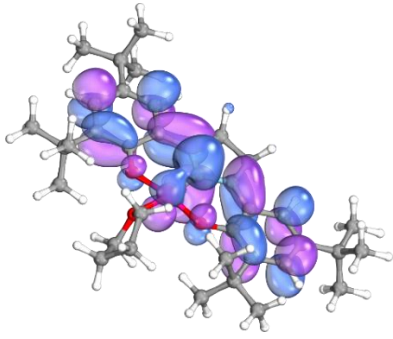
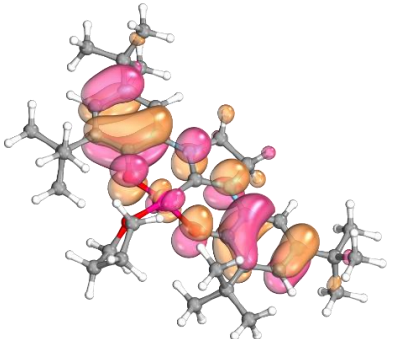
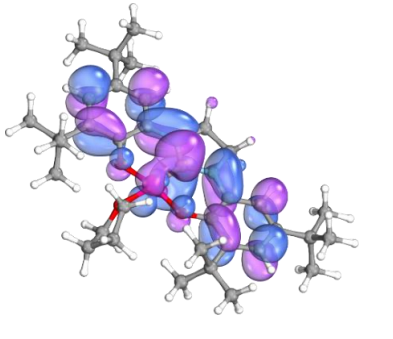
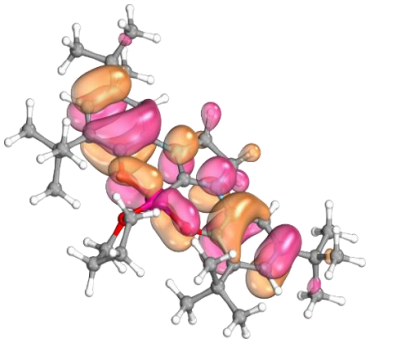
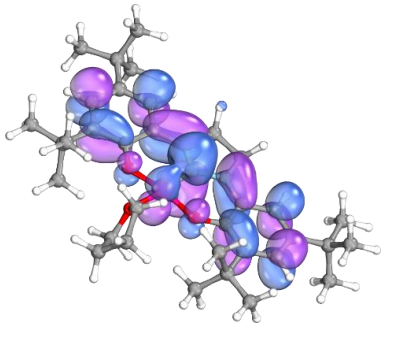


Figure 2.16. Calculated UV-Vis absorption spectrum of 1 in THF with single line absorption energies.

Table 2.3. Relevant MOs for 1. Generated with IboView, iso surface threshold set at 80.0.

λ (nm)	MO #1	MO #2	Weight
314	161a (SOMO-2) 	164a (LUMO) 	0.180518
	163a (SOMO) 	166a (LUMO+2) 	0.157477

	158b (SOMO-5)	164b (LUMO)	0.215073
			
326.2	163a (SOMO)	167a (LUMO+3)	0.289325
			
	161b (SOMO-2)	163b (SOMO)	0.183544
			

343.5	162b (SOMO-1)	164b (LUMO)	0.401245
			
439.8	163a (SOMO)	164a (LUMO)	0.709316
			
	162b (SOMO-1)	164b (LUMO)	0.186436
			

The calculated spectrum of complex $\mathbf{1}^+$ is also in good agreement with the experimental spectrum. Since $\mathbf{1}^+$ is best represented as a triplet with the unpaired electrons residing in the 182a and 183a orbitals, they are defined as SOMO(1) and SOMO(2), respectively. The numbering for the relevant orbitals is as follows:

180a/b: SOMO(1)-2

181a/b: SOMO(1)-1

182a/b: SOMO(1)

183a/b: SOMO(2)

184a/b: LUMO

185a/b: LUMO+1

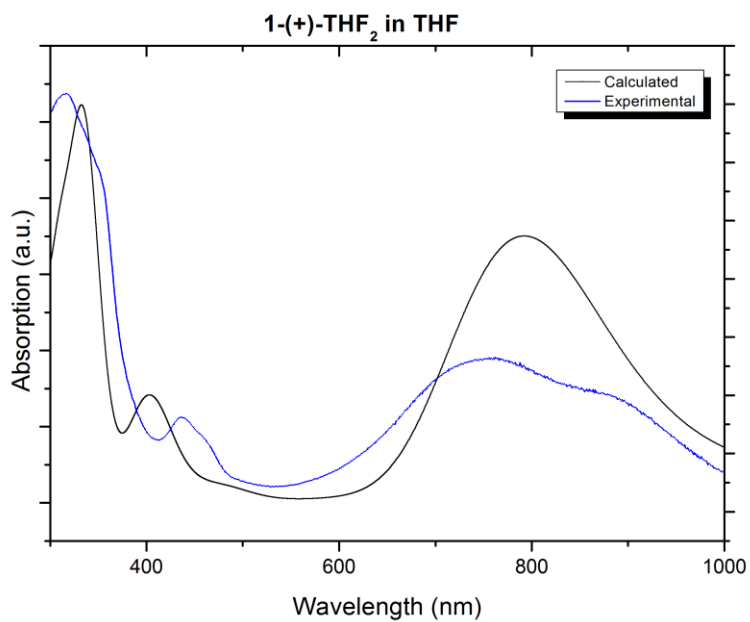


Figure 2.17. Calculated and experimental UV-Vis absorption spectrum of 1^+ in THF.

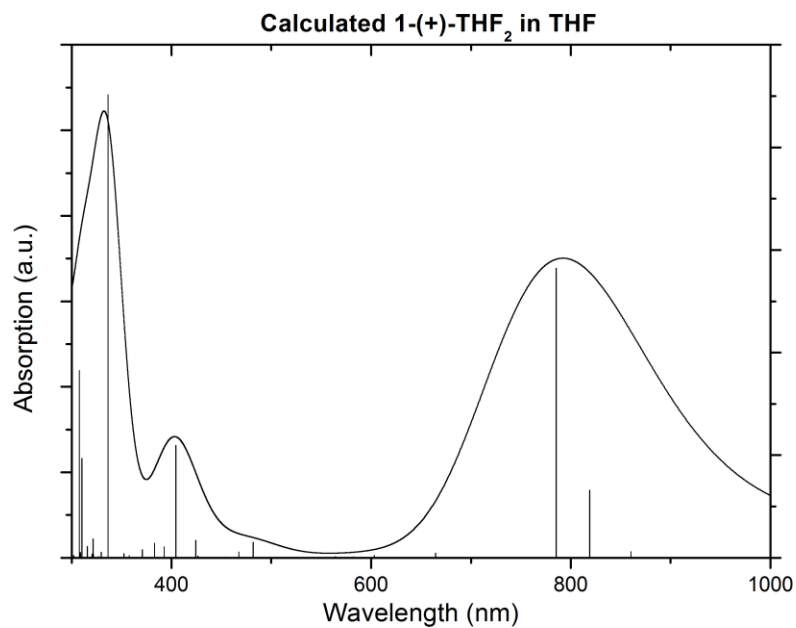
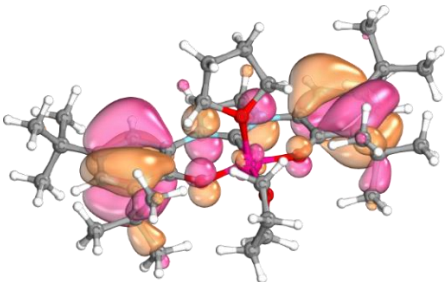
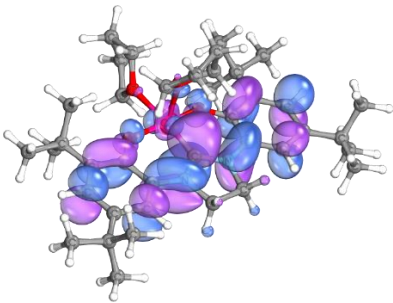
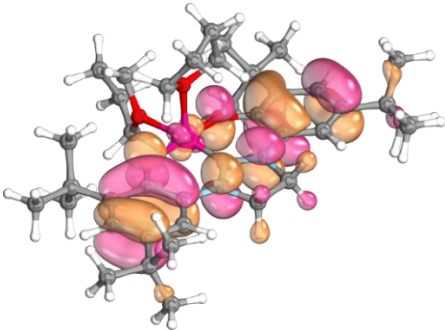
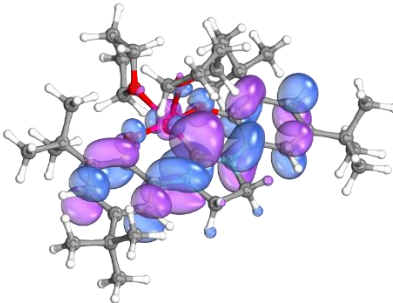
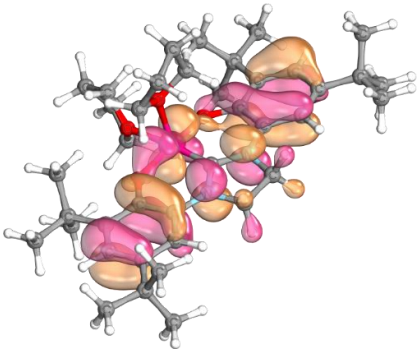
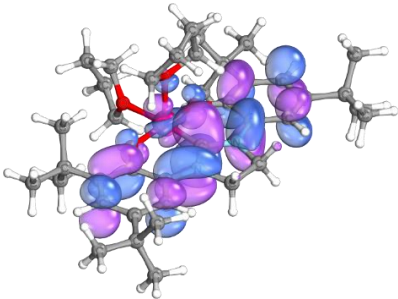
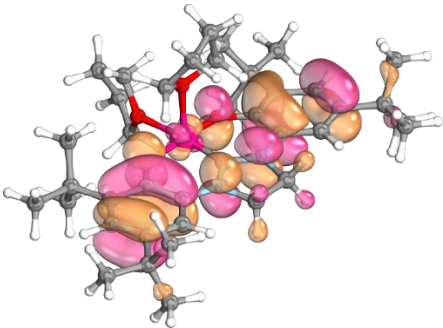
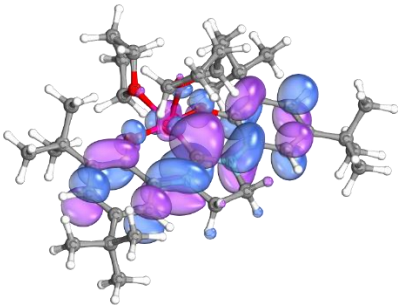
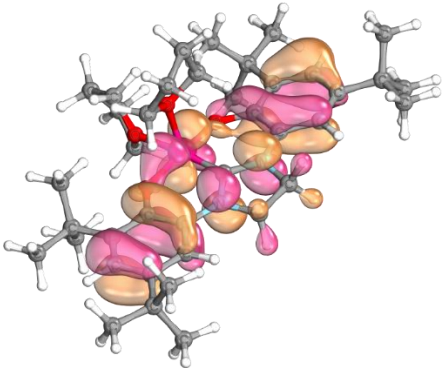
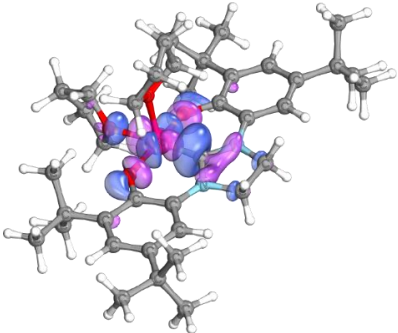


Figure 2.18. Calculated UV-Vis absorption spectrum of 1^+ in THF with single line absorption energies.

Table 2.4. Relevant MOs for 1⁺. Generated with IboView, iso surface threshold set at 80.0.

λ (nm)	MO #1	MO #2	Weight
336.4	181a (SOMO(1)-1) 	185a (LUMO+1) 	0.131697
	183a (SOMO(2)) 	185a (LUMO+1) 	0.149293

	180b (SOMO(1)-2)	184b (LUMO)	0.446359
			
404.3	183a (SOMO(2))	185a (LUMO+1)	0.425257
			
	180b (SOMO(1)-2)	185b (LUMO+1)	0.162476
			

2.4 Discussion

2.4.1 Physical Oxidation States in the (^SOCO)Co Electron Transfer Series

The bis(phenolate) NHC cobalt complexes reported herein span a remarkably broad range of redox states. Cyclic voltammograms of complexes **1** - **3** all show three quasi-reversible one-electron oxidations at <1.2 V vs. Fc⁺/Fc. These formally correspond to the generation of Co^{III}, Co^{IV} and Co^V in the mono-, di- and trications, respectively. But the combined experimental and computational data suggest the physical oxidation states of cobalt are significantly lower.⁸⁶

Complex **1** is appropriately described as [(^SOCO)Co^{II}(THF)], with a closed shell (^SOCO)²⁻ dianion supporting a low spin Co^{II} center, and the unsaturated NHC variants **2** and **3** are formulated similarly. Exclusively four coordinate, quasi-square planar structures were obtained for crystals of **1** grown from either THF or MeCN, and for **2** and **3** grown from MeCN. The reluctance to bind additional ligands is not attributable to sterics as evidenced by the quasi-octahedral structure of [(^SOCO⁰)Co^{II}(THF)₃]²⁺, which is formulated analogously as a low-spin Co^{II} ion. Rather, the preference for four coordination in the lower oxidation states is apparently electronic in origin. In the absence of significant π -bonding, the d_{x²-y²} orbital that is directed at the vacant coordination sites—when the z axis is colinear with the Co–C_{NHC} bond—is half-filled in the low spin *d*⁷ configuration. Oxidizing the ligand doesn't change the electron count at Co, so the preference for additional THF ligands in 1²⁺ most likely reflects increased Coulombic attraction to the dication. Isolation of 1²⁺ provides clear structural evidence for redox activity within the (OCO) pincer ligand. Although such ligand oxidations had

been previously suggested,^{70, 72} this is to our knowledge the first isolated (OCO) pincer complex with an oxidized ligand. X-ray data for the doubly oxidized ligand are consistent with those expected for a diradical, but calculations show it is better formulated as a closed shell ($^S\text{OCO}^0$) diamagnet, implying the NHC mediates electronic communication across the (OCO) framework.

The electronic structure of the intermediate oxidation state $\mathbf{1}^+$ species defies simple assignment. As noted above, the structural data can be reasonably interpreted as either $[(^S\text{OCO})\text{Co}^{\text{III}}(\text{THF})_2]^+$ with a closed-shell (^SOCO)²⁻ bis(phenolate) ligand on an intermediate spin Co^{III} center, or $[(^S\text{OCO}')\text{Co}^{\text{II}}(\text{THF})_2]^+$ with a low-spin Co^{II} ion bound and antiferromagnetically coupled to a monoanionic ($^S\text{OCO}'$)⁻ ligand radical, containing a single unpaired electron distributed over the (OCO) π system. DFT calculations are more consistent with the latter formulation, but reveal closed-shell singlet and open-shell singlet states at thermally accessible energies relative to the triplet ($S = 1$) ground state. In reality, the ground state of $\mathbf{1}^+$ might have multiple contributors. If the true electronic structure is indeed some combination of the formulations listed above, then the physical oxidation states of the metal and ligand should be highly susceptible to small perturbations in the solvent, temperature, and coordination environment, making the ligand truly non-innocent.⁸⁷

2.4.2 Effects of NHC Unsaturation on Ligand-Centered Oxidations

The oxidized variants of **2** and **3** were not isolated, but given the structural homology in **1** - **3** it seems reasonable to assume that $\mathbf{2}^{2+}$ and $\mathbf{3}^{2+}$ also contain ligand radicals. So how to rationalize the large (up to 400 mV) anodic shifts in the ligand-

centered oxidations upon incorporation of unsaturation into the NHC ligand backbone? Two potential explanations were considered.

1. Wolczanski and co-workers have recently suggested that the relative accessibility of ligand-centered oxidations can be understood by simple π -electron counting and the application of Hückel's rule.⁸⁸⁻⁸⁹ By this logic, the (^SOCO)²⁻ ligand is a 20e⁻ π system that becomes aromatic upon 2e⁻ oxidation to ($^S\text{OCO}^0$) (see Figure 2.14a). The unsaturated (OCO)²⁻ and (^{Ph}OCO)²⁻ ligands have 22 and 26 π -electrons, respectively, making them aromatic in their reduced forms; they should have a much lower propensity to be oxidized, which is consistent with the CV data. This argument implies that the unsaturated backbones in the imidazole and benzimidazole-derived ligands are capable of delocalizing their π -electrons across the entire (OCO) ligand. Previous literature has suggested that unsaturated imidazole-derived NHCs may⁹⁰ or may not⁹¹ be aromatic. If the backbone π -electrons are electronically decoupled from the rest of the (OCO) framework, then this rationale fails. The DFT results strongly point to full delocalization of the π system, in favor of aromaticity of the ($^S\text{OCO}^0$) ligand in **1**²⁺.

2. As detailed above, the varying Co–C bond distance across **1** - **3** might be ascribed to enhanced π -backdonation from the Co^{II} center in **1** to the NHC as compared to **2** and **3**. The saturated imidazoline-derived NHC is known to be a better π -acceptor than the unsaturated (benz)imidazole NHCs.^{65, 82} Enhanced backbonding increases π -electron density in the saturated (^SOCO)²⁻ ligand, thereby increasing its susceptibility to oxidations that generate phenoxyl radicals by removal of one or more π -electrons.

A definitive explanation for the observed shifts in the ligand-centered oxidation potentials eludes us. It might in fact arise from a combination of the factors listed above. In contrast, the relative invariance in the first oxidation events across **1** – **3**, is reasonably attributed to significant Co^{III} character in **1**⁺ - **3**⁺. From the perspective of the Co^{II} center, the coordination environment is nearly uniform in all of **1** - **3**, rendering a metal-centered oxidation relatively invariant to unsaturation or substitutions in the distal half of the NHC fragment.

2.4.3 (OCO) as a Platform for Multielectron Transformations at Cobalt

The sum of the structural and electronic data presented above presents an exciting opportunity to develop new small molecule reaction chemistry at (OCO) complexes. For instance, a list of design criteria for a new Co cross coupling catalyst might include a low-coordinate complex in a low formal oxidation state, with a multielectron capacity that favors higher coordination numbers in higher oxidation states. In this respect, the (OCO) ligand seems ideally suited for such organometallic reactivity at later 3d metals. As shown herein, it stabilizes low coordinate Co in low formal oxidation states, and higher formal oxidation states lead to higher coordination complexes. The (OCO)Co core is robust, but labile ancillary ligands afford multiple cis coordination sites for small molecule binding and activation. Most importantly, the (OCO) framework gives access to oxidation states three levels above Co^{II} at modest potentials. Accordingly, oxidative addition to Co^{II} can be envisioned to occur without formation of high energy Co^{IV} species. Furthermore, unsaturation in the NHC backbone is shown to afford a high degree of electronic tunability, allowing the reducing power of the metal complexes to be tuned by up to 400 mV without significantly perturbing the coordination environment or sterics

about the Co centers. These properties should be broadly transferrable to other organometallic catalysis cycles that utilize precious metals for multielectron bond activation and functionalization.

2.5 Reactivity of the [$^{\delta}\text{OCO}$ Co(THF)] Series

2.5.1 Transmetallation to Complex $\mathbf{1}^+$

Previous attempts to generate a second Co–C bond via transmetallation to the one-electron oxidized species [$^{\delta}\text{OCO}$ Co(THF) $_2$][OTf], complex $\mathbf{1}^+$, using organometallic reagents such as organozinc halides, organomagnesium halides, or organolithium species all resulted in the same C–C reductive elimination products. In each case, reductive elimination of the organic ligand to the carbene carbon was observed to have occurred, producing an organic imidazolium salt. The resulting metal species was not identified. This detrimental reaction has been previously reported and has even been referred to as the “Achilles heel in [NHC catalysis]”.⁹² The organic ligand would have to coordinate axially to the ligand plane, *cis* to the carbene, in order to facilitate C–C bond forming reductive elimination. We postulated an inner sphere halide complex, if coordinated *trans* to the carbene, would act as a directing group for the transmetallation process and avoid the deleterious reductive elimination pathway.

2.5.2 Reaction with One-Electron Halogen Source

To determine the coordination environment of an inner sphere halide complex, complex $\mathbf{1}$ was reacted with a 0.5 equivalents of PhICl $_2$ in THF in an attempt to generate the species [$^{\delta}\text{OCO}$ Co(Cl)(THF) $_n$]. The initial turquoise-colored solution changed to

green over the course of ~1-2 h. After 6 h, the volatiles were removed *in vacuo* to afford a green solid. The resulting solid was crystallized by layering pentane over a concentrated THF solution and storing it at -25 °C for 18 h. The solid-state structure of this complex **4** contains two ligands, two cobalt atoms, and two chlorine atoms, however the atomic connectivity was not as expected (Figure 2.19). One cobalt atom coordinates to both chlorine atoms at distances of 2.239(2) and 2.245(2) Å. The first cobalt center is bridged to the second cobalt complex through the oxygen atoms of two phenoxides. The second cobalt center is coordinated by both (^sOCO) ligands, however one ligand has been rearranged. The C67–N5 bond has been broken leading to loss of the NHC component, and the atom C67 has inserted into the Co4–O7 bond. This forms two new bonds, Co4–N5 and C67–O7, generating a Co4–C67 coordinated benzoxazole. The bonding metrics of the three remaining phenoxides do not indicate any ligand oxidation, supporting the formal oxidation state assignment of both cobalt centers as +III.

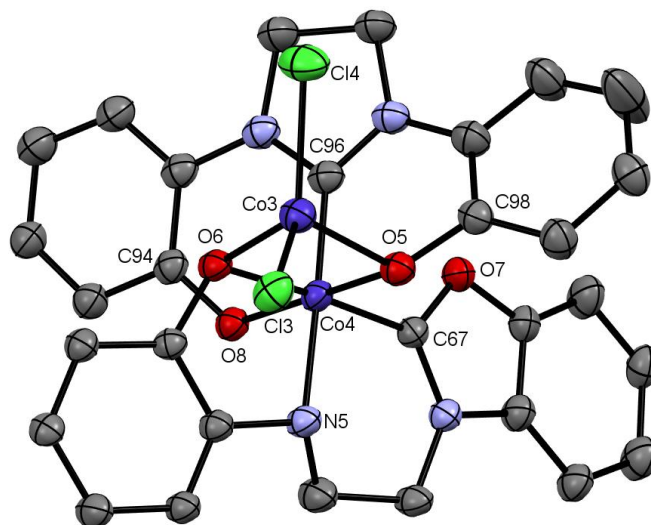


Figure 2.19. ORTEP plot of complex **4** as one molecule in an asymmetric unit cell containing two molecules. Thermal ellipsoids are drawn at 50% probability. *Tert*-butyl groups and hydrogen atoms have been removed for clarity. Selected bond lengths (Å): Co4–C96 1.835(8), Co4–O5 1.937(5), Co4–O6 1.996(5), Co4–O8 1.904(5), Co4–N5 2.011(6), Co4–C67 1.897(7), Co3–O5 2.044(5), Co4–O6 2.011(5), Co4–Cl3 2.239(2), Co4–Cl4 2.245(2).

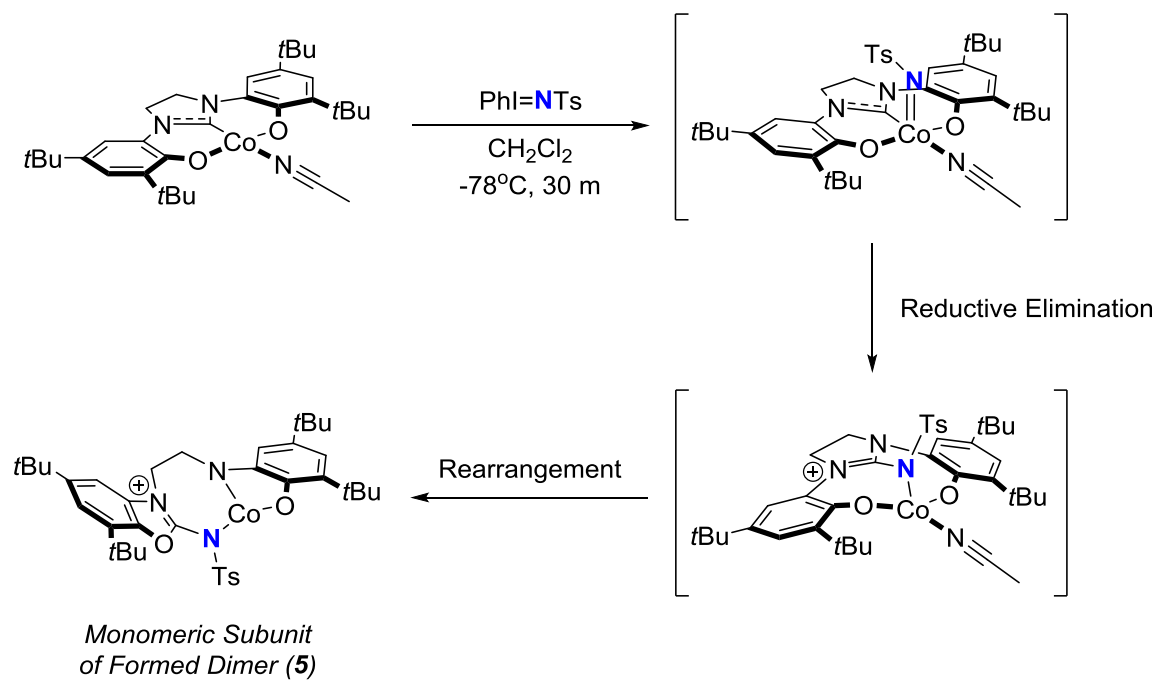
2.5.3 Reaction with (*Tosyliminoiodo*)benzene

Late transition metal imido complexes (TMIs) represent important reactive intermediate species in many useful organic and inorganic transformations.⁹³ The bonding characteristics of such complexes exhibit similarities to that of nitrido ligands, forming one σ and two π bonds. Such an assignment would assume M=N-R forms linear bond, although this is not often true. Metrical perturbations in M=N-R species are increasingly common in metals with significant electron density (i.e. high *d*-count metal centers), and are only capable of one σ and one π bond due to population of M-N antibonding orbitals.⁹³

In particular, iron imido complexes have been proposed as isoelectronic surrogates to iron oxo complexes and their utility in C-H bond amination has been explored.⁹⁴⁻⁹⁵ We proposed the (^SOCO)Co system may also be capable similar reactivity, so the synthesis of a formal Co^{IV} imido complex was attempted. Complex **1** was treated with 1 equivalent of the hypervalent iodine, (tosyliminoiodo)benzene (PhINTs) in CH₂Cl₂ at -78 °C. The solution was allowed to warm to room temperature during which time, a color change from orange to brown was observed. The solution was concentrated and then stored at -25 °C for 22 h, producing air-sensitive brown crystals suitable for X-ray diffraction.

The solid-state structure revealed a dimeric unit in which, again, the ligand had rearranged to a benzoxazole. However, this time the NTs group had inserted into the C-Co bond. A reasonable mechanism for the observed product is shown in Scheme 2.5 which involves reductive elimination from the putative Co-imido species, affording a dimeric complex in which both cobalt centers are in the +II oxidation state.

Scheme 2.5. Possible mechanistic pathway to form complex 5.



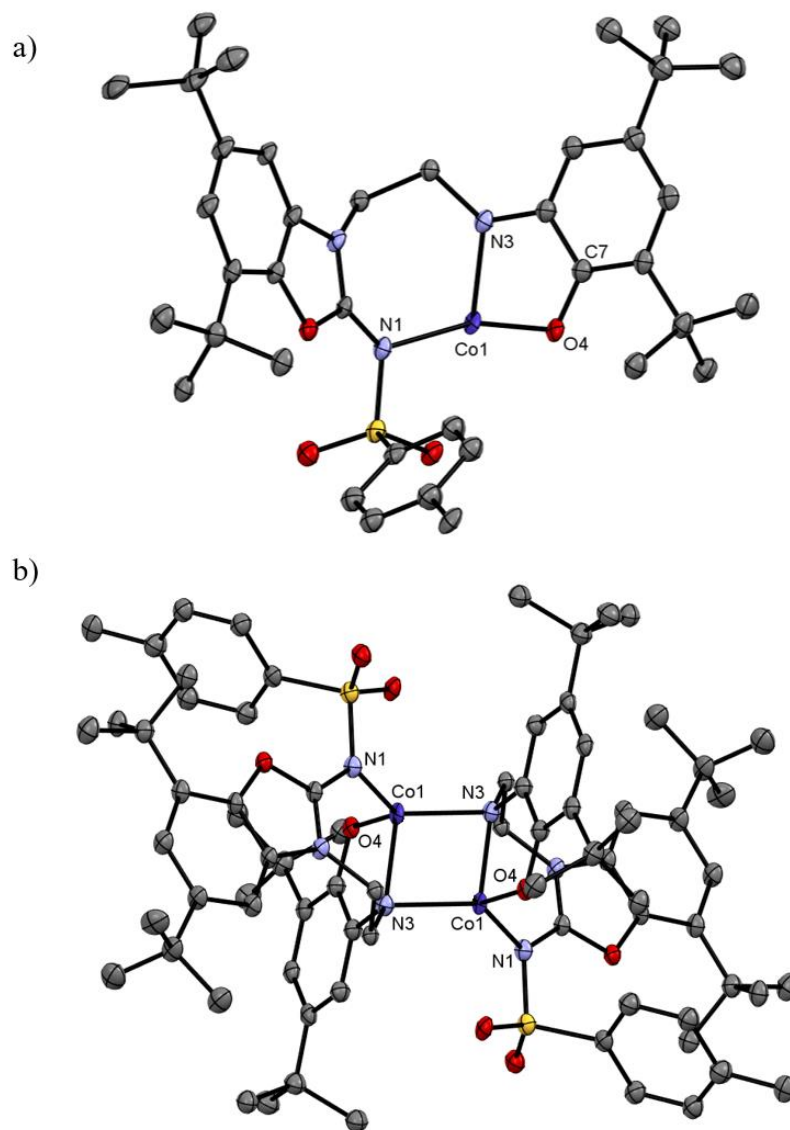


Figure 2.20. ORTEP plot of complex 5 as a monomeric subunit (a) and as the dimer (b). Thermal ellipsoids are drawn at 50% probability. Hydrogen atoms have been removed for clarity. Selected bond lengths (Å): Co1-N1 (2.012(7)), Co1-N3 (2.029(7)), Co1-O4 (1.927(5)), O4-C7 (1.319(9)).

2.6 Conclusions and Future Work

Tridentate, *mer* pincer-type ligands are now ubiquitous in catalysis, and the (OCO) pincer appears to be well positioned to take a place alongside "privileged" ligands for base metal catalysis, such as bis(imino)pyridine (NNN) pincers.⁶⁰ The factors that make

this system particularly attractive as a platform for new reaction chemistry include the capacity to stabilize Co over three or more formal oxidation states at relatively modest potentials, along with an impressive flexibility in coordination number and geometry. All of these are predicated on the capacity of the (OCO) ligand to persist in oxidation states that span multiple electrons. Although this redox-capacity had been previously inferred, this report describes, to our knowledge, the first structurally characterized (OCO) ligand radicals and provides unequivocal proof for the redox activity of this ligand scaffold.

The (OCO) pincer ligands additionally show a remarkable and unexpected electronic tunability, with ligand-centered oxidations spanning over 400 mV depending on the degree of unsaturation in the NHC ligand backbone. Going forward, we posit that these properties will be broadly beneficial for the development of new methods for selective, organometallic-type small molecule redox transformations at later 3d metals. In addition, because in the singly oxidized state, the singlet state is only ~5 kcal/mol higher than the triplet state observed at ambient temperature, VT-NMR and SQUID magnetic measurements may provide interesting insights to other physical peculiarities.

2.7 Experimental

2.7.1 General Considerations

Unless otherwise specified, all manipulations were performed under anaerobic conditions using standard vacuum line techniques, or in an inert atmosphere glove box under purified nitrogen. Routine NMR spectra were acquired on either a Varian Mercury 300 spectrometer (300.323 MHz for ¹H; 75.5 MHz for ¹³C) or a Varian Mercury 400 spectrometer (399.94 MHz for ¹H; 101.1 MHz for ¹³C). All chemical shifts are reported

in parts per million (ppm) relative to TMS, with the residual solvent peak serving as an internal reference.⁹⁶ Solution magnetic moments were obtained by Evan's NMR method,⁹⁷⁻⁹⁸ and are reported as the average of three independent measurements, unless otherwise specified. UV–visible absorption spectra were acquired using a Varian Cary 50 spectrophotometer. Unless otherwise noted, all electronic absorption spectra were recorded at ambient temperatures in 1 cm quartz cells. IR absorption spectra were obtained via attenuated total reflection (ATR) with a diamond plate using a Bruker ALPHA Fourier-transform infrared spectrophotometer. All mass spectra were recorded in the Georgia Institute of Technology Bioanalytical Mass Spectrometry Facility. Electrospray ionization mass spectrometry (ESI–MS) was carried out with acetonitrile solutions using a Micromass Quattro LC spectrometer. Electron impact mass spectra (EI–MS) were obtained using a VG instruments model 70-SE spectrometer. The EPR spectrum was recorded on a Bruker EMX X-band spectrometer equipped with a He-cryostat. The spectrum was analyzed and simulated using the W95EPR program of Prof. F. Neese. Cyclic voltammetry experiments were performed inside an N₂-filled glove box in MeCN with 0.1 M ([nBu₄N][PF₆]) as the supporting electrolyte, unless otherwise noted. The voltammograms were recorded with a CH Instruments 620C potentiostat, using a 2.5 mm (O.D) 1.0 mm (I.D.) Pt disk working electrode, Ag wire quasi-reference electrode, and a Pt wire auxiliary electrode, at a scan rate of 0.1 V s⁻¹, unless reported otherwise. Reported potentials are referenced to the ferrocenium/ferrocene (Fc⁺/Fc) redox couple, added as an internal standard at the conclusion of each experiment. Elemental analyses were performed by Atlantic Microlab, Inc., Norcross, GA. All analyses were performed in duplicate, and the reported compositions are the average of the two runs.

2.7.2 Materials and Methods

Anhydrous acetonitrile (MeCN), dichloromethane, pentane, and toluene solvents for air- and moisture-sensitive manipulations were purchased from Sigma-Aldrich and further dried by passage through columns of activated alumina, degassed by at least three freeze-pump-thaw cycles, and stored under N₂ prior to use. Anhydrous diethyl ether (Drisolv), methanol (Drisolv), and benzene (Drisolv) were purchased from EMD Millipore and used as received. Dichloromethane-*d*₂ and acetonitrile-*d*₃ (Cambridge Isotope Labs) were dried over excess calcium hydride and vacuum distilled to an oven-dried sealable flask, and degassed by successive freeze-pump-thaw cycles. Tetrahydrofuran-*d*₈, chloroform-*d*₁, and methanol-*d*₁ (Cambridge Isotope Labs) were used as received. The materials (N,N'-bis(2-hydroxy-3,5-di-*tert*-butylphenyl)ethylenediamine,⁷³ (N,N'-bis(2-hydroxy-3,5-di-*tert*-butylphenyl)phenylenediamine,⁷⁴ and the ligand H₃[(OCO)]Cl⁶³ were prepared according to published procedures. Complexes **1** - **12**⁺ were previously reported in the thesis of Dr. Michael B. Bayless. [N(*p*-C₆H₄Br)₃][PF₆] was synthesized following a literature procedure.⁹⁹ Sodium *tert*-butoxide (5.4 M in MeOH; Alfa Aesar), triethyl orthoformate (Alfa Aesar), paraformaldehyde (Alfa Aesar), formic acid (Alfa Aesar), and anhydrous CoCl₂ (Strem) were used as received.

2.7.3 Synthesis of [H₃(^sOCO)]Cl

In a modified procedure from literature,⁶⁸ (N,N'-bis(2-hydroxy-3,5-di-*tert*-butylphenyl)ethylenediamine (5.65g; 12.1 mmol) was dissolved in (EtO)₃CH (250 mL) and heated to 70 °C open to air. Conc. HCl (1.33 mL; 16.1 mmol) was added dropwise

over ~5 mins resulting in a color change from golden yellow to red/purple. After approx. 15 min., a thick white precipitate formed and the stirring was increased to ensure even mixing. After stirring for 1 h, the reaction was cooled to r.t. and filtered. The white solid was washed with copious amounts of Et₂O (~ 150 mL) and dried under high vacuum at 50 °C overnight (4.93g; 79% yield). All characterization data matched those previously reported.⁶⁸

2.7.4 Synthesis of [H₃(^{Ph}OCO)]Cl

In a modified procedure from literature,⁷⁴ (N,N'-bis(2-hydroxy-3,5-di-*tert*-butylphenyl)phenylenediamine (3.52g; 6.81 mmol) was dissolved in (EtO)₃CH (150 mL) and heated to 70 °C open to air. Conc. HCl (0.84 mL; 10.2 mmol) was added dropwise over ~5 mins resulting in a color change from golden yellow to red/purple. After approx. 15 min., a thick white precipitate formed and the stirring was increased to ensure even mixing. After stirring for 1 h, the reaction was cooled to r.t. and filtered. The white solid was washed with copious amounts of Et₂O (~ 150 mL) and dried under high vacuum at 50 °C overnight (3.14g; 82% yield). All characterization data matched those previously reported.⁷⁴

2.7.5 Synthesis of Complexes **1** – **3**

The same general procedure was followed for all of **1** - **3**. A 20 mL scintillation vial was charged with a solution of [H₃(^SOCO)]Cl (515 mg, 1.0 mmol) in MeOH (8 mL). NaOMe (5.4 M in MeOH, 555 µL, 3.0 mmol) was added dropwise. The resulting yellow colored solution was stirred for 5 m and then added dropwise to a separate 20 mL vial containing anhydrous CoCl₂ (129.8 mg, 1.0 mmol) in MeOH (10 mL). The solution

became dark red and a red/orange precipitate formed within 0.5 h. The suspension was stirred for an additional 6 h and the solids were then separated by vacuum filtration.

2.7.6 Synthesis of $[(^S\text{OCO})\text{Co}(\text{MeCN})]$ (**1**)

Following the above representative procedure, the collected solids were suspended in MeCN (5 mL) and a minimal amount of toluene was added to completely dissolve the material. This solution was stored at $-25\text{ }^{\circ}\text{C}$ for 18 h, producing orange colored crystals of **1** suitable for XRD analysis (507.5 mg, 0.88 mmol, 88%). Satisfactory elemental analysis required the inclusion of solvent-derived MeOH, the reported analysis is for $[(^S\text{OCO})\text{Co}(\text{MeCN})]\cdot 1.5\text{MeOH}$. Anal. Calc. for $\text{C}_{34.5}\text{H}_{53}\text{CoN}_3\text{O}_{3.5}$: C, 66.33; H, 8.55; N, 6.73. Found: C, 66.84; H, 8.16; N, 6.23. UV-vis (MeCN) λ_{max} , nm (ϵ , $\text{M}^{-1}\text{ cm}^{-1}$): 438 (5600). FTIR (ATR, cm^{-1}): 2949(m), 2900(m), 2865(m), 1627(w), 1477(s), 1449(s), 1389(m), 1357(m), 1325(s), 1285(m), 1236(m), 1201(m), 1073(w), 982(w), 842(m), 760(m), 701(m), 678(m), 644(m), 579(m), 514(m), 434(m), 413(m).

2.7.7 Synthesis of $[(^S\text{OCO})\text{Co}(\text{THF})]$ (**1**)

The THF adduct to **1** was obtained analogously using THF solvent in place of MeCN. Crystalline solids suitable for single crystal X-ray diffraction were obtained by slow diffusion of pentane into a saturated THF solution at $-20\text{ }^{\circ}\text{C}$. UV-vis (THF) λ_{max} , nm (ϵ , $\text{M}^{-1}\text{ cm}^{-1}$): 430 (5300). FTIR (ATR, cm^{-1}): 2947(m), 2899(m), 2866(m), 1506(s), 1478(m), 1447(m), 1389(m), 1358(m), 1325(s), 1283(m), 1270(m), 1240(m), 1200(m), 1159(m), 1076(m), 1051(m), 914(m), 894(m), 869(m), 836(m), 756(m), 699(m), 643(m), 605(m), 578(m), 545(m), 512(m), 466(m), 434(m), 419(m).

2.7.8 Synthesis of [(OCO)Co(MeCN)] (2)

Following the above representative procedure, followed by recrystallization from MeCN-toluene at $-25\text{ }^{\circ}\text{C}$ afforded **2** as X-ray quality crystals in 93% yield. Anal. Calc. for $\text{C}_{33}\text{H}_{45}\text{CoN}_3\text{O}_2$: C, 68.97; H, 7.89; N, 7.31. Found: C, 68.54; H, 7.78; N, 7.28. UV-vis (MeCN) λ_{max} , nm (ϵ , $\text{M}^{-1}\text{ cm}^{-1}$): 308 (23,000), 327 (2200), 418 (5100). FTIR (ATR, cm^{-1}): 2953(m), 2907(m), 2873(m), 1444(s), 1328(m), 1323(s), 1274(w), 1239(m), 1204(w), 1096(m), 914(w), 843(s), 774(m), 695(m), 663(s), 605(m), 587(m), 577(m), 550(m), 507(m), 422(m).

2.7.9 Synthesis of [$^{\text{Ph}}$ OCO)Co(MeCN)] (3)

Following the above representative procedure, followed by recrystallization from MeCN-toluene at $-25\text{ }^{\circ}\text{C}$ afforded **3** as single crystals suitable for XRD in 89% yield. Anal. Calc. for $\text{C}_{37}\text{H}_{47}\text{CoN}_3\text{O}_2$: C, 71.14; H, 7.58; N, 6.73. Found: C, 71.41; H, 7.51; N, 6.77%. ESI-MS (m/z): 655.4 $[\text{M}]^+$. UV-vis (MeCN) λ_{max} , nm (ϵ , $\text{M}^{-1}\text{ cm}^{-1}$): 305 (19000), 427 (4900). FTIR (ATR, cm^{-1}): 2952(m), 2903(m), 2865(m), 1476(m), 1459(m), 1427(m), 1377(m), 1356(s), 1335(m), 1301(m), 1218(m), 1199(m), 1179(w), 1158(w), 921(w), 860(s), 770(m), 737(s), 719(m), 632(m), 553(m), 436(m), 421(m).

2.7.10 Synthesis of Complex 4

Complex **1-THF** (303.9 mg; 0.5 mmol) was dissolved in THF (10 mL) and PhICl_2 (61.9 mg; 0.25 mmol) was added in portions over 5 m. The resulting turquoise solution was stirred for 6 h in which time the solution changed to a dark green color. The volatiles were removed *in vacuo* to afford a green powder. The green solid was dissolved

in a minimal amount of THF, layered with pentane, and stored at -25 °C for 18 h, producing green crystals of the formula $C_{62}H_{88}Cl_2Co_2N_4O_4$ (96% yield based on the structure **4**). UV-vis (CH_2Cl_2) λ_{max} , nm (ϵ , L/mol*cm): 451, 571.

2.7.11 Synthesis of Complex **5**

Complex **1-THF** (303.9 mg; 0.5 mmol) was dissolved in C_6H_6 (10 mL) and (tosyliminoiodo)benzene (61.9 mg; 0.5 mmol) was added all-at-once. The resulting dark orange solution was stirred for 16 h. The volatiles were removed *in vacuo* to afford a green powder. The green solid was dissolved in a minimal amount of THF, layered with pentane, and stored at -25 °C for 18 h, producing air-sensitive brown crystals of the formula $C_{70}H_{102}Co_2N_6O_8S_2$ (82% yield based on the structure **4**).

2.8 X-ray Crystallography

2.8.1 General Considerations

Unless otherwise noted, X-ray diffraction data were collected using a Bruker APEX-II CCD diffractometer equipped with an Oxford Cryosystems low-temperature apparatus. Unit cell indexing was performed by using the APEX2 (Bruker) software. Data were measured with MoK_{α} radiation (fine-focus sealed tube, 45 kV, 35 mA). The total number of runs and images was based on the strategy calculation from the program **APEX2** (Bruker). Unit cell indexing was performed by using the **APEX2** (Bruker) software and refined using **SAINT** (Bruker, V8.34A, 2013). Data reduction, scaling and absorption corrections were performed using **SAINT** (Bruker, V8.34A, 2013) and **SADABS-2014/5** (Bruker, 2014) was used for absorption correction. The $\lambda/2$ correction

factor is 0.00150. The software also corrects for Lorentz polarization. The crystal structures were refined by Least Squares using version 2014/7 of **XL** (Sheldrick, 2008). All non-hydrogen atoms were refined anisotropically. Hydrogen atom positions were calculated geometrically and refined using the riding model.

2.8.2 $[(^S\text{OCO})\text{Co}(\text{MeCN})]$ (**1**)

An orange, prism-shaped crystal with dimensions 0.382×0.228×0.149 mm was mounted on a loop with paratone oil. X-ray diffraction data were collected at $T = 100(2)$ °K. The maximum resolution achieved was $\Theta = 29.675^\circ$.

Unit cell indexing was performed and refined based on 10495 reflections, 17% of the observed reflections. The ratio of minimum to maximum transmission is 0.8753. The final completeness is 99.4% out to 29.675° in Θ . The absorption coefficient (μ) of this material is 0.496mm^{-1} and the minimum and maximum transmissions are 0.6530 and 0.7460.

The structure was solved in the space group P1 with the **ShelXT** (Sheldrick, 2015) structure solution program using combined Patterson and dual-space recycling methods. The space group Pnnm (# 58) was determined by **ShelXT** (Sheldrick, 2015) structure solution program.

2.8.3 $[(\text{OCO})\text{Co}(\text{MeCN})]$ (**2**)

A yellow, prism-shaped crystal with dimensions 0.65×0.16×0.14 mm was mounted on a loop with paratone oil. X-ray diffraction data were collected at $T = 100(2)$ °K. The maximum resolution achieved was $\Theta = 24.709^\circ$.

Unit cell indexing was performed on 9857 reflections, 36% of the observed reflections. $wR_2(\text{int})$ was 0.1730 before and 0.0738 after correction. The ratio of minimum to maximum transmission is 0.6290. The final completeness is 97.8% out to 24.709° in θ . The absorption coefficient (μ) of this material is 0.463mm^{-1} and the minimum and maximum transmissions are 0.6290 and 1.0000.

The structure was solved with the **ShelXT** (Sheldrick, 2015) structure solution program using combined Patterson and dual-space recycling methods. The space group $P2_1/c$ was determined by **ShelXT** (Sheldrick, 2015) structure solution program.

2.8.4 $[(^{\text{Ph}}\text{OCO})\text{Co}(\text{MeCN})]$ (**3**)

An orange, prism-shaped crystal with dimensions $0.585 \times 0.284 \times 0.112$ mm was mounted on a loop with paratone oil. X-ray diffraction data were collected at $T = 100(2)$ °K. The maximum resolution achieved was $\theta = 27.484^\circ$.

Unit cell indexing was performed and refined based on 3059 reflections, 60% of the observed reflections. The ratio of minimum to maximum transmission is 0.8808. The final completeness is 93.2% out to 27.484° in θ . The absorption coefficient (μ) of this material is 0.553mm^{-1} and the minimum and maximum transmissions are 0.828 and 0.940.

The structure was solved with the **ShelXT** (Sheldrick, 2015) structure solution program using combined Patterson and dual-space recycling methods. The space group *Pmca* was determined by **ShelXT** (Sheldrick, 2015) structure solution program.

2.8.5 $[(^8\text{OCO})\text{Co}(\text{THF})]$ (**1-THF**)

A red block-shaped crystal with dimensions 0.22×0.10×0.05 mm was mounted on a loop with paratone oil. X-ray diffraction data were collected using a Bruker APEX-II CCD diffractometer equipped with an Oxford Cryosystems low-temperature apparatus operating at $T = 173(2)^\circ\text{K}$.

Data were measured using MoK_α radiation (fine-focus sealed tube, 45 kV, 35 mA). The total number of runs and images was based on the strategy calculation from the program APEX2 (Bruker). The maximum resolution achieved was $\Theta = 27.484^\circ$.

Unit cell indexing was performed by using the APEX2 (Bruker) software and refined using SAINT (Bruker, V7.68A, 2009) on 3263 reflections. $wR_2(\text{int})$ was 0.0717 before and 0.0642 after correction. The ratio of minimum to maximum transmission is 0.8806. The final completeness is 100.00% out to 27.484° in Θ . The absorption coefficient (μ) of this material is 0.555 mm^{-1} and the minimum and maximum transmissions are 0.6569 and 0.7460.

The structure was solved with the ShelXS (Sheldrick, 2015) structure solution program using Direct Methods. The crystal structure was refined by Least Squares using ShelXL (Sheldrick, 2008).

The value of Z' is 2. This means that there are two independent molecules in the asymmetric unit.

2.8.6 $[(^sOCO)Co(THF)_2](Ph_4B) (I^+)$

A green plate-shaped crystal with dimensions 0.34×0.27×0.13 mm was mounted on a loop with paratone oil. X-ray diffraction data were collected at $T = 173(2) ^\circ K$. The maximum resolution achieved was $\Theta = 27.483^\circ$.

Unit cell indexing was performed and refined based on 6346 reflections, 7% of the observed reflections. $wR_2(int)$ was 0.0866 before and 0.0769 after correction. The ratio of minimum to maximum transmission is 0.8089. The final completeness is 100.00% out to 27.483° in Θ . The absorption coefficient (μ) of this material is 0.349 mm^{-1} and the minimum and maximum transmissions are 0.6032 and 0.7457.

The structure was solved with the ShelXS (Sheldrick, 2015) structure solution program using Direct Methods. The space group $P2_1/n$ (# 14) was determined from the systematic absences.

2.8.7 $[(^sOCO)Co(THF)_3](PF_6)_2 (I^{2+})$

A black prism-shaped crystal with dimensions 0.53×0.15×0.08 mm was mounted on a loop with paratone oil. X-ray diffraction data were collected at $T = 100(2) ^\circ K$. The maximum resolution achieved was $\Theta = 26.372^\circ$.

Unit cell indexing was performed and refined based on 9972 reflections, 17% of the observed reflections. $wR_2(int)$ was 0.0664 before and 0.0551 after correction. The ratio of minimum to maximum transmission is 0.7487. The final completeness is 99.8% out to 26.372° in Θ . The absorption coefficient (μ) of this material is 0.504 and the minimum and maximum transmissions are 0.3223 and 0.4305.

The structure was solved with **Superflip** (L. Palatinus & G. Chapuis, 2007) using the Charge Flipping algorithm. The space group *Pbca* (# 61) was confirmed by **Superflip** (L. Palatinus & G. Chapuis, 2007).

2.8.8 *Complex 4*

A green block-shaped crystal with dimensions 0.2×0.1×0.1 mm was mounted on a loop with paratone oil. X-ray diffraction data were collected using a CuK α radiation source on a Bruker D8 diffractometer with APEX2 detector diffractometer equipped with an Oxford Cryosystems low-temperature apparatus operating at T = 100(2) K.

The total number of runs and images was based on the strategy calculation from the program CrysAlisPro (Agilent). The maximum resolution achieved was $\theta = 70.358^\circ$.

Unit cell indexing was performed by using the CrysAlisPro (Agilent) software and refined using CrysAlisPro (Agilent) on 22656 reflections, 58% of the observed reflections. Data reduction, scaling and absorption corrections were performed using CrysAlisPro (Agilent) and CrysAlisPro 1.171.38.41 (Rigaku Oxford Diffraction, 2015). Empirical absorption correction using spherical harmonics, implemented in SCALE3 ABSPACK scaling algorithm. The final completeness is 86.7% out to 70.358° in θ . The absorption coefficient μ of this material is 4.845 mm $^{-1}$ at this wavelength ($\lambda = 1.54178$) and the minimum and maximum transmissions are 0.587 and 0.616.

The structure was solved in the space group *P1* (#2) with the ShelXT-2014/4 (Sheldrick, 2015) structure solution program using combined Patterson and dual-space

recycling methods. The space group P1 (# 2) was determined by the ShelXT-2014/4 (Sheldrick, 2015) structure solution program.

The value of Z' is 2. This means that there are two independent molecules in the asymmetric unit.

2.8.9 *Complex 5*

A dark brown prism-shaped crystal with dimensions 0.39×0.27×0.26 mm was mounted on a loop with paratone oil. X-ray diffraction data were collected using a Bruker D8 diffractometer with APEX2 detector diffractometer equipped with an Oxford Cryosystems low-temperature apparatus operating at $T = 100(2)$ K.

Data were measured using ω scans scans of 1.0° per frame for 60.0 s. The total number of runs and images was based on the strategy calculation from the program CrysAlisPro (Agilent). The maximum resolution achieved was $\Theta = 25.349^\circ$.

Unit cell indexing was performed by using the CrysAlisPro (Agilent) software and refined using CrysAlisPro (Agilent) on 9824 reflections, 51% of the observed reflections. Data reduction, scaling and absorption corrections were performed using CrysAlisPro (Agilent) and CrysAlisPro 1.171.38.41 (Rigaku Oxford Diffraction, 2015). Empirical absorption correction using spherical harmonics, implemented in SCALE3 ABSPACK scaling algorithm. The final completeness is 96.5% out to 25.349 in Θ . The absorption coefficient μ of this material is 0.793 mm^{-1} at this wavelength ($\lambda = 0.71073 \text{ \AA}$) and the minimum and maximum transmissions are 0.37031 and 1.00000.

The structure was solved in the space group P1 with the ShelXT-2014/4 (Sheldrick, 2015) structure solution program using combined Patterson and dual-space recycling methods. The space group P1 (# 2) was determined by the ShelXT-2014/4 (Sheldrick, 2015) structure solution program.

2.9 Computational Studies

DFT geometry optimizations were performed using TURBOMOLE¹⁰⁰ coupled to the PQS Baker optimizer¹⁰¹⁻¹⁰² via the BOpt package¹⁰³ at the BP86,¹⁰⁴⁻¹⁰⁵ def2-TZVP,¹⁰⁶⁻¹⁰⁷ level of theory (m4 grid), on full models (including tBu groups) in the gas phase, using Grimme's version 3 (disp3, 'zero damping') dispersion corrections.¹⁰⁸ All minima (no imaginary frequencies) were characterized by numerically calculating the Hessian matrix.

EPR parameters were calculated with the ADF¹⁰⁹⁻¹¹¹ program system at the B3LYP/TZ2P level, using the coordinates from the structures optimized in Turbomole as input. ZORA basis sets as supplied with the ADF program were used. Unrestricted SPINORBIT ZORA COLLINEAR calculations were used to obtain the SOC corrected HFI-tensors and Zeeman corrected g-tensors.

Spin density pictures were generated using IQMol (<http://www.iqmol.org/>).

2.10 References

1. Friend, C. M.; Sanford, M. S.; Abruna, H. D., Catalytic Chemistry Workshop on Defining Critical Directions for the Future. National Science Foundation: 2011.
2. Chirik, P. J.; Jarvo, E. R., Report on NSF SusChem Workshop and American Chemical Society Symposium. National Science Foundation: 2014.
3. Chirik, P. J.; Wieghardt, K., Radical Ligands Confer Nobility on Base-Metal Catalysts. *Science* **2010**, 327, 794-795.
4. Negishi, E.-I., Fundamental Properties of Palladium and Patterns of the Reactions of Palladium and Its Complexes. In *Handbook of Organopalladium Chemistry for Organic Synthesis*, Negishi, E.-i.; de Meijere, A., Eds. Wiley-Interscience: New York, 2002; pp 17-35.
5. Tasker, S. Z.; Standley, E. A.; Jamison, T. F., Recent Advances in Homogeneous nickel catalysis. *Nature* **2014**, 509 (7500), 299-309.
6. Meijere, A. d.; Diederich, F., *Metal-catalyzed Cross-coupling Reactions*. 2nd ed.; Wiley-VCH: Weinheim, 2004.
7. Greenwood, N. N.; Earnshaw, A., *Chemistry of the Elements*. 2nd ed.; Butterworth Heinemann: 1997.
8. Luca, O. R.; Crabtree, R. H., Redox-active Ligands in Catalysis. *Chem. Soc. Rev.* **2013**, 42 (4), 1440-1459.
9. Lyaskovskyy, V.; de Bruin, B., Redox Non-Innocent Ligands: Versatile New Tools to Control Catalytic Reactions. *ACS Catal.* **2012**, 2 (2), 270-279.
10. Praneeth, V. K. K.; Ringenberg, M. R.; Ward, T. R., Redox-Active Ligands in Catalysis. *Angew. Chem., Int. Ed.* **2012**, 51 (41), 10228-10234.
11. Jacquet, J.; Desage-El Murr, M.; Fensterbank, L., Metal-Promoted Coupling Reactions Implying Ligand-Based Redox Changes. *Chemcatchem* **2016**, 8 (21), 3310-3316.
12. Broere, D. L. J.; Plessius, R.; van der Vlugt, J. I., New avenues for Ligand-mediated Processes - Expanding Metal Reactivity by the use of Redox-active Catechol, *o*-aminophenol and *o*-phenylenediamine Ligands. *Chemical Society Reviews* **2015**, 44 (19), 6886-6915.
13. Haneline Mason, R.; Heyduk Alan, F., C-C Bond-forming Reductive Elimination from a Zirconium(IV) Redox-active Ligand Complex. *J. Am. Chem. Soc.* **2006**, 128 (26), 8410-1.

14. Munha, R. F.; Zarkesh, R. A.; Heyduk, A. F., Group Transfer Reactions of d^0 Transition Metal Complexes: Redox-active Ligands Provide a Mechanism for Expanded Reactivity. *Dalton Trans.* **2013**, 42 (11), 3751-3766.
15. Zarkesh, R., A.; Ziller, J., W.; Heyduk, A., F., Four-electron Oxidative Formation of Aryl Diazenes Using a Tantalum Redox-active Ligand Complex. *Angew. Chem., Int. Ed.* **2008**, 47 (25), 4715-8.
16. Myers, T. W.; Berben, L. A., Redox Active Aluminium(III) Complexes Convert CO_2 into MgCO_3 or CaCO_3 in a Synthetic Cycle Using Mg or Ca Metal. *Chem. Commun.* **2013**, 49 (39), 4175-4177.
17. Bouwkamp, M. W.; Bowman, A. C.; Lobkovsky, E.; Chirik, P. J., Iron-Catalyzed $[2\pi + 2\pi]$ Cycloaddition of α, ω -Dienes: The Importance of Redox-Active Supporting Ligands. *J. Am. Chem. Soc.* **2006**, 128 (41), 13340-13341.
18. Sylvester, K. T.; Chirik, P. J., Iron-Catalyzed, Hydrogen-Mediated Reductive Cyclization of 1,6-Enynes and Diynes: Evidence for Bis(imino)pyridine Ligand Participation. *J. Am. Chem. Soc.* **2009**, 131 (25), 8772-8774.
19. Russell, S. K.; Lobkovsky, E.; Chirik, P. J., Iron-Catalyzed Intermolecular $[2\pi + 2\pi]$ Cycloaddition. *J. Am. Chem. Soc.* **2011**, 133 (23), 8858-8861.
20. Darmon, J. M.; Stieber, S. C. E.; Sylvester, K. T.; Fernandez, I.; Lobkovsky, E.; Semproni, S. P.; Bill, E.; Wieghardt, K.; DeBeer, S.; Chirik, P. J., Oxidative Addition of Carbon-carbon Bonds with a Redox-active Bis(imino)pyridine Iron Complex. *J. Am. Chem. Soc.* **2012**, 134 (41), 17125-17137.
21. Jacquet, J.; Blanchard, S.; Derat, E.; Desage-El Murr, M.; Fensterbank, L., Redox-ligand Sustains Controlled Generation of CF_3 Radicals by Well-defined Copper Complex. *Chem. Sci.* **2016**, 7 (3), 2030-2036.
22. Wong, J. L.; Sanchez, R. H.; Logan, J. G.; Zarkesh, R. A.; Ziller, J. W.; Heyduk, A. F., Disulfide Reductive Elimination from an Iron(III) Complex. *Chem. Sci.* **2013**, 4 (4), 1906-1910.
23. Tondreau, A. M.; Atienza, C. C. H.; Darmon, J. M.; Milsman, C.; Hoyt, H. M.; Weller, K. J.; Nye, S. A.; Lewis, K. M.; Boyer, J.; Delis, J. G. P.; Lobkovsky, E.; Chirik, P. J., Synthesis, Electronic Structure, and Alkene Hydrosilylation Activity of Terpyridine and Bis(imino)pyridine Iron Dialkyl Complexes. *Organometallics* **2012**, 31 (13), 4886-4893.
24. Yu, R. P.; Darmon, J. M.; Hoyt, J. M.; Margulieux, G. W.; Turner, Z. R.; Chirik, P. J., High-activity iron catalysts for the hydrogenation of hindered, unfunctionalized alkenes. *ACS Catal.* **2012**, 2 (8), 1760-1764.
25. Hojilla, A. C. C.; Tondreau, A. M.; Weller, K. J.; Lewis, K. M.; Cruse, R. W.; Nye, S. A.; Boyer, J. L.; Delis, J. G. P.; Chirik, P. J., High-selectivity bis(imino)pyridine

iron catalysts for the hydrosilylation of 1,2,4-trivinylcyclohexane. *ACS Catal.* **2012**, *2* (10), 2169-2172.

26. Tondreau, A. M.; Atienza, C. C. H.; Weller, K. J.; Nye, S. A.; Lewis, K. M.; Delis, J. G. P.; Chirik, P. J., Iron Catalysts for Selective Anti-Markovnikov Alkene Hydrosilylation Using Tertiary Silanes. *Science* **2012**, *335*, 567-570.

27. Villanueva, O.; Weldy, N. M.; Blakey, S. B.; MacBeth, C. E., Cobalt catalyzed sp³ C-H amination utilizing aryl azides. *Chem. Sci.* **2015**, *6* (11), 6672-6675.

28. Bagh, B.; Broere, D. L. J.; Sinha, V.; Kuijpers, P. F.; van Leest, N. P.; de Bruin, B.; Demeshko, S.; Siegler, M. A.; Vlucht, J. I. D., Catalytic Synthesis of N-Heterocycles via Direct C(sp³)-H Amination Using an Air-Stable Iron(III) Species with a Redox-Active Ligand. *J. Am. Chem. Soc.* **2017**, *139* (14), 5117-5124.

29. Kuijpers, P. F.; Tiekink, M. J.; Breukelaar, W. B.; Broere, D. L. J.; van Leest, N. P.; van der Vlucht, J. I.; Reek, J. N. H.; de Bruin, B., Cobalt-Porphyrin-Catalysed Intramolecular Ring-Closing C-H Amination of Aliphatic Azides: A Nitrene-Radical Approach to Saturated Heterocycles. *Chemistry-a European Journal* **2017**, *23* (33), 7945-7952.

30. Lyaskovskyy, V.; Suarez, A. I. O.; Lu, H. J.; Jiang, H. L.; Zhang, X. P.; de Bruin, B., Mechanism of Cobalt(II) Porphyrin-Catalyzed C-H Amination with Organic Azides: Radical Nature and H-Atom Abstraction Ability of the Key Cobalt(III)-Nitrene Intermediates. *J. Am. Chem. Soc.* **2011**, *133* (31), 12264-12273.

31. Suarez, A. I. O.; Jiang, H. L.; Zhang, X. P.; de Bruin, B., The radical mechanism of cobalt(II) porphyrin-catalyzed olefin aziridination and the importance of cooperative H-bonding. *Dalton Trans.* **2011**, *40* (21), 5697-5705.

32. Das, B. G.; Chirila, A.; Tromp, M.; Reek, J. N. H.; de Bruin, B., Co-III-Carbene Radical Approach to Substituted 1H-Indenes. *J. Am. Chem. Soc.* **2016**, *138* (28), 8968-8975.

33. Paul, N. D.; Mandal, S.; Otte, M.; Cui, X.; Zhang, X. P.; de Bruin, B., Metalloradical Approach to 2H-Chromenes. *J. Am. Chem. Soc.* **2014**, *136* (3), 1090-1096.

34. Paul, N. D.; Chirila, A.; Lu, H. J.; Zhang, X. P.; de Bruin, B., Carbene Radicals in Cobalt(II)-Porphyrin-Catalysed Carbene Carbonylation Reactions; A Catalytic Approach to Ketenes. *Chemistry-a European Journal* **2013**, *19* (39), 12953-12958.

35. Dzik, W. I.; Zhang, X. P.; de Bruin, B., Redox Noninnocence of Carbene Ligands: Carbene Radicals in (Catalytic) C-C Bond Formation. *Inorg. Chem.* **2011**, *50* (20), 9896-9903.

36. Dzik, W. I.; Xu, X.; Zhang, X. P.; Reek, J. N. H.; de Bruin, B., 'Carbene Radicals' in Co-II(por)-Catalyzed Olefin Cyclopropanation. *J. Am. Chem. Soc.* **2010**, *132* (31), 10891-10902.

37. Corcos, A. R.; Villanueva, O.; Walroth, R. C.; Sharma, S. K.; Bacsa, J.; Lancaster, K. M.; MacBeth, C. E.; Berry, J. F., Oxygen Activation by Co(II) and a Redox Non-Innocent Ligand: Spectroscopic Characterization of a Radical-Co(II)-Superoxide Complex with Divergent Catalytic Reactivity. *J. Am. Chem. Soc.* **2016**, *138* (6), 1796-1799.
38. Hoffman, J. M.; Oliver, A. G.; Brown, S. N., The Metal or the Ligand? The Preferred Locus for Redox Changes in Oxygen Atom Transfer Reactions of Rhenium Amidodiphenoxides. *J. Am. Chem. Soc.* **2017**, *139* (12), 4521-4531.
39. Randolph, A. H.; Seewald, N. J.; Rickert, K.; Brown, S. N., Tris(3,5-di-tert-butylcatecholato)molybdenum(VI): Lewis Acidity and Nonclassical Oxygen Atom Transfer Reactions. *Inorg. Chem.* **2013**, *52* (21), 12587-12598.
40. Lippert, C. A.; Arnstein, S. A.; Sherrill, C. D.; Soper, J. D., Redox-Active Ligands Facilitate Bimetallic O₂ Homolysis at Five-Coordinate Oxorhenium(V) Centers. *J. Am. Chem. Soc.* **2010**, *132* (11), 3879-3892.
41. Lippert, C. A.; Soper, J. D., Deoxygenation of Nitroxyl Radicals by Oxorhenium(V) Complexes with Redox-Active Ligands. *Inorg. Chem.* **2010**, *49* (8), 3682-3684.
42. Lippert, C. A.; Hardcastle, K. I.; Soper, J. D., Harnessing Redox-Active Ligands for Low-Barrier Radical Addition at Oxorhenium Complexes. *Inorg. Chem.* **2011**, *50* (20), 9864-9878.
43. Beletskaya, I. P.; Cheprakov, A. V., Copper in cross-coupling reactions: The post-Ullmann chemistry. *Coord. Chem. Rev.* **2004**, *248* (21-24), 2337-2364.
44. Phapale, V. B.; Cardenas, D. J., Nickel-catalysed Negishi cross-coupling reactions: scope and mechanisms. *Chem. Soc. Rev.* **2009**, *38* (6), 1598-1607.
45. Sherry, B. D.; Fürstner, A., The Promise and Challenge of Iron-Catalyzed Cross Coupling. *Acc. Chem. Res.* **2008**, *41* (11), 1500-1511.
46. Wendlandt, A. E.; Suess, A. M.; Stahl, S. S., Copper-Catalyzed Aerobic Oxidative C-H Functionalizations: Trends and Mechanistic Insights. *Angew. Chem., Int. Ed.* **2011**, *50* (47), 11062-11087.
47. Hu, X. L., Nickel-catalyzed cross coupling of non-activated alkyl halides: a mechanistic perspective. *Chem. Sci.* **2011**, *2* (10), 1867-1886.
48. Hirano, K.; Miura, M., Copper-mediated oxidative direct C-C (hetero)aromatic cross-coupling. *Chem. Commun.* **2012**, *48* (87), 10704-10714.
49. Truong, T.; Klimovica, K.; Daugulis, O., Copper-Catalyzed, Directing Group-Assisted Fluorination of Arene and Heteroarene C-H Bonds. *J. Am. Chem. Soc.* **2013**, *135* (25), 9342-9345.

50. Yoshikai, N.; Matsumoto, A.; Norinder, J.; Nakamura, E., Iron-Catalyzed Direct Arylation of Aryl Pyridines and Imines Using Oxygen as an Oxidant. *Synlett* **2010**, (2), 313-316.
51. Sarhan, A. A. O.; Bolm, C., Iron(III) chloride in oxidative C-C coupling reactions. *Chem. Soc. Rev.* **2009**, 38 (9), 2730-2744.
52. Mako, T. L.; Byers, J. A., Recent advances in iron-catalysed cross coupling reactions and their mechanistic underpinning. *Inorg. Chem. Front.* **2016**, 3 (6), 766-790.
53. Bedford, R. B.; Brenner, P. B., The Development of Iron Catalysts for Cross-Coupling Reactions. *Top Organometal Chem* **2015**, 50, 19-46.
54. Itazaki, M.; Nakazawa, H., Iron-Catalyzed Cross-Dehydrogenative-Coupling Reactions. *Top Organometal Chem* **2015**, 50, 47-81.
55. Liu, C.; Zhang, H.; Shi, W.; Lei, A. W., Bond Formations between Two Nucleophiles: Transition Metal Catalyzed Oxidative Cross-Coupling Reactions. *Chem. Rev.* **2011**, 111 (3), 1780-1824.
56. Seyferth, D., The Grignard Reagents. *Organometallics* **2009**, 28 (6), 1598-1605.
57. Tan, G.; He, S.; Huang, X.; Liao, X.; Cheng, Y.; You, J., Cobalt-Catalyzed Oxidative C-H/C-H Cross-Coupling between Two Heteroarenes. *Angew. Chem., Int. Ed.* **2016**, 55 (35), 10414-10418.
58. de Bruin, B.; Bill, E.; Bothe, E.; Weyhermuller, T.; Wieghardt, K., Molecular and electronic structures of bis(pyridine-2,6-diimine)metal complexes [ML₂](PF₆)(n) (n=0, 1, 2, 3; M = Mn, Fe, Co, Ni, Cu, Zn). *Inorg. Chem.* **2000**, 39 (13), 2936-2947.
59. Budzelaar, P. H. M.; de Bruin, B.; Gal, A. W.; Wieghardt, K.; van Lenthe, J. H., Metal-to-ligand electron transfer in diiminopyridine complexes of Mn-Zn. A theoretical study. *Inorg. Chem.* **2001**, 40 (18), 4649-4655.
60. Chirik, P. J., Electronic Structures of Reduced Manganese, Iron, and Cobalt Complexes Bearing Redox-Active Bis(imino) pyridine Pincer Ligands. *Pincer and Pincer-Type Complexes: Applications in Organic Synthesis and Catalysis* **2014**, 189-212.
61. Smith, A. L.; Hardcastle, K. I.; Soper, J. D., Redox-Active Ligand-Mediated Oxidative Addition and Reductive Elimination at Square Planar Cobalt(III): Multielectron Reactions for Cross-Coupling. *J. Am. Chem. Soc.* **2010**, 132 (41), 14358-14360.
62. Dzik, W. I.; van der Vlugt, J. I.; Reek, J. N. H.; de Bruin, B., Ligands that Store and Release Electrons during Catalysis. *Angew. Chem., Int. Ed.* **2011**, 50 (15), 3356-3358.

63. Borré, E.; Dahm, G.; Aliprandi, A.; Mauro, M.; Dagorne, S.; Bellemin-Laponnaz, S., Tridentate Complexes of Group 10 Bearing Bis-Aryloxide N-Heterocyclic Carbene Ligands: Synthesis, Structural, Spectroscopic, and Computational Characterization. *Organometallics* **2014**, *33* (17), 4374-4384.
64. Lee, M.-T.; Hu, C.-H., Density Functional Study of N-Heterocyclic and Diamino Carbene Complexes: Comparison with Phosphines. *Organometallics* **2004**, *23* (5), 976-983.
65. Lummiss, J. A. M.; Higman, C. S.; Fyson, D. L.; McDonald, R.; Fogg, D. E., The Divergent Effects of Strong NHC Donation in Catalysis. *Chemical Science* **2015**, *6* (12), 6739-6746.
66. Clavier, H.; Coutable, L.; Toupet, L.; Guillemin, J.-C.; Mauduit, M., Design and Synthesis of New Bidentate Alkoxy-NHC Ligands for Enantioselective Copper-catalyzed Conjugate Addition. *Journal of Organometallic Chemistry* **2005**, *690* (23), 5237-5254.
67. Waltman, A. W.; Grubbs, R. H., A New Class of Chelating N-Heterocyclic Carbene Ligands and Their Complexes with Palladium. *Organometallics* **2004**, *23* (13), 3105-3107.
68. Bellemin-Laponnaz, S.; Welter, R.; Brelot, L.; Dagorne, S., Synthesis and Structure of V(V) and Mn(III) NHC Complexes Supported by a Tridentate Bis-aryloxide-N-heterocyclic Carbene Ligand. *Journal of Organometallic Chemistry* **2009**, *694* (5), 604-606.
69. Dagorne, S.; Bellemin-Laponnaz, S.; Romain, C., Neutral and Cationic N-Heterocyclic Carbene Zirconium and Hafnium Benzyl Complexes: Highly Regioselective Oligomerization of 1-Hexene with a Preference for Trimer Formation. *Organometallics* **2013**, *32* (9), 2736-2743.
70. Romain, C.; Choua, S.; Collin, J.-P.; Heinrich, M.; Bailly, C.; Karmazin-Brelot, L.; Bellemin-Laponnaz, S.; Dagorne, S., Redox and Luminescent Properties of Robust and Air-Stable N-Heterocyclic Carbene Group 4 Metal Complexes. *Inorganic Chemistry* **2014**, *53* (14), 7371-7376.
71. Romain, C.; Fliedel, C.; Bellemin-Laponnaz, S.; Dagorne, S., NHC Bis-Phenolate Aluminum Chelates: Synthesis, Structure, and Use in Lactide and Trimethylene Carbonate Polymerization. *Organometallics* **2014**, *33* (20), 5730-5739.
72. Weinberg, D. R.; Hazari, N.; Labinger, J. A.; Bercaw, J. E., Iridium(I) and Iridium(III) Complexes Supported by a Diphenolate Imidazolyl-Carbene Ligand. *Organometallics* **2010**, *29* (1), 89-100.
73. Min, K. S.; Weyhermüller, T.; Bothe, E.; Wieghardt, K., Tetradentate Bis(*o*-iminobenzosemiquinonate(¹⁻)) π Radical Ligands and Their *o*-Aminophenolate(¹⁻) Derivatives in Complexes of Nickel(II), Palladium(II), and Copper(II). *Inorganic Chemistry* **2004**, *43* (9), 2922-2931.

74. Despagne-Ayoub, E.; Henling, L. M.; Labinger, J. A.; Bercaw, J. E., Addition of a phosphine ligand switches an N-heterocyclic carbene-zirconium catalyst from oligomerization to polymerization of 1-hexene. *Dalton Transactions* **2013**, 42 (44), 15544-15547.
75. Chaudhuri, P.; Wieghardt, K., Phenoxyl Radical Complexes. In *Progress in Inorganic Chemistry*, John Wiley & Sons, Inc.: 2002; pp 151-216.
76. Meng, Y.-S.; Mo, Z.; Wang, B.-W.; Zhang, Y.-Q.; Deng, L.; Gao, S., Observation of the Single-ion Magnet Behavior of d^8 ions on Two-coordinate Co(I)-NHC Complexes. *Chemical Science* **2015**, 6 (12), 7156-7162.
77. Massard, A.; Braunstein, P.; Danopoulos, A. A.; Choua, S.; Rabu, P., Studies on Three-Coordinate $[\text{Co}\{\text{N}(\text{SiMe}_3)_2\}_2\text{L}]$ Complexes, L = N-Heterocyclic Carbene. *Organometallics* **2015**, 34 (11), 2429-2438.
78. Harrison, D. J.; Daniels, A. L.; Korobkov, I.; Baker, R. T., Tetracarbonyl(trifluoromethyl)cobalt(I) $[\text{Co}(\text{CO})_4(\text{CF}_3)]$ as a Precursor to New Cobalt Trifluoromethyl and Difluorocarbene Complexes. *Organometallics* **2015**, 34 (18), 4598-4604.
79. Danopoulos, A. A.; Braunstein, P., Mono-N-heterocyclic carbene amido and alkyl complexes. Cobalt-mediated C-H activation and C-C coupling reactions involving benzyl ligands on a putative 3-coordinate intermediate. *Dalton Transactions* **2013**, 42 (20), 7276-7280.
80. Gibson, S. E.; Johnstone, C.; Loch, J. A.; Steed, J. W.; Stevenazzi, A., Novel Structures and Pauson-Khand Activities of N-Heterocyclic Carbene Dicobalt Complexes. *Organometallics* **2003**, 22 (25), 5374-5377.
81. Coleman, A. W.; Hitchcock, P. B.; Lappert, M. F.; Maskell, R. K.; Müller, J. H., Routes to Optically Active Electron-rich Olefins (L^*2 and Some Derived Carbene Metal Complexes; X-ray Structures of $[\text{Co}(\text{CO})(\text{L}^*)(\text{NO}(\text{PPh}_3))]$ and $\text{cis-}[\text{Rh}(\text{Cl})(\text{COD})(\text{L}^*)][\text{L}^* = (\text{S})\text{-CN}(\text{Me})\text{CH}(\text{Me})\text{CH}_2\text{NMe}]$. *Journal of Organometallic Chemistry* **1983**, 250 (1), 9-14.
82. Liske, A.; Verlinden, K.; Buhl, H.; Schaper, K.; Ganter, C., Determining the pi-Acceptor Properties of N-Heterocyclic Carbenes by Measuring the Se-77 NMR Chemical Shifts of Their Selenium Adducts. *Organometallics* **2013**, 32 (19), 5269-5272.
83. Miessler, G. L.; Tarr, D., A., *Inorganic Chemistry*. Second ed.; Prentice Hall: New Jersey, 1998.
84. Addison, A. W.; Rao, T. N.; Reedijk, J.; van Rijn, J.; Verschoor, G. C., Synthesis, structure, and spectroscopic properties of copper(II) compounds containing nitrogen-sulphur donor ligands; the crystal and molecular structure of aqua[1,7-bis(N-methylbenzimidazol-2[prime or minute]-yl)-2,6-dithiaheptane]copper(II) perchlorate. *Journal of the Chemical Society, Dalton Transactions* **1984**, (7), 1349-1356.

85. Radonovich, L. J.; Klabunde, K. J.; Behrens, C. B.; McCollor, D. P.; Anderson, B. B., Crystal and molecular structures of π -toluene complexes of bis(pentafluorobenzene)cobalt and bis(pentafluorobenzene)nickel. *Inorganic Chemistry* **1980**, *19* (5), 1221-1226.
86. Chaudhuri, P.; Verani, C. N.; Bill, E.; Bothe, E.; Weyhermüller, T.; Wieghardt, K., Electronic Structure of Bis(o-iminobenzosemiquinonato)metal Complexes (Cu, Ni, Pd). The Art of Establishing Physical Oxidation States in Transition-Metal Complexes Containing Radical Ligands. *J. Am. Chem. Soc.* **2001**, *123* (10), 2213-2223.
87. Chirik, P. J., Preface: Forum on Redox-Active Ligands. *Inorg. Chem.* **2011**, *50* (20), 9737-9740.
88. Morris, W. D.; Wolczanski, P. T.; Sutter, J.; Meyer, K.; Cundari, T. R.; Lobkovsky, E. B., Iron and Chromium Complexes Containing Tridentate Chelates Based on Nacnac and Imino- and Methyl-Pyridine Components: Triggering C-X Bond Formation. *Inorg. Chem.* **2014**, *53* (14), 7467-7484.
89. Williams, V. A.; Wolczanski, P. T.; Sutter, J.; Meyer, K.; Lobkovsky, E. B.; Cundari, T. R., Iron Complexes Derived from {nacnac-(CH(2)py)(2)}(-) and {nacnac-(CH(2)py)(CHpy)}(n) Ligands: Stabilization of Iron(II) via Redox Noninnocence. *Inorg. Chem.* **2014**, *53* (9), 4459-4474.
90. Boehme, C.; Frenking, G., Electronic structure of stable carbenes, silylenes, and germylenes. *J. Am. Chem. Soc.* **1996**, *118* (8), 2039-2046.
91. Herrmann, W. A., N-heterocyclic carbenes: A new concept in organometallic catalysis. *Angew. Chem., Int. Ed.* **2002**, *41* (8), 1290-1309.
92. Jeletic, M. S.; Jan, M. T.; Ghiviriga, I.; Abboud, K. A.; Veige, A. S., New Iridium and Rhodium Chiral di-N-heterocyclic Carbene (NHC) Complexes and Their Application in Enantioselective Catalysis. *Dalton Transactions* **2009**, (15), 2764-2776.
93. Berry, J. F., Terminal Nitrido and Imido Complexes of the Late Transition Metals. *Comments on Inorganic Chemistry* **2009**, *30* (1-2), 28-66.
94. King, E. R.; Hennessy, E. T.; Betley, T. A., Catalytic C-H Bond Amination from High-Spin Iron Imido Complexes. *Journal of the American Chemical Society* **2011**, *133* (13), 4917-4923.
95. Thu, H.-Y.; Yu, W.-Y.; Che, C.-M., Intermolecular Amidation of Unactivated sp² and sp³ C-H Bonds via Palladium-Catalyzed Cascade C-H Activation/Nitrene Insertion. *Journal of the American Chemical Society* **2006**, *128* (28), 9048-9049.
96. Fulmer, G. R.; Miller, A. J. M.; Sherden, N. H.; Gottlieb, H. E.; Nudelman, A.; Stoltz, B. M.; Bercaw, J. E.; Goldberg, K. I., NMR Chemical Shifts of Trace Impurities: Common Laboratory Solvents, Organics, and Gases in Deuterated Solvents Relevant to the Organometallic Chemist. *Organometallics* **2010**, *29* (9), 2176-2179.

97. Evans, D. F., The Determination of the Paramagnetic Susceptibility of Substances in Solution by Nuclear Magnetic Resonance. *J. Chem. Soc.* **1959**, (Jun), 2003-2005.
98. Piguet, C., Paramagnetic susceptibility by NMR: The "solvent correction" removed for large paramagnetic molecules. *J. Chem. Educ.* **1997**, 74 (7), 815-816.
99. Rhile, I. J.; Markle, T. F.; Nagao, H.; DiPasquale, A. G.; Lam, O. P.; Lockwood, M. A.; Rotter, K.; Mayer, J. M., Concerted Proton–Electron Transfer in the Oxidation of Hydrogen-Bonded Phenols. *Journal of the American Chemical Society* **2006**, 128 (18), 6075-6088.
100. *TURBOMOLE Version 7.1*, TURBOMOLE GmbH: Karlsruhe, Germany, 2013.
101. *PQS Version 2.4*, Parallel Quantum Solutions: Fayetteville, Arkansas, USA, 2001.
102. Baker, J., An Algorithm for the Location of Transition-States. *J. Comput. Chem.* **1986**, 7 (4), 385-395.
103. Budzelaar, P. H. M., Geometry optimization using generalized, chemically meaningful constraints. *J. Comput. Chem.* **2007**, 28 (13), 2226-2236.
104. Becke, A. D., Density-Functional Exchange-Energy Approximation with Correct Asymptotic-Behavior. *Phys. Rev. A* **1988**, 38 (6), 3098-3100.
105. Perdew, J. P., Density-Functional Approximation for the Correlation-Energy of the Inhomogeneous Electron-Gas. *Phys Rev B* **1986**, 33 (12), 8822-8824.
106. Weigend, F.; Ahlrichs, R., Balanced basis sets of split valence, triple zeta valence and quadruple zeta valence quality for H to Rn: Design and assessment of accuracy. *Phys. Chem. Chem. Phys.* **2005**, 7 (18), 3297-3305.
107. Weigend, F.; Haser, M.; Patzelt, H.; Ahlrichs, R., RI-MP2: optimized auxiliary basis sets and demonstration of efficiency. *Chem. Phys. Lett.* **1998**, 294 (1-3), 143-152.
108. Grimme, S.; Antony, J.; Ehrlich, S.; Krieg, H., A consistent and accurate ab initio parametrization of density functional dispersion correction (DFT-D) for the 94 elements H-Pu. *J. Chem. Phys.* **2010**, 132 (15).
109. Baerends, E. J.; Ellis, D. E.; Ros, P., Self-consistent molecular Hartree-Fock-Slater calculations - I. The computational procedure. *Chem. Phys.* **1973**, 2 (1), 41-51.
110. Velde, G. T.; Baerends, E. J., Numerical-Integration for Polyatomic Systems. *J. Comput. Phys.* **1992**, 99 (1), 84-98.
111. Guerra, C. F.; Snijders, J. G.; te Velde, G.; Baerends, E. J., Towards an order-N DFT method. *Theor. Chem. Acc.* **1998**, 99 (6), 391-403.

CHAPTER 3. PHOTOINDUCED RADICAL TRIFLUOROMETHYLATION OF (HETERO)ARYL C–H BONDS

3.1 Introduction

Fluorine is the most abundant halogen in the Earth's crust and represents the 13th most abundant element overall; however, only a few naturally-occurring fluorinated organic compounds are known.¹ The trifluoromethyl functionality is completely absent in nature and is considered a privileged moiety in agricultural and medicinal chemistry.² Introduction of the CF₃ group into organic molecules substantially influences lipophilicity, bioavailability, and capacity of the substrate to penetrate the blood-brain barrier.³⁻⁹ As a result, in recent years a number of methodologies for the introduction of this functional group have been developed.¹⁰⁻¹⁴ Routes based on nucleophilic,¹⁵⁻¹⁷ electrophilic,¹⁸⁻¹⁹ and radical²⁰ CF₃ sources are all well-established and offer versatile approaches. However, the vast majority of these routes often rely on pre-functionalized or electronically activated starting materials.²¹⁻²⁷ Although the direct trifluoromethylation of unactivated C–H bonds represents, from a synthetic standpoint, the most attractive target in this field, this is a difficult challenge and most often requires the use of rare and costly transition metals.²⁸⁻²⁹

The use of Earth-abundant transition metals in this arena is comparatively rare, though a few examples of copper facilitated trifluoromethylation reactions are known.³⁰⁻³⁴ Efforts to utilize other base metals for direct C–H functionalization have been elusive for several reasons. Metal promoted trifluoromethylations often invoke the formation of

a M–CF₃ containing intermediate. However, the electropositivity of early first-row trifluoromethyl complexes readily promotes activation of the C–F bond via metal-centered α -fluoride abstraction, producing a difluoromethyl carbene species.³⁵⁻³⁷ On the contrary, later 3d metals form an inherently strong covalent M–CF₃ bond, often resulting in thermodynamically favored complexes which hamper any associated reactivity.³⁸⁻⁴⁰

We therefore proposed a methodology to expand the library of Earth-abundant transition metals capable of C–H bond trifluoromethylation by incorporating a bioinspired design principle. The family of vitamin B12 derivatives, alkyl cobalamins, represents a quintessential example of Co^{III}–alkyl bonds that are capable of homolytic cleavage under relatively low-energy conditions.⁴¹⁻⁴⁴ We hypothesized that a complex which contains a Co^{III}–CF₃ bond, might circumvent the pitfalls involved with M–CF₃ bonds listed above.

Although alkyl cobalamin derivatives have been heavily studied over the past four decades, a definitive mechanism for the Co–C bond homolysis has yet to be established.⁴¹⁻⁴⁴ There is, however, a body of literature which supports the idea that ancillary ligands, especially redox-active ligands, can have a substantial influence on the reactivity of the Co–alkyl bond.^{41-42, 45-47} In a 1992 report, Finke and coworkers described that single-electron reduction of methylcobalamin from Co^{III} to Co^{II} resulted in a Co–CH₃ “half-bond strength”, thereby weakening the bond by 68% and increasing the rate of homolysis by up to a factor of $\sim 10^{15}$.⁴⁸ This was rationalized using MO considerations where the addition of one electron to the system populates the σ^* molecular orbital with respect to the Co–CH₃ bond. Assuming a purely covalent interaction, this electronic configuration results in a formal Co–C bond order of 0.5.

Parallel studies by Pierpoint and Hendrickson reported valence tautomerism between redox non-innocent dioxolene ligands and Co^{III} metal centers.⁴⁹ This electronic isomerization occurs via a ligand-to-metal charge transfer (LMCT) process, producing a singly oxidized ligand radical and a Co^{II} metal. In this respect, the capacity of redox-active ligands to destabilize [(L)Co^{III}(CF₃)] via thermal or photolytic formation of [(L[•])Co^{II}(CF₃)] redox isomers is particularly attractive in the context of delivering [•]CF₃ under mild conditions.

3.2 Results and Discussion

3.1.1 Synthesis and Characterization of the Complexes

Initial synthetic efforts focused on the synthesis of Co–CF₃ complexes bearing the redox non-innocent ligands (^SOCO) and (^{Ph}OCO) described in Chapter 2. Treatment of [(^{Ph}OCO)Co(MeCN)], **1**, with one equivalent of AgCF₃ in acetonitrile produced a dark-colored suspension which yielded a green solid upon removal of the solvent. Crystals of the material suitable for X-ray diffraction were obtained by solvent diffusion of pentane into a concentrated THF solution of **1** at 25 °C, however the structure did not contain the desired Co–CF₃ bond (Figure 3.1). Rather, the CF₃ group was found to have ultimately reacted with the (^{Ph}OCO) ligand at the position *ipso* to the N atom of the NHC, forming an unusually elongated C_{sp3}–CF₃ bond (1.583(3) Å). The cobalt center also coordinated a second equivalent of the (^{Ph}OCO) ligand, producing a slightly distorted octahedral complex of the formula [(^{Ph}OCO)Co(^{Ph}OCO–CF₃)], complex **2**. Bonding metrics of the aryl C–O distances indicate that one of the phenoxide components had been oxidized to a

phenoxy radical (O4–C47 (1.229(2) Å). The combined charge of the two ligands is 3⁻ overall, making the pseudo-octahedral cobalt center +III.

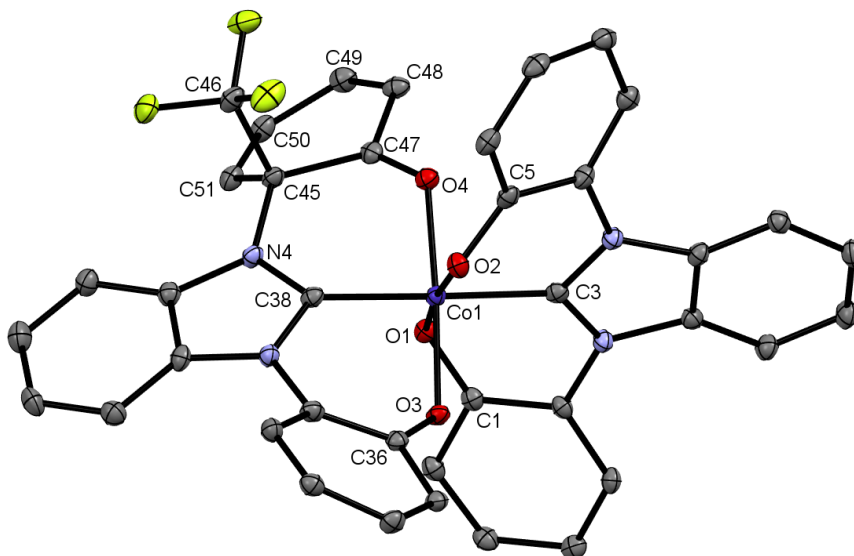
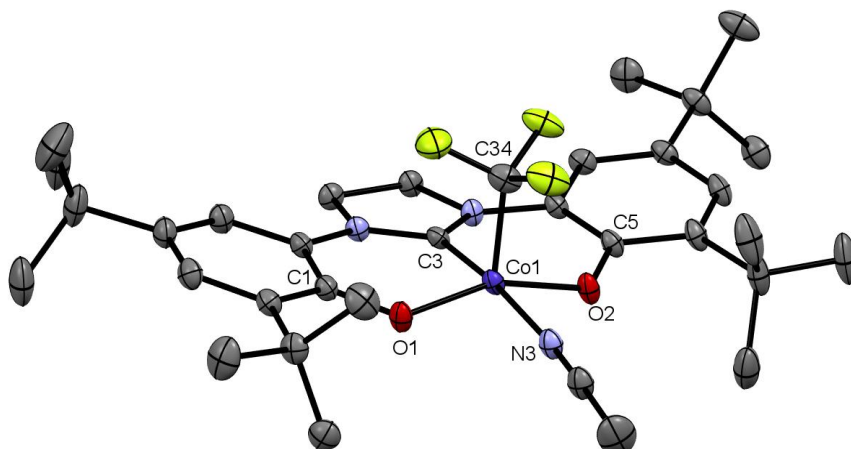


Figure 3.1. ORTEP plot of $[(^{Ph}OCO)Co(^{Ph}OCO-CF_3)]$, **2**. Thermal ellipsoids are drawn at 50% probability. The *tert*-butyl groups and hydrogen atoms have been removed for clarity. Selected bond lengths (Å): Co1–C3 1.874(2), Co1–C38 1.899(2), Co1–O1 1.9390(13), Co1–O2 1.9122(13), Co1–O3 1.8816(14), Co1–O4 1.9324(14), O1–C1 1.329(2), O2–C5 1.324(2), O3–C36 1.323(2), O4–C47 1.229(2), C47–C48 1.474(3), C48–C49 1.351(3), C49–C50 1.462(3), C50–C51 1.335(3), C51–C45 1.513(3), C45–N4 1.479(2), C45–C46 1.583(3).

When $[(^SOCO)Co(MeCN)]$, **3**, was treated with $AgCF_3$ in MeCN, a dark green suspension was initially formed which dried to a burgundy colored solid upon workup. This material, **4**, exhibited an interesting solvent-based color dependency. The observed color was independent of polarity, yet directly correlated with the ability of the solvent to bind the metal center. For instance, dissolution of **4** in coordinating solvents such as THF or MeCN produced emerald green solutions of **5**, while non-coordinating solvents such as CH_2Cl_2 or Et_2O maintained the dark red color observed in the solid state. Red colored crystals of **4** suitable for single crystal X-ray diffraction were obtained from a

concentrated toluene solution at $-25\text{ }^{\circ}\text{C}$, while green crystals of **5** were prepared from a mixture of MeCN and benzene (Figures 3.2 and 3.3).

a)



b)

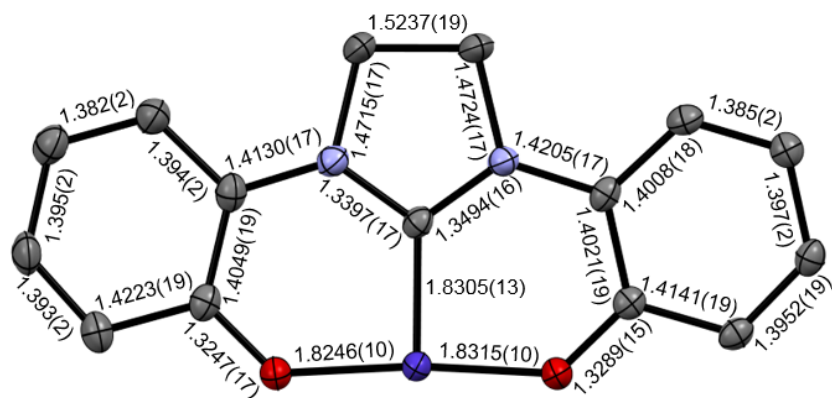
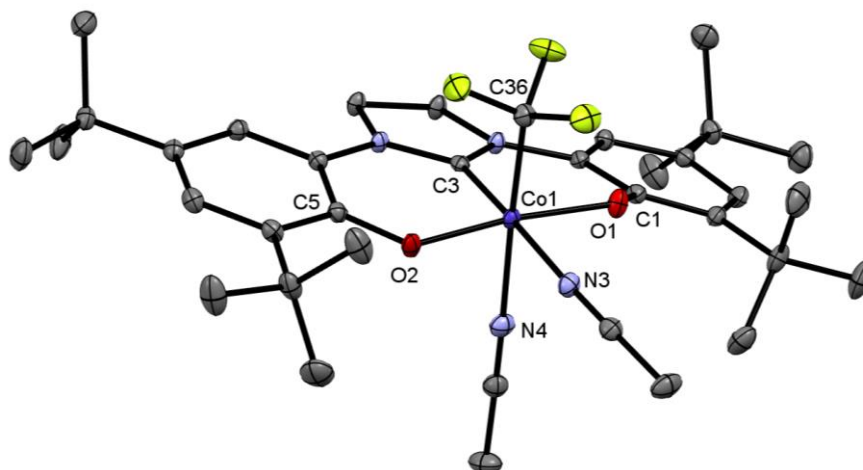


Figure 3.2. (a) ORTEP plot of the red crystals, [$^{\delta}\text{OCO}$ Co(CF₃)(MeCN)], **4**. (b) Selected bond lengths of the OCO ligand. Thermal ellipsoids are drawn at 50% probability. The rotational disorder of the *tert*-butyl groups and hydrogen atoms have been removed for clarity. Additional bond lengths (Å): Co1–N3 1.9813(12), Co1–C34 1.8687(15).

a)



b)

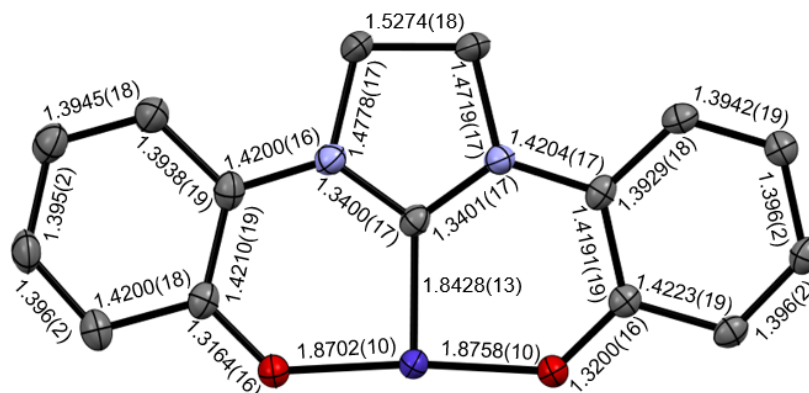


Figure 3.3. (a) ORTEP plot of green crystal, $[(^S\text{OCO})\text{Co}(\text{CF}_3)(\text{MeCN})_2]$, **5**. (b) Selected bond lengths of the OCO ligand. Thermal ellipsoids are drawn at 50% probability. Hydrogen atoms have been removed for clarity. Additional bond lengths (Å): Co1–N3 2.0165(12), Co1–N4 2.0126(13), Co1–C36 1.9189(14).

As shown in Figure 3.2, **4** is a 5-coordinate complex with distorted square pyramidal geometry in which the O1–Co1–O2 and C3–Co1–N3 angles measure $170.34(3)^\circ$ and $172.25(3)^\circ$, respectively. The CF_3 group is orthogonal to the (OCO) ligand plane and

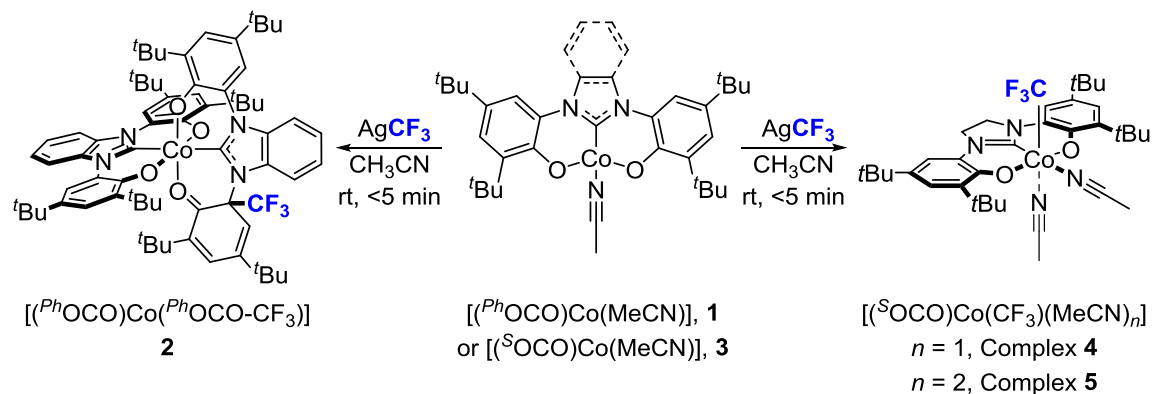
the Co-CF₃ bond length is 1.8687(15) Å, suggesting significant covalency. A search of the CCDC database in June of 2017 revealed that this matches within error with the shortest Co-CF₃ bond currently reported in literature (*cf.* trifluoromethylcobalamin; 1.878(12) Å).⁵⁰ The ligand remains nearly planar with the O1-C1-C5-O2 torsional angle remaining unchanged from the parent complex [(^sOCO)Co(MeCN)], **3**, at 2.63°. Around the metal center, the Co1-O1/O2(avg.) and Co1-C8 bonds undergo elongations by 0.016(25) and 0.020(13) Å, respectively, as compared to **3**. Conversely, the Co-acetonitrile bond contracts by 0.030(12) Å vs. the parent complex.

Solid-state structural analysis of the green crystals showed complex **5** is 6-coordinate with the coordination sphere completed by the addition of a second acetonitrile molecule (Figure 3.3). The cobalt center is in a distorted octahedral geometry with ligand-metal-ligand bonding angles ranging between 85.30(4)° and 94.25(5)°. A significant twisting of (^sOCO) ligand is observed with the O1-C1-C5-O2 torsional angle measuring 36.42(5)°. Due to the increase in coordination number, substantial bond elongations around the metal center are observed as compared to the 5-coordinate complex, **4**, including Co1-O1/2(avg) and Co1-C8 distances by 0.045(20) and 0.012(9) Å, respectively. The Co-CF₃ distance is also lengthened by 0.050(21) Å.

At room temperature in the solid state, the green complex **5** rapidly loses the second coordinated solvent molecule and converts back to the red solid, **4**. Additionally, when concentrated solutions of **5** in MeCN are diluted with non-coordinating solvents, the color of the solution quickly changes to red, with an electronic spectrum indicating significant conversion to **4**, suggesting the lability of one of the MeCN molecules. This

is further evidenced in attempts to obtain satisfactory elemental analysis data for complex **5** which resulted in data close to that expected for **4**.

Scheme 3.1. Outcomes of **1 and **3** when treated with AgCF₃.**



3.1.2 Electronic Absorption Spectra of $[(^SOCO)Co(CF_3)(MeCN)]$

The UV-Vis absorption spectra of complexes **4** and **5** were recorded in Et_2O and MeCN, respectively, revealing significant differences (Figure 3.4). In both spectra, large charge transfer (CT) bands are observed at 387 nm (MeCN) and 408 nm (Et_2O) with shoulders present at 467 nm (MeCN) and 462 nm (Et_2O). An additional, smaller CT absorbance is observed in MeCN at 616 nm ($612\ M^{-1}\ cm^{-1}$) with no other observable transitions in the range of wavelengths scanned. This is in sharp contrast to the spectrum in Et_2O in which a broad CT band is observed at 785 nm ($2790\ M^{-1}\ cm^{-1}$).

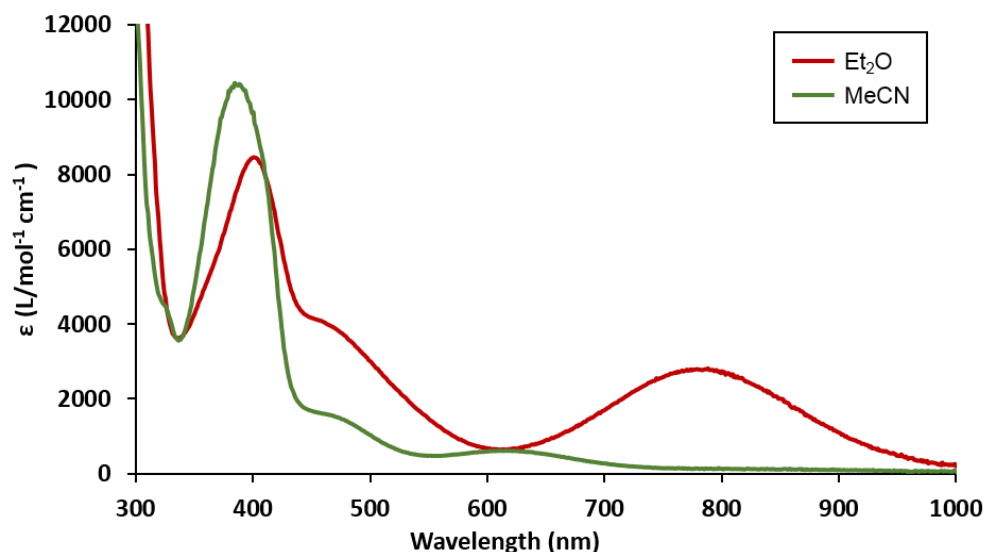


Figure 3.4. UV-Vis absorption spectra of **4** in Et₂O and MeCN at 22°C.

Both spectra are sensitive to changes in temperature. Upon cooling to approximately -60 °C in Et₂O, a visual color change of the solution from red to green occurred which was reversible upon warming back to room temperature. Variable temperature UV-Vis from -30 to 20 °C confirmed the color change was completely reversible over that temperature range (Figure 3.5). Upon cooling, the characteristic CT band at 785 nm and the shoulder at 462 nm decreased in intensity while the absorbances at 408 and 629 nm increased. There are four isosbestic points present at 319, 425, 566, and 675 nm.

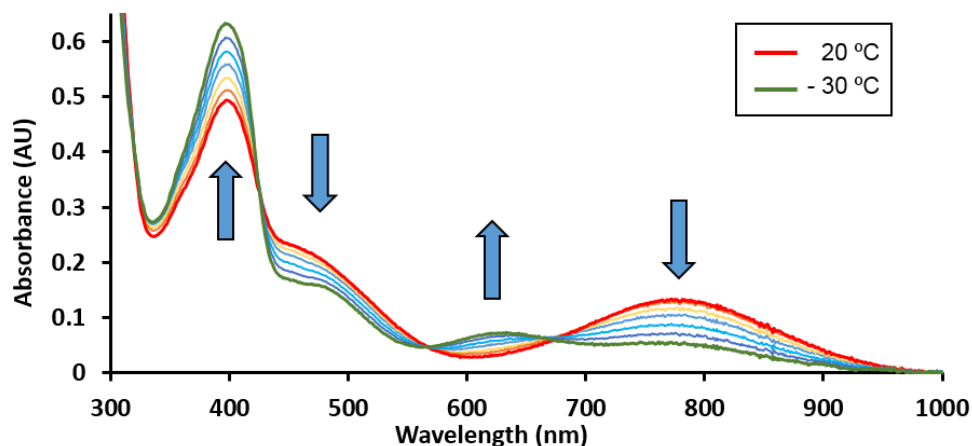


Figure 3.5 Variable temperature UV-Vis spectra of 4 in Et₂O with a temperature range of -30 to 20 °C.

Heating a sample of **5** dissolved in acetonitrile produced an opposite effect. By heating to near the boiling point of the solvent, a visible change in color from green to orange occurred which was reversible upon cooling. Variable temperature UV-Vis from 20 to 80 °C produced a decrease in the absorbances at 387 and 614 nm and an increase at the local minima 545 and 820 nm (Figure 3.6). These collective changes are consistent with loss of the sixth MeCN ligand at elevated temperatures as well as the binding of Et₂O in chilled solutions.

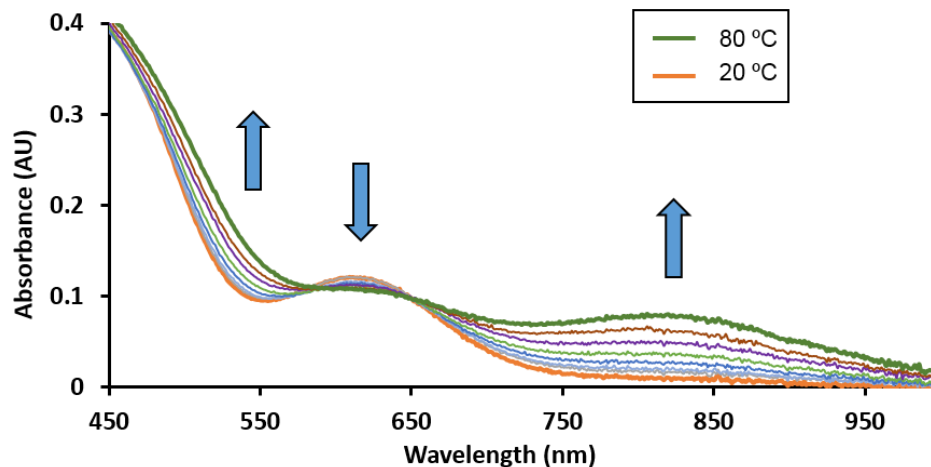


Figure 3.6. Variable temperature UV-Vis spectra in MeCN with a temperature range of 20 to 80 °C.

3.1.3 Nuclear Magnetic Resonance

The trifluoromethyl complex exhibits a diamagnetic NMR signal in both coordinating solvents, where **5** is the dominant species, and non-coordinating solvents where **4** is most prevalent. In the ^1H NMR spectrum collected in acetonitrile- d_3 , three sets of signals are observed between 1.28 and 6.85 ppm (Figure 3.7). The upfield signals correspond to the two inequivalent *tert*-butyl environments while NHC backbone protons appear as a broad singlet at 4.46 ppm. The aryl C–H signals fall between 6.77 and 6.85 ppm and exhibit *meta* splitting ($J = 1.9$ Hz). There are two large differences present in the spectrum recorded in CDCl_3 . These involve a more complex splitting pattern of the NHC backbone signals in addition to the presence of a signal at 2.44 ppm, corresponding to the coordinated MeCN ligand. No assignable coordinated MeCN ligand signals are observed in the acetonitrile- d_3 spectrum, likely due to exchange with the deuterated solvent, although two minor peaks are observed at approximately 2.20 and 2.50 ppm.

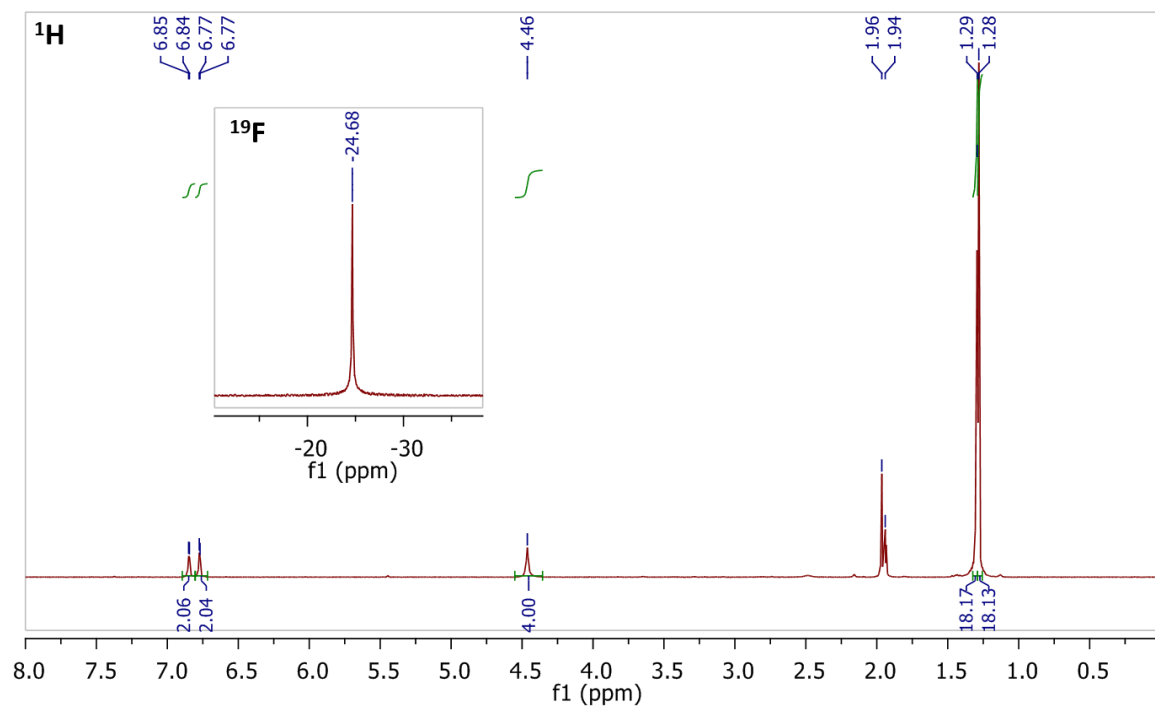


Figure 3.7. ¹H NMR spectrum of **5** in acetonitrile-*d*₃.

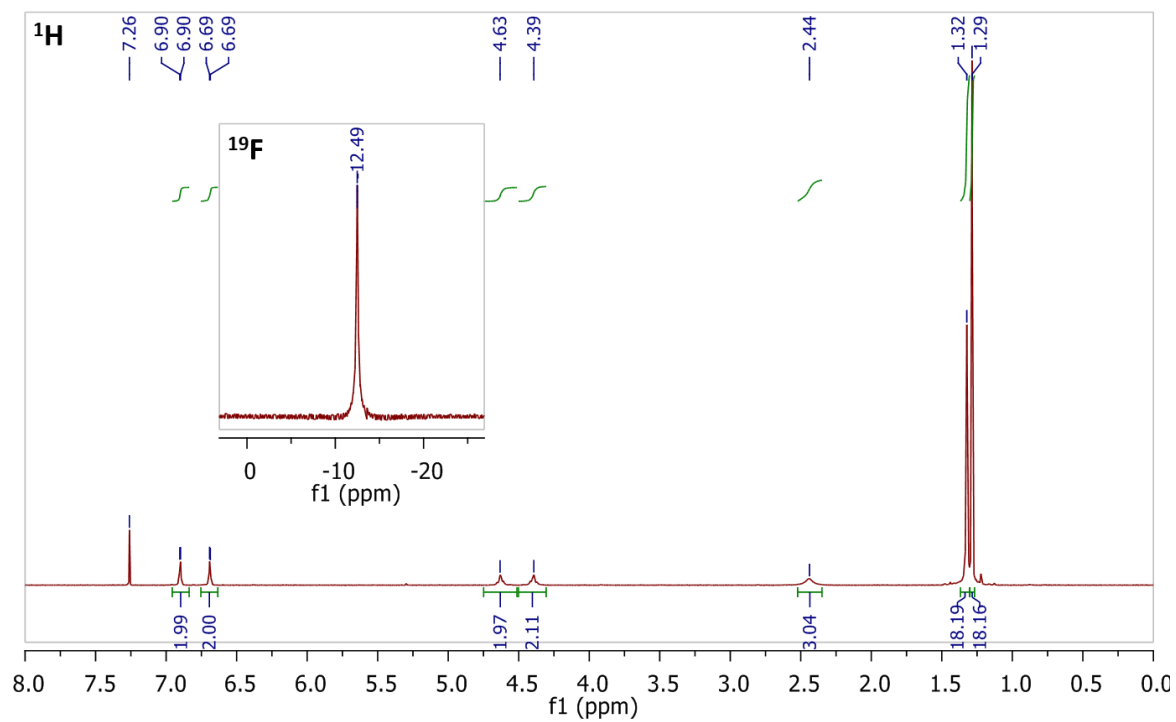


Figure 3.8. ¹H NMR spectrum of **4** in CDCl₃.

A variable temperature ^1H NMR experiment was performed in acetonitrile- d_3 over the temperature range of 25 - 75 $^\circ\text{C}$ in 10 $^\circ\text{C}$ increments (Figure 3.9). As the temperature was increased, all signals were shifted downfield by a range of 0.05 - 0.08 ppm. The singlet corresponding to the NHC backbone protons broadened into the baseline as the temperature increased from 25 - 45 $^\circ\text{C}$. It subsequently began to sharpen back until about 65 $^\circ\text{C}$, after which the singlet began to split into a more complex pattern. The two minor signals observed at 2.20 and 2.50 ppm were also sensitive to the change in temperature, however they shifted upfield with increasing temperature. The peak at 2.50 ppm began to sharpen as it shifted until it reached approximately 2.30 ppm, while the signal that originated at 2.20 ppm gradually shifted into the static signal observed at 1.96 ppm which represents free, protonated MeCN. It is reasonable to assign these two minor peaks to the two coordinated MeCN ligands in the octahedral geometry; their smaller-than-expected integration values are a result of there being a significantly large ratio of deuterated to protonated MeCN ligands available in the deuterated acetonitrile solution. These data, combined with the variable temperature UV-Vis spectroscopic results, seem to suggest the coordination environment is directly affected by temperature in addition to solvent effects, and that **4** and **5** exist in equilibrium.

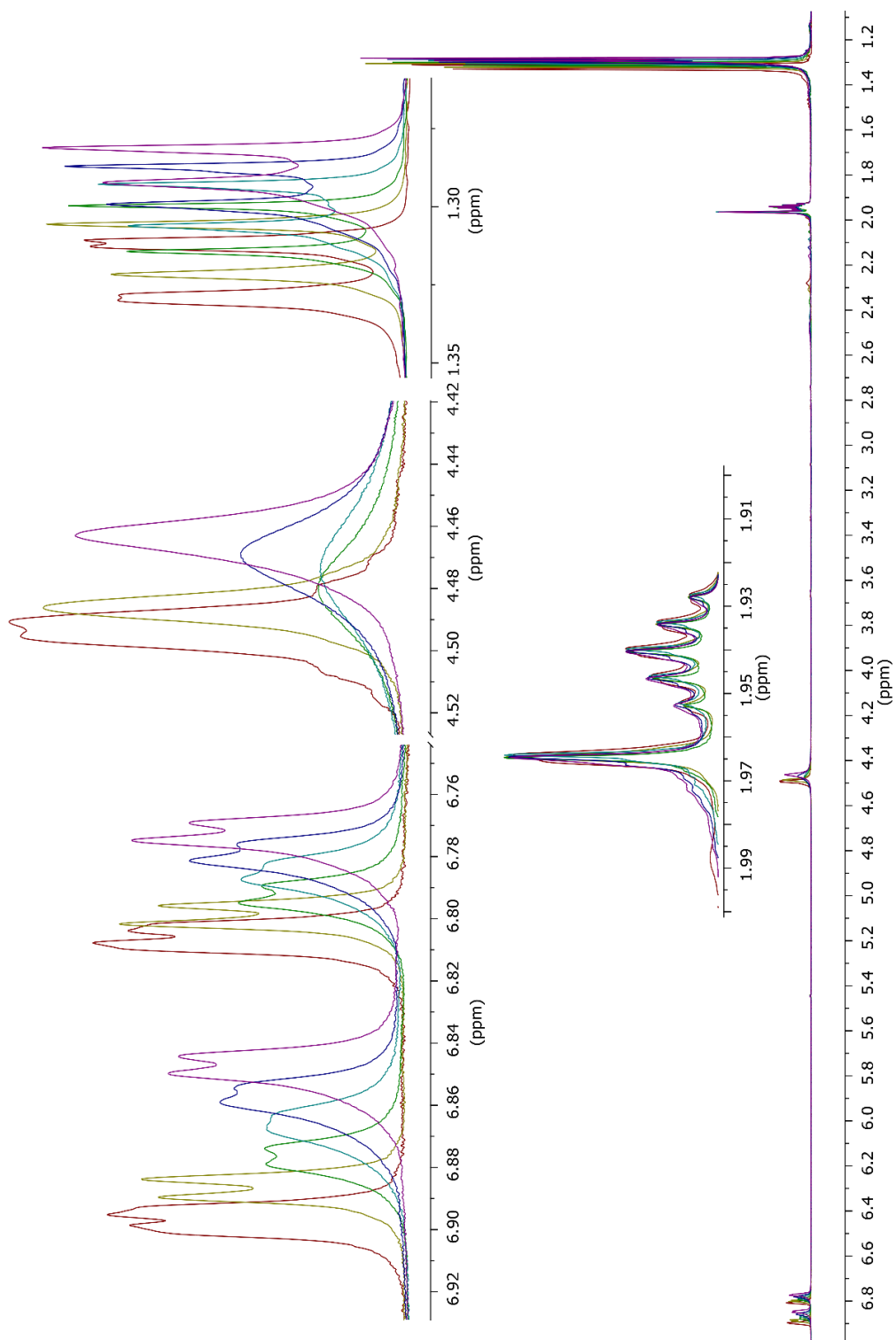
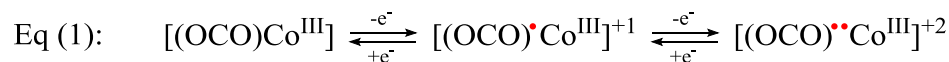


Figure 3.9. VT-¹H NMR spectra of 5 in acetonitrile-*d*₃ from 25 (purple) to 75 °C (red) in 10 °C increments.

3.2 Electrochemistry

Cyclic voltammograms of **4** and **5** were measured at 22 °C in both coordinating (MeCN) and non-coordinating solvents (CH₂Cl₂) with ([Bu₄N][PF₆]) used as the supporting electrolyte. As shown in Figure 3.10 and Table 3.1, the complex exhibits two reversible oxidative waves at a scan rate of 100 mV/s in either solvent. Thus, the neutral species, **4/5**, may form a mono- or dication, **4⁺/5⁺** and **4²⁺/5²⁺**. These potentials lie in the typical range for metal-coordinated phenoxide to phenoxyl radical oxidations and are much lower than typically observed for Co^{III/IV} oxidation (Eq. 1).⁵¹ However, given the electronic promiscuity of this metal/ligand combination, described in Chapter 2, other electronic structures should be considered, including one where the ligand becomes doubly oxidized and the metal center is reduced by a single electron (Eq. 2).



To evaluate these possibilities experimentally, **4** was chemically oxidized with one and two equivalents of AgOTf in CH₂Cl₂. The two-electron oxidized species **4²⁺** was found to be unstable in both coordinating and non-coordinating solvents, even in the absence of light. However, the singly oxidized product **4⁺** was isolated and characterized by X-ray crystallography (Figure 3.11). Crystals suitable for X-ray crystallography were obtained from solvent diffusion of hexamethyldisiloxane into a concentrated THF solution of **4⁺** in air. As shown in Figure 3.11, **4⁺** exhibits a quasi-octahedral geometry about the Co center, where the two sites *trans* to CF₃ and C_{NHC} are occupied by water

molecules. The two water molecules were likely introduced during the workup involving silica gel column chromatography and remained coordinated through crystallization. Examination of the ligand metrical data (Figure 3.11; bottom) shows a clear quinoid-type pattern of four long and two short C–C bonds in both phenoxide moieties. Compared to **4**, the $C_{Ar}-O(\text{avg.})$ and $C_{Ar}-N(\text{avg.})$ bond lengths are contracted by 0.030(6) and 0.025(5) Å, respectively, and are most consistent with formulation as a charge neutral, doubly-oxidized ligand. Charge balance implies the Co center is in the +II oxidation state, so the complex is assigned as $[(^{\delta}OCO)^{\bullet\bullet}Co^{II}(CF_3)(OH_2)_2][OTf]$, in agreement with Eq (2). Although given the data presented in Chapter 2, a closed shell ligand assignment is also possible.

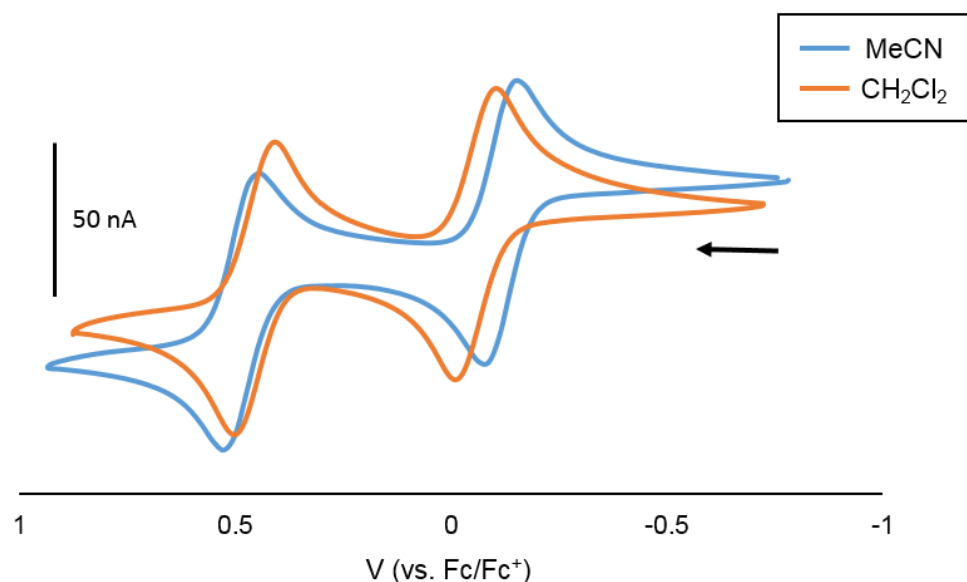
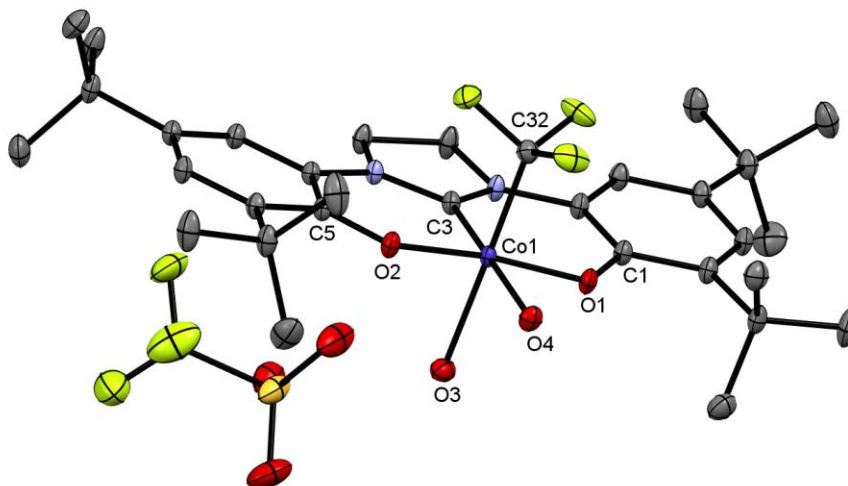


Figure 3.10. Cyclic voltammogram of complex **4** in both coordinating (MeCN; blue) and non-coordinating (CH_2Cl_2 ; orange) solvents.

Table 3.1. Redox potentials (V) in coordinating vs. non-coordinating solvent.

	$E_{1/2}^1$ (ΔE_p)	$E_{1/2}^2$ (ΔE_p)
CH₂Cl₂	-0.124 (0.104)	0.473 (0.101)
MeCN	-0.076 (0.100)	0.436 (0.116)

a)



b)

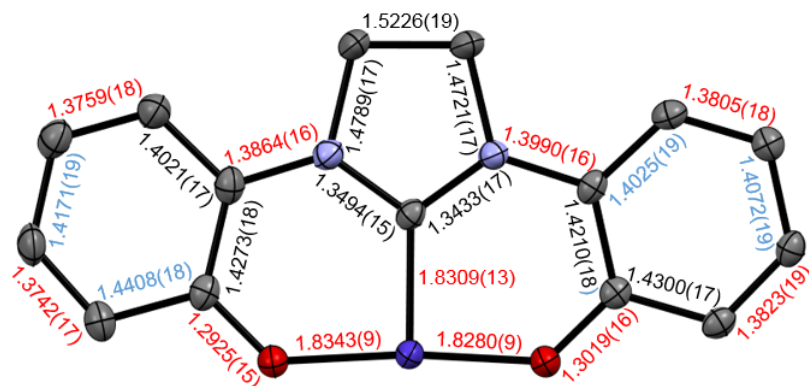


Figure 3.11. (a) ORTEP plot of **4⁺** and (b) selected bond lengths of the (OCO) ligand. Thermal ellipsoids are drawn at 50% probability. Hydrogen atoms have been removed for clarity. Bond contractions (red) and elongations (blue) greater than 0.01 Å vs. the parent complex **4** are indicated by color. Additional bond lengths (Å): Co1–O3 2.0876(11), Co1–O4 2.0012(10), Co1–C32 1.9183(14).

3.2.1 Stability Studies

I observed that exposure of **4** to ambient light in a non-coordinating solvent gave significant decomposition over 18 hours. As shown in Figure 3.12, a loss of intensity of the CT bands at 400 and 788 nm occurred in Et₂O which coincided with the introduction of a new absorbance at 356 nm and isosbestic points at 324 and 369 nm. However, when a solution of the same material in MeCN, generating **5**, was subjected to the same conditions, no measurable change was observed (Figure 3.13).

The identity of the decomposition product in the ethereal solution was determined to be the one-electron reduced [^SOCO)Co(MeCN)], complex **3**. Accordingly, conversion of **4** to **3** requires the loss of [•]CF₃ during the photolytic process. However, no fluorine containing product was observed in the ¹⁹F NMR spectrum after the photolysis experiment concluded. A possible byproduct of the reaction is gaseous HCF₃ which could form via radical H-atom abstraction from diethyl ether and be lost during the transfer of the sample from the cuvette. The viability of such H-atom abstraction from the solvent is discussed below.

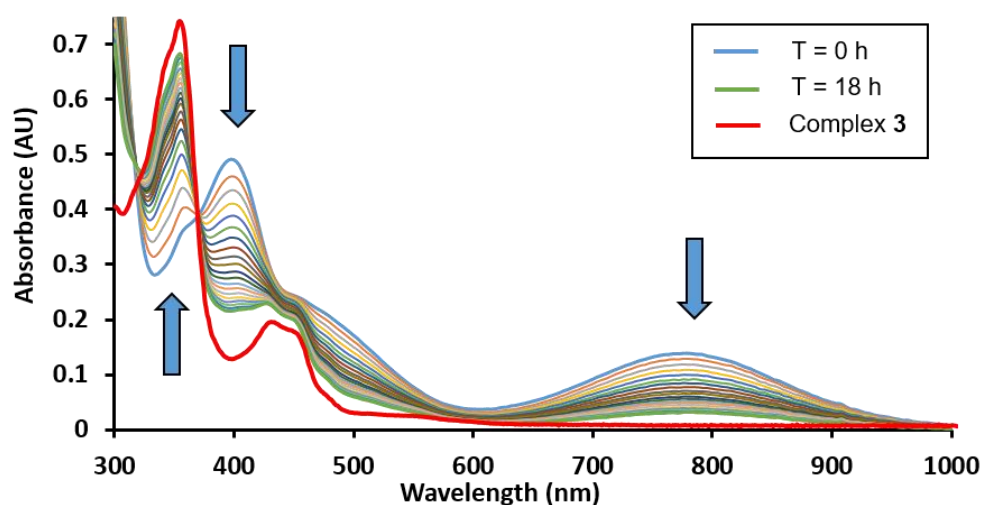


Figure 3.12. UV-Vis spectra of **4** in Et₂O over 18 h with scans each hour from T = 0 h (blue) to T = 18 h (green) under ambient light. A normalized spectrum of complex **3** in Et₂O is overlaid in red.

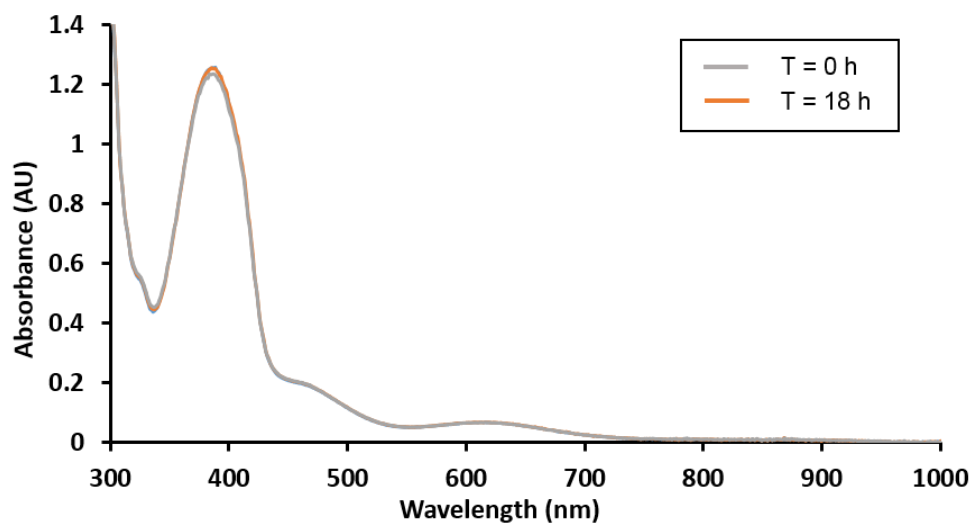


Figure 3.13. UV-Vis spectra of **5** in MeCN at T = 0 h (gray) and after 18 h (orange) under ambient light.

3.2.2 Calculated Absorbance Spectrum of $[(^S\text{OCO})\text{Co}(\text{CF}_3)(\text{MeCN})]$

The absorption spectra of **4** and **5** were examined by TD-DFT calculations, performed by Mr. Nicolaas P. van Leest and Prof. Bas de Bruin of the University of

Amsterdam. The calculated and experimental UV-Vis spectra of complex **4** in Et₂O are in reasonable agreement (Figure 3.14). The calculated UV-Vis spectrum with single energy absorption lines is shown in Figure 3.15. A selection of the molecular orbitals (MOs) involved in these transitions (MO #1 to MO #2) are collected in Table 3.2. MO #170 is the calculated HOMO and #171 is the calculated LUMO. The letters ‘a’ and ‘b’ represent the calculated alpha and beta spins, respectively.

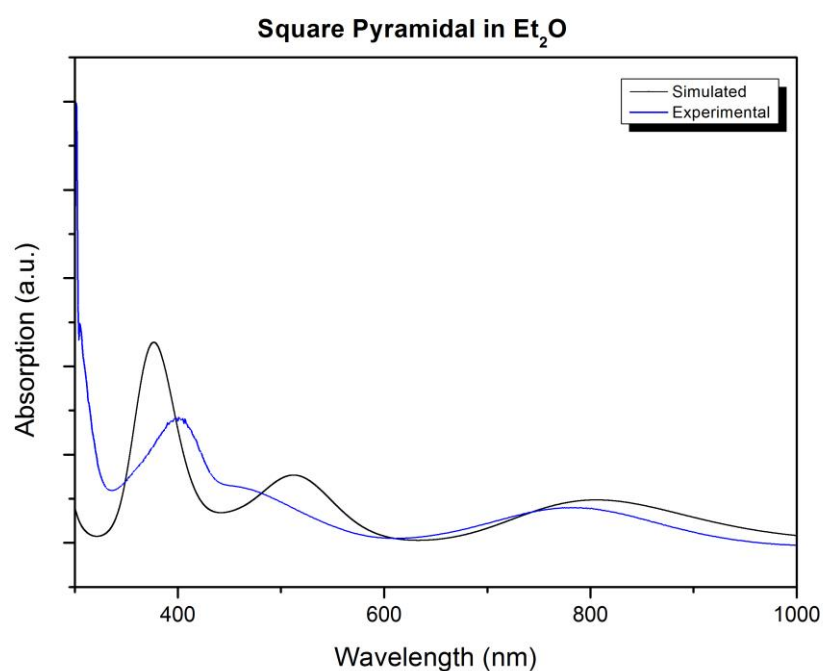


Figure 3.14. Simulated and experimental UV-Vis spectra for complex **4 in Et₂O.**

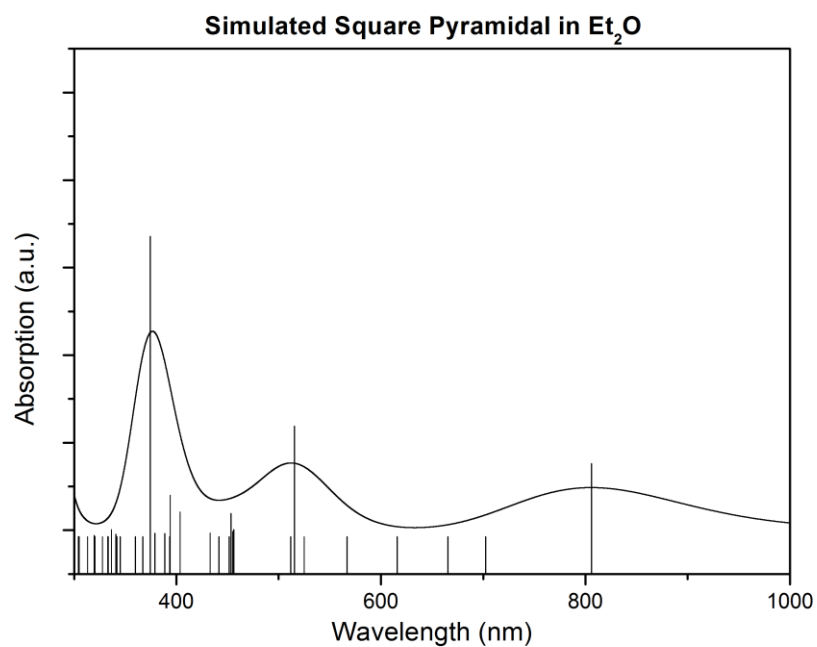
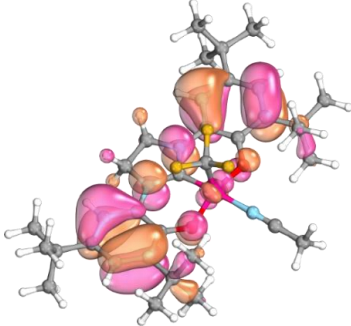
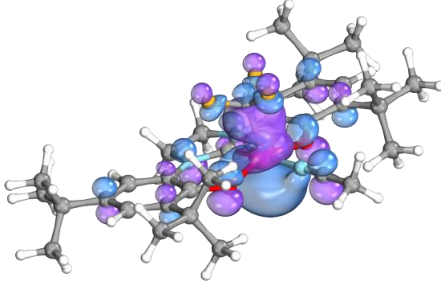


Figure 3.15. Calculated single line absorption spectrum of complex 4 in Et₂O.

Table 3.2. Relevant calculated MOs for complex 4 generated with IboView with the iso surface set at 80.0.

λ (nm)	MO #1	MO #2	Weight
374.4	168a (HOMO-2)	171a (LUMO)	0.16835
			

	170a (HOMO)	173a (LUMO+2)	0.14339
	168b (HOMO-2)	171b (LUMO)	0.16835
	170b (HOMO)	173b (LUMO+2)	0.14339
515.5	170a (HOMO)	171a (LUMO)	0.16022

	170b (HOMO)	171b (LUMO)	0.16022
805.8	170a (HOMO)	171a (LUMO)	0.28369
	170b (HOMO)	171b (LUMO)	0.28369

The calculated absorption band at 806 nm can be used to describe the experimental absorption band at 788 nm. In this absorption band, the transitions on 170a→171a and 170b→171b (HOMO to LUMO) are major contributors. As shown in Table 3.2, 170a and 170b are almost purely ligand based, while 171a and 171b are predominantly metal based. The 171a and 171b MOs describe significant antibonding character between the Co center and CF₃ ligand very well. These transitions are therefore

described as ligand-to-metal-charge-transfer (LMCT) bands, which result in population of the Co-CF₃ antibonding orbital. It is this transition that likely promotes facile Co-CF₃ bond cleavage under photolysis conditions.⁴⁷

3.3 Radical Trifluoromethylation

3.3.1 Radical Trapping of $\cdot\text{CF}_3$ with TEMPO

Photolysis experiments were performed to determine if the new Co-CF₃ complex, **4**, could be used as a radical CF₃ transfer reagent. Initial experiments used TEMPO as the radical acceptor and a 16W compact fluorescent lamp (CFL) was used as the light source. Benzene and MeCN were individually evaluated as solvents. After 3 h, the reaction in benzene was analysed by ¹⁹F NMR spectroscopy and four individual signals were observed at δ 11.9, δ 23.9, δ 55.6, and δ 62.7 ppm relative to an external reference of CFCl₃. These correspond to integration values of 0.09, 0.02, 0.85, and 0.04, respectively, indicating successful trifluoromethylation of TEMPO (85% yield). Surprisingly, C-H bond activation of benzene also occurred (4% yield) while 9% of the starting material remained unreacted after that time (Figure 3.16). Running the reaction without light gave only complex **4** in solution after 18 h.

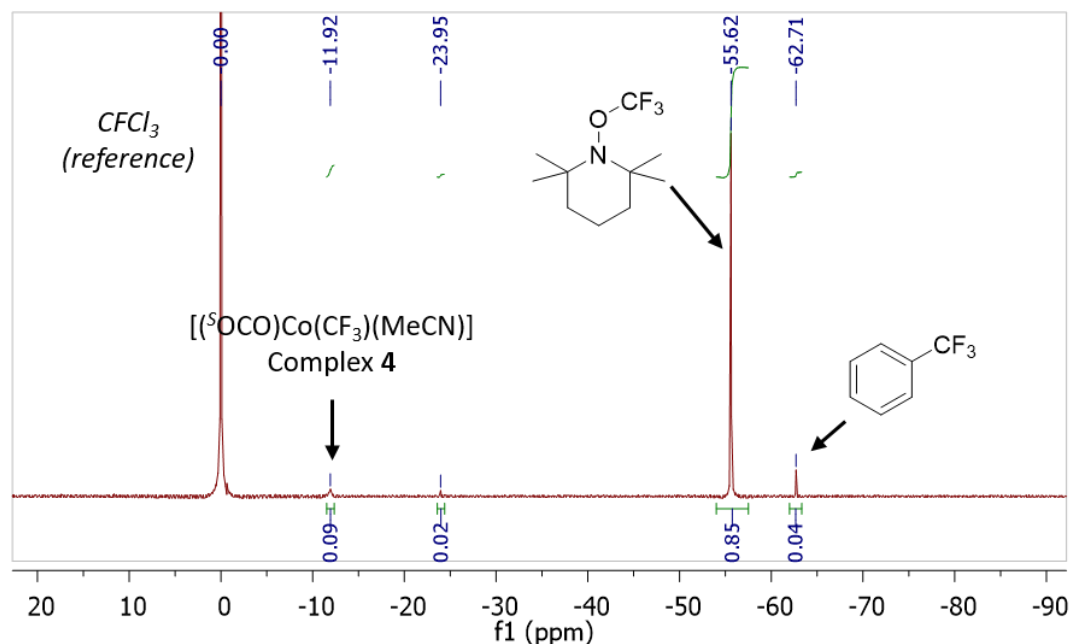


Figure 3.16. ^{19}F NMR spectrum of a radical trap experiment in C_6H_6 after 3h under a 16W CFL at ambient temperature.

Photolysis of **4** under analogous conditions, but using MeCN solvent, gave only one signal at -24.7 ppm. This corresponds to the starting material, complex **5**, indicating no reaction occurred (Figure 3.17). This is ascribed to the absence of a MLCT band in the visible light region of the electronic spectrum when the complex is in 6-coordinate geometry and can be understood by considering the MO diagram in Figure 3.18. Coordination of the second solvent molecule along the z-axis stabilizes the d_{z^2} orbital, which is σ -antibonding with respect to the $\text{Co}-\text{CF}_3$ bond.⁴⁸ Without the ability to promote an electron to the $\text{Co}-\text{CF}_3$ antibonding orbital, the complex is unreactive under the CFL light source.

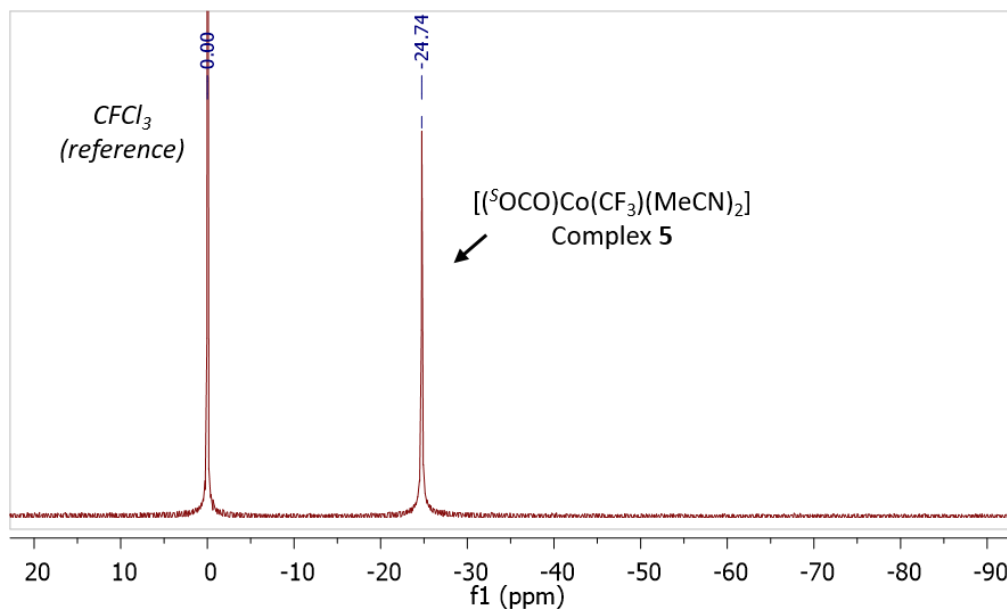


Figure 3.17. ^{19}F NMR spectrum of a radical trap experiment in MeCN after 3h under a 16W CFL at ambient temperature.

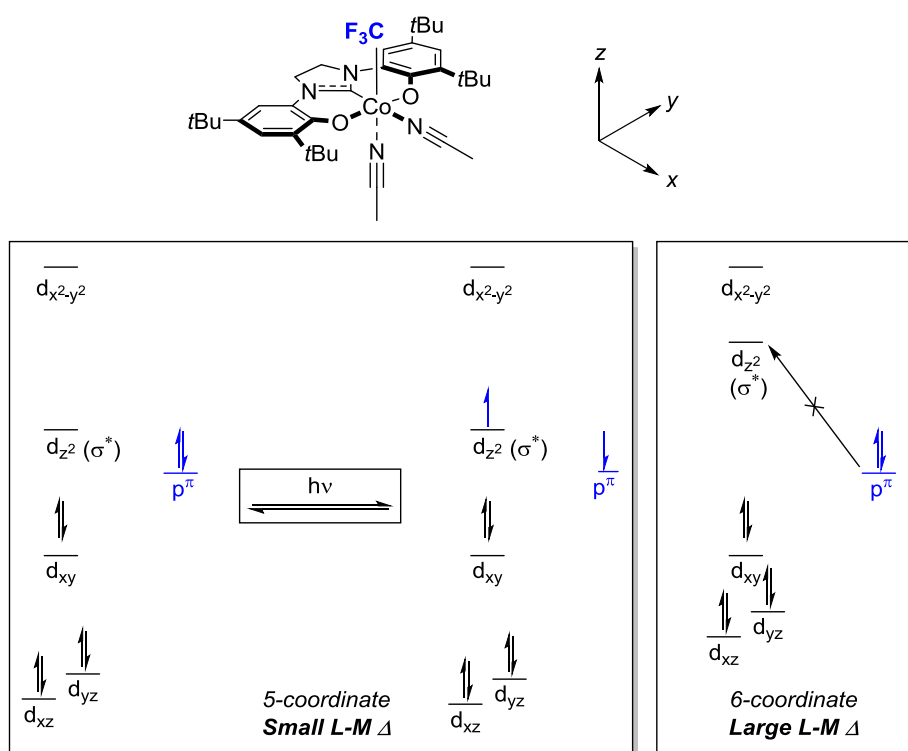


Figure 3.18. Qualitative molecular orbital description of the 5- and 6-coordinate complexes.

3.3.2 Radical Trifluoromethylation of Organic Substrates

The observation of CF₃ transfer to benzene in the experiments described above prompted us to pursue photolytic trifluoromethylation of unactivated C–H bonds. This represents an area of acute interest due to the possibility of late-stage installation of the CF₃ group without the necessity of pre-functionalization. Until the seminal report in 2011 by Nagib and MacMillan, direct C–H trifluoromethylation of (hetero)aryl substrates was considered an ‘unsolved challenge’.⁵² Although a number of methods are available today, the majority involve precious metal sources including Pd, Ir, or Ru.^{28, 52-53}

Photolysis of **4** using a 16W compact fluorescent lamp (CLF) source for 16 h in neat, non-coordinating aromatic solvents (i.e. benzene, mesitylene, and pyrrole), gave quantitative conversions to the corresponding mono trifluoromethylated (hetero)arenes, as determined by ¹⁹F NMR. Further screening revealed that the expected trifluoromethylated products could be obtained in high yields with arene loadings at 20 eq. vs the Co–CF₃ complex in N-methyl pyrrolidinone (NMP) solvent. The selectivity of the [•]CF₃ was similar to those observed in other radical functionalization processes (Figure 3.19).⁵²⁻⁵³

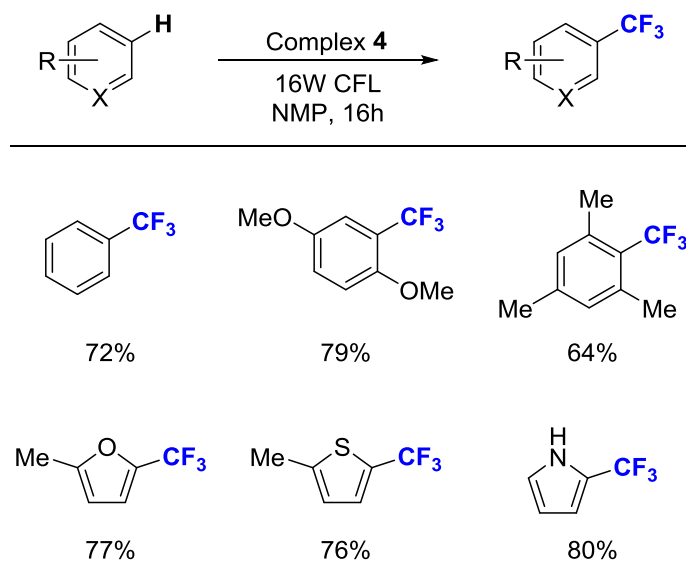


Figure 3.19. Radical trifluoromethylation of arenes and heteroarenes by complex 4 under photolytic conditions. Yields were determined by integration of diagnostic ^{19}F resonances against an internal standard.

In each reaction, complex 4 was completely consumed after 16 h and a signal for HCF_3 was present, accounting for the balance of the $\cdot\text{CF}_3$ that was not incorporated into a (hetero)arene. When a halogenated solvent such as CH_2Cl_2 , CHCl_3 , or CCl_4 was used, exclusively ClCF_3 was formed after ~6 h. The utilization of aliphatic solvents such as pentane or cyclohexane provided high conversion to HCF_3 . In order to determine if the solvent was acting as the H atom source, the reaction was run in both C_6H_{12} and C_6D_{12} (Figure 3.20).

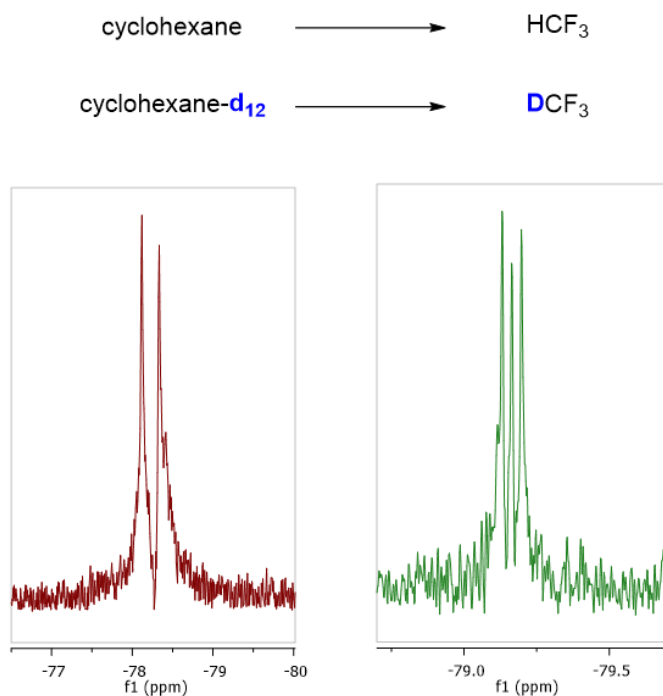


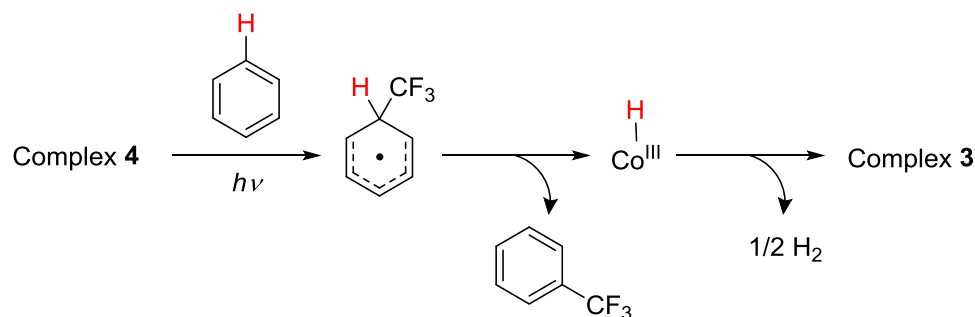
Figure 3.20. Signals observed for HCF₃ (left) and DCF₃ (right) when 4 was exposed to photolytic conditions in protic vs. deuterated cyclohexane.

Evaluation of the reaction mixtures by ¹⁹F NMR spectroscopy revealed a doublet present at -78.3 ppm in the reaction run in protonated solvent. The reaction in deuterated solvent produced a triplet at -79.2 ppm, indicating that the solvent was indeed the source of H/D. The sum of these observations suggests that the [•]CF₃ radical generated under photolysis reacts differently in aryl vs. non-aromatic substrates. In non-aryl hydrocarbon systems, the [•]CF₃ abstracts an H-atom from the substrate, but in aryl systems the [•]CF₃ apparently attacks the arene directly to generate a non-aromatic, radical intermediate. Generation of the aromatic trifluoromethylated products requires subsequent loss of an H atom, the fate of which is unknown.

We speculated that [•]H transfer to the Co center, might generate a Co^{III} hydride intermediate, which would be susceptible to H₂ production, thereby reducing the complex

to the known Co^{II} species, **3** (Scheme 3.2). Such Co^{III} hydrides are well-known intermediates for the electrocatalytic generation of H_2 .⁵⁴⁻⁵⁷ Molecular H_2 should be observable by ^1H NMR, but the paramagnetic Co^{II} complex formed upon reduction can obscure its signal. Accordingly, to determine if this was a viable pathway for the reduction of a Co^{III} species, a salt metathesis reaction with NaH and the complex $[(^{\delta}\text{OCO})\text{Co}(\text{THF})_2][\text{OTf}]$ was performed in THF to form $[(^{\delta}\text{OCO})\text{Co}(\text{H})(\text{THF})_2]$ and NaOTf *in situ*. Rapid effervescence was observed immediately upon addition of the NaH which coincided with a color change of the solution from green to orange over ~10 mins. This orange solution was the one-electron reduced $[(^{\delta}\text{OCO})\text{Co}(\text{THF})]$, **3**, as evidenced by a UV-Vis spectrum which matches that from an isolated sample of **3**.

Scheme 3.2. Possible free radical pathway for Co-mediated trifluoromethylation of arenes.



3.3.3 Attempts at Ligand Directed C-H Trifluoromethylation

A major challenge in C–H bond activation, particularly with radical substrates, is achieving selective functionalization of a single C–H bond within a complex molecule. Indeed, the substrate specificities above are all a consequence of the innate selectivity of the trifluoromethyl radical, wherein the trifluoromethylation occurs at the most reactive position on a molecule relative to the electrophilic $^{\bullet}\text{CF}_3$. An alternative strategy might

utilize a functional group in the substrate itself for programmed trifluoromethylation via a so-called ligand-directed approach.⁵⁸⁻⁶²

This approach was pursued to determine whether **4** can impart selectivity in Co mediated radical C–H trifluoromethylation. We envisioned substrate design criteria to include: 1) The substrate positioning an aryl C–H bond in close distance to the Co–CF₃ bond. 2) The substrate blocking coordination to the open site *trans* to the CF₃ (*i.e.* not a bidentate directing group). Initially, we considered 2-phenyl pyridine (2-phpy) which would hold the C6–H bond in close proximity to the CF₃ group while preventing coordination to the open site on the Co center by the flanking phenyl ring. The material was synthesized by treating an ethereal solution of complex **4** with 1.5 equivalents of 2-phpy. The solution was evaporated to near dryness (the b.p. of 2-phpy is 268 – 270 °C), and triturated with pentane. The solid material was filtered and dissolved in a minimal amount of benzene and layered with pentane, producing X-ray quality crystals of the material [(^sOCO)Co(CF₃)(2-phpy)], complex **6** (Figure 3.21). Aside from the 2-phpy ligand, the metrical parameters of **6** are indistinguishable from **4**, suggesting that it's reasonably formulated as Co^{III} with a reduced, dianionic (^sOCO) ligand.

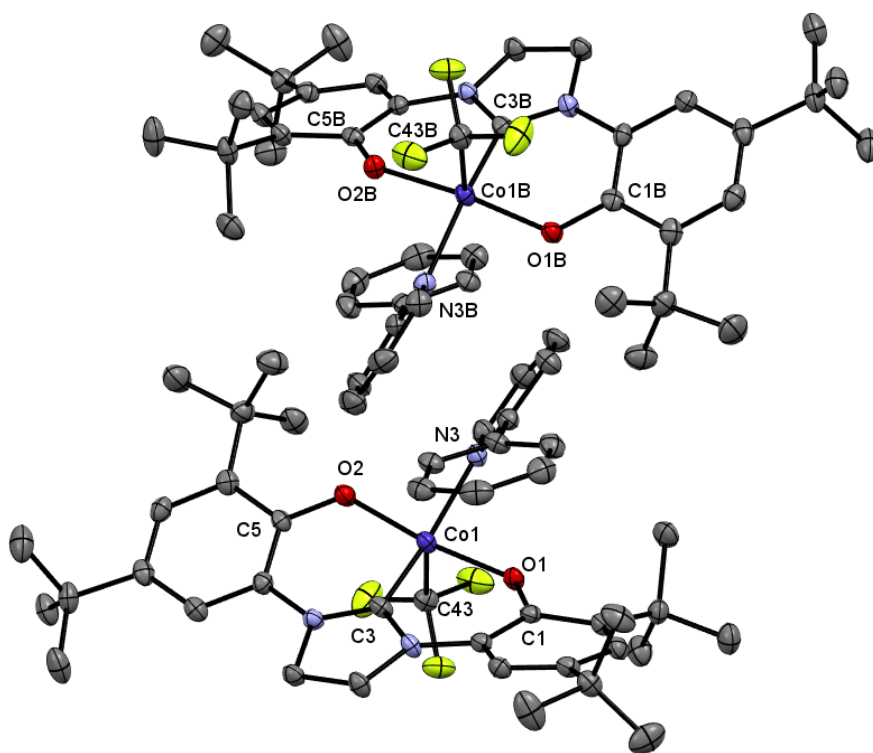


Figure 3.21. ORTEP plot of $[(^o\text{OCO})\text{Co}(\text{CF}_3)(2\text{-phpy})]$, **6**. Thermal ellipsoids are drawn at 50% probability. The rotational disorder of the CF_3 group and hydrogen atoms have been removed for clarity. Selected bond lengths (\AA): Co1–C3 1.831(3), Co1B–C3B 1.831(3), Co1–O1 1.874(2), Co1–O2 1.859(2), Co1B–O1B 1.863(2), Co1B–O2B 1.874(2), Co1–N3 2.038(2), Co1B–N3B 2.031(2), O1–C1 1.323(3), O2–C5 1.327(3), O1B–C1B 1.331(4), O2B–C5B 1.324(3), Co1–C43 1.881(3), Co1B–C43B 1.881(3).

Coordinating solvents were avoided to minimize potential displacement of the phenyl pyridine adduct. Surprisingly, exposure of complex **6** to photolysis conditions in benzene, NMP, and even nitrobenzene resulted in preferential trifluoromethylation of the solvent over any CF_3 incorporation into 2-phenyl pyridine. These observations suggest direct coordination to the metal center inhibits heteroaryl C–H bond activation. This could arise from deactivation of the aryl C–H bonds on coordination of the py functionality to the Co center. Additional substrates were evaluated which provided a

variety of aryl C–H bonds that were not directly coordinated to the metal center (Figure 3.22). In these cases, the substrate was successfully trifluoromethylated, but unselectively. A multitude of products were produced in moderate yields (30–45%). In all cases the major product derived from the trifluoromethylation of the solvent.

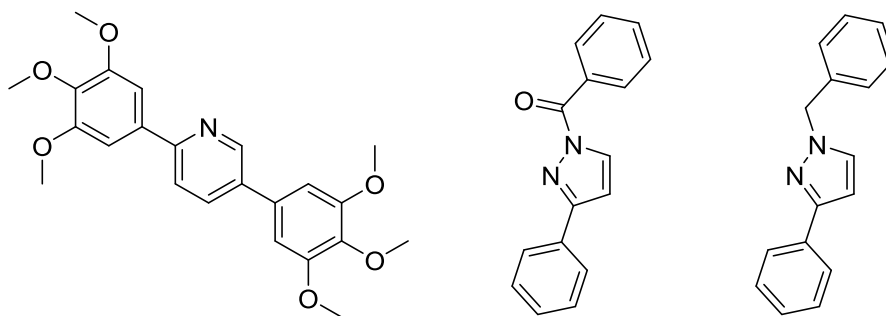


Figure 3.22. Substrates evaluated for ligand directed C–H trifluoromethylation by **4**.

3.4 Towards Catalytic Methods

3.4.1 Synthesis and Characterization of a Trifluoroacetate Complex

Having proven the system capable of stoichiometric C–H bond activation, we shifted our focus towards catalytic applications. Since AgCF_3 isn't considered a viable source of the trifluoromethyl group for large-scale reactions, we proposed that the trifluoroacetate fragment $-\text{O}_2\text{CCF}_3$ might provide an economical trifluoromethyl radical alternative. If visible light could be used to facilitate $\text{Co}-\text{O}$ bond cleavage in the same fashion as $\text{Co}-\text{CF}_3$, the resulting trifluoroacetate radical species should be susceptible to radical decarboxylation, providing $^{\bullet}\text{CF}_3$ and CO_2 .⁵³

To test this hypothesis, **3** was treated with stoichiometric AgO_2CCF_3 in MeCN, affording a dark green suspension. After ~10 minutes of stirring, the reaction mixture

was filtered and concentrated *in vacuo*, affording $[(^{\delta}\text{OCO})\text{Co}(\text{O}_2\text{CCF}_3)]$, **7**, as a green solid. The complex was dissolved in CH_2Cl_2 and a few drops of benzene was added to aid in crystallization. The solution was stored at $-25\text{ }^{\circ}\text{C}$ overnight, producing dark green, X-ray quality crystals in 88% yield. Solid-state structural analysis determined the complex is 5-coordinate, with the κ^2 -acetate coordinated through both oxygen atoms (Figure 3.23).

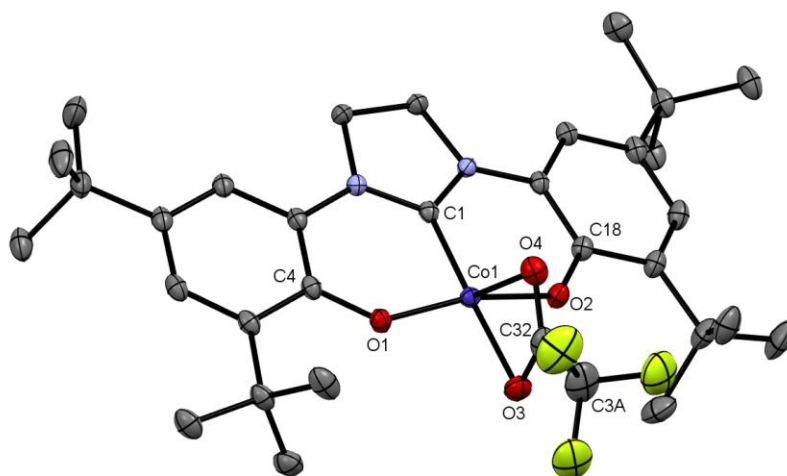


Figure 3.23 ORTEP plot of $[(^{\delta}\text{OCO})\text{Co}(\text{O}_2\text{CCF}_3)]$, **7**. Thermal ellipsoids are drawn at 50% probability. The rotational disorder of the CF_3 group and hydrogen atoms have been removed for clarity. Selected bond lengths (\AA): Co1–C1 1.8500(15), Co1–O1 1.7994(11), Co1–O2 1.7988(11), Co1–O3 2.0593(13), Co1–O4 2.2280(13), O3–C32 1.256(2), O4–C32 1.244(2), C32–C3A 1.545(5), O1–C4 1.3224(19), O2–C18 1.3248(19).

The complex **7** contains distorted square pyramidal geometry in which the O1–Co1–O2 and C3–Co1–O3 angles measure $167.12(3)^{\circ}$ and $179.94(3)^{\circ}$, respectively. The O3–Co1–O4 angle is $61.76(3)^{\circ}$. The κ^2 -acetate is bound asymmetrically, with the Co1–O4 bond length elongated vs the Co1–O3 bond at $2.2280(13)\text{ \AA}$ vs. $2.0593(13)\text{ \AA}$. The C32–O3 and C32–O4 bond lengths are comparable at $1.256(2)\text{ \AA}$ and $1.244(2)\text{ \AA}$, respectively, consistent with delocalization of the $\text{C}=\text{O}$ double bond across both oxygen

donor atoms. The ligand remains nearly planar with the O1-C4-C18-O2 torsional angle measuring $1.16(4)^\circ$. The absence of the quinoidal pattern in the phenoxides along with the single bond character of the C_{Ar}-N and C_{Ar}-O bonds support the assignment of the cobalt center as Co^{III} with a dianionic ligand.

3.4.2 Electronic Absorption Spectra of [^SOCO)Co(O₂CCF₃)]

The UV-Vis absorption spectrum of complex **7** in NMP shows absorptions at 345 nm ($20,800\text{ M}^{-1}\text{ cm}^{-1}$), 435 nm ($2680\text{ M}^{-1}\text{ cm}^{-1}$), and 690 nm ($3464\text{ M}^{-1}\text{ cm}^{-1}$) with a shoulder present at 870 nm ($1238\text{ M}^{-1}\text{ cm}^{-1}$). Excitation of the CT band at 690 nm was performed with a 16W strip of 700 nm emissive LEDs. This resulted in a decrease in intensity of the CT band at 690 nm and the shoulder at 870 nm with an increase in the absorbance band at 435 nm into two separate CT bands at 433 and 448 nm, characteristic of the UV-Vis spectrum of complex **3** in NMP. After 18 h of exposure to the LED source, the spectrum matched very well with the one electron reduced complex **3**. Interestingly, exposure to a 365 nm light source produces the same result, however the transition from **7** to **3** was complete in under 3 h. The presence of isobestic points at 403, 499, and 536 nm provide evidence that the transition occurs with no observable intermediates (Figure 3.24).

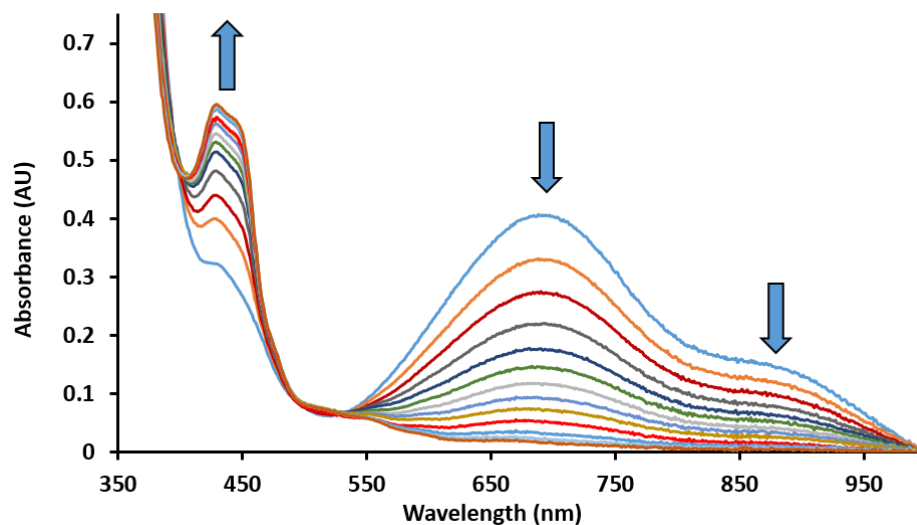


Figure 3.24. UV-Vis spectrum of **7** in NMP over 2 h with scans every 10 min from T = 0 min (blue) to T = 120 min (brown) under 365 nm light.

3.4.3 Efforts Towards Catalytic Trifluoromethylation via $[(^s\text{OCO})\text{Co}(\text{O}_2\text{CCF}_3)]$

Photolysis of **7** in neat benzene under a 365 nm light source resulted in the quantitative conversion to **3** and trifluoromethyltoluene within 4 h as evidenced by UV-Vis and ^{19}F NMR spectroscopy. This successful stoichiometric trifluoromethylation prompted us to shift our focus towards generating **7** directly from complex **3** with alternative trifluoroacetate. Two successful routes for the formation of **7** directly from complex **3** were discovered: treatment of **3** with 0.5 eq. of I_2 in the presence of NaO_2CCF_3 or treatment of **3** with neat trifluoroacetic anhydride. Unfortunately, **7** is very susceptible to over oxidation. Excess oxidant decomposes the cobalt, resulting in a bleached UV-vis spectrum containing an unidentified mix of Co-containing products. It is feasible that slow addition of the oxidant might permit turnover without over-oxidation of the complex, but further work is needed to evaluate this proposal.

3.5 Conclusions and Future Directions

This Chapter describes novel methods for the generation of a trifluoromethyl radical from photoinduced Co–C and Co–O bond cleavage using visible light sources. These represent the first reported cobalt systems capable of C–H bond trifluoromethylation. The low-lying LUMO in the five-coordinate $[(^5\text{OCO})\text{Co}(\text{CF}_3)(\text{MeCN})]$ complex permits the use of low energy light sources. The likely Co–C homolysis mechanism involves population of a Co–CF₃ σ -antibonding MO in the excited state. The free $\cdot\text{CF}_3$ can then act to functionalize non-activated aryl and heteroaryl C–H bonds in good to high yields. This chemistry is predicated on the capacity of the redox-active (OCO) ligand to deliver an electron to the Co center via LMCT, formally generating an $(\text{OCO}^\bullet)\text{Co}^{\text{II}}$ transient. In this way, the organometallic chemistry mimics the well-known action of B12 cobalamins, but in this case the ability to use inexpensive and commercially available CF₃ sources, such as trifluoroacetic anhydride, offers an avenue towards catalytic applications that are not accessible in the enzymes. Further knowledge of the reaction kinetics is required so that the delivery of the oxidant and the substrate can be appropriately timed to avoid over-oxidation.

3.6 Experimental

3.6.1 General Considerations

Unless otherwise specified, all manipulations were performed under anaerobic conditions using standard vacuum line techniques, or in an inert atmosphere glove box under purified nitrogen. Routine NMR spectra were acquired on a Varian Mercury 300 spectrometer (300.323 MHz for ^1H ; 75.5 MHz for ^{13}C). Variable temperature ^1H and ^{13}C ,

and all ^{19}F NMR spectra were acquired on a Varian Mercury 400 spectrometer (399.94 MHz for ^1H ; 101.1 MHz for ^{13}C ; 376.28 MHz for ^{19}F). All chemical shifts are reported in parts per million (ppm) relative to TMS, with the residual solvent peak serving as an internal reference. UV–visible absorption spectra were acquired using a Varian Cary 50 spectrophotometer. Unless otherwise noted, all electronic absorption spectra were recorded at ambient temperatures in 1 cm quartz cells. IR absorption spectra were obtained using a Shimadzu 8400S Fourier transform infrared spectrophotometer or a Perkin Elmer 1000 FT-IR spectrophotometer. All mass spectra were recorded in the Georgia Institute of Technology Bioanalytical Mass Spectrometry Facility. Electrospray ionization mass spectrometry (ESI-MS) was carried out with acetonitrile solutions using a Micromass Quattro LC spectrometer. Electron impact mass spectra (EI-MS) were obtained using a VG instruments model 70-SE spectrometer. Elemental analyses were performed by Atlantic Microlab, Inc., Norcross, GA. All analyses were performed in duplicate, and the reported compositions are the average of the two runs. Cyclic voltammetry experiments were carried out inside a dinitrogen-filled glove box in 0.1 M solutions of $([\text{Bu}_4\text{N}][\text{PF}_6])$ in acetonitrile unless otherwise noted. The voltammograms were recorded with either a CH Instruments 1230A or 660C potentiostat, using a 0.25 mm Pt disk working electrode, Ag wire quasi-reference electrode, and a Pt wire auxiliary electrode. All voltammograms shown were measured with a scan rate of 0.1 V/s. Reported potentials are referenced to the ferrocenium/ferrocene (Fc^+/Fc) redox couple and were determined by adding ferrocene as an internal standard at the conclusion of each electrochemical experiment.

3.6.2 Materials and Methods

Anhydrous acetonitrile (MeCN), dichloromethane, pentane, and toluene solvents for air- and moisture-sensitive manipulations were purchased from Sigma-Aldrich and further dried by passage through columns of activated alumina, degassed by at least three freeze-pump-thaw cycles, and stored under N₂ prior to use. Anhydrous diethyl ether (Drisolv), methanol (Drisolv), and benzene (Drisolv) were purchased from EMD Millipore and used as received. Dichloromethane-*d*₂ and acetonitrile-*d*₃ (Cambridge Isotope Labs) were dried over excess calcium hydride and vacuum distilled to an oven-dried sealable flask, and degassed by successive freeze-pump-thaw cycles. Tetrahydrofuran-*d*₈, chloroform-*d*₁, and methanol-*d*₁ (Cambridge Isotope Labs) were used as received. AgCF₃⁵⁷ and 2,5-Di(3,4,5-trimethoxyphenyl)pyridine⁵⁸ were prepared according to a published procedure. Silver fluoride (Strem), TMSCF₃ (Oakwood), silver trifluoroacetate (Strem) were purchased commercially and used as received.

3.6.3 Synthesis of [(^{Ph}OCO)Co(^{Ph}OCO-CF₃)] (2)

A 20 mL scintillation vial, protected from light with electrical tape, was charged with a suspension of AgF (126.9 mg; 1.00 mmol) in MeCN (8 mL). TMSCF₃ (0.22 mL; 1.50 mmol) was added in one portion and the mixture was allowed to stir in the dark at r.t. for 0.5 h. The resulting grey suspension was transferred dropwise into a separate 20mL scintillation vial containing a dark red suspension of [(^{Ph}OCO)Co(MeCN)] (624.3 mg; 1.00 mmol) in MeCN (10 mL). The reaction mixture was stirred for 1 h, then filtered through a 2mm pad of Celite and washed with acetonitrile until the green color of the washings faded. The filtrate was concentrated *in vacuo* affording a green colored

solid. A concentrated toluene solution of the material was stored at -25 °C overnight, resulting in green block crystals suitable for X-Ray diffraction (376.8 mg, 64%).

3.6.4 Synthesis of [$^{\delta}\text{OCO}$ Co(CF_3)(MeCN)] (**4**)

A 20 mL scintillation vial, protected from light with electrical tape, was charged with a suspension of AgF (126.9 mg; 1.00 mmol) in MeCN (8 mL). TMSCF_3 (0.22 mL; 1.50 mmol) was added in one portion and the mixture was allowed to stir in the dark at r.t. for 0.5 h. The resulting grey suspension was transferred dropwise into a separate 20mL scintillation vial containing a dark red suspension of [$^{\delta}\text{OCO}$ Co(THF)] (607.8 mg; 1.00 mmol) in MeCN (10 mL). The reaction mixture was stirred for 1 h, then filtered through a 2mm pad of Celite and washed with acetonitrile until the green color of the washings faded. The filtrate was concentrated *in vacuo* affording a burgundy colored solid. A concentrated toluene solution of the material was stored at -25 °C overnight, resulting in red plate crystals suitable for X-Ray diffraction (626.3 mg, 97%). UV-Vis (Et_2O) λ_{max} , nm (ϵ , L/mol*cm): 404 (8,390), 462 (sh, 4010), 787 (2,790). Anal. Calc. for $\text{C}_{36}\text{H}_{50}\text{CoF}_3\text{N}_4\text{O}_2$: C, 63.25; H, 7.34; N, 6.51. Found: C, 63.50; H, 7.28; N, 6.34. HR-ESI-MS (m/z): 604.2672. ^1H NMR (400 MHz, CD_2Cl_2) δ : 6.91 (d, $J = 1.9$ Hz, 2H), 6.74 (d, $J = 1.9$ Hz, 2H), 4.65 – 4.40 (m, 4H), 1.30 (s, 36 H). ^{19}F (376 MHz, CD_2Cl_2) δ : -14.12 (br s, 3F).

3.6.5 Synthesis of [$^{\delta}\text{OCO}$ Co(CF_3)(OH_2) $_2$] (**4⁺**)

A solution of **4** (290.6 mg; 0.45 mmol) in THF (8 mL) was treated dropwise with a solution of AgOTf (115.6 mg; 0.45 mmol) in THF (4 mL). The reaction mixture was stirred for 1 h, then filtered through a 2mm pad of Celite and washed with THF until the

green color of the washings was no longer observed. The filtrate was concentrated *in vacuo* affording a dark green solid. The air stable solid was purified with silica gel column chromatography using CH₂Cl₂/MeOH (10:1) affording a dark green solid. The complex was crystallized in air from layering hexamethyldisiloxane on a concentrated THF solution of the complex, resulting in green block crystals suitable for X-ray diffraction (312.7 mg, 88%). UV-Vis (NMP) λ_{max} , nm (ϵ , L/mol*cm) 440 (undetermined), 466 (undetermined), 526 (undetermined), 915 (undetermined).

3.6.6 Synthesis of [$^{\delta}\text{OCO}$ Co(CF₃)(MeCN)₂] (**5**)

A concentrated acetonitrile solution of [$^{\delta}\text{OCO}$ Co(CF₃)(MeCN)] was stored at -25 °C overnight, resulting in dark green plate crystals suitable for X-ray diffraction. UV-Vis (MeCN) λ_{max} , nm (ϵ , L/mol*cm) 391 (10,290), 471 (sh, 1,500), 621 (600). ¹H NMR (400 MHz, CD₃CN) δ : 6.84 (d, J = 2.2 Hz, 2H), 6.77 (d, J = 2.2 Hz, 2H), 4.46 (s, 4H), 1.29 (s, 18 H), 1.28 (s, 18 H). ¹⁹F (376 MHz, CD₃CN) δ : -24.68 (br s, 3F).

Note: Due to the lability of the acetonitrile ligand in the 6-coordinate geometry in the solid state, satisfactory elemental analysis was not achieved.

3.6.7 Synthesis of [$^{\delta}\text{OCO}$ Co(CF₃)(2-*phpy*)] (**6**)

An ethereal solution of complex **4** was treated with 1.5 equivalents of 2-phenylpyridine. The solution was evaporated to near dryness (the b.p. of 2-phenylpyridine is 268 – 270 °C), and triturated with pentane. The solid material was filtered and dissolved in a minimal amount of benzene and layered with pentane, producing X-ray quality crystals of **6** in quantitative yield.

3.6.8 Synthesis of $[(^{\delta}\text{OCO})\text{Co}(\text{O}_2\text{CCF}_3)]$ (**7**)

A solution of $[(^{\delta}\text{OCO})\text{Co}(\text{THF})]$ (607.8 mg; 1.00 mmol) in CH_2Cl_2 (14 mL) was treated dropwise with a solution of AgO_2CCF_3 (220.9 mg; 1.00 mmol) in CH_2Cl_2 (5 mL). The reaction mixture was stirred for 1 h, then filtered through a 2mm pad of Celite and washed with THF until the green color of the washings was no longer observed. The filtrate was concentrated *in vacuo* until a precipitate just began to form. A few drops of benzene was added, creating a homogenous solution. The solution was then stored at -25 °C overnight, resulting in green block crystals suitable for X-ray diffraction (570.5 mg, 88%). UV-Vis (NMP) λ_{max} , nm (ϵ , L/mol*cm) 345 (20800), 435 (2680), 690 (3464), 870 nm (sh, 1238). Anal. Calc. for $\text{C}_{33}\text{H}_{44}\text{CoF}_3\text{N}_2\text{O}_4 \cdot (\text{CH}_2\text{Cl}_2)_{0.33} \cdot (\text{C}_6\text{H}_6)_{0.17}$: C, 59.77; H, 6.67; N, 4.06. Found: C, 59.81.41; H, 6.55; N, 4.11%. HR-ESI-MS (m/z): 648.2569.

3.6.9 General Procedure for C-H Trifluoromethylation of (Hetero)Aryls

A quartz J-Young NMR tube was charged with a 0.2M NMP solution of complex **4** and 20 equivalents of the corresponding (hetero)arene. The NMR tube was placed approx. 3 inches from a GE Helical 6G49 26W CFL for 16 h. At the completion of the reaction, an appropriate internal standard was added to determine yield and an external standard of CFCl_3 as a sealed capillary insert was added to reference the spectrum. The NMR spectra matched those previously reported.⁵¹⁻⁵²

3.7 X-ray Crystallography

3.7.1 General Considerations

Unless otherwise noted, X-ray diffraction data were collected using a Bruker APEX-II CCD diffractometer equipped with an Oxford Cryosystems low-temperature apparatus. Unit cell indexing was performed by using the **APEX2** (Bruker) software. Data were measured with MoK α radiation (fine-focus sealed tube, 45 kV, 35 mA). The total number of runs and images was based on the strategy calculation from the program **APEX2** (Bruker). Unit cell indexing was performed by using the **APEX2** (Bruker) software and refined using **SAINT** (Bruker, V8.34A, 2013). Data reduction, scaling and absorption corrections were performed using **SAINT** (Bruker, V8.34A, 2013) and **SADABS-2014/5** (Bruker, 2014) was used for absorption correction. The $\lambda/2$ correction factor is 0.00150. The software also corrects for Lorentz polarization. The crystal structures were refined by Least Squares using version 2014/7 of **XL**.⁵⁹ All non-hydrogen atoms were refined anisotropically. Hydrogen atom positions were calculated geometrically and refined using the riding model.

3.7.2 $[(^{Ph}OCO)Co(^{Ph}OCO-CF_3)]$ (**2**)

A dark green, block-shaped crystal with dimensions 0.618×0.344×0.314 mm was mounted on a loop with paratone oil. Data were collected at T = 100(2) °K. The maximum resolution achieved was $\Theta = 28.705^\circ$.

Unit cell indexing was performed and refined based on 16568 reflections, 43% of the observed reflections. The ratio of minimum to maximum transmission is 0.7534.

The final completeness is 98.9% out to 28.705° in Θ . The absorption coefficient (μ) of this material is 0.324 mm^{-1} and the minimum and maximum transmissions are 0.562 and 0.746.

The structure was solved with ShelXT in the space group $P2_1/n$ by using the Direct Methods solution and by using Olex2 as the graphical interface.⁶⁰⁻⁶¹

3.7.3 $[(^S\text{OCO})\text{Co}(\text{CF}_3)(\text{MeCN})]$ (**4**)

An orange, block-shaped crystal with dimensions $0.51 \times 0.39 \times 0.29 \text{ mm}$ was mounted on a loop with paratone oil. Data were collected at $T = 100(2)^\circ \text{K}$. Data were measured using ω scans 1° per frame. The maximum resolution achieved was $\Theta = 29.678^\circ$.

Unit cell indexing was performed and refined based on 9923 reflections, 14% of the observed reflections. $wR_2(\text{int})$ was 0.1295 before and 0.0529 after correction. The ratio of minimum to maximum transmission is 0.9213. The final completeness is 99.9% out to 29.678° in Θ . The absorption coefficient (μ) of this material is 0.448 mm^{-1} and the minimum and maximum transmissions are 0.6872 and 0.7459.

The structure was solved with ShelXT in the space group $C2/c$ (# 15) by using the Direct Methods solution and by using Olex2 as the graphical interface.⁶⁰⁻⁶¹

3.7.4 $[(^S\text{OCO})\text{Co}(\text{CF}_3)(\text{OH}_2)_2][\text{OTf}]$ (**4**⁺)

A dark green, block-shaped crystal with dimensions $0.458 \times 0.424 \times 0.222 \text{ mm}$ was mounted on a loop with paratone oil. Data were collected at $T = 100(2)^\circ \text{K}$. Data were

measured using ω scans 1° per frame. The maximum resolution achieved was $\Theta = 33.14^\circ$.

Unit cell indexing was performed and refined based on 51410 reflections, 30% of the observed reflections. $wR_2(\text{int})$ was 0.1207 before and 0.0529 after correction. The ratio of minimum to maximum transmission is 0.9213. The final completeness is 95% out to 33.14° in Θ . The absorption coefficient (μ) of this material is 0.530 mm^{-1} and the minimum and maximum transmissions are 0.6872 and 0.7459.

The structure was solved with ShelXT in the space group P1 (# 2) by using the Direct Methods solution and by using Olex2 as the graphical interface.⁶⁰⁻⁶¹

3.7.5 $[(^s\text{OCO})\text{Co}(\text{CF}_3)(\text{MeCN})_2]$ (5)

A dark green, block-shaped crystal with dimensions $0.51 \times 0.39 \times 0.29 \text{ mm}$ was mounted on a loop with paratone oil. Data were collected at $T = 100(2)^\circ \text{K}$. Data were measured using ω scans 1° per frame. The maximum resolution achieved was $\Theta = 29.678^\circ$.

Unit cell indexing was performed and refined based on 9923 reflections, 14% of the observed reflections. $wR_2(\text{int})$ was 0.1295 before and 0.0529 after correction. The ratio of minimum to maximum transmission is 0.9213. The final completeness is 99.9% out to 29.678° in Θ . The absorption coefficient (μ) of this material is 0.448 mm^{-1} and the minimum and maximum transmissions are 0.6872 and 0.7459.

The structure was solved with ShelXT in the space group $C2/c$ (# 15) by using the Direct Methods solution and by using Olex2 as the graphical interface.⁶⁰⁻⁶¹

3.7.6 $[(^SOCO)Co(CF_3)(2-ppy)]$ (6)

A green, block-shaped crystal with dimensions 0.423×0.348×0.083 mm was mounted on a loop with paratone oil. Data were collected at $T = 100(2)$ °K. The maximum resolution achieved was $\Theta = 28.705^\circ$.

Unit cell indexing was performed and refined based on 60338 reflections, 33% of the observed reflections. The ratio of minimum to maximum transmission is 0.7534. The final completeness is 95% out to 28.282° in Θ . The absorption coefficient (μ) of this material is 0.467 mm^{-1} and the minimum and maximum transmissions are 0.562 and 0.746.

The structure was solved with ShelXT in the space group $P2_1/n$ by using the Direct Methods solution and by using Olex2 as the graphical interface.⁶⁰⁻⁶¹

The value of Z' is 2. This means that there are two independent molecules in the asymmetric unit.

3.7.7 $[(^{Ph}OCO)Co(^{Ph}OCO-CF_3)]$ (7)

A dark green, block-shaped crystal with dimensions 0.618×0.344×0.314 mm was mounted on a loop with paratone oil. Data were collected at $T = 100(2)$ °K. The maximum resolution achieved was $\Theta = 28.705^\circ$.

Unit cell indexing was performed and refined based on 16568 reflections, 43% of the observed reflections. The ratio of minimum to maximum transmission is 0.7534. The final completeness is 98.9% out to 28.705° in Θ . The absorption coefficient (μ) of

this material is 0.324 mm^{-1} and the minimum and maximum transmissions are 0.562 and 0.746.

The structure was solved with ShelXT in the space group $P2_1/n$ by using the Direct Methods solution and by using Olex2 as the graphical interface.⁶⁰⁻⁶¹

3.8 Computational Methods

TD-DFT (UV-Vis) calculations were performed on the full system with implicit solvation (cpcm, fepstyle cosmo, epsilon = 7.25, refract = 1.407) at the B3lyp, def2-TZVP, ZORA level of theory. MO pictures were generated using IboView.⁶²⁻⁶³

3.9 References

1. Wang, S.-M.; Han, J.-B.; Zhang, C.-P.; Qin, H.-L.; Xiao, J.-C., An Overview of Reductive Trifluoromethylation Reactions Using Electrophilic $^+\text{CF}_3$ Reagents. *Tetrahedron* **2015**, 71 (42), 7949-7976.
2. Hagmann, W. K., The Many Roles for Fluorine in Medicinal Chemistry. *Journal of Medicinal Chemistry* **2008**, 51 (15), 4359-4369.
3. Liu, T.; Shen, Q., Progress in Copper-Mediated Formation of Trifluoromethylated Arenes. *European Journal of Organic Chemistry* **2012**, 6679-6687.
4. Müller, K.; Faeh, C.; Diederich, F., Fluorine in Pharmaceuticals: Looking Beyond Intuition. *Science* **2007**, 317, 1881-1886.
5. Purser, S.; Moore, P. R.; Swallow, S.; Gouverneur, V., Fluorine in medicinal chemistry. *Chemical Society Reviews* **2008**, 37 (2), 320-330.
6. Schlosser, M., CF_3 -Bearing Aromatic and Heterocyclic Building Blocks. *Angewandte Chemie International Edition* **2006**, 45 (33), 5432-5446.
7. Wang, J.; Sánchez-Roselló, M.; Aceña, J. L.; del Pozo, C.; Sorochinsky, A. E.; Fustero, S.; Soloshonok, V. A.; Liu, H., Fluorine in Pharmaceutical Industry: Fluorine-Containing Drugs Introduced to the Market in the Last Decade (2001–2011). *Chemical Reviews* **2014**, 114 (4), 2432-2506.
8. Zhu, W.; Wang, J.; Wang, S.; Gu, Z.; Aceña, J. L.; Izawa, K.; Liu, H.; Soloshonok, V. A., Recent Advances in the Trifluoromethylation Methodology and New CF_3 -containing Drugs. *Journal of Fluorine Chemistry* **2014**, 167, 37-54.
9. Besset, T.; Schneider, C.; Cahard, D., Tamed Arene and Heteroarene Trifluoromethylation. *Angewandte Chemie International Edition* **2012**, 51 (21), 5048-5050.
10. Furuya, T.; Kamlet, A. S.; Ritter, T., Catalysis for Fluorination and Trifluoromethylation. *Nature* **2011**, 473, 470-477.
11. Liang, T.; Neumann, C. N.; Ritter, T., Introduction of Fluorine and Fluorine-Containing Functional Groups. *Angewandte Chemie International Edition* **2013**, 52 (32), 8214-8264.
12. Roy, S.; Gregg, B. T.; Gribble, G. W.; Le, V.-D.; Roy, S., Trifluoromethylation of Aryl and Heteroaryl Halides. *Tetrahedron* **2011**, 67 (12), 2161-2195.
13. Tomashenko, O. A.; Grushin, V. V., Aromatic Trifluoromethylation with Metal Complexes. *Chemical Reviews* **2011**, 111 (8), 4475-4521.

14. Langlois, B. R.; Billard, T.; Roussel, S., Nucleophilic Trifluoromethylation: Some Recent Reagents and Their Stereoselective Aspects. *Journal of Fluorine Chemistry* **2005**, *126* (2), 173-179.
15. Liu, X.; Xu, C.; Wang, M.; Liu, Q., Trifluoromethyltrimethylsilane: Nucleophilic Trifluoromethylation and Beyond. *Chemical Reviews* **2015**, *115* (2), 683-730.
16. Prakash, G. K. S.; Yudin, A. K., Perfluoroalkylation with Organosilicon Reagents. *Chemical Reviews* **1997**, *97* (3), 757-786.
17. Charpentier, J.; Früh, N.; Togni, A., Electrophilic Trifluoromethylation by Use of Hypervalent Iodine Reagents. *Chemical Reviews* **2015**, *115* (2), 650-682.
18. Umemoto, T., Electrophilic Perfluoroalkylating Agents. *Chemical Reviews* **1996**, *96* (5), 1757-1778.
19. Studer, A., A “Renaissance” in Radical Trifluoromethylation. *Angewandte Chemie International Edition* **2012**, *51* (36), 8950-8958.
20. Gonda, Z.; Kovács, S.; Wéber, C.; Gáti, T.; Mészáros, A.; Kotschy, A.; Novák, Z., Efficient Copper-Catalyzed Trifluoromethylation of Aromatic and Heteroaromatic Iodides: The Beneficial Anchoring Effect of Borates. *Organic Letters* **2014**, *16* (16), 4268-4271.
21. Li, X.; Zhao, J.; Zhang, L.; Hu, M.; Wang, L.; Hu, J., Copper-Mediated Trifluoromethylation Using Phenyl Trifluoromethyl Sulfoxide. *Organic Letters* **2015**, *17* (2), 298-301.
22. Lishchynskiy, A.; Novikov, M. A.; Martin, E.; Escudero-Adán, E. C.; Novák, P.; Grushin, V. V., Trifluoromethylation of Aryl and Heteroaryl Halides with Fluoroform-Derived CuCF₃: Scope, Limitations, and Mechanistic Features. *The Journal of Organic Chemistry* **2013**, *78* (22), 11126-11146.
23. Liu, T.; Shen, Q., Copper-Catalyzed Trifluoromethylation of Aryl and Vinyl Boronic Acids with An Electrophilic Trifluoromethylating Reagent. *Organic Letters* **2011**, *13* (9), 2342-2345.
24. Liu, Y.; Shao, X.; Zhang, P.; Lu, L.; Shen, Q., Trifluoromethyl-Substituted Sulfonium Ylide: Rh-Catalyzed Carbenoid Addition to Trifluoromethylthioether. *Organic Letters* **2015**, *17* (11), 2752-2755.
25. Ye, Y.; Künzi, S. A.; Sanford, M. S., Practical Method for the Cu-Mediated Trifluoromethylation of Arylboronic Acids with CF₃ Radicals Derived from NaSO₂CF₃ and *tert*-Butyl Hydroperoxide (TBHP). *Organic Letters* **2012**, *14* (19), 4979-4981.
26. Ye, Y.; Sanford, M. S., Merging Visible-Light Photocatalysis and Transition-Metal Catalysis in the Copper-Catalyzed Trifluoromethylation of Boronic Acids with CF₃I. *Journal of the American Chemical Society* **2012**, *134* (22), 9034-9037.

27. Liu, H.; Gu, Z.; Jiang, X., Direct Trifluoromethylation of the C–H Bond. *Advanced Synthesis & Catalysis* **2013**, *355* (4), 617-626.
28. Alonso, C.; Martínez de Marigorta, E.; Rubiales, G.; Palacios, F., Carbon Trifluoromethylation Reactions of Hydrocarbon Derivatives and Heteroarenes. *Chemical Reviews* **2015**, *115* (4), 1847-1935.
29. Jana, S.; Ashokan, A.; Kumar, S.; Verma, A.; Kumar, S., Copper-catalyzed Trifluoromethylation of Alkenes: Synthesis of Trifluoromethylated Benzoxazines. *Organic & Biomolecular Chemistry* **2015**, *13* (31), 8411-8415.
30. Shang, M.; Sun, S.-Z.; Wang, H.-L.; Laforteza, B. N.; Dai, H.-X.; Yu, J.-Q., Exceedingly Fast Copper(II)-Promoted ortho C–H Trifluoromethylation of Arenes using TMSCF₃. *Angewandte Chemie International Edition* **2014**, *53* (39), 10439-10442.
31. Wang, X.; Ye, Y.; Ji, G.; Xu, Y.; Zhang, S.; Feng, J.; Zhang, Y.; Wang, J., Copper-Catalyzed Direct C–H Trifluoromethylation of Quinones. *Organic Letters* **2013**, *15* (14), 3730-3733.
32. Xu, J.; Fu, Y.; Luo, D.-F.; Jiang, Y.-Y.; Xiao, B.; Liu, Z.-J.; Gong, T.-J.; Liu, L., Copper-Catalyzed Trifluoromethylation of Terminal Alkenes through Allylic C–H Bond Activation. *Journal of the American Chemical Society* **2011**, *133* (39), 15300-15303.
33. Zhu, C.-L.; Zhang, Y.-Q.; Yuan, Y.-A.; Xu, H., Copper-Catalyzed Aerobic C–H Trifluoromethylation of Phenanthrolines. *Synlett* **2015**, *26* (03), 345-349.
34. Taw, F. L.; Clark, A. E.; Mueller, A. H.; Janicke, M. T.; Cantat, T.; Scott, B. L.; Hay, P. J.; Hughes, R. P.; Kiplinger, J. L., Titanium(IV) Trifluoromethyl Complexes: New Perspectives on Bonding from Organometallic Fluorocarbon Chemistry. *Organometallics* **2012**, *31* (4), 1484-1499.
35. Huang, D.; Caulton, K. G., New Entries to and New Reactions of Fluorocarbon Ligands. *Journal of the American Chemical Society* **1997**, *119* (13), 3185-3186.
36. Huang, D.; Koren, P. R.; Folting, K.; Davidson, E. R.; Caulton, K. G., Facile and Reversible Cleavage of C–F Bonds. Contrasting Thermodynamic Selectivity for RuCF₂H vs FOsCFH. *Journal of the American Chemical Society* **2000**, *122* (37), 8916-8931.
37. Hughes, R. P., Organo-Transition Metal Compounds Containing Perfluorinated Ligands. *Advances in Organometallic Chemistry* **1990**, *31*, 183-267.
38. Morrison, J. A., Trifluoromethyl-Containing Transition Metal Complexes. *Advances in Organometallic Chemistry* **1993**, *35*, 211-239.
39. Banerjee, R., The Yin-Yang of cobalamin biochemistry. *Chemistry & Biology* **1997**, *4* (3), 175-186.

40. Banerjee, R., Radical Carbon Skeleton Rearrangements: Catalysis by Coenzyme B12-Dependent Mutases. *Chemical Reviews* **2003**, *103* (6), 2083-2094.
41. Toraya, T., Radical Catalysis in Coenzyme B12-Dependent Isomerization (Eliminating) Reactions. *Chemical Reviews* **2003**, *103* (6), 2095-2128.
42. Brown, K. L., Chemistry and Enzymology of Vitamin B12. *Chemical Reviews* **2005**, *105* (6), 2075-2150.
43. Johnston, R. C.; Zhou, J.; Smith, J. C.; Parks, J. M., Toward Quantitatively Accurate Calculation of the Redox-Associated Acid-Base and Ligand Binding Equilibria of Aquacobalamin. *The Journal of Physical Chemistry B* **2016**, *120* (30), 7307-7318.
44. Qu, Z.-w.; Hansen, A.; Grimme, S., Co-C Bond Dissociation Energies in Cobalamin Derivatives and Dispersion Effects: Anomaly or Just Challenging? *Journal of Chemical Theory and Computation* **2015**, *11* (3), 1037-1045.
45. Yamazaki, N.; Hohokabe, Y., The synthesis of a cobaloxime with a polymeric ligand as a cobalamin model compound. *Chemical Communications (London)* **1968**, (15), 829-830.
46. Martin, B. D.; Finke, R. G., Methylcobalamin's Full- vs. Half-Strength Cobalt-Carbon sigma Bonds and Bond Dissociation Enthalpies: $A > 10^{15}$ Co-CH₃ Homolysis Rate Enhancement following One-Antibonding-Electron Reduction of Methylcobalamin. *Journal of the American Chemical Society* **1992**, *114* (2), 585-592.
47. Hendrickson, D. N.; Pierpont, C. G., Valence Tautomeric Transition Metal Complexes. In *Spin Crossover in Transition Metal Compounds II*, Springer Berlin Heidelberg: Berlin, Heidelberg, 2004; pp 63-95.
48. Zou, X.; Brown, K. L., The Crystal Structure of Trifluoromethylcobalamin, A Coenzyme B12 Analog. *Inorganica Chimica Acta* **1998**, *267* (2), 305-308.
49. Chaudhuri, P.; Wieghardt, K., Phenoxyl Radical Complexes. In *Progress in Inorganic Chemistry*, John Wiley & Sons, Inc.: 2002; pp 151-216.
50. Nagib, D. A.; MacMillan, D. W. C., Trifluoromethylation of Arenes and Heteroarenes by Means of Photoredox Catalysis. *Nature* **2011**, *480*, 224-228.
51. Beatty, J. W.; Douglas, J. J.; Cole, K. P.; Stephenson, C. R. J., A scalable and operationally simple radical trifluoromethylation. *Nature Communications* **2015**, *6*, 7919.
52. Thoi, V. S.; Sun, Y.; Long, J. R.; Chang, C. J., Complexes of Earth-abundant Metals for Catalytic Electrochemical Hydrogen Generation Under Aqueous Conditions. *Chemical Society Reviews* **2013**, *42* (6), 2388-2400.

53. McCrory, C. C. L.; Uyeda, C.; Peters, J. C., Electrocatalytic Hydrogen Evolution in Acidic Water with Molecular Cobalt Tetraazamacrocycles. *Journal of the American Chemical Society* **2012**, *134* (6), 3164-3170.
54. Dempsey, J. L.; Brunschwig, B. S.; Winkler, J. R.; Gray, H. B., Hydrogen Evolution Catalyzed by Cobaloximes. *Accounts of Chemical Research* **2009**, *42* (12), 1995-2004.
55. Du, P.; Schneider, J.; Luo, G.; Brennessel, W. W.; Eisenberg, R., Visible Light-Driven Hydrogen Production from Aqueous Protons Catalyzed by Molecular Cobaloxime Catalysts. *Inorganic Chemistry* **2009**, *48* (11), 4952-4962.
56. Ji, Y.; Brueckl, T.; Baxter, R. D.; Fujiwara, Y.; Seiple, I. B.; Su, S.; Blackmond, D. G.; Baran, P. S., Innate C–H Trifluoromethylation of Heterocycles. *Proceedings of the National Academy of Sciences* **2011**, *108* (35), 14411-14415.
57. Tyrra, W. E., Oxidative perfluoroorganylation methods in group 12–16 chemistry: The reactions of haloperfluoroorganics and In and InBr, a convenient new route to AgRf (Rf = CF₃, C₆F₅) and reactions of AgRf with group 12–16 elements. *Journal of Fluorine Chemistry* **2001**, *112* (1), 149-152.
58. Santoro, A.; Prokhorov, A. M.; Kozhevnikov, V. N.; Whitwood, A. C.; Donnio, B.; Williams, J. A. G.; Bruce, D. W., Emissive Metallomesogens Based on 2-Phenylpyridine Complexes of Iridium(III). *Journal of the American Chemical Society* **2011**, *133* (14), 5248-5251.
59. Sheldrick, G., A short history of SHELX. *Acta Crystallographica Section A* **2008**, *64* (1), 112-122.
60. Dolomanov, O. V.; Bourhis, L. J.; Gildea, R. J.; Howard, J. A. K.; Puschmann, H., OLEX2: a complete structure solution, refinement and analysis program. *Journal of Applied Crystallography* **2009**, *42* (2), 339-341.
61. Sheldrick, G., SHELXT - Integrated space-group and crystal-structure determination. *Acta Crystallographica Section A* **2015**, *71* (1), 3-8.
62. Knizia, G., Intrinsic Atomic Orbitals: An Unbiased Bridge between Quantum Theory and Chemical Concepts. *Journal of Chemical Theory and Computation* **2013**, *9* (11), 4834-4843.
63. Knizia, G.; Klein, J. E. M. N., Electron Flow in Reaction Mechanisms—Revealed from First Principles. *Angewandte Chemie International Edition* **2015**, *54* (18), 5518-5522.

CHAPTER 4. METAL-LIGAND COOPERATIVITY SUPPORTS

CF₃ RADICAL GENERATION FROM ELECTROPHILIC CF₃ SOURCES

4.1 Note on Collaboration

Current graduate student of the Soper lab, Mr. Chris Kuehner, has worked to provide yields for the substrates listed in Table 4.1.

4.2 Introduction

Chapter 3 discussed the pharmacological effects of the trifluoromethyl group and the desire to incorporate such functionality into organic substrates for new pharmaceutical and agrochemical development. Such functionality is most efficiently introduced by direct trifluoromethylation, either involving (1) reactions of nucleophilic CF₃ sources with electrophiles,¹ (2) reacting sources of electrophilic CF₃ reagents with nucleophiles,² or by (3) treating radical acceptors with [•]CF₃ precursors.³ Oxidative- and reductive-trifluoromethylation pathways, in which nucleophilic CF₃ sources react with nucleophiles and electrophilic CF₃ reagents react with electrophiles, respectively, have also been described.⁴⁻⁷ The latter pathway is the more established of the two and is broadly defined as an avenue in which '[substrates]' are trifluoromethylated in the presence of reductants, wherein the reactions start with the reduction of the CF₃ source.'⁸

It was established in Chapter 3 that treating [(^δOCO)Co(MeCN)], complex **1**, with a [•]CF₃ source resulted in single-electron oxidized complexes [(^δOCO)Co(CF₃)(MeCN)_{*n*}]

($n = 1$ or 2). In non-coordinating solvents, the complex $[(^{\delta}\text{OCO})\text{Co}(\text{CF}_3)(\text{MeCN})]$, **2**, undergoes photolytic Co–CF₃ bond cleavage to deliver a $^{\bullet}\text{CF}_3$ to an unactivated aryl C–H bond. Although stoichiometric trifluoromethylation reactions with **2** have been successful, efforts towards catalytic applications have not yet been fruitful.

Over the last decade, there have been an increasing number of reports which utilize transition metals as catalytic reductants of electrophilic CF₃ reagents, thereby generating $^{\bullet}\text{CF}_3$ without forming M–CF₃ bonds.⁸⁻¹¹ Such reactions make use of the vast family of $^+\text{CF}_3$ sources currently available (Figure 4.1).¹²⁻¹⁸ A number of these reagents are commercially available and are often preferred over less expensive trifluoromethyl sources, including both ICF₃ and HCF₃, due to their ease of handling and long shelf-life.¹⁹

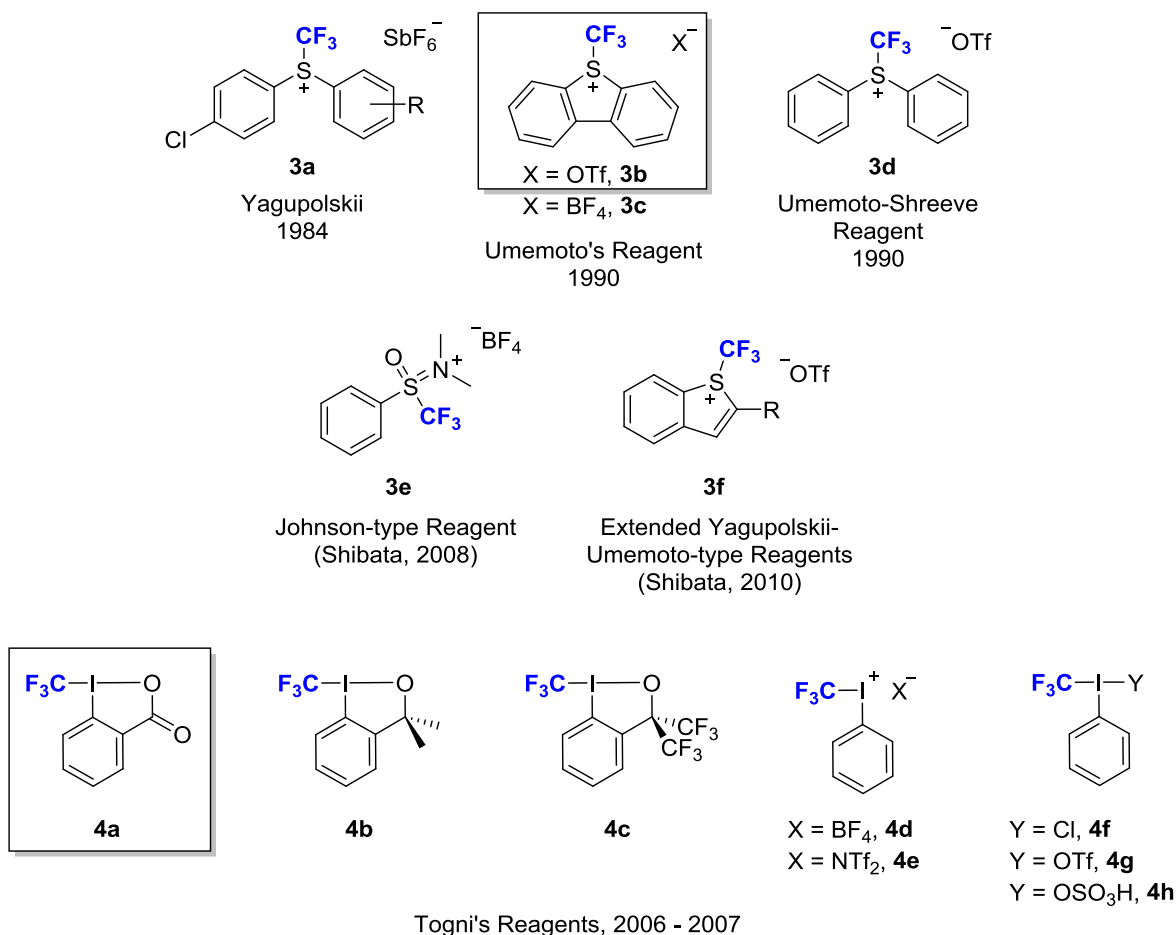
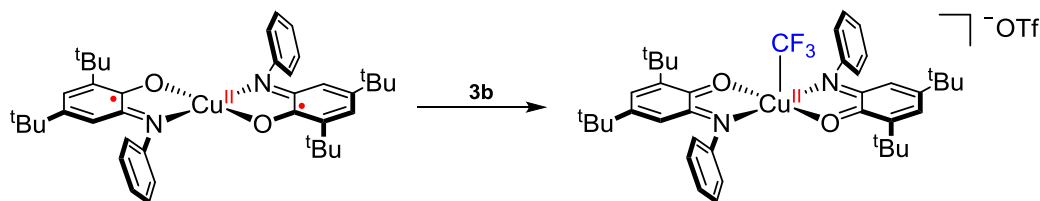


Figure 4.1. Commonly used electrophilic trifluoromethylation reagents.¹²⁻¹⁸ The two substrates in squares are the commercially available Umemoto reagent (3b**) and Togni II reagent (**4a**) utilized in this Chapter.**

Recently, Fensterbank, Murr and coworkers reported a redox-active bis(amidophenolate) ligated copper (II) complex capable of undergoing a net two-electron oxidative addition of the Umemoto reagent (**3b** in Figure 4.1), resulting in a product with an outer-sphere triflate and a Cu–CF₃ bond (Scheme 4.1).²⁰ This complex was incapable of transferring the CF₃ ligand to any organic acceptor other than one of the coordinated amidophenolate ligands. However, in a follow-up report, the reduced complex was described as catalytically competent for C–H trifluoromethylation. It was

proposed to generate an outer-sphere $\cdot\text{CF}_3$ via single electron transfer to **3b** and **4a** in the presence of a radical acceptor.¹⁰ This evidence supports the idea that the net two-electron process highlighted in Scheme 4.1 is not concerted and that the formation of an inner-sphere Cu–CF₃ bond is not a requirement for catalysis. Since the observed oxidation potential of that Cu system is >60 mV anodically shifted vs. complex **1**,²¹ I proposed that **1** could act analogously as a reductant towards commercially available electrophilic CF₃ sources, thus broadening the applications of this Cu system in the area of C–H bond trifluoromethylation.

Scheme 4.1. Reaction of a bis(amidophenolate) copper complex with 3b.^{10, 20}



4.3 Results and Discussion

4.3.1 Radical Trapping of Electrophilic CF₃ Reagents with TEMPO

Complex **1** was treated with a stoichiometric amount of a commercially available $^+\text{CF}_3$ source, either 5-(trifluoromethyl)dibenzothiophenium trifluoro-methanesulfonate (Umemoto reagent, **3b** in Figure 4.1) or 1-trifluoromethyl-1,2-benziodoxol-3(1H)-one (Togni II reagent, **4a** in Figure 4.1), in the presence of excess radical trap TEMPO (10 equivalents). After 18h in CH₂Cl₂, the reactions were evaluated by ¹⁹F NMR for the formation of TEMPO–CF₃ (Figures 4.2 and 4.3). The reaction with **3b** resulted in quantitative incorporation of the CF₃ into the TEMPO–CF₃ adduct while the reaction with

4a produced TEMPO-CF₃ in a 79% yield along with two additional fluorine containing products ($\delta = -21.6$ and -57.3 ppm vs. CFCl₃). The signal at -57.3 ppm was identified as the trifluoromethyl ester, **5** (shown in Figure 4.3), resulting from O-trifluoromethylation of reagent **4a** itself. This known side product results from a Lewis acid promoted reaction with **4a**.²²

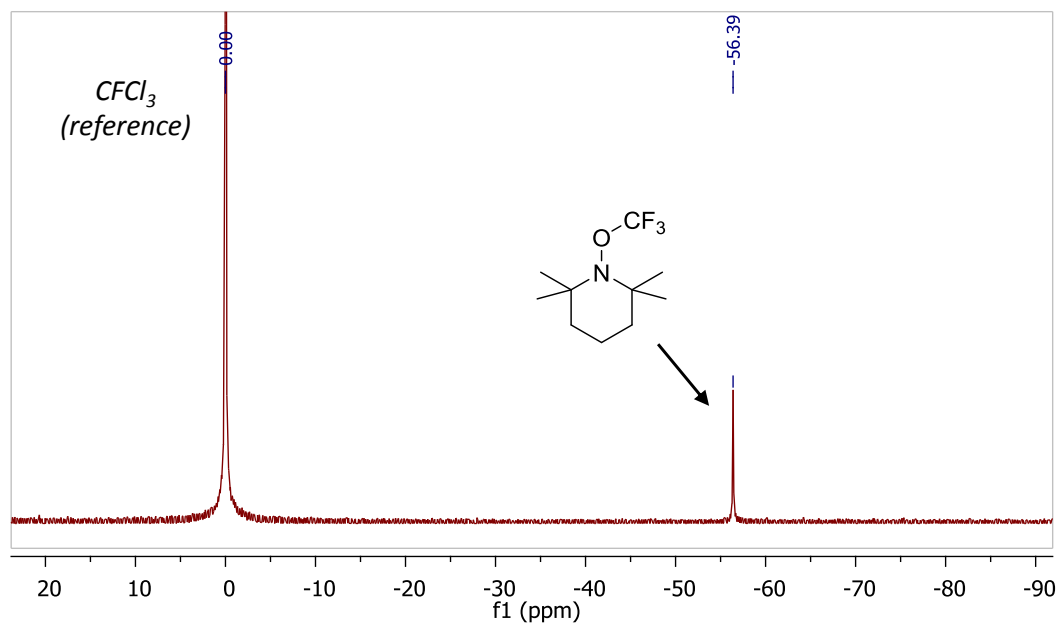


Figure 4.2. Crude ^{19}F NMR of the reaction between 1 and the Umemoto Reagent, 3b, in the presence of TEMPO.

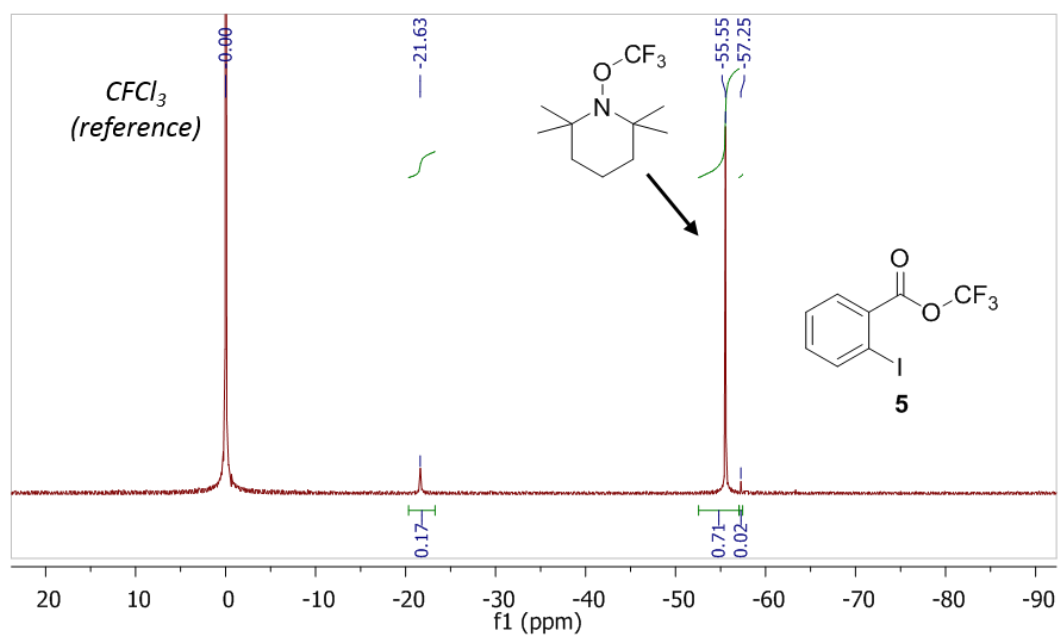
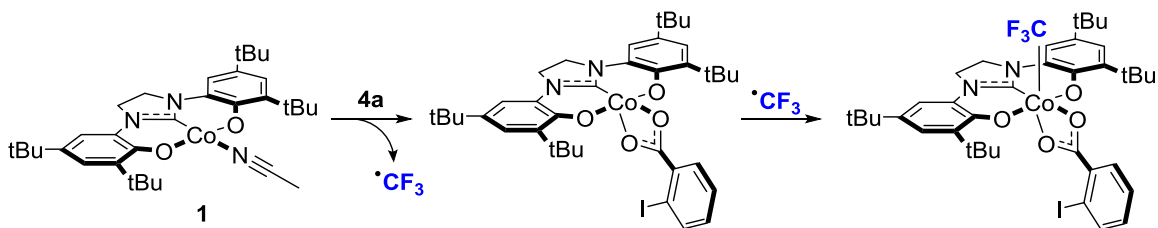


Figure 4.3. Crude ^{19}F NMR of the reaction between 1 and the Togni II Reagent, 4a, in the presence of TEMPO.

The material which produces the signal at δ 21.6 ppm falls within the range of the Co–CF₃ complexes reported in Chapter 3. It likely corresponds to a 6-coordinate complex because its upfield shift from the signal observed in the 5-coordinate species, **2** (δ 12.49 ppm vs. CFCl₃), is more typical of the formulation [(δ OCO)Co(CF₃)(L)₂], where L = MeCN, pyridine, or THF. The identity of the sixth ligand was not identified, however it is reasonable to invoke the formation of a κ^2 -carboxylate species, analogous to the trifluoroacetate complex [(δ OCO)Co(O₂CCF₃)] described in Chapter 3.

A plausible mechanism for the formation of a carboxylate complex is shown in Scheme 4.2. Single electron transfer (SET) to **4a** generates a radical species which subsequently produces \cdot CF₃ and an anionic carboxylate that can bind to the singly oxidized Co center. The equivalent of \cdot CF₃ may go on to oxidize the complex once more to a formal Co^{IV} species with an inner-sphere Co–CF₃ bond. Although this is a net two-electron process, the mechanism likely proceeds via two sequential single-electron processes.^{10, 20} Further evidence supporting the formation of this complex is discussed below.

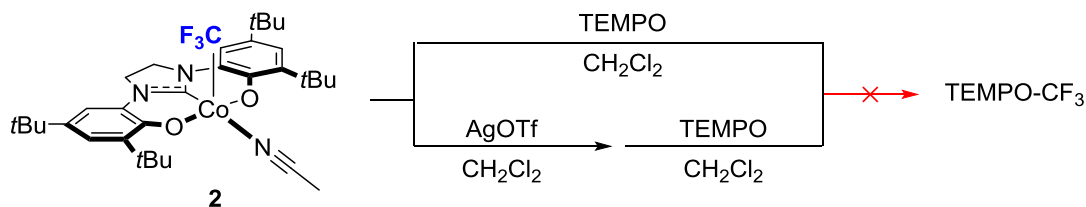
Scheme 4.2. Reasonable mechanism to produce a 6-coordinate, formal Co^{IV} complex by treating **1 with **4a**.**



4.3.2 Evaluation of High Valent Co–CF₃ Complexes for [•]CF₃ Transfer

Mixing **1** with TEMPO gives no observable change in the UV–Vis spectrum of **1** over 16 h at ambient temperature, indicating a pathway of direct electron transfer from **1** to TEMPO and subsequent ionic CF₃ transfer is unlikely. As described in Chapter 3, the isolated [(^δOCO)Co(CF₃)(MeCN)], **2**, does not deliver CF₃ radical to TEMPO under non-photolytic conditions, implying that it cannot be the active species for the trifluoromethylation of TEMPO described above. As previously mentioned, both the Togni and Umemoto reagents can act as 2-electron oxidants.^{10, 20} To determine if a doubly oxidized species is involved in the trifluoromethylation reaction pathway (vs. a singly oxidized Co species), the Co–CF₃ complex, **2**, was further oxidized with AgOTf. The resulting material, formally Co^{IV}, is analogous to the [(^δOCO)Co(CF₃)(OH₂)₂][OTf] described in Chapter 3. This species was also found to be unreactive with TEMPO as determined by UV-Vis and ¹⁹F NMR spectroscopy (Scheme 4.3).

Scheme 4.3. Attempted capture of [•]CF₃ by TEMPO from Co^{III} and “Co^{IV}” complexes containing Co–CF₃ bonds.



4.3.3 Electronic Spectroscopy

Visible color changes accompany the addition of either reagent **3b** or **4a** to a solution of **1** and TEMPO. In both cases, the reaction mixture immediately turns from orange to dark green and were therefore monitored by UV-Vis absorption spectroscopy.

As previously stated, the spectrum of complex **1** was unchanged between the range of 300-1000 nm upon addition of 10 equiv. of TEMPO. Only the CT bands of **1** are observed at 355 and 438 nm (Figure 4.4; blue and red traces). Upon addition of **3b**, broad new features appear with maxima at 542 and 906 nm (Figure 4.4; yellow trace). This spectrum is nearly identical to that observed in the single electron oxidized triflate complex $[(^{\delta}\text{OCO})\text{Co}(\text{MeCN})_2][\text{OTf}]$, **6**. Addition of a stoichiometric equivalent of dibenzothiophene, the byproduct of loss of a CF_3 from Umemoto's reagent, to an independently prepared sample of **6** produces a spectrum that closely matches that obtained from the reaction conditions (Figure 4.4; purple trace). Formation of **6** could be envisioned to occur by a SET mechanism in which reagent **3b** is reduced by one electron, generating an unstable intermediate which subsequently liberates a CF_3 radical. Concurrent oxidation of the cobalt complex and anion transfer produces complex **6** and dibenzothiophene.

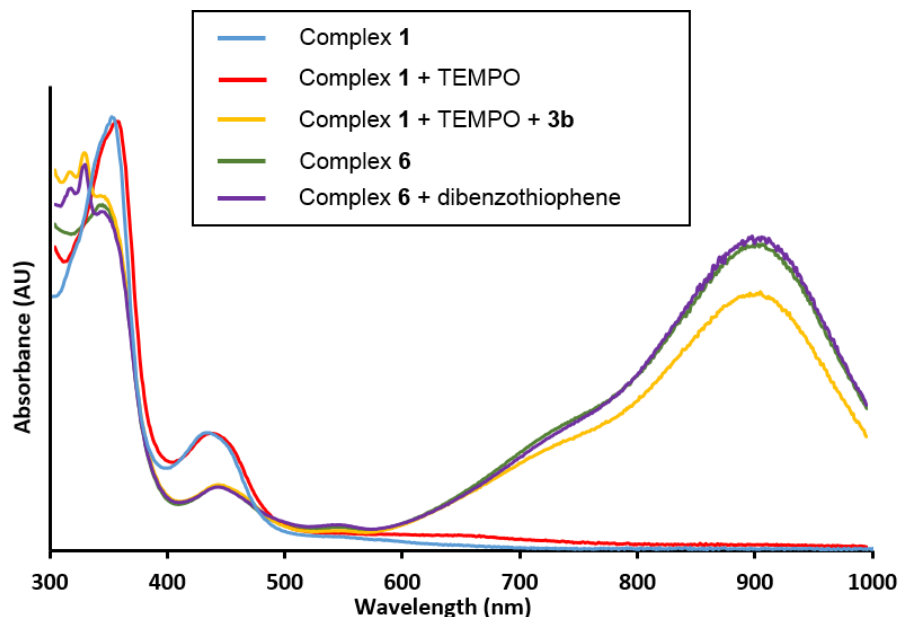


Figure 4.4. Comparison of UV-Vis spectra in CH_2Cl_2 of: **1** (blue), **1** with TEMPO (red), **1** with TEMPO and **3b** (yellow), **6** (green), and **6** with dibenzothiophene (purple).

In contrast, the reaction with **4a** produces a strikingly different UV-Vis spectrum. The characteristic bands associated with complex **1** change in intensity and the CT bands shift to 436, 696, and 875 nm. This spectrum matches quite well with that of the κ^2 -acetate complex $[(^s\text{OCO})\text{Co}(\text{O}_2\text{CCF}_3)]$, **7**, reported in Chapter 3 (Figure 4.5). The observation of **7** can be similarly rationalized by a SET mechanism. In this case, the benzoate byproduct of CF_3 loss acts as a bidentate ligand. (Scheme 4.4).

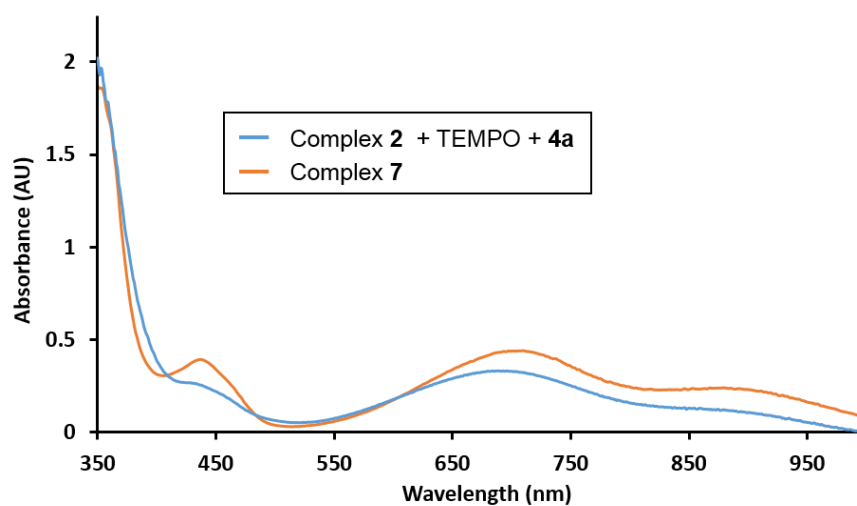
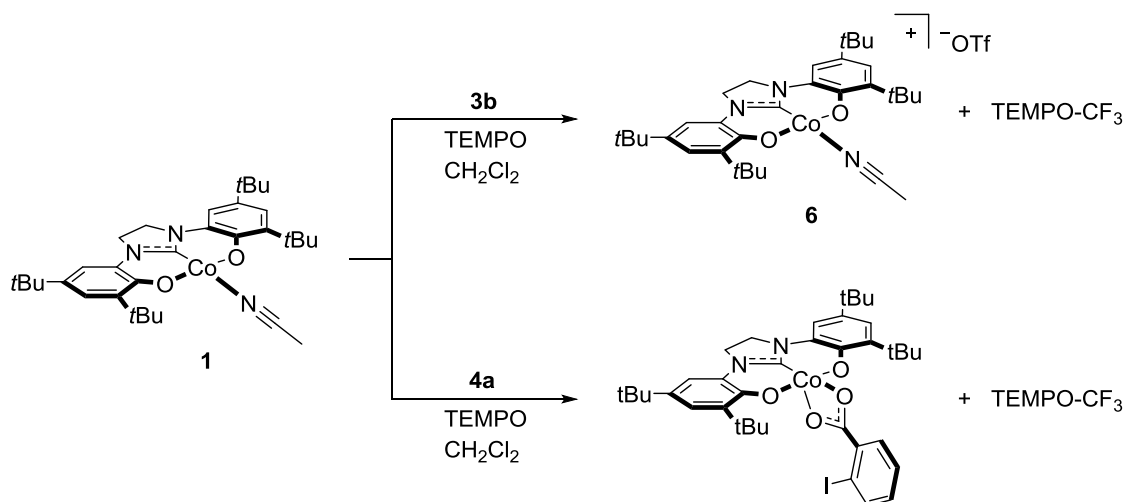


Figure 4.5. Comparison of UV-Vis spectra in CH_2Cl_2 of: **2** with **4a** and TEMPO (blue), and **7** (orange).

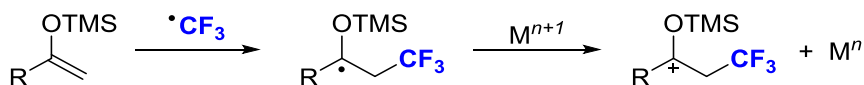
Scheme 4.4. Proposed products from the reaction of **1** with **3b** (top) and **1** with **4a** (bottom) in the presence of TEMPO.



4.3.4 Reactivity with Silyl Enol Ethers

Having demonstrated competency in stoichiometric CF₃ radical generation from electrophilic trifluoromethyl sources, efforts were then shifted towards the development of **1** as a catalyst for trifluoromethylation and expansion of the substrate scope. As highlighted above, the byproducts of CF₃ delivery are Co^{III} complexes, one oxidation state above **1**. Accordingly, for catalysis, a reductant is necessary to regenerate the active metal complex, **1**. In previously reported catalytic trifluoromethylation of silyl enol ethers to produce α -trifluoromethyl ketones, the radical intermediate generated during the reaction was thought to be a competent reductant for oxidized metal species (Scheme 4.5).²³⁻²⁴ Thus, similar chemistry was pursued using **1** as the electron shuttle.

Scheme 4.5. Proposed mechanism for the reduction of a metal complex by a tertiary organic radical formed under reaction conditions.



1-Phenyl-1-trimethylsiloxyethylene was chosen as a model substrate to evaluate this class of reactivity. Both the **3b** and **4a** were evaluated as CF₃ sources. With 5% mol of **1** in CH₂Cl₂, both reactions proceeded to complete conversion after 16 hours at ambient temperature, either consuming the CF₃ reagent (in the case of **4a**) or the silyl enol ether (when **3b** was utilized). The use of 1.5 equivalents of **3b** produced α -trifluoromethyl phenylpropanone in 94% yield with the excess Umemoto reagent remaining unreacted (Figure 4.7). Analysis by GC-MS confirmed complete consumption of the starting silyl enol ether with the balance of the substrate being converted to acetophenone.

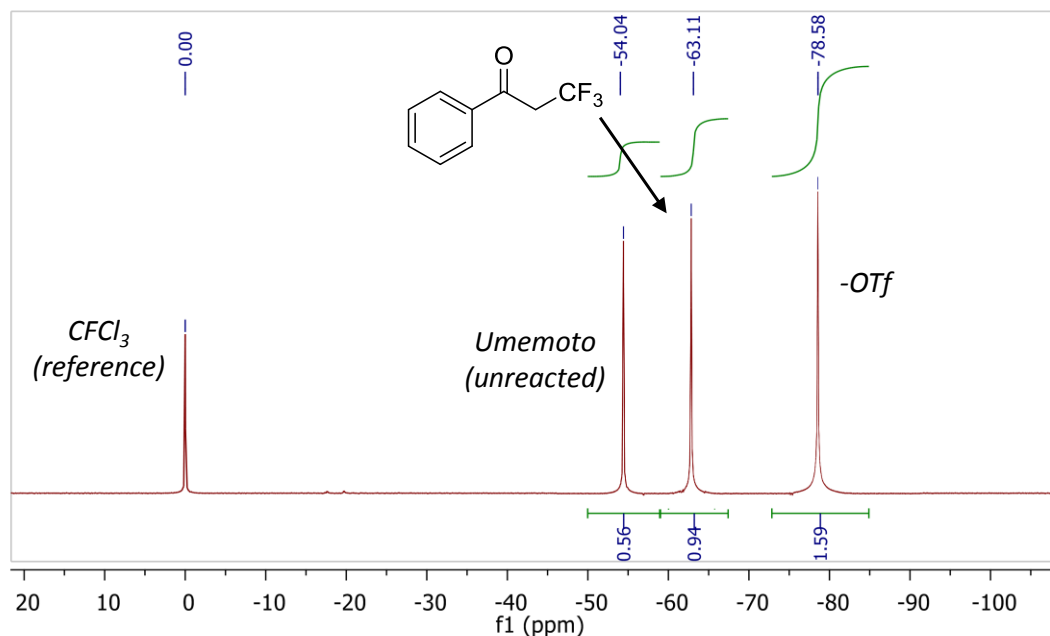


Figure 4.6. ^{19}F NMR of a reaction between 1-phenyl-1-trimethylsiloxyethylene and 1.5 eq. of the Umemoto reagent, **3b**, with 5% loading of complex **1** after 18 h in CH_2Cl_2 .

When 1.5 equivalents of **4a** was instead used as the CF_3 source, the expected α -trifluoromethyl phenylpropanone was only produced in a 13% yield. The ^{19}F NMR spectrum revealed that the major CF_3 containing product was the trifluoromethyl ester, **5**, produced from the self-trifluoromethylation of **4a** (Figure 4.8). This side product arises from a well-known reaction that occurs with Lewis acid metals.²² The Lewis acidity of the Co center in **1** makes it reasonable that similar reactivity is operable here.

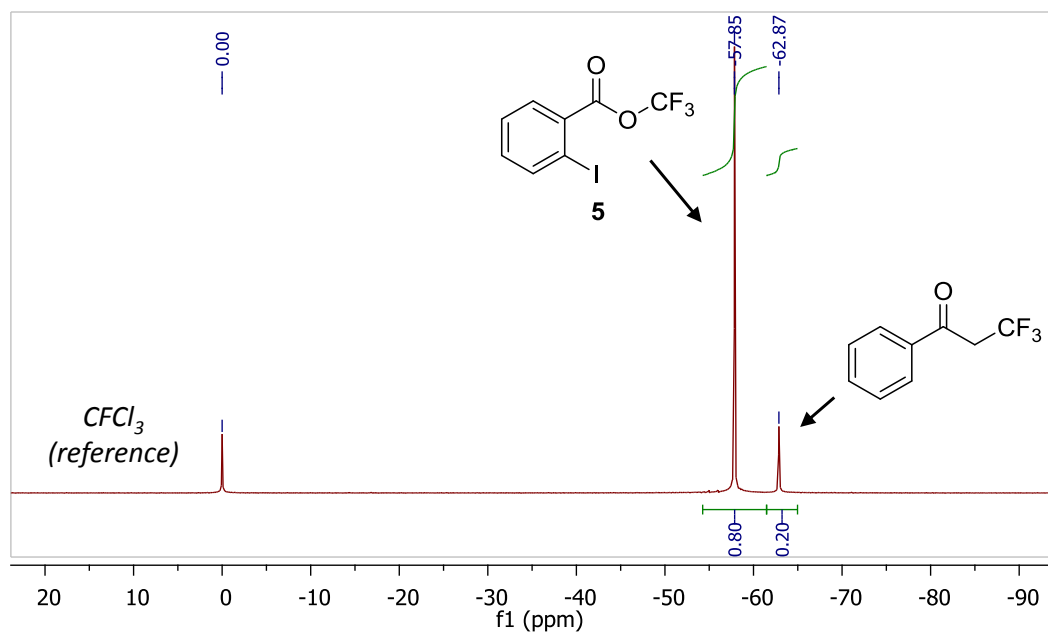
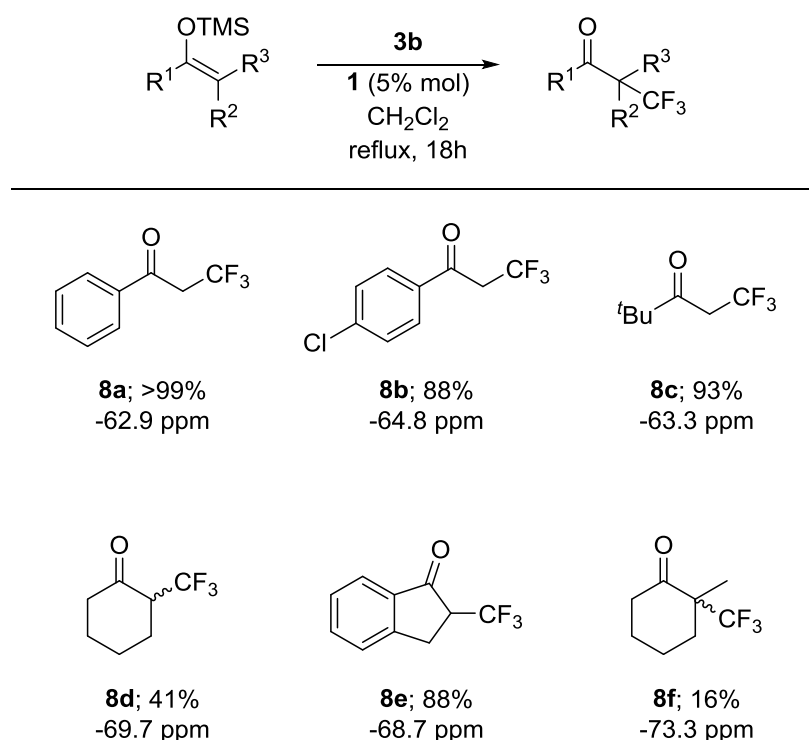


Figure 4.7. ^{19}F NMR of a reaction between 1-phenyl-1-trimethylsiloxyethylene and 1.5 eq. of the Togni II reagent, 4a, with 5% loading of 1 after 3 h in CH_2Cl_2 .

Table 4.1. Radical trifluoromethylation of silyl enol ethers by complex **1 and **3b**. Yields were determined by ^{19}F yields against an internal standard.**



In order to evaluate the scope of this reaction, five additional silyl enol ether substrates with varying steric demands were prepared. The yields of the products and their corresponding ^{19}F NMR chemical shifts vs. CFCl_3 are described in Table 4.1. The highest yields were obtained when the reactions were performed in dichloromethane and refluxed for 16 hours. A significant drop in yield was observed with increased steric crowding at the alkene (**8f**). The CF_3 radical is an electrophilic radical with a low-lying SOMO.²⁵ Consequently, reactions should be faster with electron-rich alkenes with high-lying HOMOs,³ however that trend is not observed here. The calculated reaction barrier and Gibbs free energy change for the reagent **4a** to deliver an equivalent of $\cdot\text{CF}_3$ is remarkably different depending on particular single electron reductant used,²⁶ however the use of **1** as the reductant was constant in all substrates examined. In addition, due to

the small size of the trifluoromethyl radical, the low yield of substrate **8f** seems to support the hypothesis that free $\cdot\text{CF}_3$ may not be an active species in the reaction with **3b**. Rather a sterically hindered thiophenium radical likely transfers the CF_3 radical directly upon activation by **1**.²⁷

4.4 Mechanistic Studies

Reaction kinetics of the system described in Table 4.1 were monitored by ^{19}F NMR using 1-phenyl-1-trimethylsiloxyethylene as the substrate with a 5% mol loading of **1** in CH_2Cl_2 . Within 10 minutes at room temperature, a 40% yield of the desired α -trifluoromethyl phenylpropanone, **8a**, was observed, indicating that the first 7-8 turnovers were fast. However, at the end of 1 hour, the yield had only increased to 55%. The yield continued to slowly increase up to 94% over the next 15 hours.

To probe the vast differences in reaction rates, an experiment was performed in which reagent **3b** was added in stoichiometric proportions to complex **1** in the presence of 20 equivalents of 1-phenyl-1-trimethylsiloxyethylene (0.5M in CH_2Cl_2). The consumption of **3b** was monitored by ^{19}F NMR after each addition to ensure complete consumption of the CF_3 reagent. After each addition of **3b**, an aliquot of the reaction mixture was taken and analysed by UV-vis spectroscopy (Figure 4.8).

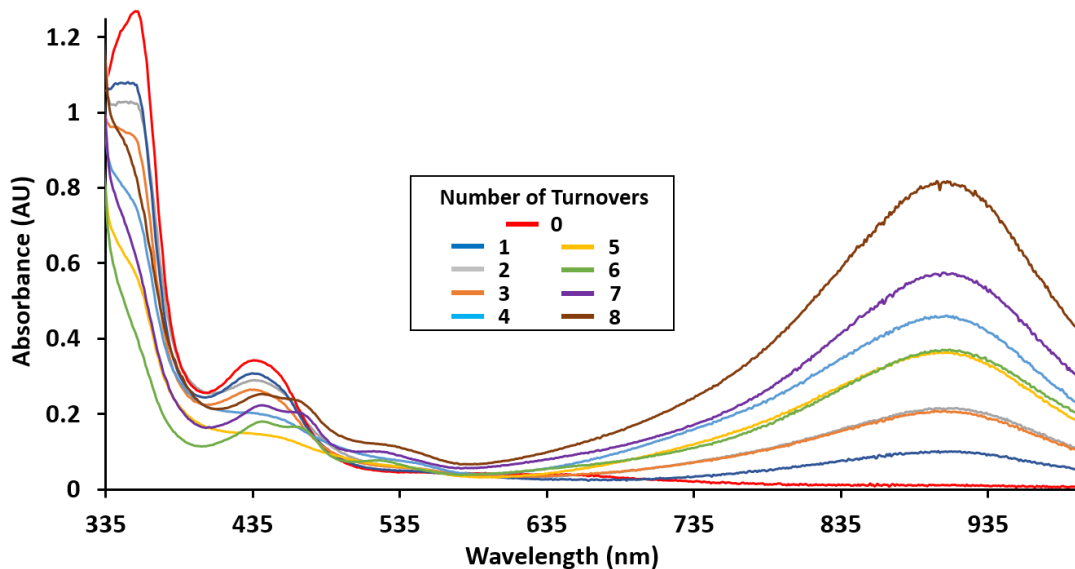


Figure 4.8. UV-Vis spectra in CH_2Cl_2 of the crude reaction mixture after each turnover for the first 8 cycles.

During the first 5 turnovers, the CT bands associated with complex **1** at 355 and 438 nm decreased in intensity while the band at 902 nm grew larger, indicating some conversion of **1** to the one-electron oxidized species $[(^{\text{S}}\text{OCO})\text{Co}(\text{MeCN})_2][\text{OTf}]$, complex **6**. After the 5th turnover, two absorbances at 440 and 466 nm began to increase along with a small band at 526 nm. These spectra match well with the formal “Co^{IV}” species $[(^{\text{S}}\text{OCO})\text{Co}(\text{CF}_3)(\text{OH}_2)_2][\text{OTf}]$ described in Chapter 3 (Figure 4.9). The continually increasing absorption at 902 nm also indicates a steady increase in the formation of **6**.

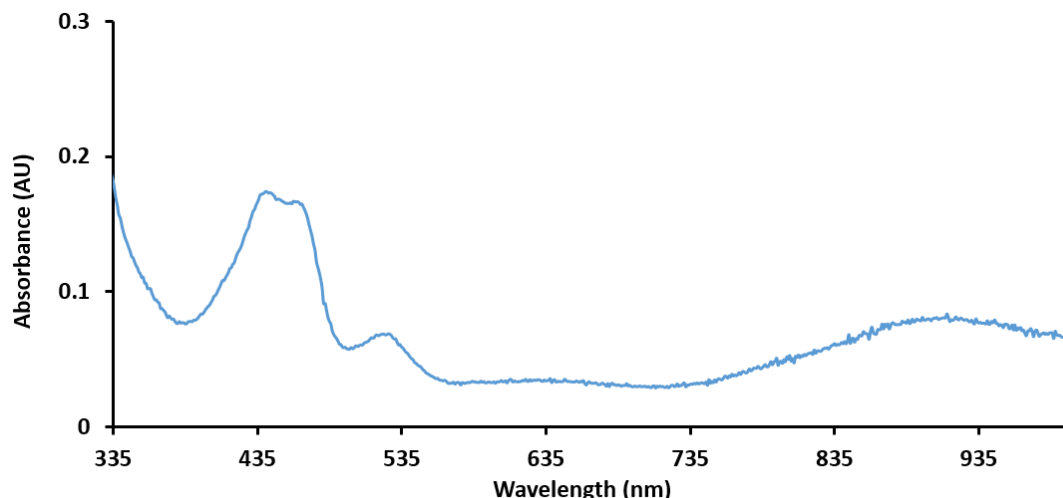


Figure 4.9. UV-Vis spectrum of $[(^S\text{OCO})\text{Co}(\text{CF}_3)(\text{OH}_2)_2][\text{OTf}]$ in CH_2Cl_2 .

To determine if these species are competent to reduce reagent **3b**, the complexes $[(^S\text{OCO})\text{Co}(\text{MeCN})_2][\text{OTf}]$ and $[(^S\text{OCO})\text{Co}(\text{CF}_3)(\text{OH}_2)_2][\text{OTf}]$ were utilized in place of **1** in the catalytic reaction conditions described for the trifluoromethylation of silyl enol ether substrates (Table 4.1). Indeed, the use of the Co^{III} complex $[(^S\text{OCO})\text{Co}(\text{MeCN})_2][\text{OTf}]$, **6**, produced only a slight decrease in yield, producing 94% of **8a**. In contrast, the Co^{IV} complex $[(^S\text{OCO})\text{Co}(\text{CF}_3)(\text{OH}_2)_2][\text{OTf}]$ only provided **8a** in 6% yield over the same reaction time. These data suggest that the decrease in reaction rate coincides with the accumulation of high-valent Co species in solution.

The observation of catalytic activity using $[(^S\text{OCO})\text{Co}(\text{MeCN})_2][\text{OTf}]$ suggests Co^{III} complexes are reasonable intermediates during catalytic turnover, as proposed above. Furthermore, the stoichiometric reaction with the doubly oxidized species, suggests multiple species might be active for C– CF_3 bond formation under the catalytic conditions. In this scenario, the fast initial turnover is attributed to rapid $\text{Co}^{\text{II/III}}$ redox

cycling. Accumulation of higher valent Co complexes might permit turnover via a $\text{Co}^{\text{III/IV}}$ cycle, but this is kinetically depressed.

A mechanism that represents the proposed catalytic cycle is shown in Scheme 4.10. In step (i), a SET from **1** to **3b** produces complex **6** and the one-electron reduced Umemoto reagent. The silyl enol ether acts as an electron acceptor in step (ii) and releases dibenzothiophene. The resulting tertiary organic radical then reduces **6** back to **1** in step (iii) and an anion exchange from the metal to the cationic organic substrate occurs. Finally, in step (iv), the triflate anion performs a nucleophilic attack on the silyl group, producing the α -trifluoromethyl ketone and TMSOTf.

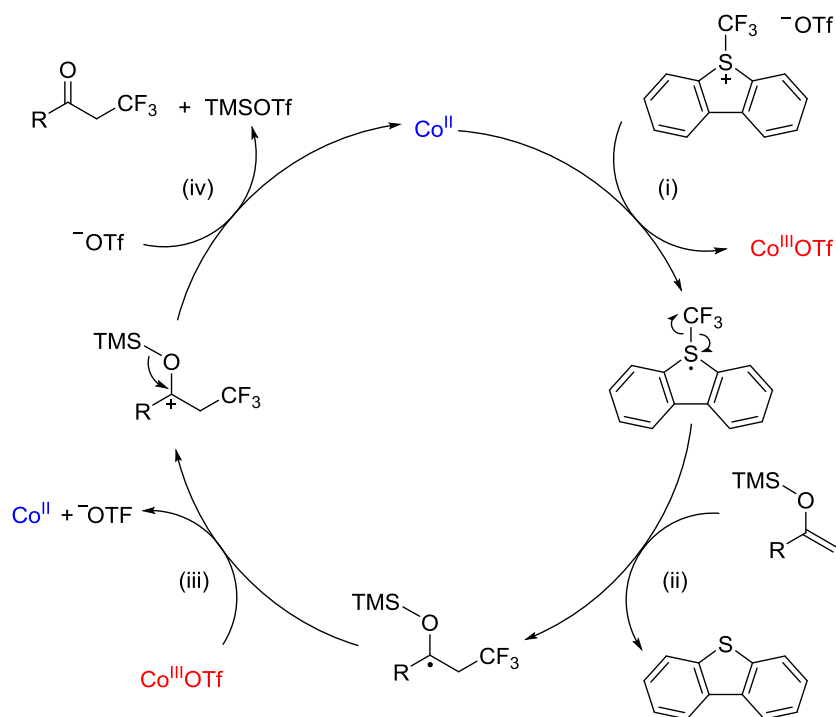


Figure 4.10. Proposed reaction mechanism for the catalytic trifluoromethylation of silyl enol ethers.

A GC-MS analysis of a crude reaction mixture showed no sign of TMSOTf, which is not unexpected given the air and water sensitivity of the species. However, two unidentified compounds were observed in the GC trace. Analysis of a commercial sample of TMSOTf under identical conditions gave the same two species, suggesting that TMSOTf is the byproduct formed during the reaction.

4.5 Conclusions and Future Direction

4.5.1 Conclusions

This Chapter describes the first example of cobalt-catalyzed radical trifluoromethylation of organic substrates. One major aspect of reactivity that is unique to this system involves the fact that is catalytically operative in multiple oxidation states.

The redox-active ($^{\text{S}}\text{OCO}$) ligand scaffold allows for access to three total oxidation states in which the SET mechanism is still active. By accessing multiple redox cycles, catalysis continues even when the complex is not reduced back to the original oxidation state. This provides a novel avenue to re-route and maintain catalytic competency in the event of 1e^- redox chemistry that would otherwise remove the Co from the catalytic cycle.

The catalytic process differs from those previously reported in the Soper laboratory in which the bond-making/breaking redox processes happen directly at the metal center. In this case, the complex apparently acts solely as an electron shuttle which imparts radical character onto the electrophilic CF_3 source directly. It is this species which acts as the direct trifluoromethylation reagent, not the cobalt center. In fact, it is imperative that an inner sphere Co– CF_3 bond not form in order to facilitate rapid electron transfer to the CF_3 reagent. If the only role of the Co, then, is to mediate 1e^- transfer, are the redox-active ligands even required? Could a purely outer-sphere ET shuttle, such as Cp_2Co or Cp_2Fe accomplish the same chemistry? Ferrocene is, in fact, not catalytically competent, suggesting the role **1** is more complicated than a simple electron shuttle.

As noted above, the electrophilic CF_3 fragment that is delivered in this system is most likely not free $^{\bullet}\text{CF}_3$. The steric sensitivity highlighted above suggests it's more likely formulated as an S-(trifluoromethyl)dibenzothiophenium radical. This is itself a potential ligand, and one possible role of the low-coordinate Co might be to bind S and activate the Umemoto reagent for CF_3 delivery. In this regard, the availability of an open coordination site in **1** becomes essential to the observed chemistry. It also highlights a key difference between the reactivity described in this Chapter vs. the trifluoromethylations in Chapter 3. There, the data suggests the free $^{\bullet}\text{CF}_3$ is the active

species for trifluoromethylation. This implies that the two methods are complimentary and might give access to orthogonal substrate specificities. For instance, the CF_3 radical is small and should not exhibit the steric sensitivity observed in this work. This suggests an opportunity to use the same catalytic platform in different ways, to access different sites within a substrate, a feature that is not common in catalysis.

4.5.2 *Future Directions*

It should be possible to move beyond silyl enol ether substrates with this method of radical trifluoromethylation. There is precedent for $\cdot\text{CF}_3$ trapping by alkenes, alkynes, and arenes and it is reasonable to expect related reactivity might be accessible using this system.^{3, 9, 25, 28-29}

4.6 **Experimental**

4.6.1 *General Considerations*

Unless otherwise specified, all manipulations were performed under anaerobic conditions using standard vacuum line techniques, or in an inert atmosphere glove box under purified nitrogen. Routine NMR spectra were acquired on a Varian Mercury 400 spectrometer (399.94 MHz for ^1H ; 101.1 MHz for ^{13}C). All chemical shifts are reported in parts per million (ppm) relative to CFCl_3 . UV–visible absorption spectra were acquired using a Varian Cary 50 spectrophotometer. Unless otherwise noted, all electronic absorption spectra were recorded at ambient temperatures in 1 cm quartz cells. All mass spectra were recorded in the Georgia Institute of Technology Bioanalytical Mass Spectrometry Facility. Gas chromatography–mass spectrometry (GC–MS) analyses

used an Agilent 6890 GC equipped with an autosampler and a Restek Rxi-5ms column (30 m x 0.25 mm i.d., 0.25 μ m film thickness). 1 μ L injections were made at a 50:1 split ratio. The mass spectrometer used in tandem was a Micromass AutoSpec electro-ionization (EI) detector.

4.6.2 *Materials and Methods*

Anhydrous dichloromethane for air- and moisture-sensitive manipulations was purchased from Sigma-Aldrich and further dried by passage through columns of activated alumina, degassed by at least three freeze-pump-thaw cycles, and stored under N₂ prior to use. With the exception of 1-phenyl-1-trimethylsiloxyethylene (Alfa Aesar), all silyl enol ethers were prepared according to a published procedure.³⁰ The cobalt complexes were prepared as described in Chapters 2 and 3. All ketone precursors, triethylamine, and NaI were purchased from Alfa Aesar and used as received.

4.6.3 *General Procedures for Radical Trifluoromethylation*

Representative procedure: Under a nitrogen atmosphere, a Schlenk tube was charged with complex **2** (10 mg, 0.015mmol, 5 mol%), the silyl enol ether (0.308 mmol, 1 equiv.) and CH₂Cl₂ (1.5 mL). To this solution, was added the Umemoto reagent **3b** (124 mg, 0.308 mmol, 1.0 equiv.). The resulting mixture was stirred at 45 °C for 18 h, at which time the reaction was allowed to cool to room temperature. An internal standard of trifluorotoluene was added and an aliquot of the reaction mixture was transferred to an NMR tube containing an external reference of CFCl₃. The yields were determined against the internal standard and the ¹⁹F spectra matched those previously reported.²⁴

4.7 References

1. Mu, X.; Wu, T.; Wang, H.-y.; Guo, Y.-l.; Liu, G., Palladium-Catalyzed Oxidative Aryltrifluoromethylation of Activated Alkenes at Room Temperature. *Journal of the American Chemical Society* **2012**, *134* (2), 878-881.
2. Charpentier, J.; Früh, N.; Togni, A., Electrophilic Trifluoromethylation by Use of Hypervalent Iodine Reagents. *Chemical Reviews* **2015**, *115* (2), 650-682.
3. Studer, A., A “Renaissance” in Radical Trifluoromethylation. *Angewandte Chemie International Edition* **2012**, *51* (36), 8950-8958.
4. Pawelke, G., Tetrakis(dimethylamino)ethylene/trifluoroiodomethane. a specific novel trifluoromethylating agent. *Journal of Fluorine Chemistry* **1989**, *42* (3), 429-433.
5. Zhao, Y.; Zhu, J.; Ni, C.; Hu, J., Magnesium Metal-Mediated Reductive Trifluoromethylation of Aldehydes with Phenyl Trifluoromethyl Sulfone. *Synthesis* **2010**, *2010* (11), 1899-1904.
6. Yasui, H.; Yamamoto, T.; Tokunaga, E.; Shibata, N., Robust synthesis of trifluoromethionine and its derivatives by reductive trifluoromethylation of amino acid disulfides by $\text{CF}_3\text{I}/\text{Na}/\text{Liq.NH}_3$ system. *Journal of Fluorine Chemistry* **2011**, *132* (3), 186-189.
7. Chu, L.; Qing, F.-L., Oxidative Trifluoromethylation and Trifluoromethylthiolation Reactions Using (Trifluoromethyl)trimethylsilane as a Nucleophilic CF_3 Source. *Accounts of Chemical Research* **2014**, *47* (5), 1513-1522.
8. Wang, S.-M.; Han, J.-B.; Zhang, C.-P.; Qin, H.-L.; Xiao, J.-C., An overview of reductive trifluoromethylation reactions using electrophilic ‘ $^+\text{CF}_3$ ’ reagents. *Tetrahedron* **2015**, *71* (42), 7949-7976.
9. Beatty, J. W.; Douglas, J. J.; Cole, K. P.; Stephenson, C. R. J., A scalable and operationally simple radical trifluoromethylation. *Nature Communications* **2015**, *6*, 7919.
10. Jacquet, J.; Blanchard, S.; Derat, E.; Desage-El Murr, M.; Fensterbank, L., Redox-ligand sustains controlled generation of CF_3 radicals by well-defined copper complex. *Chemical Science* **2016**, *7* (3), 2030-2036.
11. Nagib, D. A.; MacMillan, D. W. C., Trifluoromethylation of arenes and heteroarenes by means of photoredox catalysis. *Nature* **2011**, *480*, 224-228.
12. Eisenberger, P.; Gischig, S.; Togni, A., Novel 10-I-3 Hypervalent Iodine-Based Compounds for Electrophilic Trifluoromethylation. *Chemistry – A European Journal* **2006**, *12* (9), 2579-2586.

13. Kieltch, I.; Eisenberger, P.; Togni, A., Mild Electrophilic Trifluoromethylation of Carbon- and Sulfur-Centered Nucleophiles by a Hypervalent Iodine(III)–CF₃ Reagent. *Angewandte Chemie International Edition* **2007**, 46 (5), 754-757.
14. Matsnev, A.; Noritake, S.; Nomura, Y.; Tokunaga, E.; Nakamura, S.; Shibata, N., Efficient Access to Extended Yagupolskii–Umemoto-Type Reagents: Triflic Acid Catalyzed Intramolecular Cyclization of ortho-Ethynylaryltrifluoromethylsulfanes. *Angewandte Chemie International Edition* **2010**, 49 (3), 572-576.
15. Teruo, U.; Sumi, I., Power-variable trifluoromethylating agents, (trifluoromethyl)dibenzothio- and -selenophenium salt system. *Tetrahedron Letters* **1990**, 31 (25), 3579-3582.
16. Umemoto, T., Electrophilic Perfluoroalkylating Agents. *Chemical Reviews* **1996**, 96 (5), 1757-1778.
17. Umemoto, T.; Ishihara, S., Power-variable electrophilic trifluoromethylating agents. S-, Se-, and Te-(trifluoromethyl)dibenzothio-, -seleno-, and -tellurophenium salt system. *Journal of the American Chemical Society* **1993**, 115 (6), 2156-2164.
18. Yang, J.-J.; Kirchmeier, R. L.; Shreeve, J. n. M., New Electrophilic Trifluoromethylating Agents. *The Journal of Organic Chemistry* **1998**, 63 (8), 2656-2660.
19. Liang, T.; Neumann, C. N.; Ritter, T., Introduction of Fluorine and Fluorine-Containing Functional Groups. *Angewandte Chemie International Edition* **2013**, 52 (32), 8214-8264.
20. Jacquet, J.; Salanouve, E.; Orio, M.; Vezin, H.; Blanchard, S.; Derat, E.; Desage-El Murr, M.; Fensterbank, L., Iminosemiquinone radical ligands enable access to a well-defined redox-active CuII-CF₃ complex. *Chemical Communications* **2014**, 50 (72), 10394-10397.
21. Chaudhuri, P.; Verani, C. N.; Bill, E.; Bothe, E.; Weyhermüller, T.; Wieghardt, K., Electronic Structure of Bis(o-iminobenzosemiquinonato)metal Complexes (Cu, Ni, Pd). The Art of Establishing Physical Oxidation States in Transition-Metal Complexes Containing Radical Ligands. *Journal of the American Chemical Society* **2001**, 123 (10), 2213-2223.
22. Fantasia, S.; Welch, J. M.; Togni, A., Reactivity of a Hypervalent Iodine Trifluoromethylating Reagent toward THF: Ring Opening and Formation of Trifluoromethyl Ethers. *The Journal of Organic Chemistry* **2010**, 75 (5), 1779-1782.
23. Langlois, B. R.; Laurent, E.; Roidot, N., “Pseudo-cationic” trifluoromethylation of enol esters with sodium trifluoromethanesulfinate. *Tetrahedron Letters* **1992**, 33 (10), 1291-1294.

24. Li, L.; Chen, Q.-Y.; Guo, Y., Synthesis of α -Trifluoromethyl Ketones via the Cu-Catalyzed Trifluoromethylation of Silyl Enol Ethers Using an Electrophilic Trifluoromethylating Agent. *The Journal of Organic Chemistry* **2014**, 79 (11), 5145-5152.
25. Dolbier, W. R., Structure, Reactivity, and Chemistry of Fluoroalkyl Radicals. *Chemical Reviews* **1996**, 96 (5), 1557-1584.
26. Ling, L.; Liu, K.; Li, X.; Li, Y., General Reaction Mode of Hypervalent Iodine Trifluoromethylation Reagent: A Density Functional Theory Study. *ACS Catalysis* **2015**, 5 (4), 2458-2468.
27. Ma, J.-A.; Cahard, D., Mild Electrophilic Trifluoromethylation of β -Ketoesters and Silyl Enol Ethers with 5-Trifluoro Methylidibenzothiophenium Tetrafluoroborate. *The Journal of Organic Chemistry* **2003**, 68 (22), 8726-8729.
28. Presset, M.; Oehrich, D.; Rombouts, F.; Molander, G. A., Copper-Mediated Radical Trifluoromethylation of Unsaturated Potassium Organotrifluoroborates. *The Journal of Organic Chemistry* **2013**, 78 (24), 12837-12843.
29. Ye, Y.; Künzi, S. A.; Sanford, M. S., Practical Method for the Cu-Mediated Trifluoromethylation of Arylboronic Acids with CF_3 Radicals Derived from NaSO_2CF_3 and tert-Butyl Hydroperoxide (TBHP). *Organic Letters* **2012**, 14 (19), 4979-4981.
30. Connors, D. M.; Goroff, N. S., Regioselective Synthesis of Substituted Cyclopenta[1]phenanthrenes. *Organic Letters* **2016**, 18 (17), 4262-4265.

CHAPTER 5. CONCLUSIONS AND FUTURE DIRECTIONS

5.1 Conclusions

This thesis describes the synthesis and characterization of a variety of cobalt complexes containing a pincer-type, NHC-centered, bis(phenoxide) ligand scaffold. These ligands were observed to behave in a redox non-innocent manner in which the fine balance between metal- and ligand-centered redox is easily perturbed by changes in coordination environment. These complexes were all electrochemically capable of reaching a formal Co^{V} oxidation state, with one complex doing so at less than 0.45 V vs. Fc^+/Fc ($[(^{\text{S}}\text{OCO})\text{Co}(\text{CF}_3)(\text{MeCN})]$; Chapter 3).

An electron transfer series was prepared in which three oxidation states were isolated and characterized by single crystal X-ray crystallography, NMR, EPR, UV-Vis, and modeled by DFT calculations. These revealed that the physical oxidation assignment of the cobalt remained +II across the series. High oxidation state complexes have ligand-centered oxidations, but in intermediate oxidation state complexes there are likely a number of contributors to the ground states. These interesting physical peculiarities permit unique applications of this system in reaction chemistry with small molecule substrates.

Stoichiometric and catalytic applications of these complexes in C–C coupling were discovered and described in Chapters 3 and 4. In one case, visible light induced valence tautomerism, via ligand-to-metal charge transfer, allows for the population of a $\text{Co}-\text{CF}_3$ σ^* orbital. This promotes facile homolytic Co–C bond cleavage, producing a CF_3 radical

which acts to functionalize unactivated aryl and heteroaryl C–H bonds. This type of reactivity is a feature of this particular ligand/metal combination, in which the frontier ligand orbitals exist in near energetic degeneracy with those of the metal. In addition, we learned that the geometry of the cobalt center has a large impact on the ability of the complex to undergo such reactivity. Simply by coordinating an additional solvent molecule, shifting the geometry from square pyramidal to octahedral, this reactivity was completely turned off due to orbital restructuring.

In addition to the ability of the system to deliver a trifluoromethyl radical from an inner-sphere Co–CF₃ complex, it also acts as an electron shuttle in catalytic trifluoromethylation. Through a single electron transfer pathway, an electrophilic CF₃ source is destabilized, generating an equivalent of [•]CF₃ which acts with divergent selectivity from that observed with the Co–CF₃ complex. This system has proven competent to catalyze the trifluoromethylation of silyl enol ether substrates using commercially available electrophilic CF₃ sources. These reactions, in total, represent the first examples of cobalt C–H bond trifluoromethylation reported in literature. The contrast in reactivity, however, is very interesting from the perspective of catalyst design. It suggests the same Co complex can deliver net [•]CF₃ in two different ways under subtly different conditions. The chemistry which utilizes a SET pathway can apparently remain catalytically operative in two or more redox cycles (formally Co^{II/III}, Co^{III/IV}, Co^{IV/V}). All of this reactivity is predicated on the ability of these systems to access multiple oxidation states by utilization of the redox non-innocent (OCO) ligand scaffold.

5.2 Future Directions

The potential of this system for C–C cross-coupling is severely limited by undesirable side reactions with the NHC backbone, including insertion into the Co–C bond or reductive elimination to the NHC. Since C–N, C–O, or C–S bond reductive elimination to form a charged species is expected to be thermodynamically less favorable than the formation of a C–C bond, different linkers to bridge the bis(phenoxide) framework should be investigated in which the central chelating atom is a charge-neutral heteroatom (Figure 5.1). Systems of this nature have been previously reported and include pyridine, thiophene, and furan linkers.¹⁻³ The synthesis and characterization of the pyridine ligand as well as preliminary efforts to generate Co complexes are discussed in Appendix B.

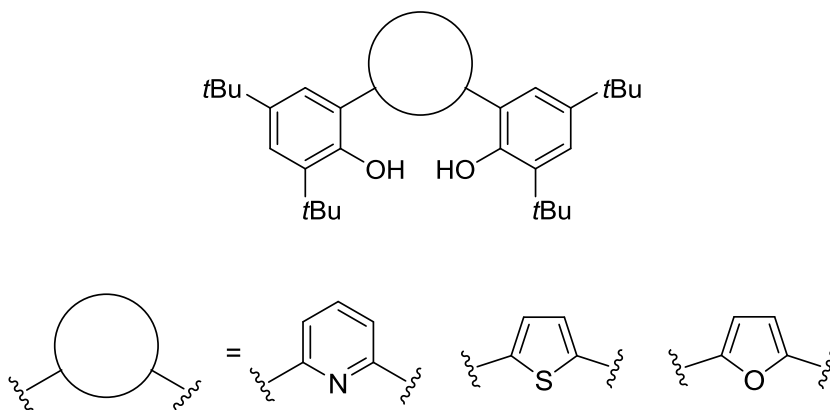


Figure 5.1. Proposed ligands for future studies.

5.3 References

1. Agapie, T.; Bercaw, J. E., Cyclometalated Tantalum Diphenolate Pincer Complexes: Intramolecular C–H/M–CH₃ σ -Bond Metathesis May Be Faster than O–H/M–CH₃ Protonolysis. *Organometallics* **2007**, 26 (12), 2957-2959.
2. Li, Y.; Liu, Y.; Bu, W.; Guo, J.; Wang, Y., A Mixed Pyridine-Phenol Boron Complex as an Organic Electroluminescent Material. *Chemical Communications* **2000**, (16), 1551-1552.
3. Agapie, T.; Golisz, S.; Tofan, D.; Bercaw, J. Non-metallocene Organometallic Complexes and Related Methods and Systems. WO 2008/036882 A12008, March 27, 2008.

APPENDIX A. MECHANISTIC STUDIES ON NICKEL-CATALYZED DIRECT OXIDATIVE ALKYNYLATION OF AZOLE DERIVATIVES

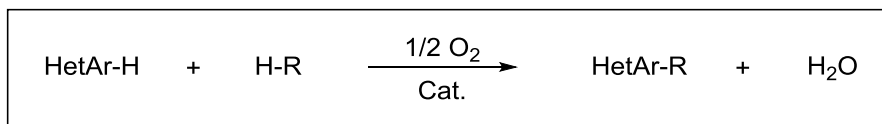
A.1 Introduction

Substituted heteroaryl moieties are abundant in medicinal, agricultural and materials chemistry,¹⁻² thus over the last decade an increasing number of direct synthetic strategies to their preparation have emerged.³⁻⁵ The most straightforward approaches to heteroarenes employ transition metal catalysts to promote direct C-H activation without requiring pre-functionalization of the starting materials. From an atom economical and green chemistry standpoint, the direct oxidative coupling of two unactivated C-H bonds, using O₂ as the terminal oxidant, represents an ultimate goal in C-C bond forming reactions (Scheme A.1).

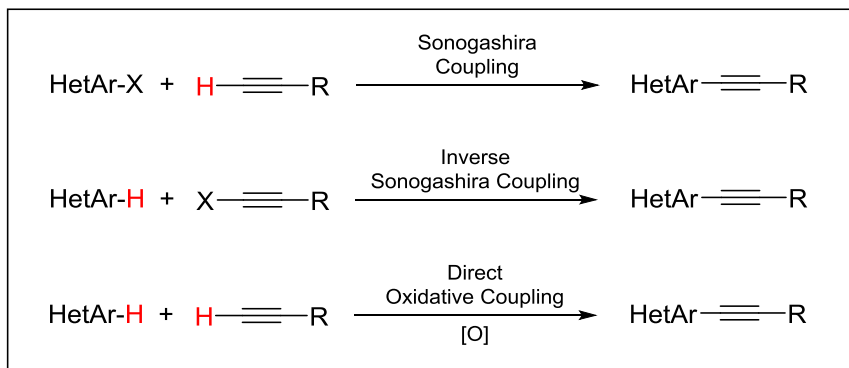
A number of advances have been made in recent years for the direct coupling of unactivated C-H bonds,⁶⁻¹¹ particularly in the area of direct heteroaryl C-H alkynylation.¹²⁻²⁰ However, challenges remain due to the propensity of alkynes to homocouple under standard oxidative coupling conditions.¹⁴ Traditionally, Sonogashira coupling²¹ (or its inverse)²² is utilized for the installation of an alkynyl group to heteroaryl synthons; however, pre-functionalized starting materials are required (Scheme A.2). Due to the prevalence of alkynyl heteroarenes in organic synthesis,²³ conducting materials,²⁴⁻²⁵ and pharmaceuticals,²⁶⁻²⁹ a synthetic strategy in which selective C-H bond activation of both substrates that does not necessitate pre-activation of the starting

materials (i.e. metalation or halogenation), is environmentally and economically beneficial.

Scheme A.1. General approach to metal-catalyzed direct oxidative coupling.



Scheme A.2. Methods for alkynylation of heteroaryl moieties.

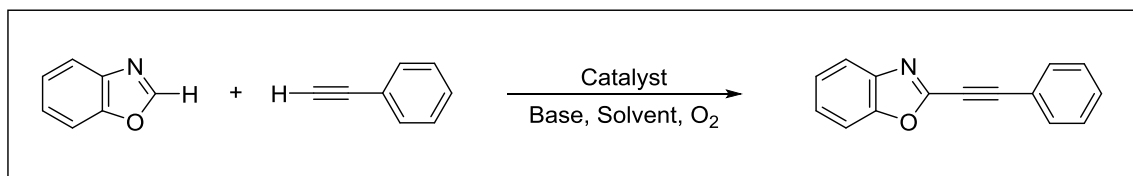


Within the past decade, there have been a number of reports involving Cu,^{12, 15, 19} Ni,¹⁶ Au,¹³ Pd,^{14, 17, 20} and Fe¹⁸ catalyzed direct alkynylation of heteroarenes, however the mechanism of this transformation is poorly understood and has not yet been thoroughly investigated. A comprehensive understating of the exact pathways in which both cross-coupling and alkynyl homocoupling occurs is essential for better catalyst design, suppression of the undesirable homocoupling, and expansion of the substrate scope.

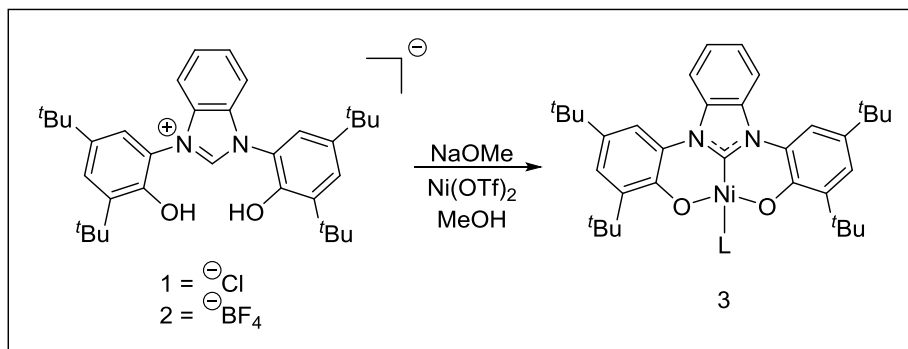
Our initial studies focused on the alkynylation of azole derivatives, utilizing benzoxazole and phenylacetylene as model substrates (Scheme A.3). A new square-planar Ni(II) complex was chosen for this mechanistic investigation because: (1) the

diamagnetic Ni complex allows for a ^1H NMR handle on the characterizations of the intermediates formed and (2) previously reported Ni complexes have proven competent for this type of reactivity.¹⁶ The Ni complex utilized in this study was based on the (^{Ph}OCO) scaffold introduced in Chapter 2.

Scheme A.3. Model reaction for mechanistic investigation.



Scheme A.4. Synthesis of the (^{Ph}OCO)Ni^{II} complex.



A.2 Synthesis and Characterization

A.2.1 Synthesis and Characterization of the (^{Ph}OCO) Nickel (II) Complex.

The ligand [^{Ph}OCO] H_3 Cl, **1**, was deprotonated with three equivalents of NaOMe , generating $\text{Na}_2[^{Ph}\text{OCO}]$ *in situ*, which was subsequently added dropwise to a suspension of $\text{Ni}(\text{OTf})_2$ in MeOH . After stirring for 5 hours at room temperature, the resulting air-stable green precipitant was filtered and recrystallized from boiling MeCN under aerobic conditions to yield green microcrystalline needles of the complex **3** in 78%

yield. The utilization of **2** (tetrafluoroborate counterion) as a precursor resulted in no significant difference in the yield or composition of the final product as determined by FTR-IR and $^1\text{H}/^{13}\text{C}$ NMR. ESI-MS data supports the formation of **3**, where L is a solvent derived MeCN or THF depending on which solvent was used for the sample preparation. This finding indicates the solvent molecules are labile, similar the square planar Co complexes described in Chapter 2.

All attempts to produce an X-ray quality crystal of **3** have failed, however the capacity of the $(^{\text{Ph}}\text{OCO})^{2-}$ ligand to chelate Ni was established by isolation of two other minor products. As shown in Figures A.1 and A.2, crystalline samples containing a ligand-to-metal ratio of 2:1 were obtained. Complex **4** (Figure A.1) contains one dianionic, tridentate $(^{\text{Ph}}\text{OCO})^{2-}$ ligand with a second $(^{\text{Ph}}\text{OCO})$ ligand coordinated through one anionic oxygen which occupies the fourth position about the square planar Ni center. Because the benzoxazole moiety contains a cationic amine, this second ligand is charge neutral, supporting the assignment of the nickel oxidation state as +II. As mentioned, the second complex, **5**, also contains two $(^{\text{Ph}}\text{OCO})$ chelates, but in this case both are monoanionic, bidentate ligands coordinated to the square planar nickel center through one oxygen and the carbene. Both structures are likely decomposition products, since they were obtained in *ca.* 5% yield after prolonged boiling in either MeCN (Figure A.1) or MeOH (Figure A.2).

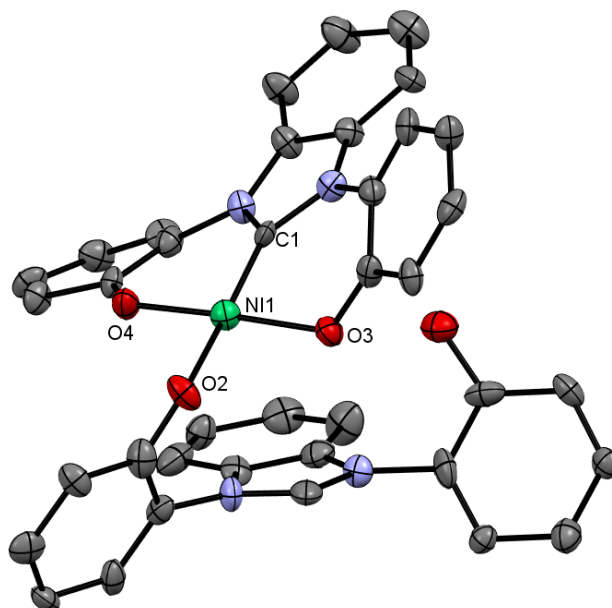


Figure A.1. Connectivity plot of the complex 4 obtained from boiling in MeCN, complex 4, with 50% probability ellipsoids. The tert-butyl groups and hydrogen atoms have been removed for clarity.

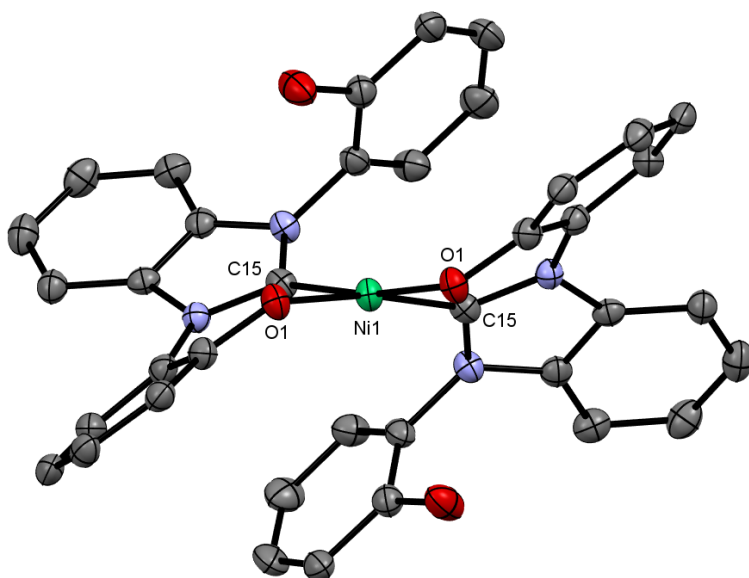


Figure A.2. Connectivity plot of the complex 5 obtained from boiling in MeOH, complex 5, with 50% probability ellipsoids. The tert-butyl groups and hydrogen atoms have been removed for clarity.

A.2.2 Nuclear Magnetic Resonance

^1H NMR spectroscopy was used to assess the solution structure of **3**. The spectra in coordinating vs. non-coordinating solvents revealed major differences in the coordination environments of this complex in solution. For example, the ^1H NMR spectrum obtained in toluene, benzene, dichloromethane, or chloroform gave rise three sets of ligand-derived resonances. Two sets of signals were in a 1:1 ratio, consistent with an asymmetric ligand environment, while the third set was independent of the other two, producing varying non-integer integration values. All three patterns were reminiscent of metal-free ligand, however none of the signals corresponded to such. Spectra taken in CD_3OD or CD_3CN showed only resonances expected of a symmetric, tridentate complex, with the fourth site occupied by a solvent molecule.

In an attempt to understand solvent effects on the spectra, a ^1H NMR experiment was performed wherein a CD_2Cl_2 solution of **3** was titrated with MeCN. As MeCN was added, the signal corresponding to complex **3** with a MeCN adduct increased in intensity while the other two signals decreased in intensity (Figure A.3). This result supports the likely formation of dimer with one phenoxide arm bridging two Ni centers. The addition of coordinating solvents acts to dissolve the dimer and complete the square planar coordination sphere around the Ni center.

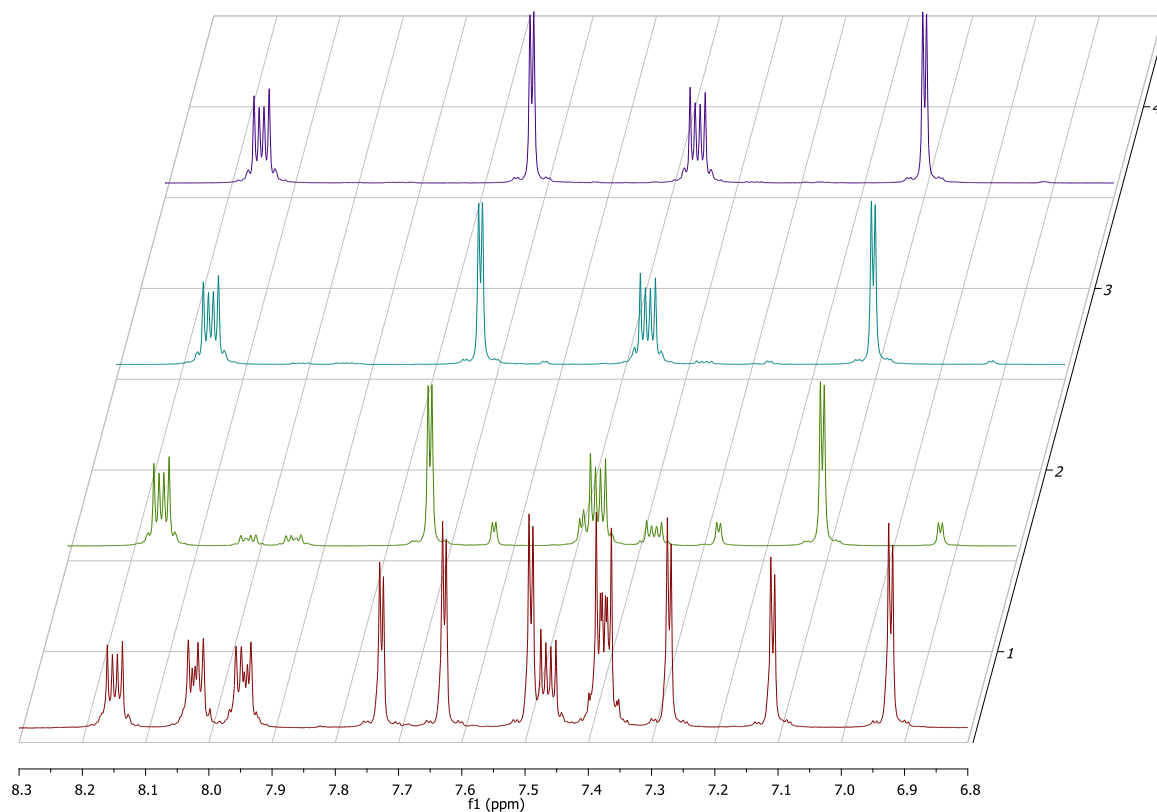


Figure A.3. Stacked ^1H NMR spectra of complex **3** in CD_2Cl_2 from 6.80 to 8.30 ppm. MeCN was titrated in from bottom to top as follows: none (red), 1 eq. (green), 5 eq. (blue), and 10 eq. (purple).

A.3 Results and Discussion

A.3.1. Oxidative Coupling

The utility of complex **3** as a catalyst for the oxidative coupling of terminal alkynes with azole derivatives was evaluated. Screening using phenylacetylene and benzoxazole as model compounds revealed that 5% mol loading of **3**, LiO^tBu as a base, toluene as a solvent, air as the oxidant, and a 3:1 ratio of benzoxazole to phenylacetylene gave the most favorable reaction conditions, affording a 62% isolated yield of the desired product (Table 1). The remaining reaction mixture contained mostly unreacted

benzoxazole and the homocoupling product of phenylacetylene according to TLC and GC-MS analysis.

Table A.1. Optimization of reaction conditions. *Reaction conditions:* All reactions were run in toluene for 1 h at 90 °C with 5% mol. loading of 3 on a 0.5 mmol scale. Isolated yields (those in parentheses are alkyne homocoupling product). ^aReaction was carried out under N₂. ^bReaction was run for 2h. ^cRapid consumption of the starting materials was observed. *The use of MeCN or THF as a solvent resulted primarily in the homocoupling product.

Ratio (Azole:Alkyne)	Base	Catalyst	Oxidant	Yield
1:2	LiO ^t Bu	(^{Ph} OCO)Ni	O ₂	50
1:2	LiO ^t Bu	(^{Ph} OCO)Ni	None^a	trace
1:2	LiO ^t Bu	None	O ₂	0
1:2	LiO ^t Bu	NiBr₂	O ₂	21(30) ^b
1:2	LiO ^t Bu	Ni(OTf)₂	O ₂	8 (90)
1:2	NaO^tBu	(^{Ph} OCO)Ni	O ₂	4 ^c
1:1	LiO ^t Bu	(^{Ph} OCO)Ni	O ₂	29
2:1	LiO ^t Bu	(^{Ph} OCO)Ni	O ₂	46
3:1	LiO ^t Bu	(^{Ph} OCO)Ni	O ₂	62

A.3.2. Base Effects

Curiously, the choice of base impacts the overall product distribution. Previous reports suggested that using NaO^tBu or KO^tBu rather than LiO^tBu gave either no reaction¹⁴ or resulted in the decomposition of the starting materials.¹⁶ Instead, the reaction of benzoxazole and phenylacetylene (2 equiv.) in the presence of Na^tBuO (3 equiv.)

cleanly produced one single product in 94% isolated yield in under 15 minutes. GC-MS analysis suggested the product consisted of both equivalents of the alkene as well as benzoxazole, however structural determination from ^1H and ^{13}C NMR was not straightforward. A single crystal structure revealed the product to be **6**, as illustrated in Scheme A.5 and Figure A.4. Notably, this reaction does not require a Ni source to proceed, however its presence did not affect the outcome.

Scheme A.5. Generation of enynimine product 6.

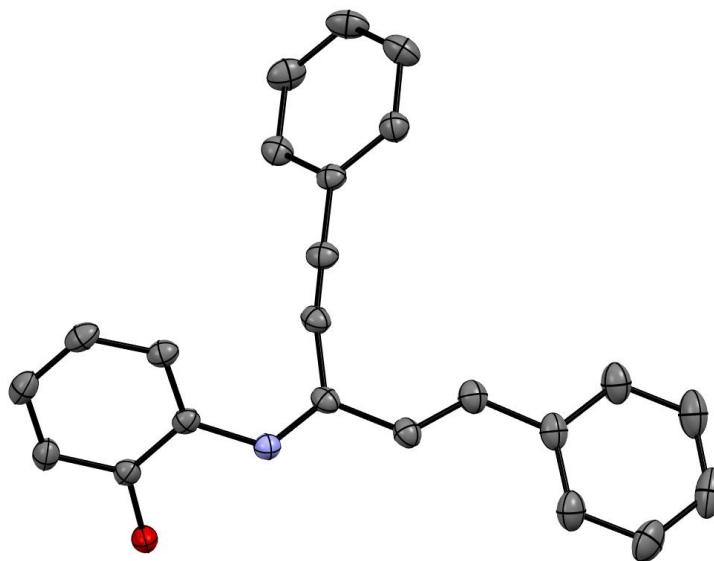
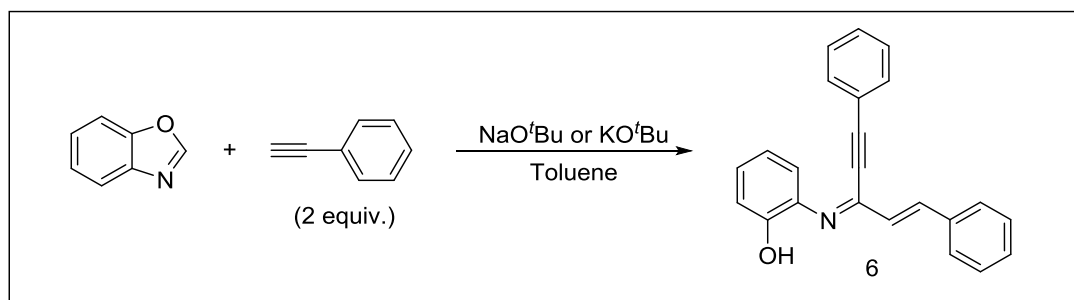


Figure A.4. Connectivity plot of 6 with 50% probability ellipsoids.

This product is not entirely surprising considering that deprotonation of benzoxazole results in ring-opened isocyanide species *in situ* in up to a 95:5 ratio.³⁰⁻³¹ In fact, mechanistic studies involving Pd-catalyzed arylation reactions of oxazole derivatives invoke the ring-open isocyanide to be the active coupling partner,³² directly contrasting the reactivity observed here. In order to rule out the isocyanide species as active in this Ni system, a control reaction was performed using standard reactions conditions outline in Table A.1, however (2-isocyanophenoxy)trimethylsilane³³ was substituted in place of benzoxazole. The reaction yielded no desirable C-C coupling product and only a number of unidentified compounds were formed. The results may be due to the fact that Ni is often employed as an isocyanide polymerization catalyst and performs particularly well under aerobic conditions.³⁴

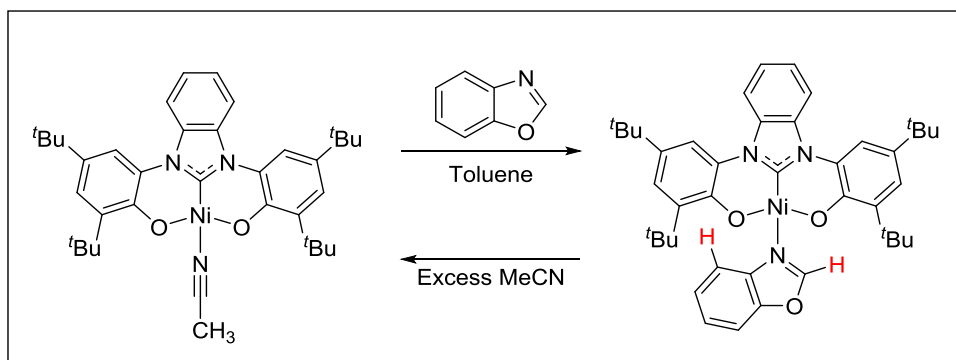
One possible explanation as to why LiO^tBu did not produce the same effect is due to the tendency of Li bases to aggregate in solution,¹⁷ thus directly deprotonating benzoxazole at a much slower rate than the NaO^tBu or KO^tBu counterparts. To determine if this was the major factor, a control reaction was run in the presence of one equivalent of TMEDA which was expected to chelate to lithium ions and minimize the tendency to aggregate in solution. Indeed, compound **6** was formed, albeit at a sluggish rate and in a lower overall yield after 1 hour.

A.3.3. *Synthesis and Characterization of the (^{Ph}OCO)Ni^{II} Benzoxazole Complex*

In order to probe the interaction of benzoxazole with Ni, attempts were made to independently prepare a benzoxazole adduct to **3**. Complex **3** was treated with a stoichiometric amount of benzoxazole in toluene for 15 mins at ambient temperature.

The ^1H NMR spectrum of the resulting species revealed a pattern of inequivalent aryl protons on benzoxazole with significant downfield shifting and broadening of the signals, consistent with a coordination complex formulated **3**-benzoxazole where the heteroarene is coordinated to the Ni center through the N-atom donor of the azole. The downfield shifts and signal broadening are likely the C-2 and C-4 associated protons of benzoxazole highlighted in Scheme A.6.

Scheme A.6. Lability of benzoxazole coordination to $(^{\text{Ph}}\text{OCO})\text{Ni}^{\text{II}}$.



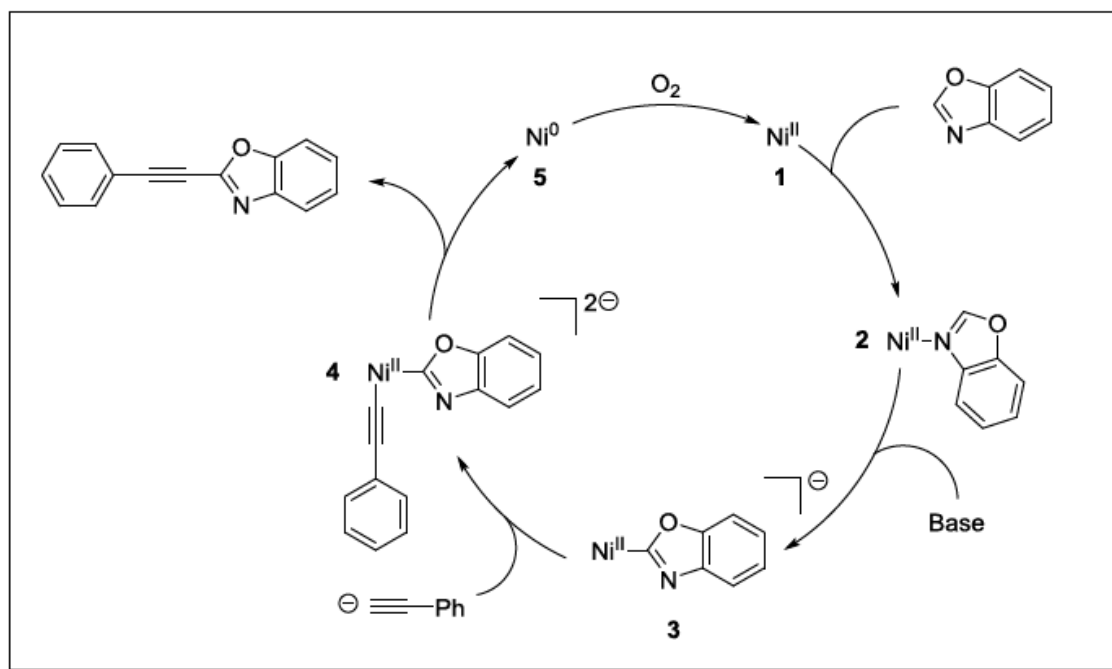
Exposure of excess MeCN to the benzoxazole adduct effects an immediate precipitation of a green solid which ^1H NMR and ATR-IR confirm to be re-generation of **3**-MeCN, suggesting the benzoxazole ligand is labile. The competition between a coordinating solvent vs. substrate may contribute significantly as to why the desired coupling reaction does not occur in solvents such as THF or MeCN. Interestingly, stoichiometric exposure of $[(^{\text{Ph}}\text{OCO})\text{Ni}^{\text{II}}(\text{benzoxazole})]$ to bases including Li^tBuO , Na^tBuO , or K^tBuO had no effect on the coordination environment of the complex as evidenced by ^1H NMR spectroscopy, suggesting that when coordinated to Ni, the C-2 carbon of benzoxazole is not readily deprotonated by such bases.

A.3.4. Attempted Synthesis of the (^{Ph}OCO)Ni^{II} Acetylene Complex

Another possible pathway to cross-coupling involves coordination of phenylacetylene prior to coordination by benzoxazole. Exposure of a stoichiometric amount of phenylacetylene to **3** in toluene gave no observable changes by ^1H NMR spectroscopy. Addition of lithium phenylacetylide to a solution of **3** in THF resulted in a significant color change of the solution from green to brown. ^1H and ^{13}C NMR in CDCl_3 of the reaction mixture in CDCl_3 displayed a diamagnetic spectrum that consisted of homocoupled phenylacetylene and **3** as observed in non-coordinating solvents. Whether this is a monometallic or bimetallic pathway which leads to an even distribution of diamagnetic Ni^0 and Ni^{II} remains to be evaluated.

A.4 Conclusions and Future Directions

Scheme A.7. Proposed catalytic cycle.



In summary, a reasonable mechanism based on the evidence so far is summarized in Scheme A.7. The pathway from **2** to **3** is still unknown and the lack of any reactivity with bases evaluated so far suggests the conversion is likely more complicated than shown. Future work should probe the mechanistic steps which have yet to be determined. Suggested experiments are outlined below.

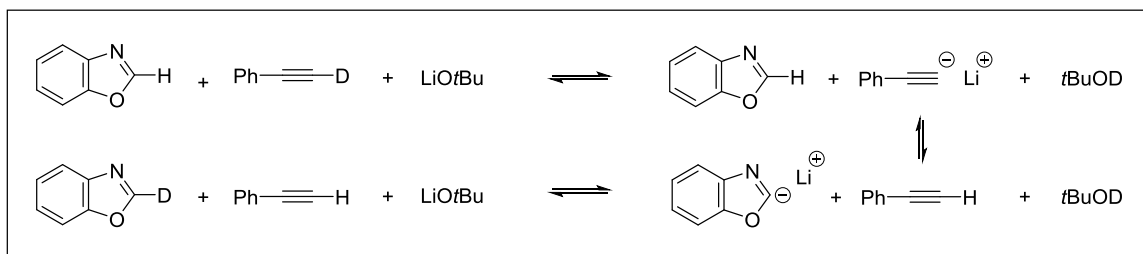
A.4.1. Activation of Benzoxazole.

The previous experiments suggest deprotonation of benzoxazole prior to metal coordination is unlikely, but the exact mechanism of how the heteroaryl moiety becomes activated is still not understood. Studies should be performed to evaluate the possibility that the *in situ* generated phenylacetylide acts to deprotonate coordinated benzoxazole. In order to determine the feasibility of this reaction pathway, the $[(^{Ph}OCO)Ni^{II}(benzoxazole)]$ complex could be treated with 1 equiv. of phenylacetylide that has been deprotonated with LiHMDS. Performing this experiment in a J-Young NMR tube would allow for facile elucidation of the composition of the product. Provided the success of this experiment, the signal from benzoxazole should be considerably different than that of $[(^{Ph}OCO)Ni^{II}(benzoxazole)]$ and protonated phenylacetylene should also be observed.

A.4.2. H/D Exchange

An independent proton/deuterium exchange experiment which utilizes a catalytic amount of base could be performed to evaluate the capacity of phenylacetylide to deprotonate benzoxazole without the presence of a metal (Scheme A.8).

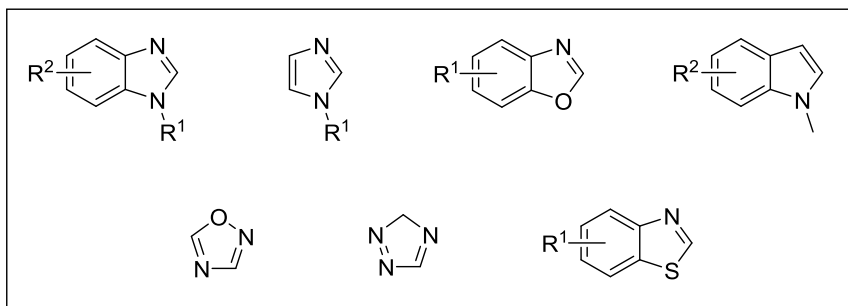
Scheme A.8. Base catalyzed deuterium/hydrogen exchange experiment.



A.4.3. Substrate Scope

Beyond oxazole derivatives, heteroaryl substrates which contain a relatively acidic proton *ortho* to the heteroatom should also be investigated. Some of the examples include, but are not limited to those shown below in Table A.2.

Table A.2. Possible substrates for future investigation.

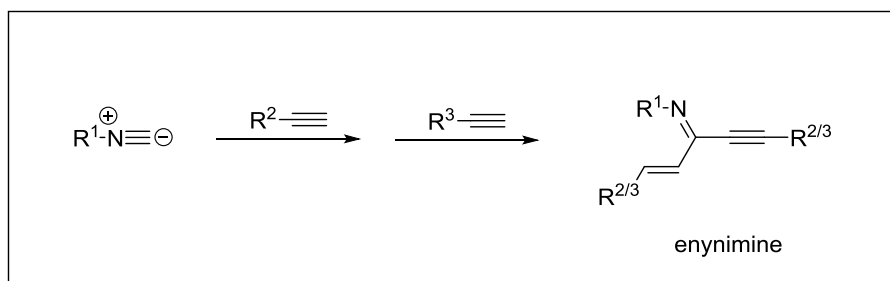


A.4.4. Facile Synthesis of Enynimine Synthons

Multicomponent reactions (MCR) have continuously evolved since their onset by Strecker in 1850.³⁶⁻³⁷ Among these reactions, those based on Ugi chemistry and isocyanide moieties are the most documented.³⁸ Although, the [1+2] cycloaddition of

isocyanides to internal alkynes have been studied sequential addition of terminal alkynes to produce enynimines has not been reported. Further investigation into the controlled addition of varying alkynes to isocyanide species could provide new one-pot methodology for producing interesting organic precursors in substituted heteroaryl cyclization reactions. Reaction conditions such as solvent choice, necessity of a base, scope, and the electronic nature of the substrates should be evaluated.

Scheme A.9. Synthesis of asymmetric enynimines.



A.5 References

1. Voronkov, A.; Holsworth, D. D.; Waaler, J.; Wilson, S. R.; Ekblad, B.; Perdreau-Dahl, H.; Dinh, H.; Drewes, G.; Hopf, C.; Morth, J. P.; Krauss, S., Structural Basis and SAR for G007-LK, a Lead Stage 1,2,4-Triazole Based Specific Tankyrase 1/2 Inhibitor. *Journal of Medicinal Chemistry* **2013**, *56* (7), 3012-3023.
2. Parlow, J. J.; Clark, R. D., Synthesis and herbicidal activity of phenylproparginols. *Journal of Agricultural and Food Chemistry* **1994**, *42* (11), 2600-2609.
3. Colby, D. A.; Bergman, R. G.; Ellman, J. A., Rhodium-Catalyzed C–C Bond Formation via Heteroatom-Directed C–H Bond Activation. *Chemical Reviews* **2010**, *110* (2), 624-655.
4. Johansson, C. C. C.; Colacot, T. J., Metal-Catalyzed α -Arylation of Carbonyl and Related Molecules: Novel Trends in C–C Bond Formation by C–H Bond Functionalization. *Angewandte Chemie International Edition* **2010**, *49* (4), 676-707.
5. Ritleng, V.; Sirlin, C.; Pfeffer, M., Ru-, Rh-, and Pd-Catalyzed C–C Bond Formation Involving C–H Activation and Addition on Unsaturated Substrates: Reactions and Mechanistic Aspects. *Chemical Reviews* **2002**, *102* (5), 1731-1770.
6. Hull, K. L.; Sanford, M. S., Catalytic and Highly Regioselective Cross-Coupling of Aromatic C–H Substrates. *Journal of the American Chemical Society* **2007**, *129* (39), 11904-11905.
7. Liégault, B.; Fagnou, K., Palladium-Catalyzed Intramolecular Coupling of Arenes and Unactivated Alkanes in Air. *Organometallics* **2008**, *27* (19), 4841-4843.
8. Lin, S.; Song, C.-X.; Cai, G.-X.; Wang, W.-H.; Shi, Z.-J., Intra/Intermolecular Direct Allylic Alkylation via Pd(II)-Catalyzed Allylic C–H Activation. *Journal of the American Chemical Society* **2008**, *130* (39), 12901-12903.
9. Stuart, D. R.; Fagnou, K., The Catalytic Cross-Coupling of Unactivated Arenes. *Science* **2007**, *316* (5828), 1172-1175.
10. Stuart, D. R.; Villemure, E.; Fagnou, K., Elements of Regiocontrol in Palladium-Catalyzed Oxidative Arene Cross-Coupling. *Journal of the American Chemical Society* **2007**, *129* (40), 12072-12073.
11. Young, A. J.; White, M. C., Catalytic Intermolecular Allylic C–H Alkylation. *Journal of the American Chemical Society* **2008**, *130* (43), 14090-14091.
12. Besselièvre, F.; Piguel, S., Copper as a Powerful Catalyst in the Direct Alkynylation of Azoles. *Angewandte Chemie International Edition* **2009**, *48* (50), 9553-9556.

13. de Haro, T.; Nevado, C., Gold-Catalyzed Ethynylation of Arenes. *Journal of the American Chemical Society* **2010**, *132* (5), 1512-1513.
14. Kim, S. H.; Yoon, J.; Chang, S., Palladium-Catalyzed Oxidative Alkynylation of Heterocycles with Terminal Alkynes under Air Conditions. *Organic Letters* **2011**, *13* (6), 1474-1477.
15. Kitahara, M.; Hirano, K.; Tsurugi, H.; Satoh, T.; Miura, M., Copper-Mediated Direct Cross-Coupling of 1,3,4-Oxadiazoles and Oxazoles with Terminal Alkynes. *Chemistry – A European Journal* **2010**, *16* (6), 1772-1775.
16. Matsuyama, N.; Kitahara, M.; Hirano, K.; Satoh, T.; Miura, M., Nickel- and Copper-Catalyzed Direct Alkynylation of Azoles and Polyfluoroarenes with Terminal Alkynes under O₂ or Atmospheric Conditions. *Organic Letters* **2010**, *12* (10), 2358-2361.
17. Parsharamulu, T.; Vishnuvardhan Reddy, P.; Likhari, P. R.; Lakshmi Kantam, M., Dehydrogenative and decarboxylative C–H alkynylation of heteroarenes catalyzed by Pd(II)–carbene complex. *Tetrahedron* **2015**, *71* (13), 1975-1981.
18. Patil, S. S.; Jadhav, R. P.; Patil, S. V.; Bobade, V. D., Ligand and solvent-free iron catalyzed oxidative alkynylation of azoles with terminal alkynes. *Tetrahedron Letters* **2011**, *52* (43), 5617-5619.
19. Wei, Y.; Zhao, H.; Kan, J.; Su, W.; Hong, M., Copper-Catalyzed Direct Alkynylation of Electron-Deficient Polyfluoroarenes with Terminal Alkynes Using O₂ as an Oxidant. *Journal of the American Chemical Society* **2010**, *132* (8), 2522-2523.
20. Yang, L.; Zhao, L.; Li, C.-J., Palladium-catalyzed direct oxidative Heck-Cassar-Sonogashira type alkynylation of indoles with alkynes under oxygen. *Chemical Communications* **2010**, *46* (23), 4184-4186.
21. Sonogashira, K., Development of Pd–Cu catalyzed cross-coupling of terminal acetylenes with sp²-carbon halides. *Journal of Organometallic Chemistry* **2002**, *653* (1), 46-49.
22. Dudnik, A. S.; Gevorgyan, V., Formal Inverse Sonogashira Reaction: Direct Alkynylation of Arenes and Heterocycles with Alkynyl Halides. *Angewandte Chemie International Edition* **2010**, *49* (12), 2096-2098.
23. Shang, M.; Sun, S.-Z.; Dai, H.-X.; Yu, J.-Q., Cu(II)-Mediated C–H Amidation and Amination of Arenes: Exceptional Compatibility with Heterocycles. *Journal of the American Chemical Society* **2014**, *136* (9), 3354-3357.
24. Chinchilla, R.; Nájera, C., The Sonogashira Reaction: A Booming Methodology in Synthetic Organic Chemistry. *Chemical Reviews* **2007**, *107* (3), 874-922.

25. Doucet, H.; Hierso, J.-C., Palladium-Based Catalytic Systems for the Synthesis of Conjugated Enynes by Sonogashira Reactions and Related Alkynylations. *Angewandte Chemie International Edition* **2007**, 46 (6), 834-871.
26. Bandini, M.; Eichholzer, A., Catalytic Functionalization of Indoles in a New Dimension. *Angewandte Chemie International Edition* **2009**, 48 (51), 9608-9644.
27. Buchgraber, P.; Domostoj, M. M.; Scheiper, B.; Wirtz, C.; Mynott, R.; Rust, J.; Fürstner, A., Synthesis-driven mapping of the dictyodendrin alkaloids. *Tetrahedron* **2009**, 65 (33), 6519-6534.
28. Kumar, D.; David, W. M.; Kerwin, S. M., N-propargyl-2-alkynylbenzothiazolium aza-enediyne: role of the 2-alkynylbenzothiazolium functionality in DNA cleavage. *Bioorganic & Medicinal Chemistry Letters* **2001**, 11 (22), 2971-2974.
29. Sato, S.; Shibuya, M.; Kanoh, N.; Iwabuchi, Y., Highly enantioselective intramolecular aza-spiroannulation onto indoles using chiral rhodium catalysis: asymmetric entry to the spiro-[β]-lactam core of chartellines. *Chemical Communications* **2009**, (41), 6264-6266.
30. Gilchrist, T. L., Ring-Opening of Five-Membered Heteroaromatic Anions. *Advances in Heterocyclic Chemistry* **1987**, 41, 41-74.
31. Rewcastle, G. W.; Katritzky, A. R., Generation and Reactions of sp^2 -Carbanionic Centers in the Vicinity of Heterocyclic Nitrogen Atoms. *Advances in Heterocyclic Chemistry* **1993**, 56, 155-302.
32. Sánchez, R. S.; Zhuravlev, F. A., Mechanistic Evidence for a Ring-Opening Pathway in the Pd-Catalyzed Direct Arylation of Benzoxazoles. *Journal of the American Chemical Society* **2007**, 129 (18), 5824-5825.
33. Hahn, F. E.; Tamm, M., Carbenkomplexe aus koordinierten 2-siloxyphenylisocyaniden. *Journal of Organometallic Chemistry* **1993**, 456 (2), C11-C14.
34. Kamer, P. C. J.; Nolte, R. J. M.; Drenth, W., Screw sense selective polymerization of achiral isocyanides catalyzed by optically active nickel(II) complexes. *Journal of the American Chemical Society* **1988**, 110 (20), 6818-6825.
35. Reich, H. J., What's Going on with These Lithium Reagents? *The Journal of Organic Chemistry* **2012**, 77 (13), 5471-5491.
36. Ugi, I., Recent progress in the chemistry of multicomponent reactions. *Pure Appl. Chem.* **2001**, 73 (1), 187-191.
37. Ugi, I.; Lohberger, S.; Karl, R., 4.6 - The Passerini and Ugi Reactions A2 - Trost, Barry M. In *Comprehensive Organic Synthesis*, Fleming, I., Ed. Pergamon: Oxford, 1991; pp 1083-1109.

38. Nguyen, L. T.; Le, T. N.; De Proft, F.; Chandra, A. K.; Langenaeker, W.; Nguyen, M. T.; Geerlings, P., Mechanism of [2 + 1] Cycloadditions of Hydrogen Isocyanide to Alkynes: Molecular Orbital and Density Functional Theory Study. *Journal of the American Chemical Society* **1999**, *121* (25), 5992-6001.

APPENDIX B. TOWARDS COBALT CATALYZED C-H BOND AMINATION AND AN (ONO) LIGAND SCAFFOLD

B.1. Introduction

Additional projects were investigated during the course of my study which involved: (1) catalytic C-H bond amination of aryl sulfonyl azides, (2) the synthesis and characterization of a Co azide complex $[(^o\text{OCO})\text{Co}(\text{N}_3)(\text{MeCN})_2]$, and (3) new synthesis and characterization of an (ONO) ligand scaffold, analogous to the (OCO) pincer, but containing a pyridine linker in place of the medial NHC. Cobalt complexes of the (ONO) ligand are also described.

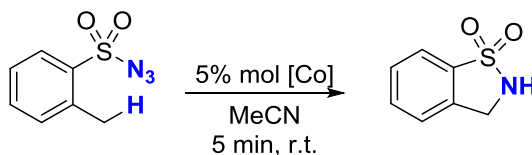
B.2. Project Summaries

B.2.1. C-H Bond Amination of Aryl Sulfonyl Azides

Activation and functionalization of unactivated C-H bonds is an area of fundamental interest and a recurring theme in this thesis. Intramolecular C-H amination represents a particularly attractive target due to the value of the N-atom containing heterocycles produced. Although a number of methods exist for such transformations, transition metal-promoted nitrene insertions are among the most established methodologies.¹⁻⁴ In this regard, azide-containing molecules incorporate a built-in oxidant for the facile generation of metal-nitrenes and serve as an ideal substrate from an atom economic and green chemistry perspective because the only reaction by-product is dinitrogen.

Cobalt porphyrin complexes have previously demonstrated utility in catalytic intramolecular C-H aminations of sulfonyl azides, but in most cases, good yields were only obtained with elevated temperature and prolonged reaction times.⁵⁻⁹ The competency of the cobalt complex $[(^S\text{OCO})\text{Co}(\text{THF})]$ as a catalyst for intramolecular C-H amination of such substrates was evaluated using 2-methylbenzenesulfonyl azide as illustrated in Scheme B.1. Treating 5% mol loading of Co complex with the aryl azide in MeCN at ambient temperature gave the desired N-heterocycle product in *ca.* 30% yield in 5 min., as determined by GC-MS. No further optimizations studies were performed.

Scheme B.1. Cobalt catalyzed C-H amination of aryl sulfonyl azide.



B.2.2. Synthesis and Characterization of an (^SOCO) Cobalt Azide Complex

Metal nitrido complexes have also been invoked as intermediates in C-H bond aminations. In one example, Chirik and co-workers reported a cobalt azide complex capable of photolytic or thermally-induced *intramolecular* C-H amination of the coordinated tridentate ligand via a proposed Co-nitrido intermediate.¹⁰ We proposed if the azide coordinated to the metal center was positioned outside of the ligand plane, the system may be capable of *intermolecular* C-H activation of a non-coordinated substrate. We therefore sought to synthesize an (OCO)-cobalt derived azide complex by treating the complex $[(^S\text{OCO})\text{Co}(\text{MeCN})_2][\text{OTf}]$ with sodium azide in MeOH (Scheme B.2). Following workup and recrystallization from MeCN, the complex was determined to

consist of an octahedral geometry in which the azide was coordinated perpendicular to the (OCO) ligand plane and the coordination sphere was completed by two MeCN ligands as shown in Figure B.1. No further studies were performed with this complex.

Scheme B.2. Synthesis of $[(^S\text{OCO})\text{Co}(\text{N}_3)(\text{MeCN})_2]$.

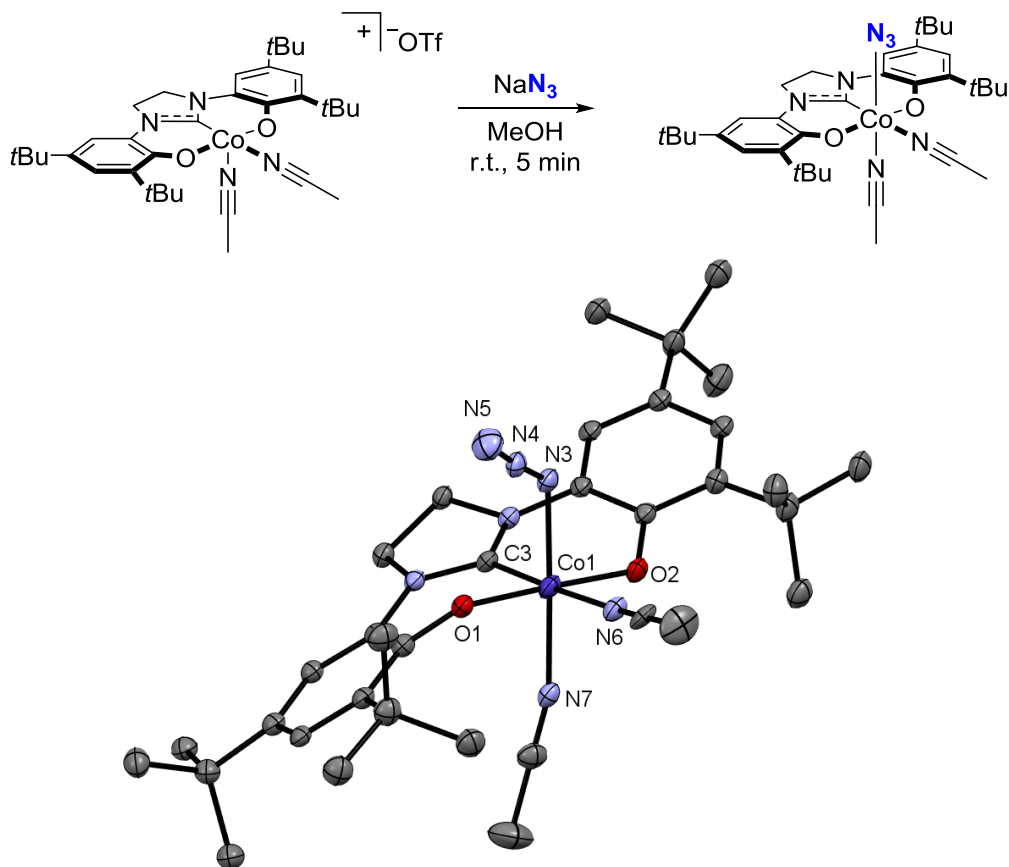
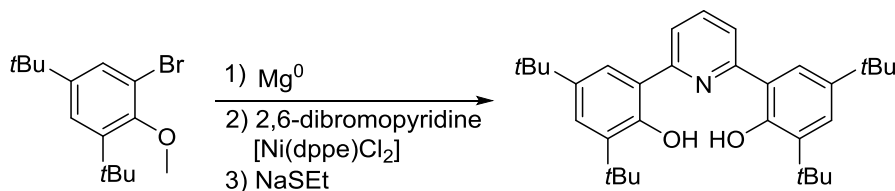


Figure B.1. ORTEP plot of $[(^S\text{OCO})\text{Co}(\text{N}_3)(\text{MeCN})_2]$. Thermal ellipsoids are drawn at 50% probability. Hydrogen atoms and non-coordinated solvent molecules have been removed for clarity. Selected bond lengths (Å): Co1–C3 1.863(7), Co1–O1, 1.898(5); Co1–O2, 1.884(5); Co1–N3, 1.929(6); Co1–N6, 2.039(7); Co1–N7, 1.964(7).

B.2.3. Synthesis and Characterization of (ONO) Cobalt Complexes

As described in Chapter 2, the major decomposition pathway for Co complexes containing the (^sOCO) ligand is reductive elimination to the carbene in the NHC ligand backbone, forming new C–C or C–N bonds. It seemed reasonable that a different central donor in the tridentate pincer might be less prone to this degradation. Our initial target replaced the NHC with a pyridine, under the assumption that C–N reductive elimination to backbone might be suppressed relative to the carbene. Accordingly, an (ONO) ligand was synthesized via a modified literature procedure,¹¹ involving a nickel-catalyzed Kumada-type coupling of a methyl-protected phenoxy Grignard reagent and 2,6-dibromopyridine, followed by deprotection with NaSEt (Scheme B.3). Metalation was accomplished by treating a solution of [Co(MeCN)₆](BF₄)₂ in MeCN with a solution of the deprotonated ligand in THF (Scheme B.4). A solid-state structure, obtained from crystals grown in MeCN at -25°C, revealed that the complex forms an eclipsed dimer in the solid-state which bridges through two cobalt-phenoxide bonds (Figure B.2). No Co–Co bond is formed, as the distances are beyond the van der Waals radii of two Co^{II} centers at 2.942(4) Å. The complex exhibits a paramagnetically shifted ¹H NMR spectrum in CDCl₃ solution, however further magnetic measurements are necessary to assign the spin state.

Scheme B.3. Synthesis of the ONO ligand.



Scheme B.4. Synthesis of the complex [(ONO)Co(MeCN)]₂.

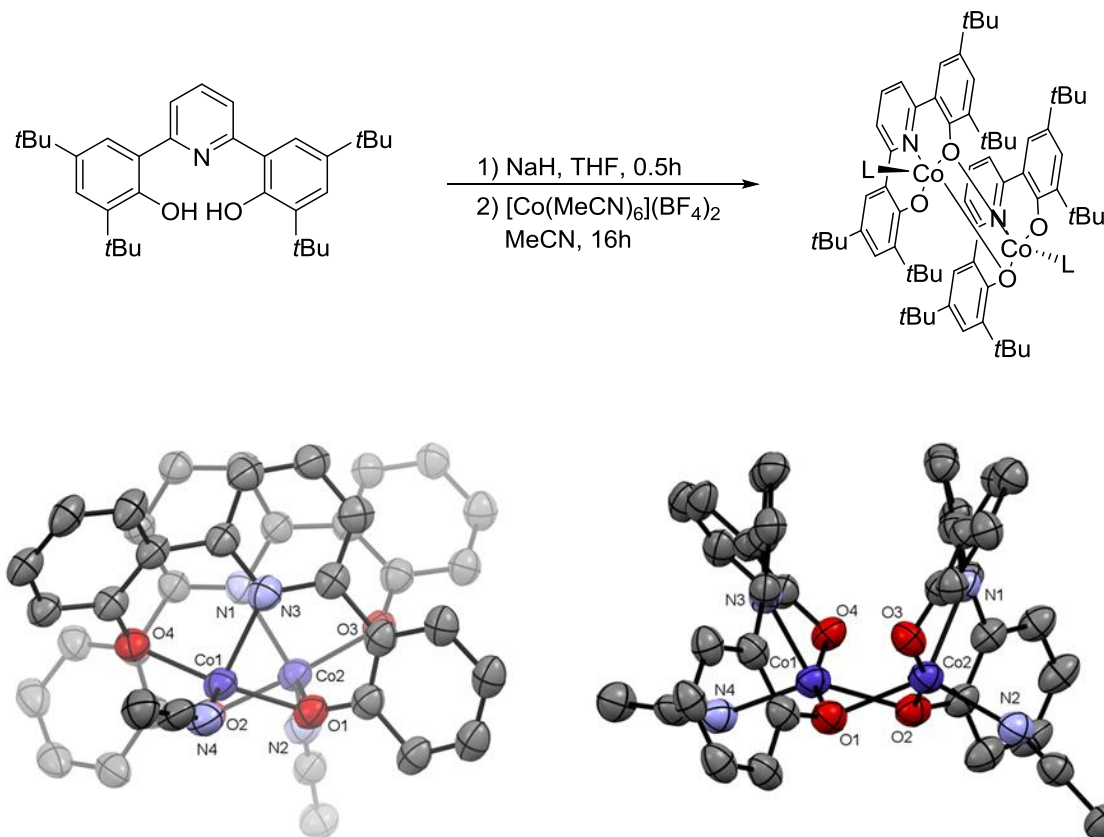


Figure B.2. ORTEP plots of complex [(ONO)Co(MeCN)]₂ as viewed from the front (left) and the side (right). Thermal ellipsoids are drawn at 50% probability. The tert-butyl groups and hydrogen atoms have been removed for clarity. Selected bond lengths (Å): Co1–O1, 1.967(3), Co1–O4, 1.910(3), Co1–N3, 2.136(4), Co1–N4, 2.132(4), Co2–O2, 1.988(3), Co2–O3, 1.901(3), Co2–N1, 2.120(4), Co2–N2, 2.071(4), Co1–O2 2.063(3), Co2–O1, 2.080(3).

Crystals of the complex are dimeric when produced from most solvents, but strong donors such as pyridine separate the complex into its monomeric form. Figure B.3 shows a crystal structure of the complex [(ONO)Co(py)₃] obtained from a pyridine/MeCN solution in which three ligated pyridines act to complete the pseudo-octahedral coordination sphere. Addition of various ionic compounds to either the monomer or dimer affords significant changes in solution color that are specific to the

anion introduced. For instance, the stoichiometric addition of sodium pyrrolide to a golden colored solution of $[(\text{ONO})\text{Co}(\text{MeCN})]_2$ in MeOH resulted in an immediate color change to deep blue; additional equivalents resulted in the formation of a purple color. When one equivalent of LiCl and a slight excess of 12-crown-4 were added instead, an emerald green colored solution was observed. The identity of the substance responsible for producing the green color was determined by X-ray diffraction and assigned as the salt $[(\text{ONO})\text{Co}^{\text{II}}\text{Cl}](\text{Li-12-c-4})$ (Figure B.4). This system may offer potential applications in anion sensing, but no further studies are needed.

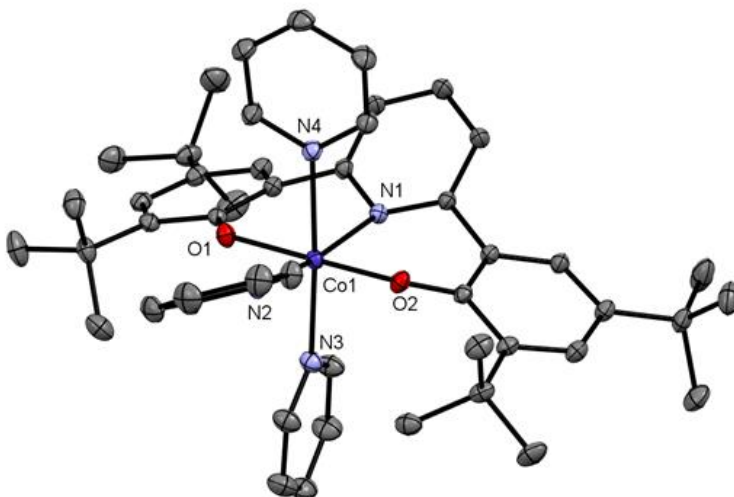


Figure B.3. ORTEP plot of [(ONO)Co(py)₃]. Thermal ellipsoids are drawn at 50% probability. The rotational disorder of the tert-butyl groups and hydrogen atoms have been removed for clarity. Selected bond lengths (Å): Co1–O1, 1.9730(8), Co1–O2, 1.9666(8), Co1–N1, 2.1676(9), Co1–N2, 2.1972(10), Co1–N3, 2.2161(10), Co1–N4, 2.2611(10).

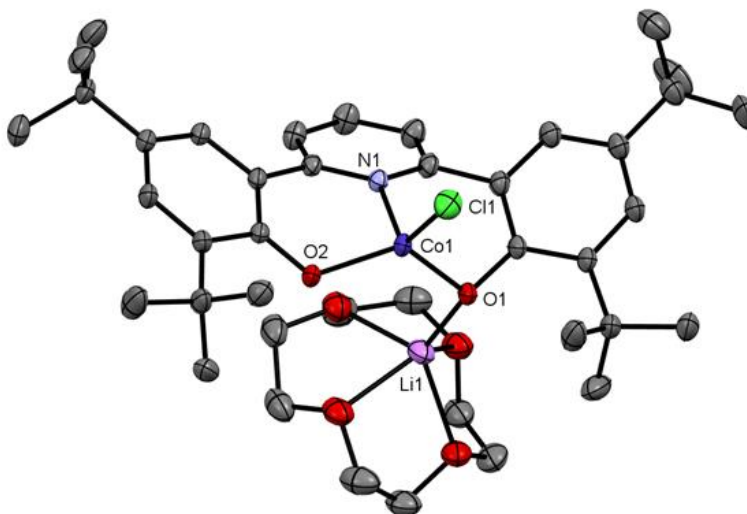


Figure B.4. ORTEP plot of [(ONO)Co^{II}Cl](Li-12-c-4). Thermal ellipsoids are drawn at 50% probability. The rotational disorder of the tert-butyl groups and hydrogen atoms have been removed for clarity. Selected bond lengths (Å): Co1–Cl1 2.2482(7), Co1–O1 1.9793(17), Co1–O2, 1.9024(17), Co1–N1, 2.014(2).

B.3. Experimental

B.3.1. General Considerations

Unless otherwise specified, all manipulations were performed under anaerobic conditions using standard vacuum line techniques, or in an inert atmosphere glove box under purified nitrogen. Routine NMR spectra were acquired on either a Varian Mercury 300 spectrometer (300.323 MHz for ^1H ; 75.5 MHz for ^{13}C) or a Varian Mercury 400 spectrometer (399.94 MHz for ^1H ; 101.1 MHz for ^{13}C). UV-visible absorption spectra were acquired using a Varian Cary 50 spectrophotometer. Unless otherwise noted, all electronic absorption spectra were recorded at ambient temperatures in 1 cm quartz cells. IR absorption spectra were obtained using a Shimadzu 8400S Fourier transform infrared spectrophotometer or a Perkin Elmer 1000 FT-IR spectrophotometer. All mass spectra were recorded in the Georgia Institute of Technology Bioanalytical Mass Spectrometry Facility.

B.3.2. Synthesis of the *ONO* Ligand

A 3-necked flask was fitted with an addition funnel and condenser and charged with Mg (0.92 g; 38.0 mmol) and anhydrous THF (30 mL). The addition funnel was charged with a solution of 1-bromo-3,5-di-*tert*-butyl-2-methoxybenzene (10.5 g; 35.0 mmol) and a single crystal of iodine in THF (20 mL). The magnesium suspension was heated to 65 °C (just below the b.p. of THF) and 1-bromo-3,5-di-*tert*-butyl-2-methoxybenzene was added at a rate which produced a hard reflux. Upon complete addition of the aryl halide, the solution was heated to reflux for 1 hour. The solution was then cooled to 0 °C, filtered under nitrogen, and added dropwise to a separate 250 mL

RBF charged with a suspension of 2,6-dibromopyridine (3.77 g; 15.9 mmol) and Ni(dppe)Cl₂ (668 mg; 1.27 mmol) in THF (30 mL) at 0 °C. After heating the solution to reflux for 16 h, the reaction was cooled to r.t. and quenched with water (75 mL). THF was removed by rotary evaporation, producing an orange colored precipitate which was collected by suction filtration. The light orange colored solid was then suspended in MeOH (50 mL), vigorously stirred for 15 mins and then placed in a freezer at -50 °C. The resulting white solid was filtered off and washed with a minimal amount of cold MeOH until the washings ran colorless, providing the methyl-protected ONO precursor which was not purified further before the deprotection. Demethylation of the phenoxides was performed with NaSEt as previously described.¹¹

B.3.3. Synthesis of [$^{13}\text{C}(\text{OCO})\text{Co}(\text{N}_3)(\text{MeCN})_2$]

A solution of [$^{13}\text{C}(\text{OCO})\text{Co}(\text{MeCN})_2$][OTf] (172 mg; 0.22 mmol) in MeOH (5 mL) was treated with NaN₃ (14.5 mg; 0.22 mmol) and stirred for 5 mins. All volatiles were then removed *in vacuo* and MeCN was added to the resulting solid material. The suspension was filtered and stored at -25 °C for 16 h, affording dark green crystals suitable for X-ray analysis (107 mg, 0.16 mmol, 72%). FTIR (ATR): 2947(m), 2900(m), 2866(m), 2128(w), 2061(m), 2017(w), 1597(w), 1477(s), 1438(s), 1988(m), 1358(m), 1315(s), 1239(m), 1201(m), 1073(w), 835(m), 760(m), 675(m), 642(w), 576(w), 497(w), 396(w) cm⁻¹.

B.3.4. Synthesis of [(ONO)Co(MeCN)]₂

A 20 mL scintillation vial was charged with a solution of the ONO proligand (487 mg; 1.00 mmol) in THF (8 mL) and NaH (49.2 mg; 2.05 mmol) was added in one portion

at ambient temperature. The suspension was stirred until the bubbling ceased (~30 m). The deprotonated ligand solution was passed through a 2.5 micron syringe filter and added dropwise to a homogenous solution of $\text{Co}(\text{BF}_4)_2 \cdot \text{MeCN}_6$ (479 mg; 1.00 mmol) in MeCN (8 mL). The resulting golden colored solution was stirred at room temperature for 1 hour and then concentrated in vacuo, affording a yellow-green colored solid. The solid was dissolved in THF and layered with pentane, producing yellow-green crystals suitable for X-ray analysis (504 mg; 0.43 mmol; 86%). UV-vis (THF) λ_{max} , nm (ϵ , L/mol*cm): 371 (19.2×10^3). FTIR (ATR): 2949(m), 2900(m), 2865(m), 1627(w), 1477(s), 1449(s), 1389(m), 1357(m), 1325(s), 1285(m), 1236(m), 1201(m), 1073(w), 982(w), 842(m), 760(m), 701(m), 678(m), 644(m), 579(m), 514(m), 434(m), 413(m) cm^{-1} .

B.3.5. Synthesis of $[(\text{ONO})\text{Co}(\text{py})_3]$

The complex $[(\text{ONO})\text{Co}(\text{MeCN})]_2$ was dissolved in MeCN and pyridine (10 eq.) was added. The solution was stored at -25°C for 16 h, affording golden crystals suitable for X-ray analysis (94% yield). UV-vis (benzene) λ_{max} , nm (ϵ , L/mol*cm): 349 (16.8×10^3), 403 (12.1×10^3).

B.4. X-ray Crystallography

B.4.1. General Considerations

Unless otherwise noted, X-ray diffraction data were collected using a Bruker APEX-II CCD diffractometer equipped with an Oxford Cryosystems low-temperature apparatus. Unit cell indexing was performed by using the APEX2 (Bruker) software. Data were measured with MoK_α radiation (fine-focus sealed tube, 45 kV, 35 mA). The

total number of runs and images was based on the strategy calculation from the program **APEX2** (Bruker). Unit cell indexing was performed by using the **APEX2** (Bruker) software and refined using **SAINT** (Bruker, V8.34A, 2013). Data reduction, scaling and absorption corrections were performed using **SAINT** (Bruker, V8.34A, 2013) and **SADABS-2014/5** (Bruker, 2014) was used for absorption correction. The $\lambda/2$ correction factor is 0.00150. The software also corrects for Lorentz polarization. The crystal structures were refined by Least Squares using version 2014/7 of **XL** (Sheldrick, 2008). All non-hydrogen atoms were refined anisotropically. Hydrogen atom positions were calculated geometrically and refined using the riding model.

B.4.2. $[(^S\text{OCO})\text{Co}(\text{N}_3)(\text{MeCN})_2]$

A prism-shaped crystal with dimensions 0.299×0.146×0.05 mm was mounted on a loop with paratone oil. X-ray diffraction data were collected at $T = 100(2)^\circ\text{K}$. The maximum resolution achieved was $\Theta = 24.711^\circ$.

Unit cell indexing was performed and refined based on 17947 reflections, 37% of the observed reflections. The ratio of minimum to maximum transmission is 0.8753. The final completeness is 99.4% out to 24.711° in Θ .

The structure was solved in the space group P-1 (#2) with the **ShelXT** (Sheldrick, 2015) structure solution program using combined Patterson and dual-space recycling methods.

B.4.3. $[(ONO)Co(MeCN)]_2$

A yellow, prism-shaped crystal with dimensions 0.65×0.16×0.14 mm was mounted on a loop with paratone oil. X-ray diffraction data were collected at $T = 100(2)$ °K. The maximum resolution achieved was $\Theta = 24.709^\circ$.

Unit cell indexing was performed on 9857 reflections, 36% of the observed reflections. $wR_2(\text{int})$ was 0.1730 before and 0.0738 after correction. The ratio of minimum to maximum transmission is 0.6290. The final completeness is 97.8% out to 24.709° in Θ . The absorption coefficient (μ) of this material is 0.463mm^{-1} and the minimum and maximum transmissions are 0.6290 and 1.0000.

The structure was solved with the **ShelXT** (Sheldrick, 2015) structure solution program using combined Patterson and dual-space recycling methods. The space group $P2_1/c$ was determined by **ShelXT** (Sheldrick, 2015) structure solution program.

B.4.4. $[(ONO)Co(py)_3]$

A prism-shaped crystal with dimensions 0.499×0.304×0.234 mm was mounted on a loop with paratone oil. X-ray diffraction data were collected at $T = 100(2)$ °K. The maximum resolution achieved was $\Theta = 37.02^\circ$.

Unit cell indexing was performed and refined based on 82104 reflections, 26% of the observed reflections. The ratio of minimum to maximum transmission is 0.8753. The final completeness is 96.4% out to 37.02° in Θ .

The structure was solved in the space group $P2_1/c$ (#14) with the **ShelXT** (Sheldrick, 2015) structure solution program using combined Patterson and dual-space recycling methods.

B.5. References

1. Delphine, K.; Robert, H. D., Recent Progress in Iminoiodane-Mediated Aziridination of Olefins. *Current Organic Chemistry* **2011**, *15* (10), 1507-1538.
2. Dequierez, G.; Pons, V.; Dauban, P., Nitrene Chemistry in Organic Synthesis: Still in Its Infancy? *Angewandte Chemie International Edition* **2012**, *51* (30), 7384-7395.
3. Díaz-Requejo, M. M.; Pérez, P. J., Coinage Metal Catalyzed C–H Bond Functionalization of Hydrocarbons. *Chemical Reviews* **2008**, *108* (8), 3379-3394.
4. Jason, A. H., Recent Advances in Metal-Mediated Carbon-Nitrogen Bond Formation Reactions: Aziridination and Amidation. *Current Organic Chemistry* **2005**, *9* (7), 657-669.
5. Jiang, H.; Lang, K.; Lu, H.; Wojtas, L.; Zhang, X. P., Intramolecular Radical Aziridination of Allylic Sulfamoyl Azides by Cobalt(II)-Based Metalloradical Catalysis: Effective Construction of Strained Heterobicyclic Structures. *Angewandte Chemie International Edition* **2016**, *55* (38), 11604-11608.
6. Lu, H.; Hu, Y.; Jiang, H.; Wojtas, L.; Zhang, X. P., Stereoselective Radical Amination of Electron-Deficient C(sp³)–H Bonds by Co(II)-Based Metalloradical Catalysis: Direct Synthesis of α -Amino Acid Derivatives via α -C–H Amination. *Organic Letters* **2012**, *14* (19), 5158-5161.
7. Lu, H.; Lang, K.; Jiang, H.; Wojtas, L.; Zhang, X. P., Intramolecular 1,5-C(sp³)-H radical amination via Co(II)-based metalloradical catalysis for five-membered cyclic sulfamides. *Chemical Science* **2016**, *7* (12), 6934-6939.
8. Lu, H.; Li, C.; Jiang, H.; Lizardi, C. L.; Zhang, X. P., Chemoselective Amination of Propargylic C(sp³)-H Bonds by Cobalt(II)-Based Metalloradical Catalysis. *Angewandte Chemie International Edition* **2014**, *53* (27), 7028-7032.
9. Lyaskovskyy, V.; Suarez, A. I. O.; Lu, H.; Jiang, H.; Zhang, X. P.; de Bruin, B., Mechanism of Cobalt(II) Porphyrin-Catalyzed C–H Amination with Organic Azides: Radical Nature and H-Atom Abstraction Ability of the Key Cobalt(III)–Nitrene Intermediates. *Journal of the American Chemical Society* **2011**, *133* (31), 12264-12273.
10. Hojilla Atienza, C. C.; Bowman, A. C.; Lobkovsky, E.; Chirik, P. J., Photolysis and Thermolysis of Bis(imino)pyridine Cobalt Azides: C–H Activation from Putative Cobalt Nitrido Complexes. *Journal of the American Chemical Society* **2010**, *132* (46), 16343-16345.
11. Agapie, T.; Bercaw, J. E., Cyclometalated Tantalum Diphenolate Pincer Complexes: Intramolecular C–H/M–CH₃ σ -Bond Metathesis May Be Faster than O–H/M–CH₃ Protonolysis. *Organometallics* **2007**, *26* (12), 2957-2959.

VITA

Caleb was born in Greenville, North Carolina in September 1983, and grew up in parts of eastern North Carolina. He attended both Roanoke Rapids High School and West Carteret High School, graduating in 2001. In 2010, he graduated from East Carolina University with a B.A. in chemistry and a minor in neuroscience. He remained at East Carolina University an additional two years where he obtained his M.S. in organic chemistry under the supervision of Professor Shouquan Huo. Afterwards, he began graduate school at the Georgia Institute of Technology in Atlanta, Georgia where he worked in Professor Jake Soper's laboratory, earning his Ph.D. in inorganic chemistry in 2017. He will begin his postdoctoral studies under the supervision of Professor John F. Berry at the University of Wisconsin – Madison in the Fall of 2017.